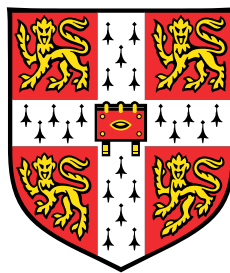


Kinematics and Dynamics of Continental Deformation



Camilla Emily Penney

Department of Earth Sciences
University of Cambridge

This dissertation is submitted for the degree of
Doctor of Philosophy

Kinematics and Dynamics of Continental Deformation

Camilla Emily Penney

In contrast to the oceans, deformation in the continental lithosphere is distributed over broad regions. This dissertation is composed of three separate but related studies investigating the kinematics and dynamics of such deformation. The first two studies look at the Makran subduction zone, and the third focusses on deformation in South East Tibet.

The first study is an investigation of the 11 May 2013 M_w 6.1 Minab earthquake which occurred at the western end of the Makran subduction zone, adjacent to the transition to continent-continent collision in the Zagros mountains. Seismological, geodetic and field results are used to study the source parameters and slip distribution of this earthquake, and demonstrate that the earthquake was left-lateral and occurred on a fault striking ENE–WSW; approximately perpendicular to previously studied faults in the adjacent Minab-Zendan-Palami fault zone. Geological and geomorphological observations of similar faults in the vicinity are used to infer that vertical-axis rotations allow a series of such faults to accommodate $\sim 15\text{--}19$ mm/yr of N–S right-lateral shear. The dynamic implications for the transition between subduction and continental collision are discussed.

The second study looks at the Makran region as a whole. First, the shape and depth of the interface with the Arabian plate is constrained by modelling the depths and mechanisms of earthquakes across the region, and combining these with additional seismological constraints. These constraints on the subduction interface are used to investigate elastic strain accumulation on the megathrust in the western Makran, which has important implications for seismic and tsunami hazard in the region. Second, the kinematics at the northern edge of the Makran accretionary prism are investigated using a combination of geodetic and geomorphological observations, addressing the long-standing tectonic problem of how the right-lateral shear taken up by strike-slip faulting in the Sistan Suture Zone in eastern Iran is accommodated at the zone's southern end. Finally, the kinematics and dynamics of the accretionary prism are investigated. By considering the kinematics of the 2013 Balochistan and Minab earthquakes, local gravitational and far-field compressive forces in the Makran accretionary prism are inferred to be balanced. This force balance allows the mean shear stress and effective coefficient of friction on the Makran megathrust to be calculated, 5–35 MPa and 0.01–0.03 respectively.

The final part of this thesis focusses on the temporal evolution of topography in South East Tibet. Recently published paleoaltimetry results based on stable-isotope geochemistry are used to provide constraints on vertical motions. These demonstrate that uplift is much slower than had previously been suggested from thermochronometric data. Numerical modelling of the time evolution of a gravitationally-driven fluid is used to investigate the effect of lateral rheological contrasts on the shape and evolution of topography. In such a flow, material at the surface can be transported hundreds of kilometres, an effect which should be accounted for in paleoaltimetric analysis. Lateral rheological contrasts, analogous to the relatively undeforming Sichuan Basin and Central Lowlands of Myanmar, can reproduce the main features of the present-day topography, GPS velocity field and earthquake-derived strain rate without the need for a low-viscosity lower-crustal channel.

Declaration

I hereby declare that except where specific reference is made to the work of others, the contents of this dissertation are original and have not been submitted in whole or in part for consideration for any other degree or qualification in this, or any other university. This dissertation is my own work and contains nothing which is the outcome of work done in collaboration with others, except as specified in the text and Acknowledgements. This dissertation contains fewer than 275 numbered pages of which not more than 225 pages are text, appendices, illustrations and bibliography.

Camilla Emily Penney
August 2018

“To add to their difficulties, the time came when the guides admitted that they no longer knew the way; all the marks, they declared, had been obliterated by the blown and drifting sand. There was nothing in the vast and featureless desert to determine what course they should take - no trees, as elsewhere, by the roadside, no hills of solid earth rising from the sand.”

Arrian (*Alexander in the Gedrosian Desert*, Anabasis 6.26.4)

Acknowledgements

I would like to start by thanking my supervisors, Alex Copley and James Jackson. Alex's generosity with his time and ideas, has been invaluable in teaching me how to go about understanding tectonics and the Earth. I am very grateful to have had both space to learn and solve problems for myself, and a willing source of discussion and encouragement. James' encouragement to improve my geological understanding has, eventually, allowed me to add the "geo" to my "physicist", and his simultaneous attention to detail and understanding of the bigger picture has improved the work in this dissertation immeasurably.

The work in this dissertation would not have been possible without the help of collaborators in Iran and Pakistan. Benham Ovesi made the field observations after the Minab earthquake. Farokh Tavakoli, Abdolreza Saadat, Hamid Reza Nankali, Morteza Sedighi and Fateme Khorrami at the National Cartographic Centre in Iran collected and processed the new GPS data used in Chapter 3. Farhad Sobouti and Zahid Rafi provided seismic data for the receiver functions in Chapter 3. I would also like to thank Morteza Talebian, at the Geological Survey of Iran, and Karim Aoudia, at ICTP Trieste, for making it possible for me to visit Iran and meet with other scientists interested in the Makran region.

I would not have started down this route at all without James' first year lectures on earthquake hazard, and I wouldn't have got much further without the help of Arwen Deuss, who was first an excellent supervisor, and has remained an excellent mentor and role model. I would also like to thank Keith Priestley, who, in addition to carrying out the receiver function analysis in this paper, gave me my first insights into the world of seismic data and allowed me to go to Jammu and Kashmir to catch the fieldwork bug.

The Tectonics group at Bullard has been a great source of support, laughter and, of course, scientific discussion throughout my PhD. Thanks to Grace, Kirsty and Andy for leading the way and showing me that writing a thesis can be less stressful than moving house, Christoph and Romain, for sharing their expertise and enthusiasm, and Thomasina, Sam, Jonny, Kieran, Beth and Alice for interesting discussions, gossip and furthering my understanding of geology and tectonics.

Bullard has been a great place to do a PhD, largely thanks to the people. Coffee time has been the source of many interesting discussions, an occasion which, like much of the rest of Bullard, would cease to function without the hard work of Joyce and Gill. Ian and Dave have been invaluable in helping to fix various computer problems. I have really enjoyed connecting with people across the department, and I am particularly grateful to Sasha, Sanne and Lotty for their advice on negotiating the academic world.

I have also been lucky to have excellent house mates in Ophelia and Jenny. Who knows how much I more might have achieved were it not for the eternal pile of cryptic crosswords gracing our kitchen tables. CUHWC has also been a welcome distraction from research,

providing regular reminders that there is a world outside Cambridge which isn't flat. Pembroke College has been a great source of both funding and friends. My time there would have been a lot less entertaining without Emily, Catherine, Lizzie and my other fellow New Court-ers, physicists and GP friends. I am particularly grateful to Hannah and Matt for having kept me company for all these years. From that perspective, I would also like to thank Ella and Saskia, for over half a lifetime of friendship and intellectual stimulus.

Finally, I would like to thank my family – Auntie V for being my greatest reader, Dad, for forgetting to persuade me not to do a PhD and for being sympathetic to the woes of coding in ancient Fortran, Mum, for her willingness to listen and advice, particularly on the subject of camels, Sophie, for understanding Cambridge and being the pragmatic one, and Tom, who understands more about what I do than any other art historian is ever likely to. Last of all, Chris, for being there for me through all the ups and and downs of the last seven years, and without whom I would never have known the answer to the question “how do you write a PhD thesis?” Hello to Jason Isaacs.

Table of contents

List of figures	xv
List of tables	xvii
1 Introduction	1
1.1 Background and motivation	1
1.2 Overview	8
1.2.1 Chapter 2	8
1.2.2 Chapter 3	9
1.2.3 Chapter 4	9
1.2.4 Chapter 5	10
1.2.5 Chapter 6	11
I The Makran Subduction Zone	13
2 Subduction tractions and vertical axis rotations in the Zagros-Makran transition zone, SE Iran: the 11 May 2013 Mw 6.1 Minab earthquake	15
2.1 Introduction	17
2.2 Body-Waveform Modelling	17
2.3 Constant Slip Inversion of InSAR data	20
2.4 Distributed Slip Inversion of InSAR data	22
2.5 Field Observations and Geomorphology	26
2.6 Discussion	30

2.6.1	Regional Tectonics	31
2.6.2	Relationship to Slab Geometry	33
2.6.3	Strike-Slip Faulting in the Accretionary Wedge	33
2.7	Conclusions	35
3	Megathrust properties and behaviour in the Makran subduction zone	37
3.1	Introduction	37
3.2	Shape and Location of the Subduction Interface	40
3.2.1	Earthquake Compilation	40
3.2.2	Receiver Functions	43
3.2.3	Interpretation of Subduction Interface Geometry	45
3.3	Elastic Strain Accumulation on the Subduction Interface	48
3.4	Conclusions	52
4	Southern Termination of N–S Strike-Slip Faulting in the Sistan Suture Zone	53
4.1	Introduction	54
4.2	Thrust Faulting	55
4.3	Vertical-Axis Rotations	57
4.4	The Jaz Murian Depression as an Extensional Basin	61
4.4.1	Slip Rates	61
4.4.2	Geomorphology	62
4.4.3	Temporal Strain Variations	64
4.5	Conclusion	65
5	Dynamics of accretionary prism deformation	67
5.1	Introduction	67
5.2	Strike-Slip Faulting on the Wedge Top	70
5.3	Megathrust Shear Stress	74

II	South East Tibet	77
6	The role of lateral rheology contrasts in the evolution of mountain ranges	79
6.1	Introduction	80
6.2	Regional Kinematics	82
6.3	Palaeoaltimetry	86
6.4	Dynamical modelling	90
6.4.1	Previous models	90
6.4.2	Model set-up	92
6.4.3	Results	96
6.5	Discussion	102
6.6	Conclusions	108
7	Concluding remarks	109
	References	113
	Appendix A Body-Waveform Modelling	133
	Appendix B Earthquake Compilation	143
	Appendix C Vertical-Axis Rotations	149
C.1	Vertical-Axis Rotations accommodating Simple Shear	149
C.2	Vertical-Axis Rotations accommodating Pure Shear	150
	Appendix D Calculating the temporal evolution of topography	155

List of figures

1.1	Map showing the locations discussed in this dissertation.	2
2.1	Map of the western Makran	16
2.2	Body-waveform modelling solution for Minab earthquake	19
2.3	Constant slip modelling of InSAR data	21
2.4	Distributed slip inversion of InSAR data	23
2.5	Misfit-roughness trade-off for distributed slip inversion	25
2.6	Surface expression of faulting	27
2.7	Locations of left-lateral faults and aftershocks	28
2.8	Satellite images of activity faulting near the Minab 2013 earthquake	29
2.9	Kinematics of the Minab earthquake	32
2.10	Dynamics of the transition from continent-continent collision to subduction	34
3.1	Map of the Makran	39
3.2	Earthquakes in the Makran	42
3.3	Receiver functions from CHBR and TURB	44
3.4	Profiles through Makran earthquake distribution	47
3.5	Elastic strain accumulation in the western Makran	50
4.1	Possible methods of accommodating right-lateral motion	56
4.2	Slip rates required on E–W striking left-lateral faults	58
4.3	Rotation and structural trends across the Makran	60
4.4	Geomorphology of the Jaz Murian depression	63

5.1	Earthquakes in the Makran	69
5.2	Kinematics of the Hoshab fault	71
5.3	Accommodation of N–S shortening (pure shear) by vertical-axis rotations	73
5.4	Megathrust rheology	75
6.1	Major active faults and earthquakes in South East Tibet	81
6.2	Filtered topography and GPS in South East Tibet	84
6.3	Results of stable-isotope palaeoaltimetry studies in South East Tibet	87
6.4	Model Geometry	93
6.5	Modelling results for symmetric model	97
6.6	Effect of changing basal thickness	99
6.7	Effect of changing inter-basin width	101
6.8	Modelling results for asymmetric model	103
A.1	Body-waveform modelling solution for 12th May 2013 A	134
A.2	Body-waveform modelling solution for 12th May 2013 B	135
A.3	Body-waveform modelling solution for 7th February 2017	136
A.4	Body-waveform modelling solution for 18th January 2011	137
A.5	Body-waveform modelling solution for 25th October 2009	138
A.6	Body-waveform modelling solution for 18th July 2006	139
A.7	Body-waveform modelling solution for 13th March 2005	140
A.8	Body-waveform modelling solution for 14th January 2003	141
A.9	Body-waveform modelling solution for 17th December 1992	142
C.1	Geometry of vertical-axis rotations accommodating simple shear	151
C.2	Geometry of vertical-axis rotations accommodating pure shear	151

List of tables

2.1	Source parameters of 2013 Minab earthquake	22
2.2	Velocity model used for distributed slip inversion	24
B.1	Source parameters of well-constrained earthquakes in the Makran	144

Chapter 1

Introduction

1.1 Background and motivation

The strength of the lithosphere provides a first-order control on the distribution of strain within it. Strength, here, means resistance to deformation, which might be in the stresses transmitted across faults in the brittle part of the lithosphere, or ductile stress controlled by the hotter parts of the lithosphere, depending on the time and length scales being considered. The strength, and relative homogeneity, of oceanic lithosphere allows large regions to be described as essentially undeforming tectonic plates, with strain focussed along their edges. The theory of Plate Tectonics (McKenzie and Parker, 1967) describes the velocities of these plates (kinematics) without reference to the driving forces (dynamics). In contrast, strain in the continental lithosphere is distributed inhomogeneously over wide regions (e.g. McKenzie, 1972) and the velocities at the boundaries of the continents do not predict their interior motion (Jackson and McKenzie, 1988; England and Jackson, 1989). This distribution of strain means that the kinematics of continental deformation depend on both the forces applied to the continental lithosphere and its material properties (rheology, e.g. Molnar, 1988). The distributed nature of continental deformation leads to spectacular geographic features, such as mountains and plateaux, but also poses a societal challenge – how to mitigate earthquake hazard across these vast areas. As populations concentrate into megacities, the locations of which are often determined by the active faulting (e.g. Jackson et al., 2002; Talebian et al., 2016; Grützner et al., 2017), understanding the mechanics of active faults and the behaviour of the systems of such faults which make up deforming continental regions is increasingly important (e.g. Bilham et al., 2007; England and Jackson, 2011). This dissertation uses techniques from seismology, geodesy, fluid dynamics, elastic-dislocation modelling, geochemistry and geomorphology to study the kinematics of continental deformation in two regions of the Alpine-Himalayan belt (Figure 1.1), and then suggests dynamical explanations, with

particular reference to the spatial and temporal variation in the forces and rheology controlling continental deformation. These regions have been chosen because recent observations allow new insights in their kinematics, which can then be used to make progress in understanding continental dynamics.

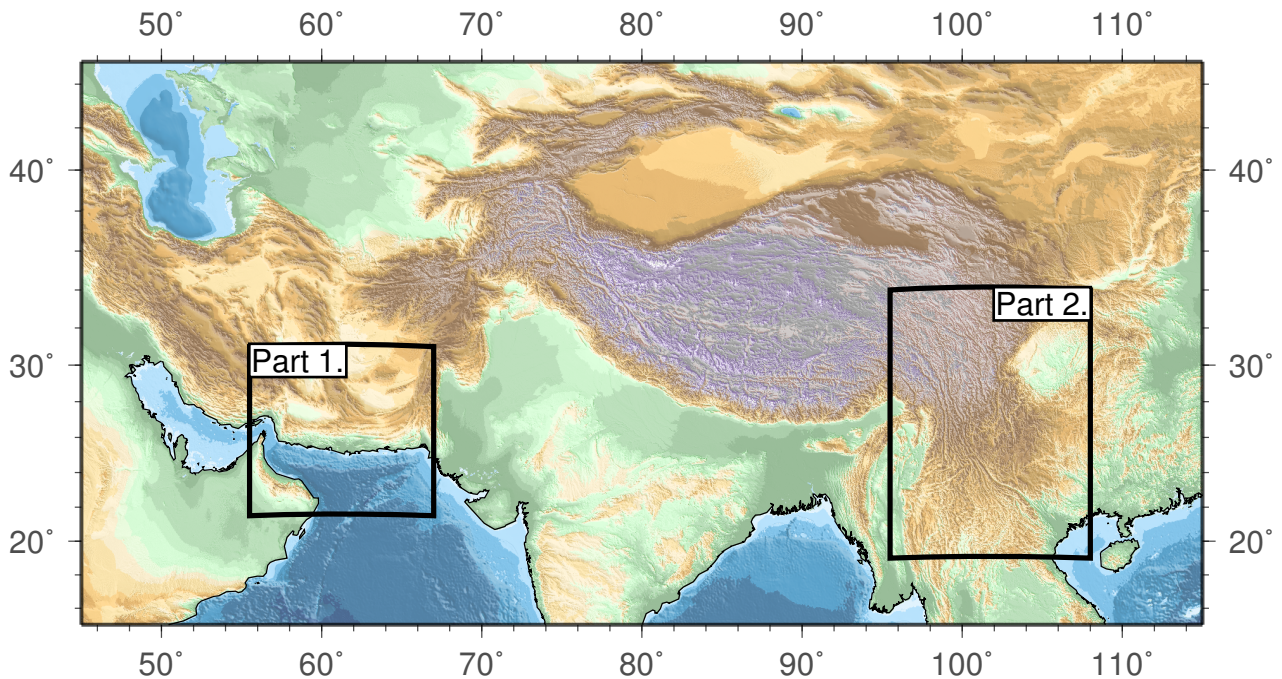


Figure 1.1: Map showing the locations discussed in this dissertation.

Studying the deformation of the lithosphere across a range of time and length scales necessitates the use of multiple models and ways of thinking. On the scale of individual faults it may be appropriate to think in terms of rigid (i.e. undeforming) blocks, with motion concentrated along their edges. There are also larger regions of the continents where rigid blocks provide an appropriate kinematic description, the significance of which is discussed below. However, in some regions deformation is distributed across multiple faults and much of the lithosphere is able to deform by viscous creep. In such regions, and when the length scales being considered are much larger than those of individual faults, but much smaller than the overall size of the deforming region, a continuum approach may give insights into the deformation (e.g. England and McKenzie, 1982; England and Houseman, 1988; England and Jackson, 1989). Much attention has been given to the question of whether block models, in which deformation is concentrated at the edge of rigid blocks, or continuum descriptions of continental deformation

are more appropriate. Such debates miss the fundamental point that the aim of using models at all is to investigate underlying features of, and controls on, deformation, making the appropriate choice of model dependent on the question being addressed. This dissertation, therefore, takes a range of approaches, with the aim of considering the underlying physics which can explain first-order features of the deformation.

The debate surrounding block and continuum models is conceptually similar to the physically important question of how applied forces relate to brittle and viscous deformation in the lithosphere, an area of ongoing research and debate. The key points for the purposes of this dissertation are as follows: 1) The correlation between elastic thickness (which represents the long-term strength of the lithosphere) and seismogenic thickness in both the oceans (e.g. McKenzie et al., 2005) and the continental forelands (Maggi et al., 2000a) implies that applied stresses are predominantly supported in the seismogenic part of the lithosphere in these regions. 2) A low (<20 km) seismogenic thickness, and distributed deformation across multiple faults, in rapidly-deforming regions of the continents suggest that the strength of these regions is likely to be controlled by the properties of the ductile layer (e.g. Sloan et al., 2011). 3) In some parts of the continental lithosphere earthquakes occur throughout the whole crust at temperatures of up to 600°C (in the bulk of the continents earthquakes occur at temperatures less than ~350°C; Maggi et al., 2000b; Priestley et al., 2008). For the crust to deform in a brittle manner at such temperatures it must be anhydrous (Jackson et al., 2004; Bürgmann and Dresen, 2008, and references therein), forming long-lived strong regions of continental lithosphere, known as cratons, which are predominantly composed of Precambrian crust (Jackson et al., 2004, 2008). The margins of such cratons, although not always of thick lithosphere, correlate with the front of both active and ancient orogenies (McKenzie and Priestley, 2008), an observation which will be discussed further below.

The implication of these results is that how much differential stress is supported in the continental lithosphere, and where, is likely to vary laterally. As such, two further questions need to be addressed. In regions where viscous processes dominate lithospheric deformation, what is the associated rheology? In foreland regions and cratons, where the strength of the lithosphere is in the seismogenic layer, what are the frictional properties of the faults which determine the stress which can be supported?

The constitutive relationship between stress and strain rate in the part of the continental lithosphere which deforms by viscous creep is complex. Experimental tests of mineral rheology suggest that this relationship depends, amongst other things, on composition, stress, grain size, water and temperature, so is likely to be highly heterogeneous. A fundamental question

is whether viscous flow occurs by diffusion creep, in which case the relationship between stress and strain-rate is linear (a Newtonian rheology), or dislocation creep, in which case the strain-rate depends on stress to a power greater than 1. The mineralogical arguments have been summarised by Bürgmann and Dresen (2008). Despite significant advances in laboratory techniques, the rheology of the ductile lithosphere remains poorly constrained due to difficulties in extrapolating laboratory experiments to geological strain rates and uncertainty in the geology at depth. Most important for purposes of this dissertation, however, is the observation that measurements of horizontal velocities at the surface cannot discriminate between different vertical rheology structures; rates of vertical motion are also required (Copley, 2008; Flesch et al., 2018, Chapter 6).

In regions where the strength of the continental lithosphere is primarily concentrated in the brittle crust the stresses which the lithosphere can support are likely to be governed by the frictional properties of pre-existing weaknesses within it. These weaknesses may be inherited from previous episodes of deformation; here again the material properties of continental crust distinguish it from that in the oceans since its lower density means that it is not subducted and can survive multiple cycles of deformation, inheriting the associated weaknesses. The abundance of such weaknesses is probably another reason why deformation in the continents is distributed over wide regions, and why the velocity field of continental lithosphere is not sufficient to predict the configuration of faulting. The control which such weaknesses exert on how the brittle crust accommodates the regional velocity field, is another theme of this dissertation (Chapters 2, 5, 6). A lower bound on the coefficient of friction on faults can be obtained from the stress drops in earthquakes, since the deviatoric stress across the fault prior to the earthquake must have been at least that released in the earthquake. If an independent estimate of the stress transmitted through the lithosphere can be made, an upper bound can also be placed on the coefficient of friction by the fault breaking subject to the applied stress (e.g. Copley et al., 2011a, 2014). A greater depth extent of faulting, as in regions where the lower crust is seismogenic, allows faults to support greater shear, and therefore deviatoric, stresses for the same coefficient of friction (since the normal stress on the fault increases with depth). Coefficients of friction from the application of such bounds, as well as from newly-formed faults in the outer rise of subduction zones (Craig et al., 2014b), are <0.3 (see e.g. review by Copley, 2018). In subduction zones, low coefficients of friction (0.015–0.1, Lamb, 2006) have been proposed to result from the presence of (possibly overpressured) sediments or hydrous minerals (e.g. Bayer et al., 2006). Importantly, low coefficients of friction on faults do not necessarily imply a tendency to move aseismically (Wang and Dixon, 2004, Chapter 3, Chapter 5).

Pre-existing weaknesses are particularly important where the style of deformation is time-dependent. Deformation above a subduction megathrust interface as a result of elastic strain

accumulation, which is then relaxed coseismically, can be preserved in the geological record, and also measured geodetically (e.g. Atwater, 1987; Chlieh et al., 2008). Whether elastic strain is accumulating on a subduction megathrust has important implications for seismic hazard, since subduction zones host many of the world's largest earthquakes, which may also be tsunamigenic (Chapter 3). The proportion of strain which is elastic also has implications for the long-term growth of topography. Recent studies have reported time-dependent strain in the overriding plate associated with the megathrust seismic cycle, in particular observations of normal-faulting aftershocks following thrust-faulting earthquakes on subduction megathrusts (e.g. Farías et al., 2011; Asano et al., 2011; McKenzie and Jackson, 2012; Hicks and Rietbrock, 2015). The control of the style of strain in the overriding plate by a subduction megathrust has important implications for continental deformation as it means that the properties of such megathrusts are important in controlling onshore faulting (Chapter 4), and that inferences about the properties of the megathrust can be made using onshore geodetic data, albeit with fewer constraints than the advent of widespread seafloor geodesy would provide.

The seismic cycle is not the only timescale on which the balance of forces and thus style of strain in continental deformation changes. The growth of mountain belts is controlled by the relative importance of far-field compressive forces and gravity acting on buoyancy forces due to crustal thickness contrasts. Deformation will be concentrated in the weaker lithosphere (e.g. Tibet in the India-Eurasia collision, continental lithosphere in subduction zones). In the initial phase of topographic growth, compressive stresses dominate and the crust thickens by thrust faulting. Once the gravitational potential energy due to the growth of topography reaches the maximum that can be supported by the compressive stresses, the topographic elevation can no longer increase and the range instead grows laterally by outwards migration of the thrust front (e.g. Molnar and Lyon-Caen, 1988). If the strength of faults within the stronger lithosphere in a continental collision controls the maximum compressive stress which the lithosphere can support, this implies that faults in the continental forelands have a role in controlling the maximum elevation of the topography associated with the collision. Once this maximum elevation has been reached, gravitational forces then balance the compressive stresses and the topography develops a wide, flat top, such as is seen in the Tibetan Plateau (e.g. Houseman and England, 1986). Thrust structures which have been active during shortening and topographic growth may then become inactive, or be reactivated as strike-slip or normal faults. Subsequent changes in the applied forces, the gravitational potential energy of the high region or the strength of the adjacent lithosphere may lead to a regime in which gravity acting on lateral contrasts in lithospheric thickness is the dominant force (England and Houseman, 1988), as is the case, for example, in Tibet and the Albanian mountains (e.g. Copley and McKenzie, 2007; Copley et al., 2009).

The balance between gravitational and compressive forces, and indeed continental dynamics in general, has predominantly been studied in the context of continental collisions, in particular that between India and Eurasia (e.g. Molnar and Tapponnier, 1975; Tapponnier et al., 1982; England and Houseman, 1986; Flesch et al., 2001; Copley and McKenzie, 2007). However, the same forces govern the deformation of the accretionary prisms formed by the compression of sediment in subduction zones (e.g. Davis et al., 1983; Dahlen et al., 1984; Craig and Copley, 2018). In subduction zones, the relative strength of the oceanic crust means that deformation is concentrated within the accretionary prism or continental lithosphere. Here again the strength of faults is important for determining the maximum topographic elevation, although in subduction zones it is likely to be the shear stress which can be supported by the underlying megathrust which determines elevation, rather than faulting within the oceanic lithosphere. Deformation early in prism growth is accommodated by the growth of thrust faults perpendicular to the maximum compression direction (e.g. Dahlen et al., 1984). These thrust faults form planes of weakness which are steepened within the accretionary prism as it develops. Such prisms, therefore, offer an insight into the role that fault reactivation plays in accommodating temporal variations in the style of strain after a change in the balance of forces (Chapter 5), which is simpler than the analogous fault reactivation in a continental collision, where pre-existing weaknesses may result from multiple cycles of deformation. A problem with such studies is that many accretionary prisms are predominantly underwater. The large subaerial exposure of the Makran accretionary prism in southern Iran and Pakistan (Figure 1.1, Chapter 3) makes it an ideal place in which to study time-dependent strain and the role of fault reactivation in accommodating such time-dependence (Chapter 5). Since the Makran is bordered by continent–continent collisions to the east and west, its deformation also provides an opportunity to study the effects of along-strike variations in relative strength within a collision (Chapter 2).

Subduction zones epitomise the contrast in strength between oceanic and continental lithosphere, which leads to deformation in subduction zones being concentrated in the continental lithosphere. As discussed above, variations in strength within the continental lithosphere have long been proposed to control the present-day distribution of strain, for example in the case of India, which remains relatively undeformed by its collision with Eurasia (e.g. Molnar and Tapponnier, 1975), and the Tarim basin, which transmits stresses to the Tien Shan with little internal deformation (e.g. Molnar and Lyon-Caen, 1989). Such strength variations have also been assumed to exert a control on the temporal evolution of mountain belts (Argand, 1924; Molnar and Tapponnier, 1975; Tapponnier et al., 1982; Vilotte et al., 1984; England and Houseman, 1985; McKenzie and Priestley, 2008; Copley, 2008). Attempts to include lateral rheology contrasts have been made since the early days of continuum modelling (e.g. Tapponnier and Molnar, 1976; Vilotte et al., 1984; England and Houseman, 1985), but a

rigorous treatment requires the inclusion of additional terms in the Stokes' equations (e.g. Molnar and Lyon-Caen, 1988) which make the solution of these equations more computationally expensive than has, until recently, been feasible. So far the models including these extra terms have predominantly been instantaneous (e.g. Copley, 2008; Copley et al., 2011b). These models demonstrate that lateral rheology contrasts can reproduce the present-day strain rate, with the assumption that this would also be true if the continuum were to have evolved through time. However, the contrast between instantaneous models, which can reproduce extension in high plateaux (e.g. Tapponnier and Molnar, 1976), and those accounting for finite deformation, which cannot (e.g. England and Houseman, 1988), in the simplified case, suggest that the inclusion of temporal evolution in such models is necessary to ascertain the role of contrasts in lateral rheology in controlling the temporal evolution of mountain belts (Chapter 6).

To discuss the forces and rheology controlling continental deformation first requires a description of what deformation is occurring. The kinematics of continental deformation involve both the velocity field, more specifically the gradients of this field, and the configuration of faults which accommodate it in the brittle crust. The velocity gradient tensor can be divided into a rotational component, which can be measured by palaeomagnetic rotations, and a strain rate component, the seismically released part of which can be determined from earthquakes (England and Jackson, 1989). The deformation of the continents' surface is being measured with increasing spatial and temporal resolution by the Global Positioning System (GPS) and interferometric synthetic aperture radar (InSAR). However, despite global compilations of velocities and inferences of strain rate (e.g. Kreemer et al., 2000, 2014), many deforming regions, especially those where velocity gradients are low, or which are logistically challenging to access, remain poorly instrumented. This limited spatial resolution means that the full velocity gradient tensor is not resolved (Appendix A of Copley, 2008), making it important to use observations from multiple techniques. InSAR and GPS allow the distribution of slip in earthquakes, and the interseismic accumulation of elastic strain, to be constrained (e.g. Konca et al., 2008, Chapter 2), subject to assumptions about the geometry of the faulting (Vergne et al., 2001). Such measurements therefore need to be combined with well-constrained earthquake depths and mechanisms in order to understand the kinematics (Chapters 2, 3). The timescale of geodetic measurements is also short compared to the length of earthquake cycles. Longer term information comes from the effects of active faulting on landscapes; the recent widespread availability of high resolution topographic data and satellite imagery makes studying geomorphological features feasible even in regions which are not accessible for fieldwork. In combination these techniques now provide the possibility of studying the kinematics of inaccessible and complex regions, a theme throughout this dissertation.

1.2 Overview

Part I

The Makran (Part I, Figure 1.1) is formed by the northwards subduction of the Arabian plate beneath the southern coasts of Iran and Pakistan. The subduction zone hosts the world's largest sub-aerially exposed accretionary prism (Fruehn et al., 1997). As such, the Makran provides an ideal setting in which to study the kinematics and dynamics of such prisms. As discussed above, accretionary prisms may show a temporal evolution in the style of strain within them similar to that of orogenies in continent-continent collisions, and elucidate the role of fault reactivation in accommodating such evolution. However, the Makran remains poorly documented, particularly onshore, as a result of its inaccessibility; a challenging environment since the early attempts to cross it made by Semiramis and Alexander the Great (Arrian, 1st century CE), more recent logistical constraints have brought an end to the field investigations of the twentieth century (e.g. Harrison, 1943; Harms et al., 1982; Falcon, 1974). By combining techniques and results from seismology, geomorphology, GPS and modelling, the first part of this dissertation addresses fundamental questions about this subduction zone, which have implications for the kinematics and dynamics of accretionary prisms and thickly-sedimented subduction zones in general.

1.2.1 Chapter 2

The May 2013 Minab earthquake occurred at the western end of the Makran accretionary prism, near to the transition to continent–continent collision in the Zagros mountains. Few previous earthquakes have been recorded in this region, so this event offers an opportunity to investigate the kinematics and dynamics of the transition from subduction to continent–continent collision. I use observations from seismology, geodesy and geomorphology to study the source parameters and slip distribution of this earthquake. The earthquake was strike-slip with a left-lateral sense of motion, conjugate to the adjacent, previously mapped faults of the Minab-Zendan-Palami fault zone, with the opposite sense of motion. This fault, and a series of other left-lateral faults observed from geological offsets in satellite imagery, accommodate a regional velocity field equivalent to right-lateral shear on N–S planes, through clockwise rotation about vertical axes. The longitudinal extent of shear accommodated by such faults is consistent with the distance over which microseismicity associated with the interface between Arabian and Iranian lithosphere has been observed to deepen, suggesting that the shape of the interface involved in the transition from subduction to continent–continent collisions may play an important role in determining the kinematics in the overriding plate. The reason

why such shear is accommodated by left-lateral faulting and rotations about vertical axes is likely to relate to the reactivation of pre-existing thrust faults within the Makran accretionary prism.

1.2.2 Chapter 3

Chapters 3–5 should be viewed as aspects of a single study, and represent an overall picture of the kinematics and dynamics of the Makran subduction zone.

In contrast to many subduction zones globally, the shape and location of the subduction interface between Arabian and Iranian lithosphere in the Makran is poorly constrained. I address this issue by making a compilation of earthquakes with well-constrained depths and mechanisms (listed in Appendix B) and combine this with other constraints on the location of the interface from receiver functions and seismic reflection surveys. This compilation incorporates my own solutions from body-waveform modelling which are shown in Appendix A. Although earthquakes have been reported on the subduction megathrust in the eastern Makran, including a M_w 8.1 earthquake in 1945, no such earthquakes have been recorded in the western Makran, where the interface has been suggested to be aseismic (Byrne et al., 1992). Whether the western Makran is accumulating elastic strain has important implications for earthquake and tsunami hazard in a region where populations have grown rapidly since the last major earthquake, and are concentrated in vulnerable urban areas, such as Karachi. My improved constraints on the geometry of the interface allows me to investigate whether elastic strain accumulation on this interface is consistent with geodetic and geological constraints, including those from newly measured GPS sites.

1.2.3 Chapter 4

To the north of the Makran, right-lateral shear between Afghanistan and the Lut Block is accommodated by N–S striking right-lateral faults in the Sistan Suture Zone. However, such faults do not cut the E–W structures of the accretionary prism. The question of how right-lateral shear is accommodated at the southern end of the suture zone is one which has been discussed since the early days of continental tectonics (e.g. Jackson and McKenzie, 1984). I use recently published geodetic data, combined with geomorphological observations to assess three possibilities for how such motion is accommodated and their kinematic implications. The rate of compression across the northern margin of the prism is <2 mm/yr, insufficient to accommodate the 5–15 mm/yr of right-lateral motion across the Sistan Suture Zone on thrust faults. Structural trends across the prism are not consistent with right-lateral shear being accommodated through combined left-lateral faulting and vertical-axis rotations. I

therefore propose that right-lateral motion is transferred across the Jaz Murian depression to the region of right-lateral shear at the western end of the accretionary prism (Chapter 2). Geomorphological observations suggest that the Jaz Murian depression is bounded by dip-slip faults which are likely to be extensional, consistent with this mechanism for accommodating right-lateral shear. However, the absence of geodetic extension across the basin margins and the lack of recorded earthquakes, suggest that the strain in the Makran accretionary prism is likely to be time-dependent, controlled by the elastic strain accumulation on the subduction megathrust inferred in Chapter 3.

1.2.4 Chapter 5

In this chapter I first discuss the role of strike-slip faulting in the Makran accretionary prism, and propose that the 2013 strike-slip Balochistan earthquake accommodates the regional velocity field through pure shear rotations. In both the Balochistan and Minab (Chapter 2) earthquakes strike-slip faulting is likely to have occurred on reactivated faults which were formed as thrusts earlier in the formation of the accretionary prism, demonstrating that pre-existing faults provide a strong control on the accommodation of the regional velocity field. Such fault reactivation also implies a change in the style of strain within the prism through time. This strike-slip faulting, and the topographic form of the prism, allows me to infer a balance between gravitational and compressive forces within the prism. I then calculate the range of shear stresses and coefficients of friction consistent with this force balance and find values of 5–35 MPa and 0.01–0.03 respectively. These values are consistent with those in other subduction zones, suggesting that the thick sediments in the Makran do not significantly alter the shear stress which can be supported by the megathrust.

Part II

In the second part of this dissertation I turn my attention to the temporal evolution of topography in South East Tibet. The shallow and distributed nature of the faulting in South East Tibet, suggests a continuum approach to lithospheric deformation in this region. The eastwards extrusion of material from the Tibetan Plateau, and the large scale strike-slip faulting in the region led to one of the major controversies of early continental dynamics; the importance of gravity (exemplified by Tapponnier and Molnar, 1976; Tapponnier et al., 1982; England and McKenzie, 1982; England and Houseman, 1986; Tapponnier et al., 2001). GPS measurements and the slip vectors of earthquakes suggest that the present-day deformation is governed by gravity acting on lateral contrasts in crustal thickness (e.g. Copley and McKenzie, 2007).

1.2.5 Chapter 6

Recently published results from stable-isotope palaeoaltimetry provide the constraints on vertical motions required to distinguish between competing models of viscous flow in the lithosphere. By combining such results with numerical modelling of a viscous fluid, I study the role of lateral rheology contrasts in controlling the temporal evolution of topography in South East Tibet. Such contrasts, analogous to that between the Sichuan Basin and Central Lowlands of Myanmar and the rapidly deforming region between them, can explain the main features of the present-day topography, GPS velocity field and earthquake derived strain-rate in South East Tibet. Uplift rates based on stable-isotope palaeoaltimetry are ~ 0.2 mm/yr, an order of magnitude lower than has previously been inferred based on river incision. My results therefore suggest that the low-viscosity, lower-crustal channel which has previously been proposed in the region (e.g. Royden et al., 1997; Clark and Royden, 2000), does not exist. My models further suggest that lateral rheology contrasts provide a first-order control on the temporal evolution of mountain ranges generally, providing an explanation for the correlation of cratons with the fronts of mountain ranges (McKenzie and Priestley, 2008).

Part I

The Makran Subduction Zone

Chapter 2

Subduction tractions and vertical axis rotations in the Zagros-Makran transition zone, SE Iran: the 11 May 2013 Mw 6.1 Minab earthquake[†]

Overview

The source parameters and slip distribution of the 11 May 2013 M_w 6.1 Minab earthquake are studied using seismology, geodesy and field observations. I observe left-lateral strike-slip motion on a fault striking ENE–WSW; approximately perpendicular to previously studied faults in the Minab-Zendan-Palami fault zone. The fault that ruptured in 2013 is one of a series of \sim E–W striking left-lateral faults visible in the geology and geomorphology. These faults accommodate a velocity field equivalent to right-lateral shear on \sim N–S striking planes by clockwise rotations about vertical axes. The presence of these faults can reconcile differences in estimates of fault slip rates in the western Makran from GPS and Quaternary dating. The longitudinal range of shear in the western Makran is likely to be controlled by the distance over which the underthrusting Arabian lithosphere deepens in the transition from continent-continent collision in the Zagros to oceanic subduction in the Makran.

[†]This chapter is adapted from Penney, C., Copley, A., and Oveisi, B. (2015). Subduction tractions and vertical axis rotations in the Zagros-Makran transition zone, SE Iran: the 2013 May 11 Mw 6.1 Minab earthquake. *Geophys. J. Int.*, 202:1122–1136. doi:10.1093/gji/ggv202

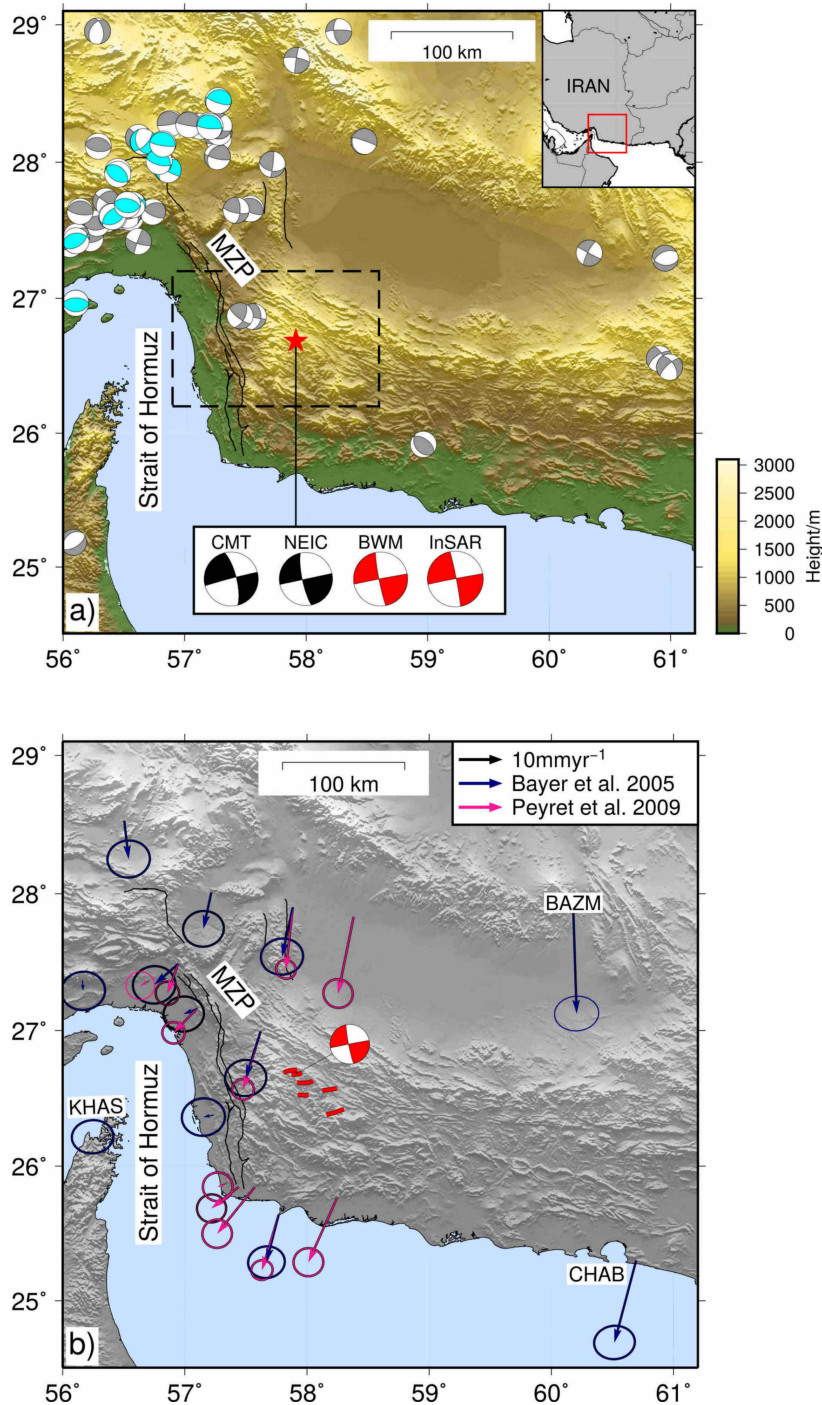


Figure 2.1: Overview of study area. MZP (black lines) is the Minab-Zendan-Palami fault zone, the trace of which is taken from Bayer et al. (2006). (a) shows the regional seismicity. The compressional quadrants of focal mechanisms are shaded. Those in blue are taken from Nissen et al. (2011) and have been constrained by body-waveform modelling, those in grey are from the gCMT (Dziewonski et al., 1981; Ekström et al., 2012) catalogue and are located at EHB epicentres until 2009 and NEIC epicentres for later events. Mechanisms to the west are dominantly thrust faulting at the eastern end of the Zagros mountains. Focal mechanisms for the 2013 Minab event are shown boxed, those in red are taken from this study from body-waveform modelling (labelled BWM, see Section 2.2) and constant slip inversion of InSAR data (labelled InSAR, see Section 2.3). The inset shows the location of the study area within Iran and the dashed box shows the location of Figures 2.7 and 2.9. (b) shows GPS velocities plotted with respect to Arabia, using the Arabia-Eurasia Euler pole of Vernant et al. (2004). Pink arrows are from Peyret et al. (2009) and blue arrows are from Bayer et al. (2006). Ellipses show 95% confidence intervals. Velocities increase to the East, causing differential shear across the region (see Section 2.6.1). The focal mechanism for the 2013 Minab earthquake from this study is shown in red. Red lines are faults visible in the geomorphology.

2.1 Introduction

The 11 May 2013 M_w 6.1 Minab earthquake occurred in the sparsely populated desert to the east of the Strait of Hormuz, in SE Iran (Figure 2.1). The earthquake was one of the first instrumentally-recorded events in the western part of the Makran subduction zone, where Arabian oceanic lithosphere is thrust beneath southern Iran and Pakistan. To the west, this oceanic subduction transitions into continent-continent collision in the Zagros mountains. The Minab earthquake presents an opportunity to address a number of open questions, such as those raised by the M_w 7.7 Balochistan earthquake in 2013; a strike-slip event that ruptured a curved fault at the eastern end of the Makran subduction zone (Avouac et al., 2014; Jolivet et al., 2014). That event highlighted that the onshore part of the accretionary wedge built above the subduction interface can be seismically active and characterised by strike-slip faulting. I examine the 2013 Minab event to better understand the deformation of the accretionary wedge in the Zagros-Makran transition zone. This earthquake is also important from the perspective of understanding the regional tectonics and distribution of strain in the western Makran, which give insights into both earthquake hazard and the factors controlling the distribution and style of faulting in the continents. This chapter addresses these issues by studying the 2013 Minab earthquake using a combination of seismology, satellite geodesy and field observations. I then consider the implications of my results for the driving forces and distribution of faulting in the region.

2.2 Body-Waveform Modelling

I use body-waveform modelling to constrain the depths and mechanisms of the Minab earthquake and two of its larger aftershocks. This technique is widely used and has been described extensively elsewhere (e.g. Molnar and Lyon-Caen, 1989; Taymaz, 1990). I summarise the key points here.

Teleseismic P and SH waveforms in the epicentral distance range 30° – 80° were extracted from the IRIS DMC. The seismograms were deconvolved from their instrument responses and reconvolved with the response of a World-Wide Standardised Seismographic Network Long Period (15–100) seismometer. In this period range, a moderate-size earthquake can be approximated as a point source. P- and SH-wave data were then inverted using the MT5 program of Zwick et al. (1994) based on the method proposed by McCaffrey and Abers (1988) and McCaffrey et al. (1991), for fault plane orientation (strike, dip and rake), source-time function, centroid depth and seismic moment. The program uses a least-squares fitting

algorithm to minimise the point-wise misfit between observed and synthetic seismograms. This procedure requires accurate alignment of the synthetics with P- and SH-wave arrivals. Long-period filtering can make impulsive arrivals difficult to observe so P- and SH-arrival times were manually picked in the broadband data.

Filtering the seismograms to long periods allows moderate-sized earthquakes ($M_w < 7$) to be modelled as point sources with temporally extended source-time functions. This filtering also reduces sensitivity to small scale variations in velocity structure in the source region. Throughout my seismic and geodetic inversions I use a velocity model in the source area derived from the local earthquake study of Yamini-Fard et al. (2007) (Table 2.2). The earthquakes modelled here are all shallower than 11 km, the depth of the uppermost crustal layer of this velocity model (which has $V_p = 5.6$ km/s, $V_s = 3.3$ km/s and $\mu = 28.3$ GPa), allowing me to use a uniform half-space for this modelling. As observed by Taymaz (1990), the details of the velocity structure had little effect on the derived source parameters using this method, changing them only within the expected errors, which have been extensively discussed in the literature (e.g. Molnar and Lyon-Caen, 1989).

A subset of seismograms was selected based on visual inspection of the signal-to-noise ratio in both the broadband and filtered records. The gCMT solution (Table 2.1, Dziewonski et al., 1981; Ekström et al., 2012) was used as the starting model. The source-time function was composed of triangular elements of half-duration 2 s, using a sufficient number of elements that the total duration was not artificially imposed in the inversion. The source was constrained to be pure double-couple. Seismograms were weighted by azimuthal density, to allow for uneven station distribution, and SH data were weighted to half of P data to allow for the greater amplitude of S waves.

My estimated focal mechanism for the Minab earthquake is shown in Figure 2.2, along with the seismograms used in the inversion and the associated synthetics for each station. The fault plane with strike 168° corresponds to the orientation of the right-lateral Minab-Zendan-Palami (MZP) fault zone; 160° (Regard et al., 2005, Figure 2.1). However, from the InSAR data discussed below I find that the earthquake occurred on the orthogonal fault plane (strike 259° , dip 89° S, rake 5° ; Section 2.3). My estimated centroid depth is 6 km. Based upon tests in which I hold one parameter at a value away from the best-fit, and re-invert the other parameters, I estimate the error in strike to be $\pm 6^\circ$. Errors in the other quantities are asymmetric; dip lies in the range $79 - 89^\circ$, rake $0 - 12^\circ$ and centroid depth from $2 - 8$ km. These are consistent with the typical errors found in other studies (e.g. Molnar and Lyon-Caen, 1989).

MINAB 11th May 2013

259/89/5/6/1.659E18

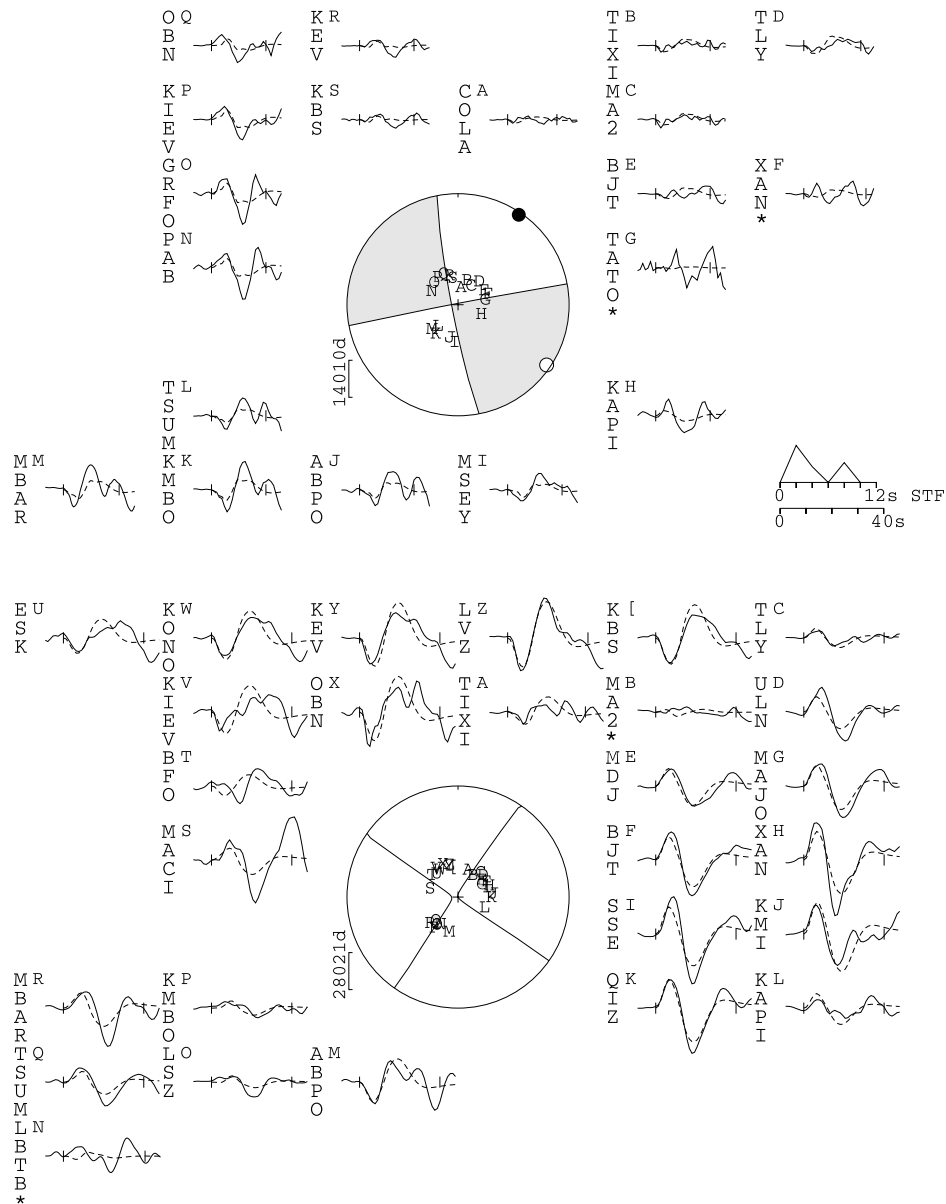


Figure 2.2: Lower hemisphere P (top) and SH (bottom) focal mechanisms from teleseismic body waves. Compressional quadrants are shaded for the P-wave mechanism. Observed seismograms are shown by solid lines and the corresponding synthetics by dashed lines. SH waves are shown at half the magnification of P waves. Stations which were not included in the inversion, due to the low signal-to-noise ratio near nodal planes, are marked by an asterisk and the letter next to each seismogram is used to mark its projection onto the focal sphere. The parameters below the title are strike ($^{\circ}$) / dip ($^{\circ}$) / rake ($^{\circ}$) / depth (km) / seismic moment (Nm).

I applied the same method to the two aftershocks of the Minab earthquake which had a sufficient signal-to-noise ratio to be analysed with this technique. These events were both predominantly strike-slip with nodal planes in approximately the same orientations as the mainshock. Body-waveform modelling solutions for these events are shown in Appendix A (Figures A.1 and A.2) and their locations are discussed below.

2.3 Constant Slip Inversion of InSAR data

Radarsat-2 SAR interferograms spanning the time of the earthquake were produced by Samsonov and Czarnogorska (2013). In this section I invert the ground displacements in these interferograms for the source parameters of the Minab earthquake, for comparison with the seismological results described in Section 2.2 above. The descending and ascending track interferograms span 1st November 2012 to 29th June 2013, and 6th November 2012 to 10th June 2013, respectively. The former includes 49 days of postseismic data, the latter 30 days. The unwrapped interferograms are shown in Figure 2.3a and d. The \sim E–W trending discontinuity in line-of-sight (LOS) displacements suggests rupture on an \sim E–W striking fault. The opposite senses of motion in the two interferograms (i.e. toward or away from the satellite) show that the measured ground motions are dominated by \sim E–W horizontal motions, which have opposite signs in ascending and descending track interferograms due to the different satellite look-angles (marked on Figure 2.3). I expect that the mainshock will dominate the ground motion signal as the largest reported aftershock, M_w 5.6, was nearly an order of magnitude smaller in seismic moment (see Appendix A). However, postseismic slip may also contribute to the ground motions measured from InSAR, as discussed below.

The earthquake was modelled as a single plane with uniform slip, using the expressions of Okada (1985). I inverted for the depths of the top and bottom of the fault plane, strike, dip, rake, fault length, average slip and the geographical location of the fault. I use an inversion routine based on a simulated annealing algorithm, in which the solution can move to higher misfits during the inversion, to avoid being trapped in local misfit minima. To increase the likelihood of finding the global minimum, I used the parameters derived from waveform modelling (Table 2.1) as a starting model, although the strike, dip and rake were allowed to take any values during the course of the inversion.

The results of the inversion are shown in Figure 2.3. The inversion yields a fault plane with parameters given in Table 2.1. Slip of 1.2 m extends from \sim 0–9 km depth on a \sim 15 km long fault plane. The motion is left-lateral strike slip on an ENE–WSW striking plane, approximately orthogonal to the faults which have previously been mapped in this region (e.g.

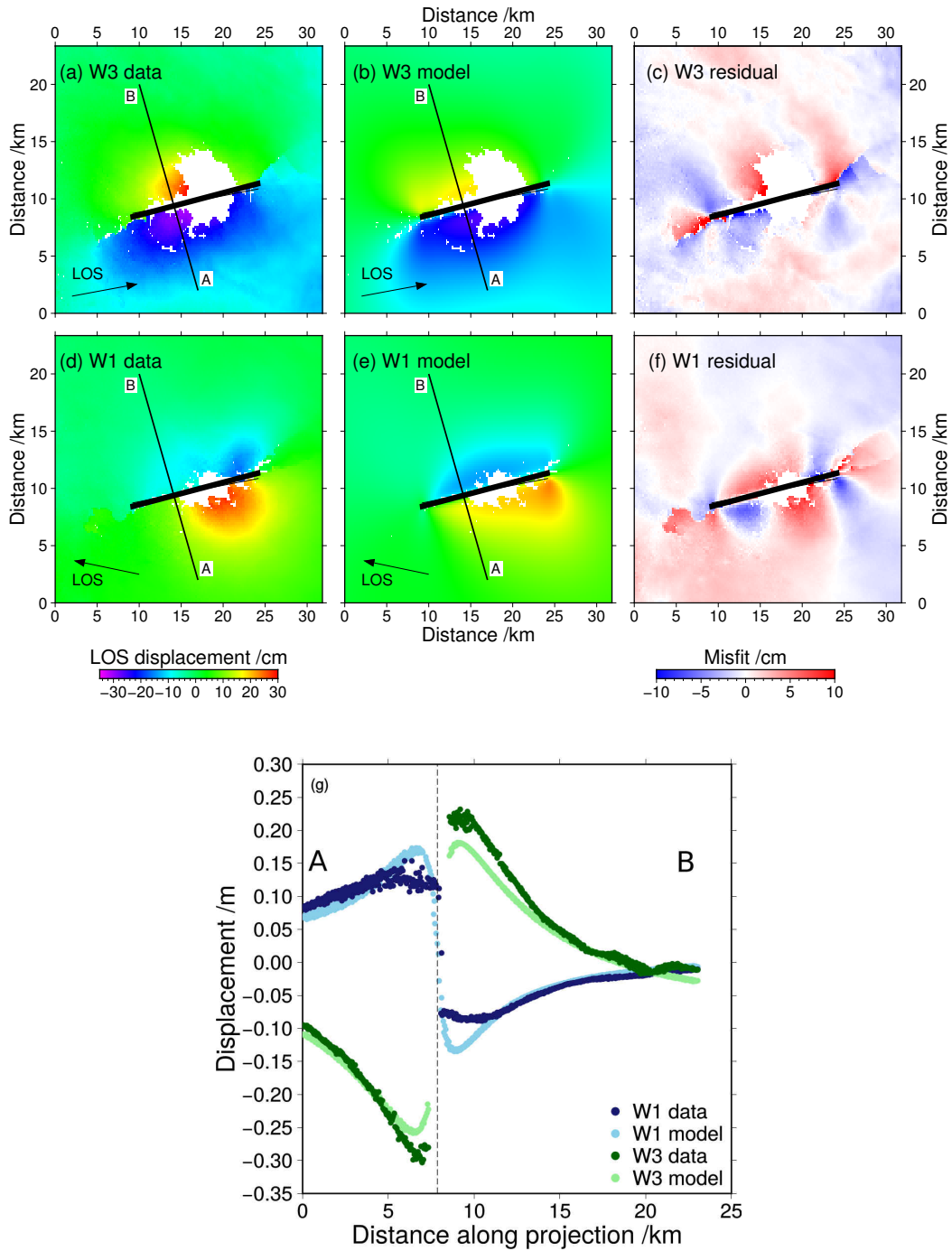


Figure 2.3: Results of the inversion of InSAR data for constant slip on a rectangular plane. The centre of the fault trace is at 57.898 E, 26.698 N. (a) and (d) are the unwrapped ascending (top, W3) and descending (bottom, W1) SAR interferograms (Samsonov and Czarnogorska, 2013), with the look direction of the satellite shown by the arrows labelled “LOS”. Positive displacements are towards the satellite (i.e. in the opposite direction to the LOS arrow). Panels (b) and (e) show the best fit model for each track, and (c) and (f) show the residual between the data and the model (calculated as the data minus the model). The thick black line in panels (a)-(f) is the surface projection of the fault plane. The thin, perpendicular line is the line of projection used in (g). (g) Ground displacements of data (dark colours) and models (light colours) S–N along the profile A–B shown in (a–f). The black, dashed line shows the intersection of the fault with the profile. The disparity between the models and the data near the fault is discussed in Section 2.3.

Peyret et al., 2009). The focal mechanism from this inversion is shown in Figure 2.1a and is consistent both with my seismological solution and the focal mechanisms calculated by the gCMT and NEIC. The source parameters are within error of those derived from teleseismic body waves, with the exception of the seismic moment, which is significantly larger from the slip inversion; 4.4×10^{18} Nm (using a shear modulus of 28.3 GPa) as opposed to 1.7×10^{18} Nm from seismology. This difference will be discussed in detail below. I find that the misfits between the model and the data are greatest near the fault. I suggest that this feature is due to the amount of slip in the earthquake decreasing towards the surface, a feature which cannot be captured in the constant-slip model used here. I return to this observation below, following inversions for the distribution of slip on the fault plane. The RMS misfit between the model and the data for the constant slip inversion is 1.8 cm, similar to the amplitude of non-tectonic signals in areas of the interferogram away from the rupture (Figure 2.3a).

Method		Strike ($^{\circ}$)	Dip ($^{\circ}$)	Rake ($^{\circ}$)	Depth (km)	M_0 (10^{18} Nm)
NEIC	plane 1	258	90	11	15	1.6
	plane 2	168	79	178		
CMT	plane 1	346	74	-178	12	2.2
	plane 2	255	88	-16		
BWM	plane 1	259	89	5	6_{-4}^{+2}	1.7
	plane 2	169	85	179		
InSAR	fault plane	259	89	-3	0–9	4.4
	auxiliary plane	349	87	-179		

Table 2.1: Source parameters from seismology (BWM) and InSAR inversions.

2.4 Distributed Slip Inversion of InSAR data

I extend my analysis of the InSAR dataset and perform inversion for the distribution of slip on the fault geometry estimated in Section 2.3. I discretise the fault plane into 1.5×1.5 km cells. The SAR interferograms are then inverted for the slip on each patch using the simulated annealing method described by Ji et al. (2002). This method has been widely used for joint inversions of geodetic and seismological data (e.g. Konca et al., 2008, 2010) to obtain earthquake source models. Given the small size of the Minab earthquake, and the absence of a local seismic network, I did not attempt a joint inversion in this case as the teleseismic data would provide limited additional insight into the spatial distribution of fault slip. The velocity model used in this inversion (detailed in Table 2.2) is based on the structure obtained by Yamini-Fard et al. (2007) slightly north of my study area.

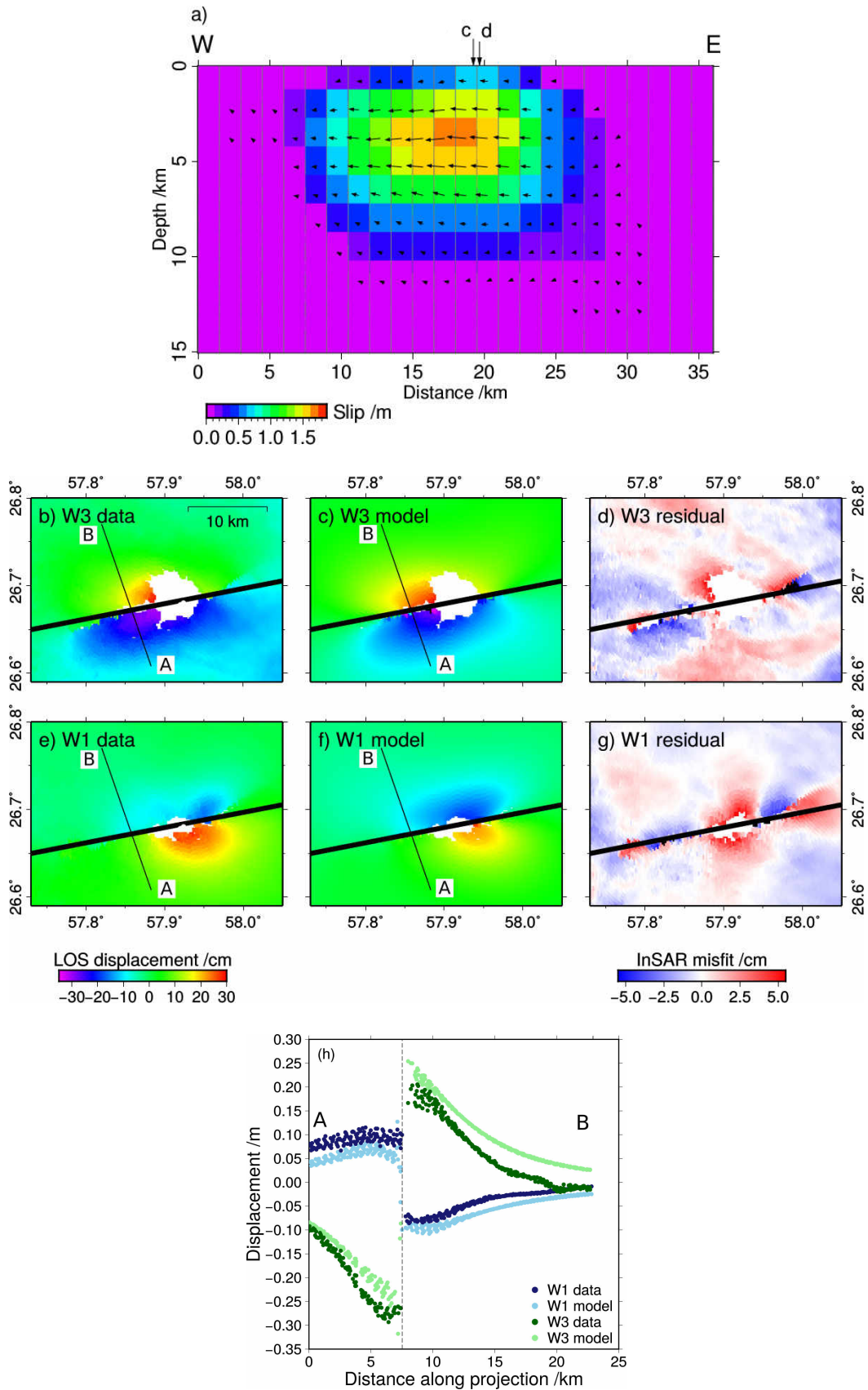


Figure 2.4: Results of distributed slip inversion for finite source. (a) shows slip distribution with depth in 1.5×1.5 km cells. The maximum slip is 1.9 m at ~ 4 km depth. The locations of Figures 2.6c and 2.6d are labelled c and d. (b)–(g) are as for Figure 2.3 panels (a)–(f). (h) shows the displacements along the same profile as Figure 2.3g. The black, dashed line shows the intersection of the fault with the profile.

The trade-off between misfit and model roughness in inversion procedures is well-known (e.g. Jónsson and Zebker, 2002). Following the approach of Freymueller et al. (1994) I select the solution in the apex of the curve relating misfit and model roughness; making the model as smooth as possible without significantly increasing the misfit (Figure 2.5a). The dominant features of the resulting model do not vary within the section of the misfit curve corresponding to low misfit, physically plausible solutions (in which connected slip patches do not show large variations in slip magnitude or direction). The trade-off between misfit and smoothness is shown in Figure 2.5 along with solutions that are rougher and smoother than the preferred model. In my preferred model, the RMS misfit to the data is 1.7 cm.

Depth to base (km)	V_p (km/s)	V_s (km/s)	μ (GPa)
11	5.6	3.3	28.3
21	6.6	3.8	39.0
30	6.9	4.0	44.8
-	8.1	4.5	66.8

Table 2.2: Velocity model used for distributed slip inversion

I find a patch of slip extending from the surface to ~ 10 km depth with an along-strike length of ~ 20 km (Figure 2.4), consistent with the fault plane extent from my constant-slip inversion. The greatest slip is ~ 1.9 m. The slip decreases towards the surface, as suggested by the near-fault misfits in my constant slip inversion (Section 2.3). The average slip from the constant slip inversion was 1.2 m, which agrees with the results of averaging over the slip patch in the distributed slip inversion. The seismic moment was allowed to vary in the inversion, with a starting value of 5×10^{18} Nm, and converged on 4.5×10^{18} Nm; similar to the constant slip inversion. The sense of motion of the patches is consistent with the nearly pure left-lateral slip found from body-waveform modelling. The ~ 20 km length of the fault plane is consistent with the ~ 6 s length of the main part of the source-time function in my seismological inversions, if this represents the time to rupture the length of the fault at a velocity close to the S-wave velocity (~ 3.3 km/s).

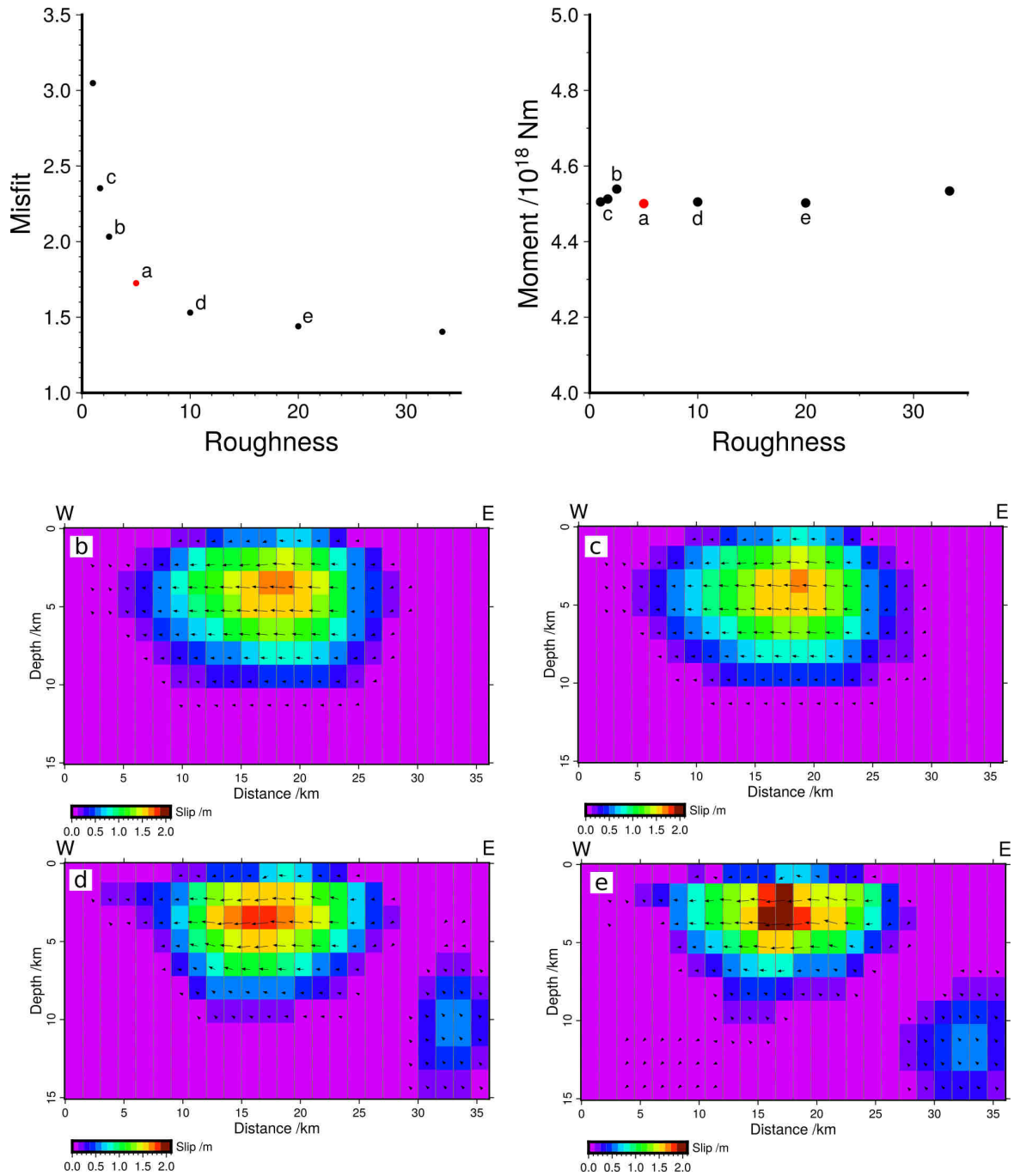


Figure 2.5: The top left panel shows the relationship between misfit and model roughness in my inversion of InSAR data for the distribution of slip on the fault plane. My preferred model, shown in Figure 2.4a, is marked in red and labelled a. The corresponding slip distributions for the points labelled b–e are shown in the lower panels; b and c represent smoother solutions than my chosen one and d and e represent rougher solutions. The moment from the different inversions is shown in the top right panel. Within the apex of the misfit-roughness curve there is good agreement with a moment of 4.5×10^{18} Nm.

2.5 Field Observations and Geomorphology

The geomorphological observations in this section were made by Alex Copley, the field observations by Benham Oveisi.

Figure 2.6a shows a satellite image of the fault that ruptured in the 2013 mainshock. Ruptures were observed in the field, by Benham Oveisi, between the two locations marked ‘R’. The ruptures followed the obvious E–W trending valley, and were en-échelon right-stepping cracks, with a sense of motion consistent with left-lateral motion on the fault (Figure 2.6c, d). The surface displacements were on the order of centimetres. Such displacements are consistent with the decrease in slip towards the surface seen in the inversions of the InSAR data (Section 2.4). The magnitude of surface slip was smaller than predicted from the geodetic results, which is a commonly observed feature thought to relate to the surface strain being distributed over a wide region of near-surface sediments, in addition to being focussed as slip on a fault plane (e.g. Zinke et al., 2014). The fault is visible in the geomorphology (shown by white arrows in Figure 2.6a), and extends beyond the area where logistical constraints concentrated field observations. The surface-rupture locations, orientations and sense of slip are consistent with my estimated fault parameters based on seismic and geodetic inversions.

The fault that ruptured in the 2013 event is characterised in the geomorphology by a linear valley that cuts across the strike of the geological units, and in places reverses the slopes of hillsides. Rivers draining from north to south across the area have sections which drain along the fault (blue lines on Figure 2.6a). These are not markers of the fault offset, as they are larger than the offset of the geological contact between brown and green rocks marked on Figure 2.6c. The fault-parallel river courses are likely to be due to the fault rocks being more easily eroded than their surroundings, concentrating the drainage along the fault. These geomorphological characteristics allow other faults in the region to be identified. We focus on the region to the east of the MZP fault zone studied by Bayer et al. (2006), Peyret et al. (2009) and Masson et al. (2004), amongst others. A number of \sim E–W striking left-lateral strike-slip faults are visible in remote sensing data (Figure 2.8, locations marked as red lines on Figure 2.7). In common with the fault that ruptured in 2013, these faults are characterised by linear valleys, the reversal of hill-slopes, and the offset of geological units. The tectonic significance of these faults is discussed below.

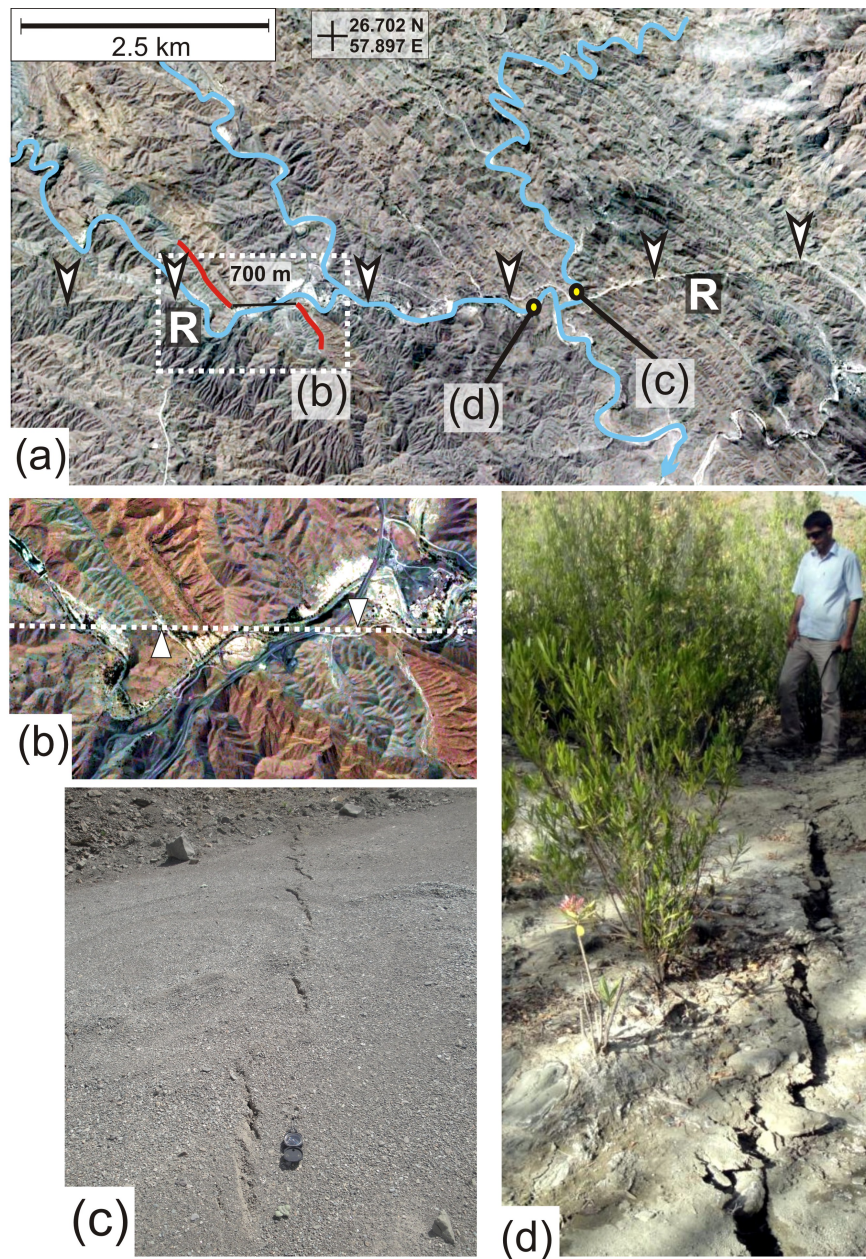


Figure 2.6: (a) Ikonos optical satellite image of the fault that ruptured in the 2013 mainshock. Image copyright Google Earth and DigitalGlobe. Surface ruptures were observed in the region between the two points marked 'R'. The white arrows show the location of the faulting visible in the geomorphology. The red line shows a contact between brown and green rocks that has been offset left-laterally by ~ 700 m. The rivers, shown in blue, do not reflect the geological offset (Section 2.5). White dashed box marks the area shown in (b). (b) Close up of offset geological contact with colours enhanced to highlight geological units (see also Figure 2.8). (c) and (d) show examples of the surface ruptures produced by the event from the points marked (c) and (d) in (a). Photos courtesy of Benham Oveisi. *This figure was prepared by Alex Copley.*

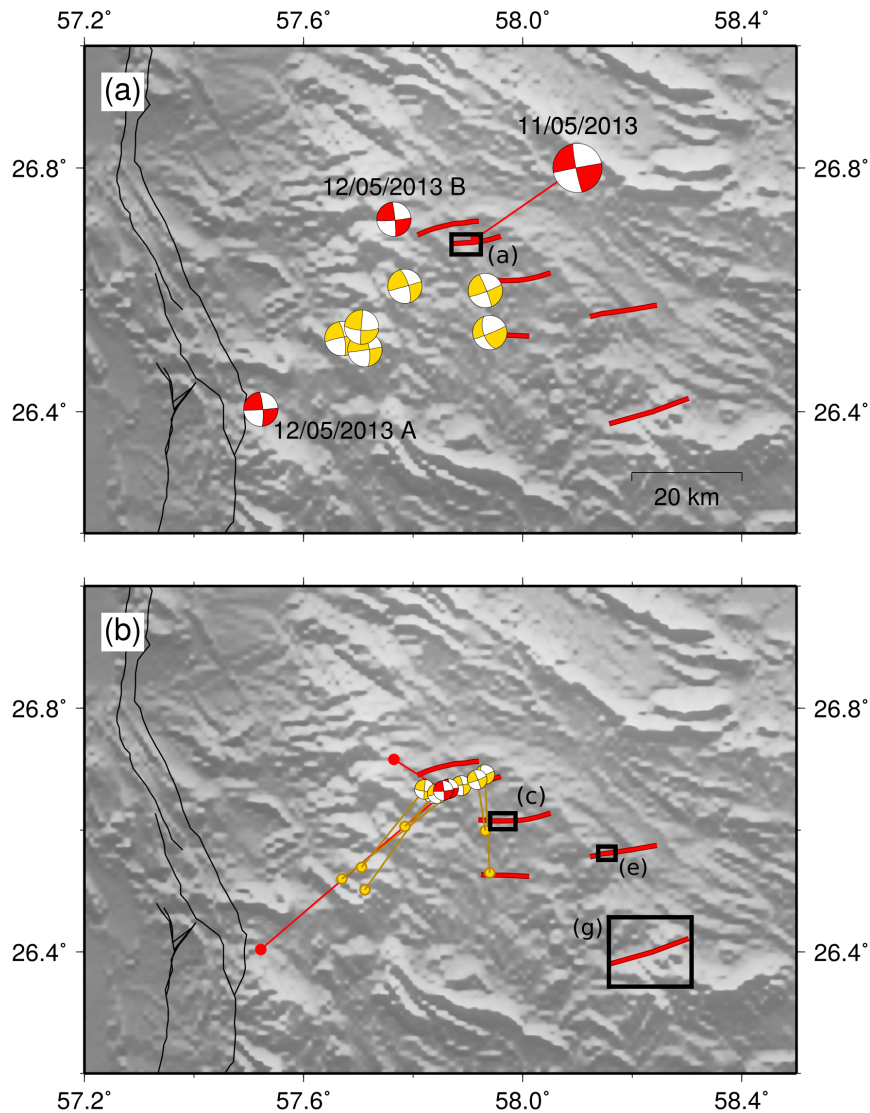


Figure 2.7: Locations of aftershocks and left-lateral faults. Lines in red are faults identified in this study. Lines in black are the Minab-Zendan-Palami fault zone from Regard et al. (2004). (a) Aftershock focal mechanisms are shown at their NEIC epicentres. Compressional quadrants are shaded. The mechanism in red labelled 11/05/2013 is the body-waveform modelling solution for the Minab mainshock from this study. Other red mechanisms are my body-waveform modelling solutions for two aftershocks, as shown in Figures A.1 and A.2. Events in yellow are from the gCMT catalogue, and have signal-to-noise ratios too low for body-waveform modelling using the methods employed here. (a) shows the location of Figure 2.8a. (b) shows aftershock focal mechanisms at their relocated epicentres from Kintner et al. (2018). All the aftershocks can be seen to lie along strike from the mainshock. Boxes show the locations of satellite images in Figure 2.8.

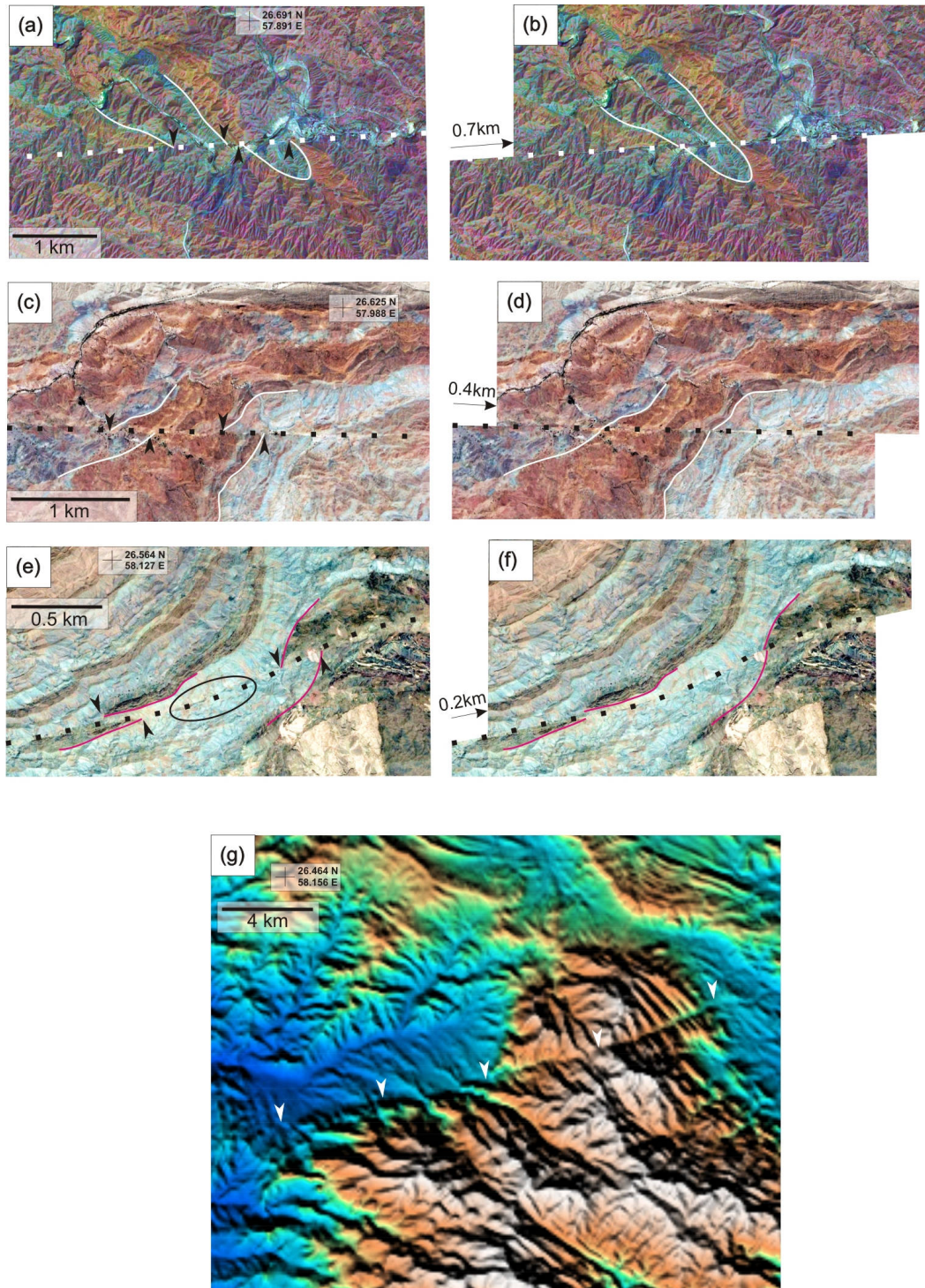


Figure 2.8: Panels (a), (c), and (e) show satellite images of fault offsets in the locations indicated in Figure 2.7. Panel (a) corresponds to the eastern part of Figure 2.6a. Offset geological units are marked by black arrows and white or pink lines. Panels (b), (d), and (f) show the same locations with the left-lateral offsets reconstructed by reversing the fault motion by the amount indicated on the figure. Panel (g) shows an example of the geomorphology in the region indicated on Figure 2.7. The location of the fault is shown by white arrows, and cuts across the strike of the geological units. The western part of the fault forms a sharp topographic step, and the eastern part results in linear valleys which cut across the geological structures and other drainage (for example in the region of steeply-dipping bedding in the east of the image). *This figure was prepared by Alex Copley.*

2.6 Discussion

The 2013 Minab earthquake was almost entirely left-lateral strike-slip with strike 259° , dip 89° and rake 5° . The earthquake ruptured a patch $\sim 20 \times 10 \text{ km}^2$ with slip decreasing towards the surface and maximum slip of $\sim 1.9 \text{ m}$. The results from the seismic and geodetic inversions, and field observations, are in agreement except in terms of the moment release. The moment estimated from the body-wave inversions ($1.7 \times 10^{18} \text{ Nm}$) is less than those from the geodetic inversions ($4.4 \times 10^{18} \text{ Nm}$) and the gCMT solution ($2.2 \times 10^{18} \text{ Nm}$), although it is similar to the NEIC value of $1.6 \times 10^{18} \text{ Nm}$. This may in part be due to the trade-off between source depth and moment. If the seismological centroid depth is forced to be 4 km (which lies within the error bounds on my solution), as implied by the geodetic results, then my estimated moment is $2.0 \times 10^{18} \text{ Nm}$, still significantly less than that from geodesy. It is likely that the inclusion of surface waveforms in the gCMT solution means that although that solution is less sensitive to the depth of the earthquake, and some components of the moment tensor (hence the benefits of my analysis above), the moment may be more accurate. However, there is relatively little difference between my seismological results and those of the gCMT and NEIC.

The difference between seismological and geodetic estimates of earthquake magnitude is known from multiple other earthquakes in this region. For example, a series of thrust earthquakes on Qeshm Island in the Arabian Gulf had geodetic moments that were larger than those estimated using body-waveform modelling by a factor of 1.5–5 (Nissen et al., 2010). A similar discrepancy of a factor of 2 was found for the 2006 Fin earthquake in the Iranian Zagros (Roustaei et al., 2010), and Lohman and Simons (2005) found systematically higher magnitude estimates from geodesy than seismology for a range of Zagros earthquakes. It therefore appears that the general pattern in the Zagros mountains of geodetically-estimated moments being consistently larger than their seismic counterparts may extend eastwards into the Makran subduction zone. Following these previous authors I suggest that the discrepancy may relate to one of two effects; postseismic slip or choice of velocity model. Postseismic afterslip is sampled by InSAR observations, but not seismic waveforms, which could result in contrasting estimates of seismic moment. It is possible that the large thicknesses of sediment in the Zagros mountains and Makran accretionary prism may lead to larger amounts of postseismic slip compared to coseismic moment release than are commonly observed where faulting is contained within crystalline basement. If this slip occurred between 30 and 49 days after the earthquake, that is, in the interval between the acquisitions of the second images in the ascending and descending track interferograms, I would expect the slip models derived from both interferograms to overpredict the observed ground motion in the ascending track and underpredict the observed ground motion in the descending track. For the constant slip case, however, I find the opposite effect (Figure 2.3g) with the model overpredicting slip for the descending track, which has more postseismic data and underpredicting slip for the ascending

track, which has less postseismic data. Postseismic slip occurring between 30 and 49 days after the Minab earthquake is, therefore, not resolvable in this InSAR data. This does not preclude postseismic slip in the period before the second set of SAR images were acquired. Alternatively, the difference in moment estimates between the seismic and geodetic models may result from systematic errors in the velocity model used, as suggested by Lohman and Simons (2005).

2.6.1 Regional Tectonics

The fault that ruptured in the 2013 Minab earthquake and the other left-lateral strike-slip faults visible in the geomorphology (Figure 2.9) are roughly perpendicular to the N160°E striking Minab-Zendan-Palami fault zone. I also observe that the aftershocks of the Minab earthquake (shown in Figure 2.9a) are all dominantly strike-slip, although the fault and auxiliary planes can not be distinguished from seismology alone. However, relocation of these aftershocks by Kintner et al. (2018) (Figure 2.7b) shows that their epicentres lie along strike from the mainshock, suggesting that they are likely to have been left-lateral. The tectonic significance of the fault which ruptured in the 2013 Minab event and the other E–W striking left-lateral strike-slip faults visible in the geology and geomorphology can be understood using the results of previous work on the active faulting and the GPS-derived velocity field of SE Iran. GPS results show that there is a velocity gradient equivalent to right-lateral shear on \sim N–S striking planes which extends from the Strait of Hormuz eastwards into the Makran (Figure 2.1b; Peyret et al., 2009). This shear is partly accommodated by the faults of the MZP fault zone, which cumulatively slip at \sim 4–8 mm/yr (REGARD et al., 2005). However, this slip rate does not entirely account for the velocity differences of 23 mm/yr and 19 mm/yr between the Strait of Hormuz and the GPS stations BAZM and CHAB respectively (labelled on Figure 2.1b). I therefore suggest that the E–W striking left-lateral strike-slip faults I have studied accommodate at least part of the remainder of this motion by rotating clockwise about vertical axes (Figure 2.9b). In order to achieve the overall rate of shear of 15–19 mm/yr, the faults would be required to slip at rates of \sim 2.5–3.2 mm/yr (calculated using the expressions of Copley and Jackson, 2006, and using block widths and lengths of 8 km and 50 km, taken from Figure 2.9). At such a rate, the geological offset of 700 m observed on the fault which ruptured in 2013 (Figure 2.6) would require 0.2–0.3 Ma to accumulate, and would allow the fault system as a whole to accommodate 4.2 km of N–S right-lateral shear. If the shear were evenly distributed east of the MZP fault zone, and the faults I have studied only accommodate the motion that occurs in the longitude range from 57.6° to 58.4°, then the corresponding slip rates and ages would be 0.7 mm/yr and 1 Ma. Within the assumption of constant slip rates the 1.9 m of slip I observe in the 2013 Minab event would correspond to \sim 3000 yr of slip accumulation. Clockwise rotations in the region east of the MZP fault zone are consistent with palaeomagnetic data (Aubourg et al., 2008).

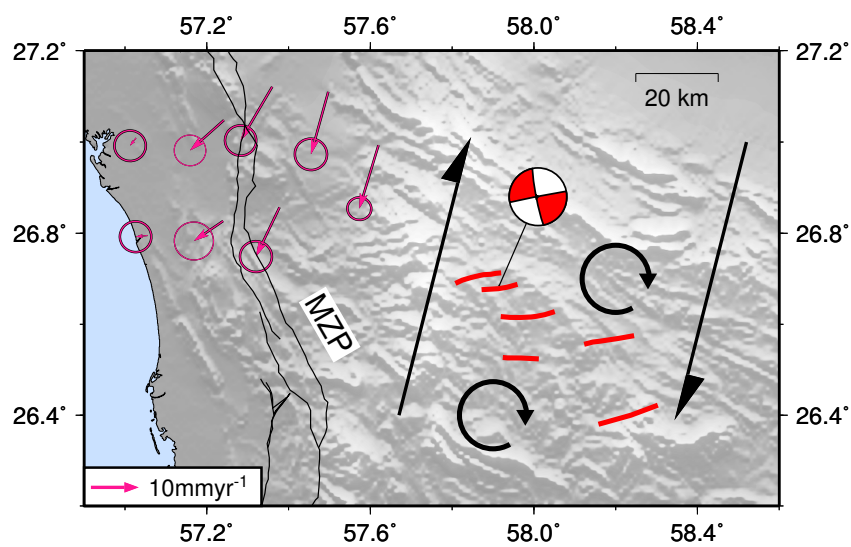


Figure 2.9: Overview of the regional kinematics (discussed in Section 2.6.1). Vectors in pink are selected GPS relative to Arabia from Peyret et al. (2009) with ellipses showing 95% confidence intervals. The GPS velocities show a W–E increase in southward velocity (see also Figure 2.1b). Half-arrows show schematically the overall shear across the region. Circular arrows show the sense of rotation (clockwise) of the left-lateral faults required to accommodate this shear.

2.6.2 Relationship to Slab Geometry

Seismological studies (e.g. Kadinsky-Cade and Barazangi, 1982; Yamini-Fard and Hatzfeld, 2008) suggest that the Arabian plate is continuous across the Oman line, with no evidence for a slab tear. The transition from continental collision to subduction along the Arabian plate's northern boundary must, therefore, involve bending of the lithosphere towards the subduction zone along a W–E profile. The depth of the plate interface, combined with the traction transmitted across this interface, will exert a strong control on the surface motion. The traction across the plate interface sets the rate of shearing on horizontal planes within the upper plate. As the subduction interface deepens from W to E, the upper plate gets thicker so will be able to support a larger velocity difference between the underthrusting plate and the surface. The eastwards deepening of the interface would, therefore, be expected to result in an eastwards increase of convergence-parallel surface velocities relative to Arabia. When the slab flattens out (on a W–E cross section) then all points will have the same thickness of material over-riding the subduction interface, and the velocity at the surface would be expected to be constant along-strike. In this simple model, the right-lateral shear on N–S striking planes would be expected to extend eastwards from the Strait of Hormuz as far as the longitude at which the subducting plate achieves a constant depth along-strike (see Figure 2.10).

Yamini-Fard et al. (2007) conducted a survey of the seismicity and velocity structure in the region 56.5–58.5°E, 27–29.5°N. Between longitudes of 56.5° and 58° there is a W–E increase in seismic velocity across horizontal slices and a SW–NE deepening of seismicity. These results suggest that the subducting Arabian plate is progressively deepening eastwards towards ~58°E. Such deepening is consistent with the shear observed at the surface and the presence of the Minab earthquake fault and other E–W trending strike-slip faults, over a region which approximately corresponds to this longitude range.

2.6.3 Strike-Slip Faulting in the Accretionary Wedge

The earthquake studied in this paper has some similarity to the 2013 M_w 7.7 Balochistan earthquake (Avouac et al., 2014; Jolivet et al., 2014). Both events were strike-slip ruptures in the onshore part of the Makran accretionary prism. During the formation of the accretionary prism both of these regions would have been characterised by thrust faulting. However, both areas are now experiencing predominantly strike-slip faulting, and the Balochistan event is thought to have reactivated a dipping thrust fault in a strike-slip sense. The implications of this strike-slip faulting for the dynamics of the accretionary prism are discussed in Chapter 3.

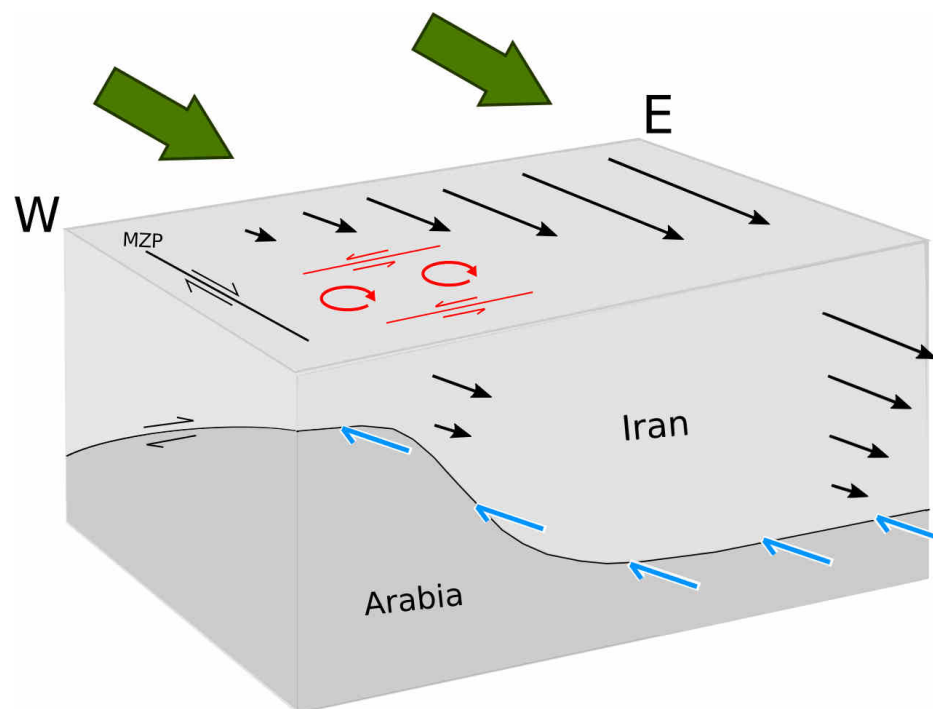


Figure 2.10: Schematic illustration of how the transition from continental to oceanic crust in the Arabian plate establishes a W–E gradient in southwards velocities relative to Arabia at the surface. Green arrows show the overall compressive force across the region due to the convergence between Arabia and South Iran. Black arrows indicate velocities relative to Arabia with longer arrows corresponding to greater velocities. Blue half arrows indicate basal traction at the interface between Iran and Arabia. MZP is the Minab-Zendan-Palami fault zone and faults in red show the left-lateral faulting described in this study.

2.7 Conclusions

I have studied the May 2013 M_w 6.1 Minab earthquake. Left-lateral strike-slip motion on a plane oriented \sim E–W broke one of a series of left-lateral strike-slip faults within the Makran accretionary prism. These faults accommodate an overall velocity field equivalent to right-lateral shear on \sim N–S striking planes. The cause of this shear, which extends \sim 200 km east of the Strait of Hormuz, is likely to be the tractions relating to the underthrusting Arabian lithosphere, which deepens over this longitude range.

Chapter 3

Megathrust properties and behaviour in the Makran subduction zone[†]

Overview

In this and the following two chapters I expand my focus to look at the kinematics and dynamics of the Makran subduction zone as a whole. This chapter focusses on the megathrust associated with subduction in the Makran. By combining techniques from seismology, geodesy and geomorphology, I am able to put constraints on the shape of the subduction interface and the style of strain across the prism. I find that the subduction interface in the western Makran may be locked, accumulating elastic strain, and move in megathrust earthquakes. Such earthquakes, and associated tsunamis, present a significant hazard to populations around the Arabian Sea.

3.1 Introduction

The Makran, formed by the subduction of the Arabian plate beneath the southern coasts of Iran and Pakistan, is one of the world's least well-documented subduction zones. Logistical constraints have made much of the Makran essentially inaccessible in recent years, curtailing earlier field investigations (e.g. Harrison, 1943; Harms et al., 1982; Falcon, 1974). Only a small number of recent field studies have been conducted, looking at the morphology and

[†]This chapter is adapted from part of Penney, C., Tavakoli, F., Saadat, A., Nankali, H. R., Sedighi, M., Khorrani, F., Sobouti, F., Rafi, Z., Copley, A., Jackson, J., and Priestley, K. (2017). Megathrust and accretionary wedge properties and behaviour in the Makran subduction zone. *Geophys. J. Int.*, 209:1800–1830. doi:10.1093/gji/ggx126

geology of the region (e.g. Ellouz-Zimmermann et al., 2007; Haghypour et al., 2012). There is little onshore seismic data, and GPS measurements are sparse. As such, many aspects of the Makran's tectonics remain enigmatic. By combining techniques and results from seismology, geomorphology, GPS and modelling, I am able to gain insights into some of the fundamental questions about this subduction zone.

The seismic hazard posed by the Makran megathrust is one such question (e.g. Smith et al., 2013; Musson, 2009). Subduction megathrusts host many of the world's largest earthquakes, and the hazard associated with such an event on this megathrust is potentially severe. If the earthquake were to cause a tsunami it could threaten densely populated coastal regions in Pakistan and western India (Bilham et al., 2007) and the Omani coast, which is undergoing rapid urbanisation (Heidarzadeh and Kijko, 2011). A significant part of the subduction interface in the eastern (Pakistani) Makran is locked and can produce large earthquakes. This locking was demonstrated by an M_w 8.1 earthquake on 27th November 1945 near Pasni (Ambraseys and Melville, 1982, the approximate rupture area is outlined in red on Figure 3.1), which caused a small tsunami (Hoffmann et al., 2013). In contrast, the western (Iranian) Makran shows an almost total absence of shallow thrust earthquakes in both the instrumental and historical periods, with reports of only a single possible megathrust earthquake in 1483 (Ambraseys and Melville, 1982), for which the source region is poorly-constrained (Musson, 2009). However, Ambraseys and Melville (1982) also note that the sparse population of the Makran throughout the historical period means that earthquakes in the region may not have been documented. A microseismic study using ocean bottom seismometers found no microseismicity in the western Makran (Niazi et al., 1980). This has led to suggestions that the megathrust in the western Makran may be sliding continuously, rather than accumulating elastic strain (Byrne et al., 1992). However, the distribution of large boulders along the Omani coast, thought to have been emplaced by tsunamis (Hoffmann et al., 2015), suggests that the megathrust in the western Makran may move in infrequent large earthquakes. A series of terraces along the Makran coast (Page et al., 1979) could have resulted from uplift in earthquakes, but could also be due to aseismic underplating and uplift (Platt et al., 1985). Whether the western Makran is locked and able to generate large earthquakes therefore remains an open question.

The mean dip of the subduction interface in the Makran is another open question. Geodetic data have been used to assess the degree of elastic strain accumulation in many other subduction zones, but this procedure requires a model for the shape and location of the subduction interface. Early results from seismic reflection surveys gave the dip of the oceanic plate Moho as less than 2° at $\sim 62.5^\circ\text{E}$ (White and Loudon, 1982). Subsequent studies have revised this estimate to $\sim 3^\circ$ in the same area, based on controlled-source seismic imaging

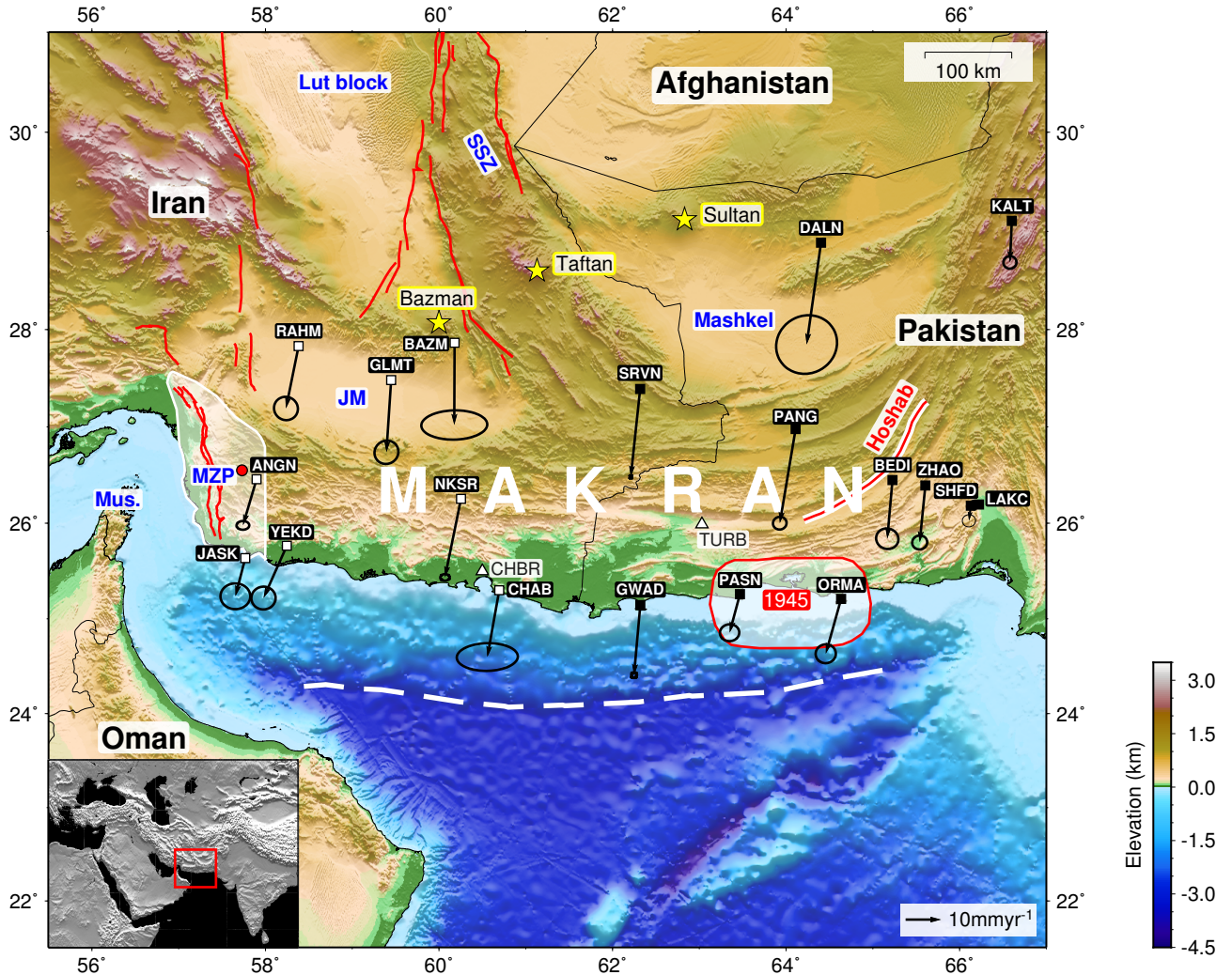


Figure 3.1: Map of the Makran region, location shown on inset. Red lines are mapped strike-slip faults in SE Iran (Walker and Jackson, 2004; Regard et al., 2005). SSZ is the Sistan Suture Zone and MZP is the Minab-Zendan-Palami fault zone. The white region surrounding the MZP shows the extent of mapped diffuse strike-slip faulting, which includes E–W oriented faults to the east of the MZP (Chapter 2). The location of the 2013 Minab earthquake is shown by a red circle. The red line outlined in white is the trace of the surface ruptures of the 2013 Balochistan (Pakistan) earthquake on the Hoshab fault (Avouac et al., 2014). The red outlined region shows the approximate rupture area of the 1945 M_w 8.1 earthquake from Byrne et al. (1992). The white dashed line indicates the bathymetric break in slope at the toe of the accretionary wedge. Yellow stars show the volcanic centres associated with subduction. White triangles show the locations of seismometers, CHBR and TURB, which are used here for receiver-function analysis. The Jaz Murian (JM) and Mashkel depressions are labelled. Mus. is the Musandam Peninsula. Black arrows are GPS velocity vectors relative to Arabia with 95% confidence ellipses. GPS velocities are taken from Vernant et al. (2004); Bayer et al. (2006); Masson et al. (2007); Peyret et al. (2009); Walpersdorf et al. (2014); Frohling and Szeliga (2016) and this dissertation. For stations with multiple reported velocities (BAZM, CHAB, JASK) I use a mean velocity; since the velocities reported by different authors are very similar, mostly within error of each other, this does not affect my results. Those GPS stations shown with white squares are used to model locking of the subduction interface in the western Makran (Section 3.3).

of the sediment-basement interface (Kopp et al., 2000; Smith et al., 2012), which is thought to approximately coincide with the subduction interface (e.g. Kopp et al., 2000). A shallow dipping subduction interface in the western Makran has been proposed as an explanation for the small number of earthquakes in the region (Dykstra and Birnie, 1979; Niazi et al., 1980). However, the curvature of subducting slabs makes the dip of the subduction interface near the toe of the wedge unrepresentative of the mean dip, and Maggi et al. (2000b) proposed a ‘true dip’ of 26° at latitudes north of 27°N , based on earthquake depths. Byrne et al. (1992) suggested that the dip of the subducting slab in the western Makran is likely to be steeper than in the east due to the smaller prism width and more southerly location of the volcanic arc in the west (Figure 3.1). Frohling and Szeliga (2016) recently modelled GPS velocities in the region and concluded that the Makran megathrust is locked to a depth of at least 38 km. However, there are significant uncertainties in their proposed interface geometry, making it important to revisit this issue. I first present a compilation of earthquakes in the region, which I use to improve the constraints on the shape and location of the subduction interface (Section 3.2). This allows me to address the question of whether elastic strain accumulation in the western Makran is consistent with the available GPS data (Section 3.3).

3.2 Shape and Location of the Subduction Interface

The mean dip of the subduction interface is important for assessing the degree of elastic strain accumulation on the interface (Section 3.3). To address this question, I present a compilation of well-located earthquakes in the Makran (Section 3.2.1), and receiver functions from local seismometers (Section 3.2.2), in order to constrain the range of possible dips of this interface (Section 3.2.3). My compilation of earthquakes also allows me to infer the style of strain across the prism (Section 5.1).

3.2.1 Earthquake Compilation

I use teleseismic body-waveform modelling and previously published results (from teleseismic body-waveform modelling, P-wave first motions and global earthquake catalogues) to produce a compilation of earthquakes with well-constrained depths and mechanisms. The criteria for a “well-constrained” earthquake from each data set are discussed below. A table giving the depths, locations and mechanisms (where available) of well-constrained earthquakes is given in Appendix B. Figure 3.2a shows earthquakes, $m_b > 4$, from 1945–2013 with published focal mechanisms (including earthquakes for which I consider the depth and/or focal mechanism to be poorly constrained, shown as semi-transparent). Figure 3.2b shows earthquakes, $m_b > 4$,

over the same time period, with well-constrained depths, and, where available, focal mechanisms.

Earthquake depths and mechanisms from teleseismic body-waveform modelling (McCaffrey and Abers, 1988; McCaffrey et al., 1991) are well-constrained, with typical errors of $\pm 10^\circ$ in strike, $\pm 5^\circ$ in dip, $\pm 10^\circ$ in rake and ± 4 km in depth (Molnar and Lyon-Caen, 1989). Where available, I use published earthquake depths and mechanisms from this technique (Laane and Chen, 1989; Byrne et al., 1992; Baker, 1993; Berberian et al., 2000; Maggi et al., 2000b; Berberian et al., 2001; Walker, 2003; Jackson et al., 2006; Talebian et al., 2006; Engdahl et al., 2006; Nissen et al., 2010, 2011; Walker et al., 2013; Barnhart et al., 2014b; Jolivet et al., 2014, Chapter 2). In addition, I have used teleseismic P and SH body-waveform modelling to determine the depths and focal mechanisms of 7 earthquakes for which solutions have not previously been published. The details of this technique have been discussed extensively elsewhere (e.g. Taymaz, 1990; Maggi et al., 2000b; Craig et al., 2014a), and will not be reproduced here. My solutions from this technique, and a more detailed discussion of the methodology, are presented in Appendix A. In particular, I have included my body-waveform modelling determined depth and focal mechanism for the M_w 6.3 7th February 2017 earthquake (Figure A.3), which occurred near the western Pakistani coast. This earthquake is also included in Figures 3.2a and b, in the cluster of shallow thrusts near the Pakistani coastline.

For earthquakes which pre-date the widespread use of body-waveform modelling I use focal mechanisms determined from P-wave first motions by Jackson and McKenzie (1984); Jacob and Quittmeyer (1979) and Byrne et al. (1992). I consider first-motion solutions to be well-constrained if depth phases are used to determine the earthquake depth. Solutions from Chandra (1981, 1984) are not included in this compilation, as the sparse distribution of polarity data and small size of many of the earthquakes suggests that these solutions may not be reliable (Jackson and McKenzie, 1984).

Where no manually processed solution, either from body-waveform modelling or first motions, is available, earthquake focal mechanisms are taken from the gCMT catalogue (Dziewonski et al., 1981; Ekström et al., 2012) and hypocentral locations from the EHB catalogue (Engdahl et al., 1998), up to the beginning of 2009, and the ISC (International Seismological Centre, 2015), from 2009 onwards. The EHB catalogue for Iran was reviewed up to 2004 by Engdahl et al. (2006), and the earthquake locations given in that review are used in preference to the original catalogue. For these earthquakes a well-constrained depth means that the hypocentre was calculated using more than 5 depth phases and at least 50 stations, with the depth free to change in the inversion. My results would not change substantially for small variations

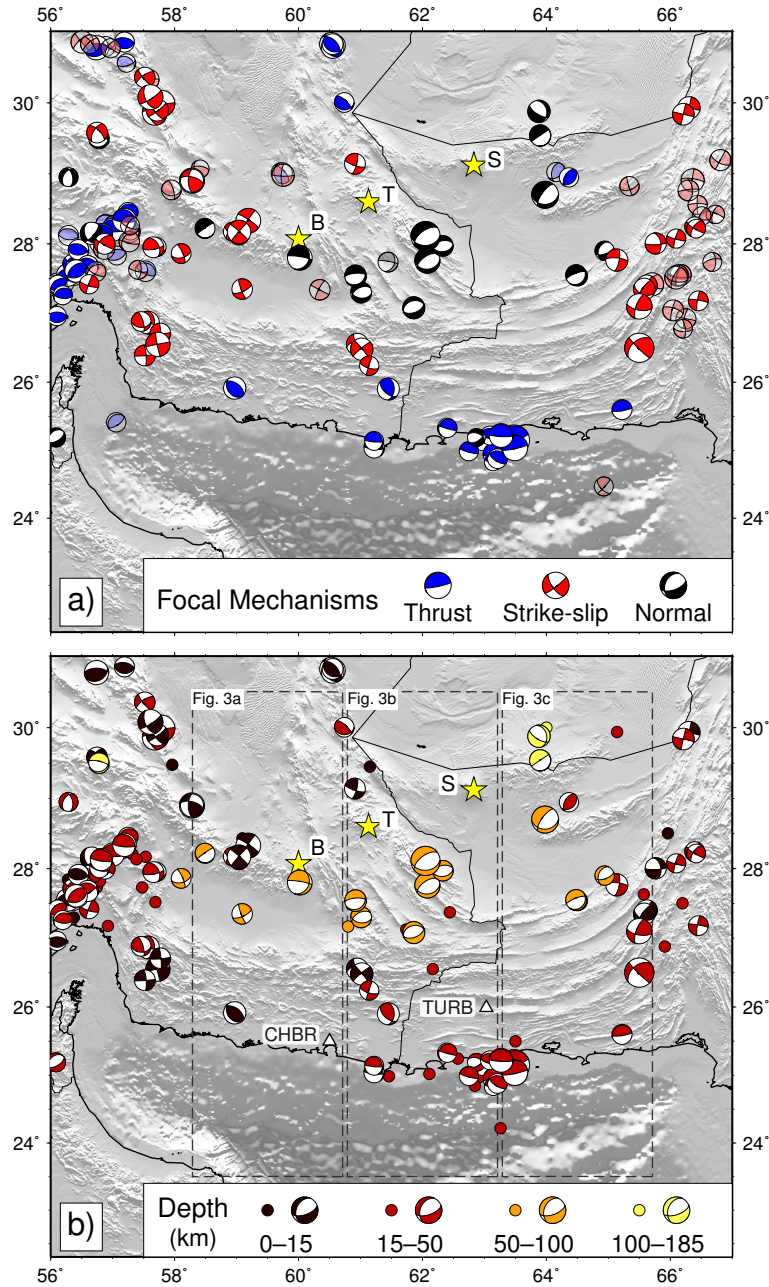


Figure 3.2: Earthquakes in the Makran. a) All earthquakes, $m_b > 4$, from 1945–2013 with focal mechanisms reported by gCMT or in the literature (see Section 3.2.1 for citations) and the M_w 6.3 7th February 2017 earthquake, which was a shallow thrust in the cluster near the Pakistani coast. Events for which I consider the depth and/or focal mechanism to be poorly constrained are shown as semi-transparent. Focal mechanisms are coloured by rake, as shown in the key. Blue: thrust earthquakes, red: strike-slip earthquakes and black: normal-faulting earthquakes. Note the spatial separation of mechanisms; shallow thrusts cluster at the coastline and strike-slip events are concentrated at the eastern and western edges of the accretionary prism. b) Earthquakes, $m_b > 4$, from 1945–2013 with well-constrained depths, as described in Section 3.2.1. Where well-constrained focal mechanisms are available (from body-waveform modelling, first motions or gCMT solutions with $>70\%$ double-couple) these are coloured by depth, as shown in the key. Earthquakes with well-constrained depths but no mechanism are plotted as circles, with the same colour scale. Dashed boxes show the region in which earthquakes are projected on to each of the profiles in Figure 3.4. White triangles show the locations of seismometers, CHBR and TURB. In a) and b) B, T, S are the volcanic centres Bazman, Taftan and Sultan.

in these cut-offs, which have been chosen based on the experience of previous authors (e.g. Jackson, 1980; Engdahl et al., 1998). With these constraints, I expect the errors in EHB/ISC locations to be 10–15 km in epicentre and ~ 10 km in depth (Engdahl et al., 2006). I view a focal mechanism as well-constrained if it has a gCMT solution which is at least 70% double couple, as defined by Jackson et al. (2002). Earthquakes shown as circles in Figure 3.2b have well-constrained depths but no reliable focal mechanism. By using only well-constrained earthquake depths I am able to improve the model for the geometry of the subduction interface proposed by Frohling and Szeliga (2016), which is based on interpolation of the ISC catalogue, without quality control or body-waveform modelled events.

3.2.2 Receiver Functions

This section was substantially written by Keith Priestley, who carried out the receiver function analysis described, using data collected at CHBR by Farhad Sobouti and at TURB by Zahid Rafi.

Further constraints on the location and depth of the subduction interface can be provided by receiver-function analysis. We used data from two broadband seismometers in the Makran; CHBR located at Chabahar in southern Iran and TURB located at Turbat in southern Pakistan (Figure 3.1), to determine receiver functions (Figure 3.3) and combine these with surface waves to find the velocity structure beneath these sites (Section 3.2.3, Figures 3.4a and b). This method has been used extensively by other authors (e.g. Julià et al., 2003; Dugda et al., 2007; Priestley et al., 2008) and is described in detail in Julià et al. (2000). Radial receiver functions are waveforms created by deconvolving the vertical component of the seismogram from the radial component to isolate the effect of the velocity structure at the receiver site from the other information in the teleseismic P-wave coda. The resulting radial-component time series corresponds closely to the impulse response of the Earth structure beneath the seismograph site (Langston, 1979). Teleseismic receiver functions from earthquakes in the $30\text{--}90^\circ$ distance range recorded at these sites were determined using the iterative deconvolution method of Ligorria and Ammon (1999) and stacked in narrow back-azimuth bins. The receiver functions from both sites show a strong, positive conversion, marked Ps in Figure 3.3, at about 4 s which probably corresponds to the top of the subducting Arabian slab.

P-wave receiver functions are sensitive to the shear-wave velocity (V_s). The delay time between the direct P arrival and the Ps conversion in the receiver function depends on the depth to the interface and the average wavespeed of the overlying layer, creating a trade-off which means that neither the layer thickness nor the average wavespeed of the layer can be uniquely determined through using only receiver-function analysis. To minimize this trade-off,

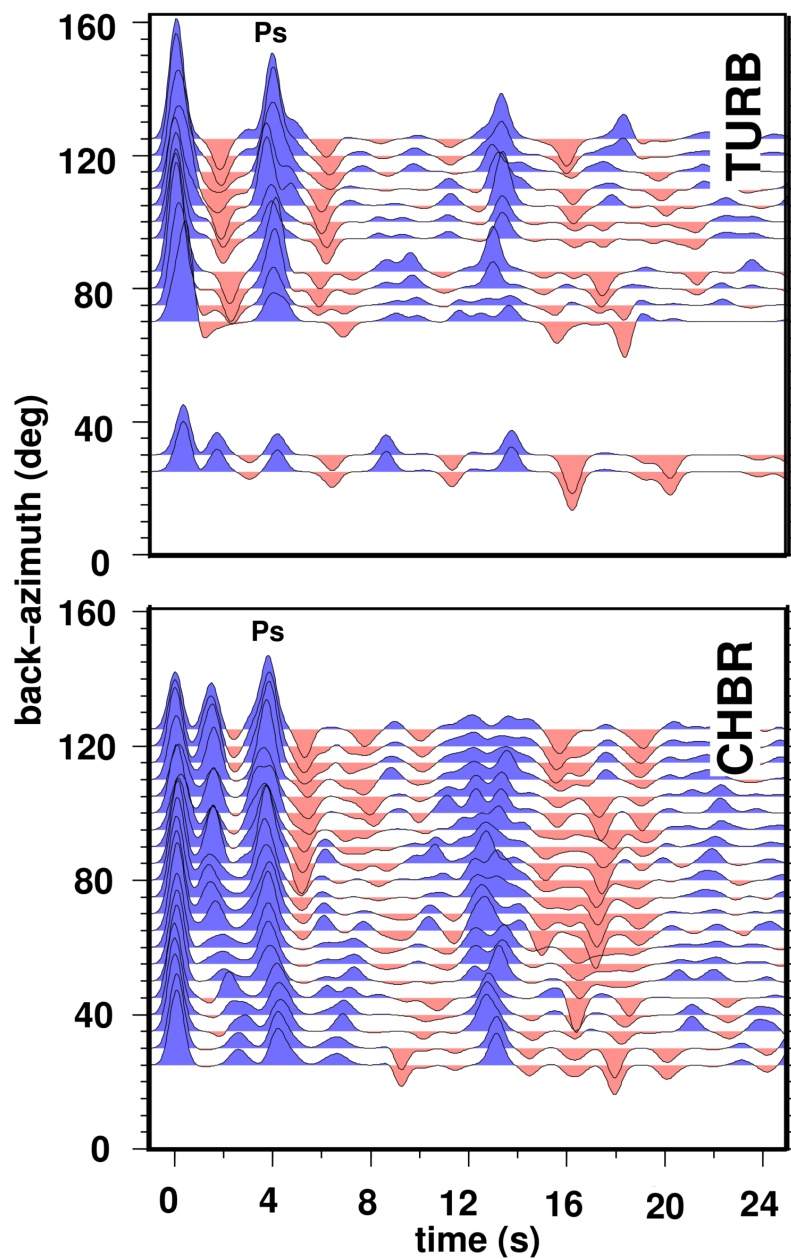


Figure 3.3: Receiver functions from CHBR and TURB (locations shown in Figure 3.1), binned by back-azimuth. The strong, positive conversion, labelled Ps, at ~ 4 s at both sites is likely to correspond to the top of the subducting Arabian plate. *This figure was prepared by Keith Priestley using data collected by Farhad Sobouti and Zahid Rafi.*

we simultaneously model the P-wave receiver functions and 10–70 s period fundamental-mode Rayleigh-wave group velocities. We interpolated the group velocity maps of Acton et al. (2010) to obtain a site-specific dispersion curve. By modelling both data sets simultaneously we can place strong constraints on the velocity structure because the surface-wave dispersion is sensitive to the absolute velocity but less so to the layer thickness, whereas the receiver functions are sensitive to discontinuities in velocity but less so to absolute wavespeed (Julià et al., 2000). The dispersion constrains the average layer wavespeed and thickness over a broader region around the site, and the receiver functions superimpose short wavelength details.

The starting Earth model in the receiver function-surface wave inversion is based on AK135 (Kennett et al., 1995) and parametrized as a stack of 2 km-thick layers, except near the surface where 1 km-thick layers provide additional freedom in the inversion to fit any strong near-surface gradients. To minimize bias in the inversion result from an a priori choice of interface depth, we replaced the AK135 crustal wave speeds with the AK135 uppermost-mantle wavespeeds so there is no a priori crustal structure in the starting inversion model. Perturbing the wavespeed structure in the starting model by ± 0.2 km/s has a negligible effect on the inverted structure.

The shear-wave velocity profiles beneath both CHBR and TURB (red lines in Figures 3.4a and b) show a thick, low-wavespeed (~ 3 km/s) layer, probably corresponding to the sediments of the accretionary wedge, overlying a high-wavespeed (~ 4.1 km/s) basement, which we interpret as the top of the oceanic crust. This velocity increase occurs at 28 ± 2 km at TURB and 26 ± 2 km at CHAB, where the errors are determined by making forward tests on the interface depth. This increase in velocity is consistent with the location of the subduction interface inferred from earthquake locations (Figure 3.4, see discussion below).

3.2.3 Interpretation of Subduction Interface Geometry

Figure 3.4 shows three N–S profiles through the Makran, marked on Figure 3.2b, plotting only those events with well-constrained depths. These profiles have several important features. First, shallow thrust earthquakes on the subduction interface cluster around 62°E (Figure 3.4b), just west of the proposed rupture area for the 1945 earthquake (Byrne et al., 1992). These events may be late-stage aftershocks of the 1945 earthquake, as aftershock sequences have been known to continue for decades or even centuries after the mainshock (Ebel et al., 2000). Taking the fault planes of the shallow thrust earthquakes to be the northward-dipping nodal planes, most have dips of $8\text{--}10^\circ$ with an estimated error of $\pm 5^\circ$. If these earthquakes occurred on the subduction interface, the dips of their nodal planes provide an estimate of the dip of that interface close to the coastline. Taking the surface projection of

the interface as 24°N , where I observe a break in the bathymetric slope (white dashed line, Figure 3.1), a line projected through the locations and depths of these earthquakes gives an average subduction-interface dip of $6\text{--}15^{\circ}$, consistent with the nodal-plane dips. This line is in very similar to the sediment-basement interface proposed by Kopp et al. (2000) (bold line in Figure 3.4b).

Another important feature of the earthquake distribution is a series of normal-faulting earthquakes at depths greater than 50 km. These earthquakes have an $\sim\text{ENE}\text{--}\text{WSW}$ linear distribution in map view (black focal mechanisms in Figure 3.2a), parallel to the strikes of their nodal-planes, and are observed across the longitudinal extent of the subduction zone. The dip of the seismogenic zone, which I infer from the earthquake distribution (dashed line, Figure 3.4c), appears to steepen to the north of this line of earthquakes. I therefore suggest that these normal-faulting earthquakes may represent extension at a hinge in the subducting Arabian plate, as has been suggested in other subduction zones with variable dip (Isacks and Barazangi, 1977).

Volcanic arcs were thought to form approximately above the 100 km contour of subducting slabs (Davis et al., 1983) but significant variations have been found (e.g. England et al., 2004; Syracuse and Abers, 2006), probably due to the dependence of thermal structure on convergence rate, plate dip and age (England and Wilkins, 2004). My proposed hinge line lies just south of the volcanic arc in the Makran. This arc is composed of three main volcanic centres (yellow stars in Figures 3.2 and 3.4), which have chemical signatures indicative of subduction volcanism (Biabangard and Moradian, 2008; Nicholson et al., 2010; Saadat and Stern, 2011). Earthquakes deeper than the proposed hinge line have only been recorded in the east (with the exception of an isolated deep event in the far west, reported by Maggi et al., 2000b), within the region profiled in Figure 3.4c, making it difficult to constrain the depth of the subduction interface beneath the arc. However, one of the normal-faulting earthquakes occurred almost directly beneath Bazman volcano, at a depth of 74 km (Jacob and Quittmeyer, 1979). This suggests that the subduction interface is no deeper than ~ 80 km under this part of the volcanic arc, allowing for ± 5 km possible error in the earthquake depth. For the subduction interface to reach a depth of ~ 100 km by the latitudes of Taftan and Sultan (at 62°E) it would need to significantly increase its dip north of the line of normal-faulting earthquakes. This geometry is consistent with my interpretation of these earthquakes as representing extension at a hinge in the subducting plate. Since these normal-faulting earthquakes occur within the descending slab, they provide an upper limit on the average dip of the subduction interface between their locations and the trench. I find maximum average dips of $\sim 11^{\circ}$ in the western Makran, $\sim 9^{\circ}$ in the central region and $\sim 8^{\circ}$ in the eastern Makran.

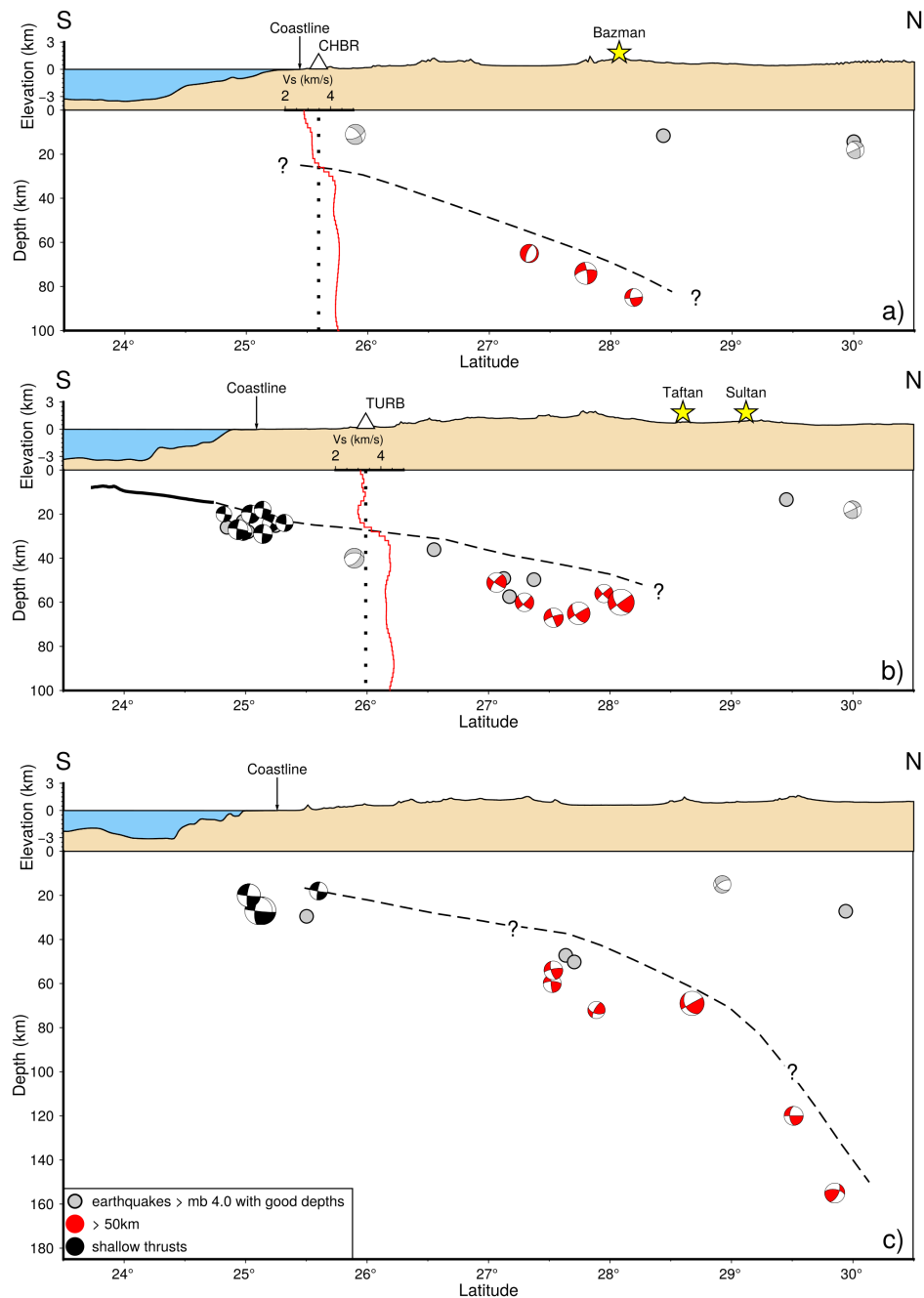


Figure 3.4: N–S profiles through the Makran showing earthquakes with well-constrained depths. Focal mechanisms are cross-sections in the plane of the projection. Black focal mechanisms are shallow thrusts likely to be on, or close to, the subduction interface. Note that these thrusts cluster near the coastline. Red focal mechanisms are earthquakes with depths greater than 50 km which I interpret as occurring within the Arabian slab. Other earthquakes are shown in grey, with well-constrained focal mechanisms if available. Dashed lines show a possible geometry for the subduction interface in each profile, based on the data shown in this figure. The depth scale is the same in each profile. a) Profile at 59.5° E. The red line shows the shear wave velocity profile at CHAB from joint inversion of receiver functions and surface waves. b) Profile at 62° E. The solid black line is the basement reflector observed by Kopp et al. (2000), which is collinear with the earthquakes which I interpret as occurring on the subduction interface. The red line shows the shear wave velocity profile at TURB from joint inversion of receiver functions and surface waves. c) Profile at 64.5° E. The deepest events in the Makran have been recorded near the location of this profile, providing the main constraints on the shape and location of the subduction interface north of the line of deep normal-faulting earthquakes (Figure 3.2, Section 3.2).

The uncertainties in my estimates of the dip of the subduction interface do not allow me to definitively identify lateral variations in the geometry of the subduction interface. However, the slight decrease in my estimates of maximum average dip from west to east is consistent with the volcanic centres in the east being further north than those in the west (Byrne et al., 1992). The contrast in deep seismicity between the east and west is also unclear. From my profiles (Figure 3.4) it might appear that the only earthquakes deeper than 100 km have occurred in the eastern Makran. However, the deep event in the western Makran, mentioned above, which does not lie within the area of my profiles, was suggested by Maggi et al. (2000b) to have occurred in the subducting Arabian plate (Figure 3.2b at ~ 57 E, 29 N). More earthquake observations will be needed in order to resolve any lateral variations.

3.3 Elastic Strain Accumulation on the Subduction Interface

The absence of shallow thrust earthquakes in the western Makran, discussed above, does not necessarily imply that the subduction interface in the western Makran is not locked and accumulating elastic strain. I use published GPS velocities over ~ 15 yrs from the Iranian Makran (marked with white squares in Figure 3.1; Bayer et al., 2006; Masson et al., 2007; Peyret et al., 2009; Walpersdorf et al., 2014; Frohling and Szeliga, 2016), to determine whether the subduction interface in the western Makran might be locked. I also include velocity estimates from two sites in the onshore part of the prism (ANGN and NKSR) which have not previously been published. These sites form part of the Iranian national network of GNSS receivers maintained by the National Cartographic Centre, Tehran and are equipped with Ashtech UZ-12 ICGRS receivers with choke-ring antennae, mounted on concrete pillars. Data were recorded continuously from August 2011 to February 2013 and processed using the GAMIT/GLOBK software, version 10.4 (Herring et al., 2010). Time-averaged linear velocities for these sites are estimated by applying the GLOBK Kalman filter to the daily solutions. *The collection and processing of GPS data was carried out by Farokh Tavakoli, Abdolreza Saadat, Hamid Reza Nankali, Morteza Sedighi and Fateme Khorrami.*

I apply the backslip technique proposed by Savage (1983) to a planar fault in an elastic halfspace and use Okada's (1985) equations to model the surface velocities resulting from different locking depths and subduction-interface positions. I then compare these model predictions with velocities measured by GPS. Subduction zones are not normally locked to depths greater than 40 km, measured vertically from the surface (Tichelaar and Ruff, 1993; Hyndman et al., 1997; Lay et al., 2005; Ye et al., 2016; Bouchon et al., 2016) and my profiles in Figure 3.4 show that a planar interface is a reasonable assumption at these shallow depths.

Frohling and Szeliga (2016) investigated the coupling of the Makran using a similar backslip approach but with a more complex model for the subduction interface. However, as discussed in Section 3.2, those authors did not apply quality control to the earthquakes used to infer the position and shape of the subduction interface, which is, in any case, poorly-constrained. I therefore consider a planar model of the interface to be more appropriate for this modelling. I also use GPS velocities not incorporated into Frohling and Szeliga (2016)'s modelling, in order to provide more realistic constraints on the degree of locking on the subduction interface.

The uncertainties in the position and shape of the subduction interface makes the choice of model parameters difficult. The overall rate of convergence is also poorly constrained due to the scarcity of GPS stations in the region (Vernant et al., 2004). Inverse methods are therefore inappropriate for analysing the degree of coupling as the inversions are very underdetermined. Instead, I calculate forward models for end-member combinations of parameters and a selection of intermediate values. The aim of this modelling is to ascertain whether coupling in the western Makran, to a geologically reasonable depth, on an interface consistent with my results from earthquakes and receiver functions, is consistent with the observed GPS velocities, rather than to determine the actual pattern of coupling on the subduction interface, which is not possible with the data which is currently available.

Since I am considering a planar interface, I must specify the average dip of the megathrust. I take 6° as the minimum dip based on the locations and depths of the shallow thrust earthquakes in Figure 3.4b, which are likely to have occurred on the subduction interface (Section 3.2.3). The depths of normal-faulting earthquakes associated with the bending of the Arabian slab, due to the increase in dip of the subduction interface (Section 3.2.3), provide an upper bound on the average dip of the interface, since they must lie within the subducting slab. There is a trade-off between the estimated maximum dip and the choice of the surface projection of the subduction interface but, by taking the most northerly possible surface projection, I ensure that this approach gives an upper bound on the range of possible dips. I find that the maximum possible average dip in the shallow (<40 km) part of the slab is $\sim 11^\circ$ (see Section 3.2.3).

Although there is no clear bathymetric trench in the Makran, due to the high sediment input (White and Ross, 1979; White and Loudon, 1982; Laane and Chen, 1989), the slope break at the toe of the accretionary wedge is visible in the bathymetry and lies at $\sim 24^\circ$ N (white dashed line, Figure 3.1). I use this slope break as a proxy for the surface projection of the subduction interface, which I vary between 23.5° N and 24.5° N to allow for errors in its location. I allow the locking depth to vary between 0 km, a freely-sliding interface, and 40 km,

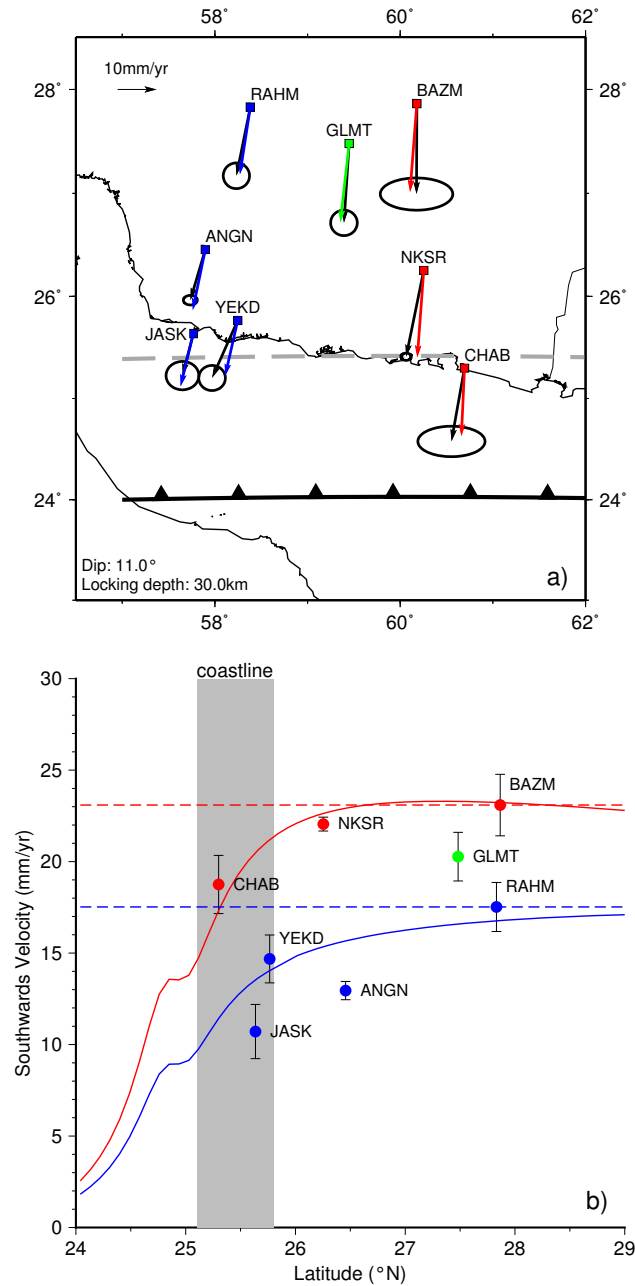


Figure 3.5: Elastic strain accumulation in the western Makran. a) Black arrows show published GPS velocities (sources as in Figure 3.1) and those presented in this thesis (ANGN and NKSR), with 95% confidence ellipses. Coloured arrows are predictions of surface velocity from a coupling model with a locking depth of 30 km, mean dip of 11° and overall convergence rates of 20.4 mm/yr and 32.6 mm/yr west and east of 59.5°E respectively. Model predictions at western stations are shown with blue arrows, at eastern stations with red arrows and at station GLMT, which is centrally positioned within the region, with a green arrow. The surface projection of the subduction interface in this model is shown by the black-toothed line and the location of the down-dip limit of locking is shown by the grey-dashed line. b) N-S profiles through surface velocities. Circles show the southwards component of published GPS velocities and those presented in this thesis, with their associated errors. Those stations in blue are located west of 59.5°E . Those stations in red are located east of 59.5°E . Solid lines are profiles at 58°E (blue) and 60.5°E (red) through the surface velocities resulting from the model in a). Dashed lines show profiles of constant surface velocity, at the velocities of the northernmost GPS stations (red at BAZM, blue at RAHM). Station GLMT lies at approximately 59.5°E and is coloured green. The grey bar shows the location of the coastline across the region.

which is the maximum depth to which subduction interfaces are normally locked (Tichelaar and Ruff, 1993; Hyndman et al., 1997; Lay et al., 2005; Ye et al., 2016; Bouchon et al., 2016). The ~ 150 km distance between the slope break and the coast means that the GPS data are not sensitive to very shallow variations in locking depth.

The overall convergence rate is varied in my calculations in order to reproduce the observed velocities. The western stations (YEKD, ANGN, RAHM, blue in Figure 3.5) require a lower overall convergence rate than those to the east (CHAB, NKSR, BAZM, red in Figure 3.5) in order to match their velocities. This is consistent with the Arabia–Eurasia convergence rate increasing from west to east across the region. Additionally, the western stations are near the western edge of the subduction zone, which may account for their lower velocities. To allow for this velocity variation, in my calculations I use two adjoining megathrust planes with the same geometry, but with different rakes (slip directions) and slip rates. My calculated surface velocities are the result of locking on both these planes. The GPS station GLMT lies at an intermediate longitude, where the parameters of both planes contributes to the surface deformation.

I find that there are multiple parameter combinations that result in reasonable agreement between the observed and synthetic surface velocities. Figure 3.5a shows an example of one such model in map view, in which the locking depth is 30 km, the dip is 11° and the convergence rates in the western and eastern regions are 20.4 mm/yr and 32.6 mm/yr respectively. This model has an RMS misfit of 1.7mm/yr, similar to the resolution of the GPS measurements. Figure 3.5b shows two profiles through the southwards component of the surface velocities from this model, at 58°E and 60.5°E , showing the faster velocities of the more easterly stations. Figure 3.5b also shows that the surface velocities which would result from a plate interface sliding freely at the velocity of the northernmost GPS stations (dashed lines) are unable to reproduce the observed velocities near the coastline. Whilst the precise geometry of locking on the interface cannot be resolved with this dataset, the decrease in velocities towards the coast does require locking to some depth, or internal deformation within the wedge (e.g. Haghypour et al., 2012), which is not accounted for in the backslip approach. I cannot distinguish between these possibilities using the GPS data alone, and internal deformation may make a contribution. Haghypour et al. (2012) suggest a shortening rate of 0.8–1.2 mm/yr between the coast and $\sim 26.5^\circ\text{N}$ in the Iranian Makran, based on ^{10}Be exposure dating and structural measurements of fluvial terraces. However, this shortening is not enough to account for all of the compression I observe, suggesting that elastic strain accumulation above a locked megathrust does play a role. I am also encouraged in my interpretation by observations in other subduction zones, such as Sumatra, where earthquakes are inferred from the palaeogeodetic record to have occurred historically in regions which GPS measurements suggest are accumulating elastic strain at the present day (Natawidjaja et al., 2004; Chlieh et al., 2008; Konca et al., 2008).

My modelling shows that a locked subduction interface in the western Makran is consistent with measured GPS velocities. This corroborates suggestions from observations of tsunami deposits and tsunami modelling (Hoffmann et al., 2015) that the western Makran megathrust may be seismogenic. If the whole along-strike extent of the megathrust were to rupture in single earthquake the subduction zone could be capable of generating a M_w 9 earthquake, as proposed by Smith et al. (2013), which has significant implications for earthquake and tsunami risk around the Arabian Sea.

3.4 Conclusions

A compilation of earthquakes with well-constrained depths and mechanisms allows me to place constraints on the position and shape of the subduction interface in the Makran subduction zone. I find that the subduction interface has an average dip of $\sim 6\text{--}11^\circ$ above 40 km depth. GPS velocities show a higher rate of shortening across the prism than is being accommodated by internal deformation within the accretionary prism. This shortening and numerical modelling demonstrate that the megathrust in the western Makran may be locked and capable of producing large earthquakes, possibly with associated tsunamis.

Chapter 4

Southern Termination of N–S Strike-Slip Faulting in the Sistan Suture Zone[†]

Overview

To the north of the Makran differential motion between Central Iran and Afghanistan results in N–S right-lateral shear which is accommodated on strike-slip faults in the Sistan Suture Zone (labelled SSZ in Figure 3.1). How this shear is accommodated at the zone’s southern end is a long-standing tectonic problem. In this chapter I present three possible solutions, discuss their kinematic implications and suggest which is most consistent with the available information. By combining information from GPS, geomorphology and the distribution of earthquakes I infer that right-lateral motion is transferred across the Jaz Murian depression onto the system of faults accommodating right-lateral motion at the western end of the prism (Chapter 2). The time-dependent strain within the accretionary prism, resulting from the megathrust earthquake cycle (Chapter 3), may play an important role in the deformation of the Makran region.

[†]This chapter is adapted from part of Penney, C., Tavakoli, F., Saadat, A., Nankali, H. R., Sedighi, M., Khorrani, F., Sobouti, F., Rafi, Z., Copley, A., Jackson, J., and Priestley, K. (2017). Megathrust and accretionary wedge properties and behaviour in the Makran subduction zone. *Geophys. J. Int.*, 209:1800–1830. doi:10.1093/gji/ggx126

4.1 Introduction

The Sistan Suture Zone (SSZ), to the north of the Makran (Figure 3.1), is an abandoned accretionary prism formed by the closure of a branch of the Neo-Tethys at 65–90 Ma (Tirrul et al., 1983; Bröcker et al., 2013). The rocks of the SSZ are now offset right-laterally by a series of NNW–SSE striking strike-slip faults, referred to collectively by Walpersdorf et al. (2014) as the East Lut fault, which have been active in the Plio-Quaternary (Tirrul et al., 1983; Walker and Jackson, 2004). These faults accommodate 5–15 mm/yr of differential motion between the Lut Block (in the eastern part of Central Iran) and Afghanistan (Figure 3.1), which moves as part of Eurasia (Vernant et al., 2004; Walker and Jackson, 2004; Reilinger et al., 2006; Meyer and Le Dortz, 2007; Walpersdorf et al., 2014). The \sim N–S striking faults are not observed south of $\sim 27^\circ$ N, and no major N–S faults cut the E–W trending structures of the Makran ranges (Figure 3.1; Jackson and McKenzie, 1984; Walker et al., 2013), leading to the long-standing tectonic question of how right-lateral motion is accommodated at the SSZ’s southern end.

Jackson and McKenzie (1984) proposed an Euler pole for the motion of Central Iran relative to Eurasia that is close to the southern end of the SSZ, so that there is very little motion to accommodate between Eurasia and Central Iran in the south. The slip on the faults within the SSZ would then die out towards their southern ends. However, this suggestion is not compatible with recent GPS measurements (Vernant et al., 2004; Walpersdorf et al., 2014). Alternatively, Byrne et al. (1992) argued that two strike-slip earthquakes on 10th January 1979 (at 61° E, 26.5° N on Figure 3.2b) indicate that right-lateral faulting does continue across the prism. However, there is no evidence of significant right-lateral offsets in the geology or geomorphology of the Makran ranges. The total offset of the SSZ is suggested to be at least 70 km, based on offset units in the Neh complex (north of Figure 3.1; Tirrul et al., 1983; Walker and Jackson, 2004), which would result in visible geological offsets if this motion continued through the accretionary wedge. Additionally, these events, which are the largest of three strike-slip events which have been observed in the central Makran, were M_w 5.8 and 5.9, accounting for only a year’s worth of strain accumulation at the slip rates proposed for the SSZ (Section 4.3). It is also not known which nodal planes are the fault planes for these two earthquakes. Kukowski et al. (2000) proposed a new plate-boundary strike-slip fault, the Sonne fault, separating the Arabian plate from the Ormara microplate (their Figure 3), with morphological expression in the accretionary prism due to high coupling. Lin et al. (2015) suggested that this fault might be a continuation of the SSZ. However, the proposed Sonne fault, the existence of which is in any case unclear since it is not observed to offset structures in the forearc in seismic reflection surveys (Smith et al., 2013), is suggested to be left-lateral (Kukowski et al., 2000), whereas the SSZ is right-lateral. How the right-lateral

shear across the SSZ is accommodated at the zone's southern end is thus an open question, to which I discuss three possible solutions. In the following discussion I consider a range of rates of right-lateral shear across the SSZ of 5–15 mm/yr. The present day rate of shear is 5.6 ± 0.6 mm/yr (Walpersdorf et al., 2014), but I use a high upper bound to allow for uncertainty in the long-term rate.

One possibility is that the right-lateral faults terminate in thrusts with decreasing slip towards their ends (Figure 4.1a), similar to those observed in Mongolia (Bayasgalan et al., 1999a). Strike-slip faults terminate in thrust faults at the northern end of the SSZ and these thrusts can move in earthquakes, either concurrently with strike-slip motion, e.g. the 1997 Zirkuh earthquake (Berberian et al., 1999), or in dominantly thrust earthquakes, e.g. the 1994 Sefidabeh earthquakes (Berberian et al., 2000). The assumption that the faults of the SSZ terminate in thrusts is implicit in much of the literature (e.g. Haghypour and Burg, 2014) but its kinematic implications have not been fully considered in previous studies.

A second possibility is that the right-lateral N–S shear, accommodated by the faults of the SSZ, is transferred onto left-lateral E–W striking faults in the Makran accretionary prism (Figure 4.1b). Left-lateral E–W striking faults can accommodate right-lateral N–S shear by rotating clockwise about vertical axes (e.g. McKenzie and Jackson, 1986). Such vertical-axis rotations accommodate some of the right-lateral shear at the northern end of the SSZ, for example on the Dasht-e-Bayaz fault (Walker et al., 2004), and have been reported at the western margin of the Makran (Chapter 2).

A final possibility is that the right-lateral motion of the SSZ is transferred onto the faults of the Minab-Zendan-Palami (MZP) fault zone (Figure 3.1) and nearby strike-slip faults (described in Chapter 2), which, combined, accommodate ~ 17 mm/yr of right-lateral shear (Peyret et al., 2009). Geometrically, this scenario requires the Jaz Murian depression to be bounded by normal faults (Figure 4.1c). I consider each of these three possibilities in turn.

4.2 Thrust Faulting

For the faults of the Sistan Suture Zone to terminate in thrusts (Figure 4.1a), the northern part of the Makran prism, immediately south of the Mashkel depression (Figure 3.1), would need to accommodate shortening. Recently published GPS velocities from Frohling and Szeliga (2016) show a difference of 2 mm/yr in southwards velocities relative to Arabia between DALN and PANG at 28.89° N and 26.98° N (Figure 3.1). This velocity difference is

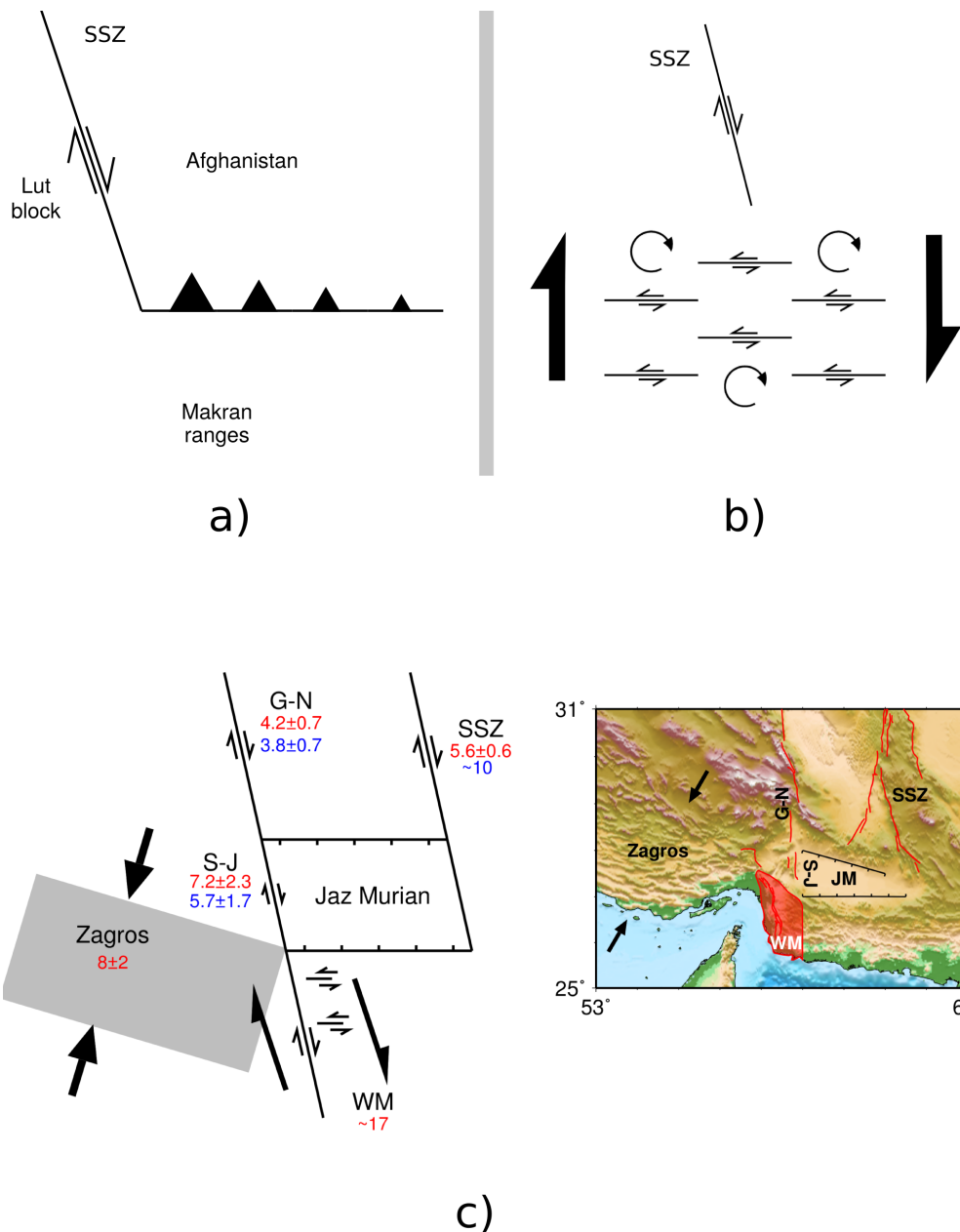


Figure 4.1: Possible methods of accommodating right-lateral motion at the southern end of the SSZ. a) Right-lateral \sim N-S faults terminate in E-W thrusts with displacements dying out towards their ends (toothed line). b) Right-lateral motion on \sim N-S striking faults is transferred on to E-W striking left-lateral faults, which rotate clockwise about vertical axes. c) Left: Right-lateral motion on the \sim N-S striking faults in the SSZ is transferred to the western Makran (WM) by normal faults bounding the Jaz Murian depression (JM). G-N and S-J are the Gowk-Nayband and Sabzevaran-Jiroft fault systems. Numbers are present day (red) and Quaternary (blue) rates in mm/yr (Walker et al., 2004; Regard et al., 2005; Walpersdorf et al., 2006; Peyret et al., 2009; Walker et al., 2010; Walpersdorf et al., 2014). Right: relationship to topography - red lines are faults as in Figure 3.1.

within the stations' formal combined error. Any shortening is therefore small relative to the combined slip rate of the faults in the SSZ (5–15 mm/yr, e.g. Walpersdorf et al., 2014; Walker and Jackson, 2004). Additionally, no shallow thrust earthquakes have been recorded along the southern margin of the Mashkel depression from 1945–2013 (Figure 3.2a and b). Taken alone this would be insufficient to rule out the possibility of shortening across the back of the prism as the repeat times of earthquakes might be longer than instrumental records. However, the absence of thrust earthquakes is consistent with the lack of shortening seen in the GPS data, suggesting that this method of termination of the strike-slip motion in the SSZ is unlikely.

4.3 Vertical-Axis Rotations

A velocity field equivalent to right-lateral shear can be accommodated by left-lateral motion on perpendicularly-oriented planes, combined with clockwise rotation about vertical axes (e.g. Freund, 1970; Nur et al., 1986; McKenzie and Jackson, 1986). The right-lateral shear on the N–S striking faults of the Sistan Suture Zone could thus be transferred on to E–W striking left-lateral faults in the Makran accretionary prism (Figure 4.1b). Since the trends of folds in the prism are E–W, I would not necessarily expect to observe large geological offsets as a result of such faulting.

Tirrul et al. (1983) used offset units within the Neh complex (north of Figure 3.1) to suggest at least 60 km of cumulative motion on the Neh fault system, one of the systems of N–S striking, right-lateral faults within the SSZ, since the Pliocene (~ 5 Ma, see also Tirrul et al., 1980). Walker and Jackson (2004) found that the cumulative offset across the SSZ, combining offsets across the multiple active faults, is at least 70 km over the same time period. Walker and Jackson (2004) suggested that the cumulative offset may be as much as 105 km, if the right-lateral faults have been slipping at 15 mm/yr over the last 7 Ma, an upper bound on both the current slip rate (Vernant et al., 2004) and the duration of the current faulting configuration (Allen et al., 2004). These offset estimates give a long-term slip rate on the SSZ of 10–21 mm/yr. The present-day GPS slip rate is 5.6 ± 0.6 mm/yr across all of the faults in the SSZ (Walpersdorf et al., 2014, referred to collectively by those authors as the “East Lut” fault). Walker and Jackson (2004) discussed the problem of reconciling these rates, and the uncertainties in the long-term slip rates associated with the duration of the current configuration of faulting. The lower short term rate may indicate that the proposed long term slip rates are overestimates, or that the rate of motion has changed. To reflect this uncertainty, in the following calculations I have used total slip rates on the faults in the SSZ

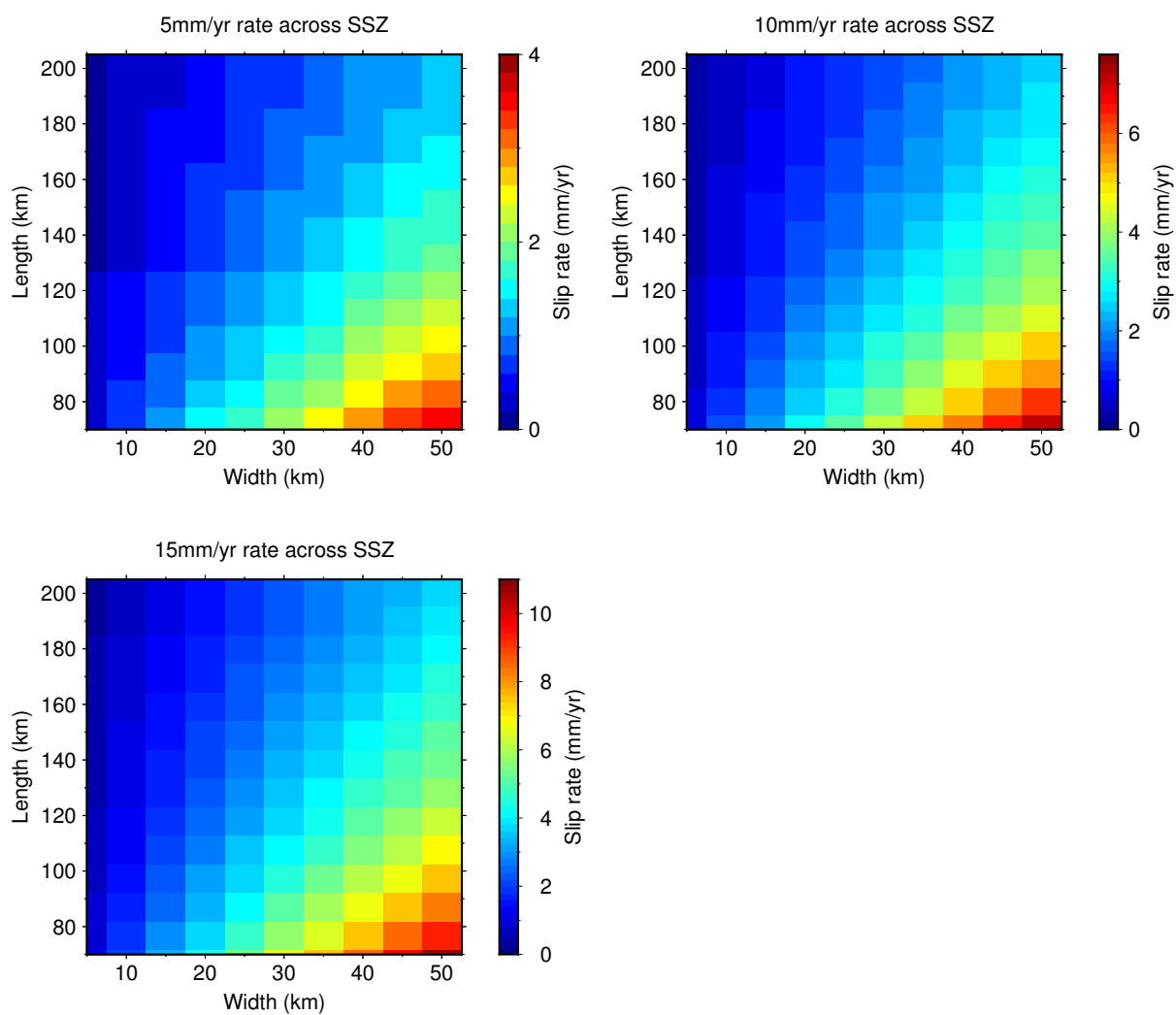


Figure 4.2: Slip rates required on E–W striking left-lateral faults bounding blocks of given length and width in order to accommodate a particular slip rate on the N–S striking right-lateral faults in the SSZ. The assumed slip rate on these right-lateral faults is given at the top of each plot. Note that the colour scale for the slip rate is different for each plot.

of 5–15 mm/yr and cumulative offsets of 70–105 km, in order to encompass the full range of possibilities.

Here I quantify the amount of rotation which would be required in the Makran to accommodate the offset on the strike-slip faults in the SSZ, and relate this to seismological and structural observations. Using the geometry shown in Figure C.1, I calculate the slip rate required on left-lateral faults bounding blocks of given length and width in order to accommodate a particular total slip rate on the N–S strike-slip faults in the SSZ. The results of this calculation are shown in Figure 4.2. I then use the calculated slip rates on these left-lateral faults to estimate the seismic moment accumulated per year. This requires me to assume a down-dip fault extent, which I take as 20 km (Figure 3.4). Although the fault length appears in the expression for seismic moment, Appendix C.1 shows that, since the fault length is much greater than the time-averaged annual slip, the seismic moment is independent of fault length to first order. I find that the accumulated moment, at the 10 mm/yr slip rate suggested by Walker and Jackson (2004), is 1.5×10^{18} Nm/yr. This moment is equivalent to a M_w 7 earthquake every 21 years or a M_w 8 every 670 years, and is independent of block width (Appendix C.1). Even for the lower, GPS-derived slip rate of ~ 5 mm/yr, the accumulated moment is 9×10^{17} Nm/yr, equivalent to a M_w 7 earthquake every 34 years. The M_w 5.8 and 5.9 earthquakes described by Byrne et al. (1992) are the largest examples of strike-slip faulting near the centre of the onshore prism, equivalent to less than a year's worth of moment accumulation for a cumulative slip rate on the faults in the SSZ of 10 mm/yr, or less than two years' worth for a rate of 5 mm/yr. However, a lack of observed left-lateral strike-slip earthquakes does not necessarily imply that such earthquakes do not occur, since the repeat time of such earthquakes may be longer than the time covered by my records.

Next, I consider the total angle through which blocks bounded by left-lateral faults would need to rotate in order to accommodate a cumulative, right-lateral offset of 70–105 km on the N–S strike-slip faults in the SSZ. The results are shown in Figure 4.3a. I use the same geometry (Figure C.1) as above but replace the slip rate on the strike-slip faults in the SSZ with the cumulative right-lateral offset across the zone. I find that the minimum angle through which the left-lateral faults would need to have rotated is $\sim 20^\circ$. Such rotation should be visible as a variation in the trends of structures across the central part of the onshore prism, and in paleomagnetic studies. Conrad et al. (1981) found that magnetization directions of recent volcanics (less than 10 Myr) are close to the present-day magnetic field, suggesting that no significant rotation has occurred in the last 10 Myr.

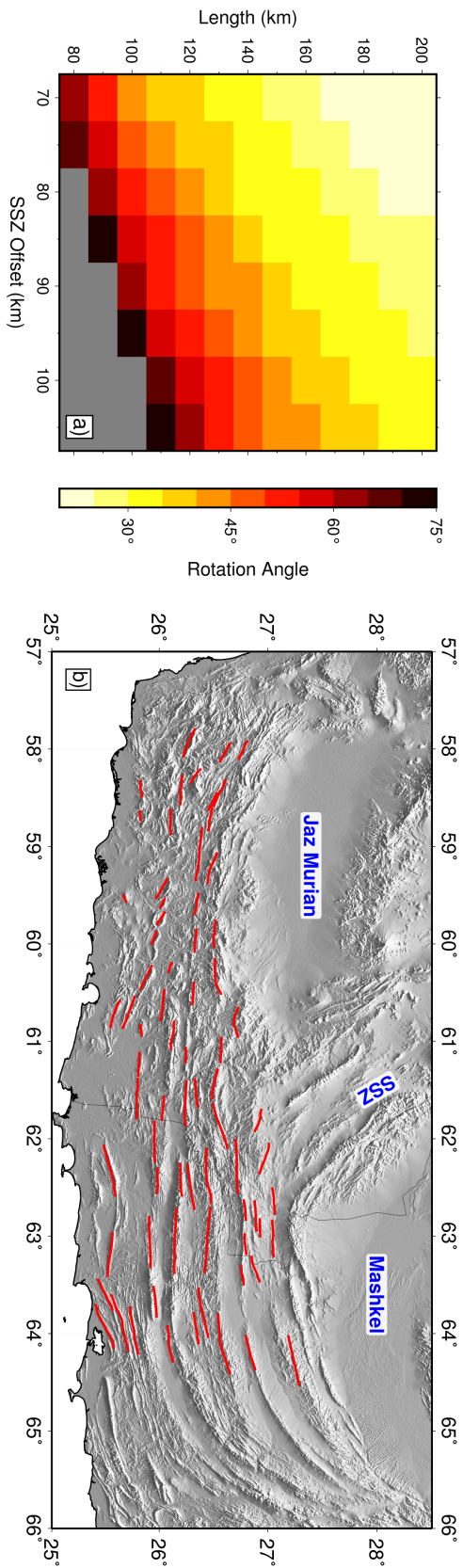


Figure 4.3: Required rotation of left-lateral faults and structural trends across the Makran. a) Plot of the cumulative angle through which blocks, of given length, bounded by left-lateral faults would need to have rotated clockwise in order to accommodate the total right-lateral offset across the SSZ. The minimum rotation required is $\sim 20^\circ$. Left-lateral faults shorter than the total offset across the SSZ cannot accommodate the offset by rotation; this part of the plot is shaded in grey. b) Map of the Makran accretionary prism with structural trends (from fold axes and bedding planes identified on satellite imagery) marked as red lines. There is no evidence of systematic vertical-axis rotations in the central section of the prism.

Figure 4.3b shows a map of structural trends in the Makran. There is a deviation of the structural trends in the west of the subduction zone, in the region where the vertical-axis rotations discussed in Chapter 2 occur (white-shaded area in Figure 3.1), but further east there is no systematic variation in structural trends across the central Makran region. This observation, combined with my calculations, suggests that right-lateral shear at the southern end of the SSZ is not accommodated by vertical-axis rotations within the Makran accretionary prism.

4.4 The Jaz Murian Depression as an Extensional Basin

The right-lateral shear across the Sistan Suture Zone could be transferred to the right-lateral shear zone at the western edge of the Makran accretionary prism, marked “WM” in Figure 4.1c. This geometry is similar to that of a releasing bend, requiring the Jaz Murian depression to be bounded by extensional faults.

I first consider how such a transfer of motion would work kinematically, by looking at the slip rates of the fault systems in the region. I then examine the geomorphology and geology of the basin to determine whether the Jaz Murian depression is bounded by active faults and, if so, what the sense of motion on these faults is. Finally, I use my results from Section 3.3 regarding the degree of coupling on the subduction interface in the western Makran in order to discuss whether the measured GPS velocities are consistent with this kinematic model.

4.4.1 Slip Rates

For the transfer of motion across the Jaz Murian to be kinematically plausible, the rate of right-lateral shear across the western Makran must be sufficient to accommodate the right-lateral motion on the Sabzevaran-Jiroft fault system to the north (S-J in Figure 4.1c), shortening across the south-eastern Zagros, and the right-lateral shear across the faults of the SSZ.

The present-day slip rate on the Sabzevaran-Jiroft fault system, at the western boundary of the Jaz Murian depression (Figure 4.1c), has been estimated from GPS measurements to be 7 ± 2 mm/yr (Peyret et al., 2009). Walpersdorf et al. (2014) found a rate of 2.4 ± 2.4 mm/yr across only the Sabzevaran fault, but their result is probably an underestimate as the GPS stations used to assess the rate lie within the region likely to be affected by elastic deformation due to fault locking. The Quaternary slip rate across these faults has been found to be 5.7 ± 1.7 mm/yr (Regard et al., 2005), which is consistent with the GPS estimates. To the

north the Sabzevaran-Jiroft faults connect with the Gowk-Nayband fault system (G-N in Figure 4.1c). The southernmost fault in this system is the Gowk fault, which has comparable GPS and Holocene slip rates of 4.2 ± 0.7 mm/yr (Walpersdorf et al., 2014) and 3.8 ± 0.7 mm/yr (Walker et al., 2010). These rates are within error of those for the Sabzevaran-Jiroft system, but are slightly lower, allowing for the possibility of slow extension across the northern margin of the Jaz Murian depression. The rate of shortening across the south-eastern Zagros is 8 ± 2 mm/yr (Walpersdorf et al., 2006). The best estimate of the present-day rate of shear across the faults in the SSZ is 5.6 ± 0.6 mm/yr (Walpersdorf et al., 2014).

GPS velocities at the western edge of the Makran show ~ 17 mm/yr right-lateral shear between 56.7°E and 58.4°E (white-shaded area in Figure 3.1; Peyret et al. (2009)). This is accommodated by both the N–S striking faults of the Minab-Zendan-Palami fault zone (e.g. Bayer et al., 2006, MZP in Figure 3.1) and left-lateral E–W striking faults to the east (Chapter 2), which rotate clockwise about vertical axes. The total motion from shortening in the Zagros, right-lateral faults to the north in the Sabzevaran-Jiroft fault system, and the faults of the SSZ is ~ 18 mm/yr, so the rate of right-lateral shear in the western Makran is sufficient to take up that motion. The agreement between these rates suggests that it is probable that the right-lateral shear across the SSZ is transferred to the western Makran by normal faulting at the boundaries of the Jaz Murian depression.

4.4.2 Geomorphology

I use a combination of SPOT (from Google Earth), Landsat and ASTER imagery, and SRTM topography, to look at the geomorphology of the Jaz Murian depression. The strike-slip faults at the western edge of the depression have very clear surface expressions (e.g. Morgan et al., 1979; Regard et al., 2005; Meyer and Le Dortz, 2007). I concentrate on the northern and southern boundaries of the basin. A first-order feature of the depression morphology is its sharply defined edges, with large topographic contrasts which have long, linear sections (Figure 4.4a). These are particularly clear on the southern edge of the basin (Figure 4.4a, b, d) and are indicative of dip-slip faulting. The faceted topography of the basin edges is also a common feature of fault-controlled range fronts. Some of the alluvial fans at the edges of the depression show breaks in slope which I interpret as scarps (e.g. Figure 4.4c). It is common to see migration of fault activity away from the range front (e.g. Avouac et al., 1993; Bayasgalan et al., 1999b) and these scarps may be evidence of such migration, or of secondary faults adjacent to the main structure (e.g. Goldsworthy and Jackson, 2001). There is, therefore, convincing evidence for the Jaz Murian depression being bounded by active dip-slip faults.

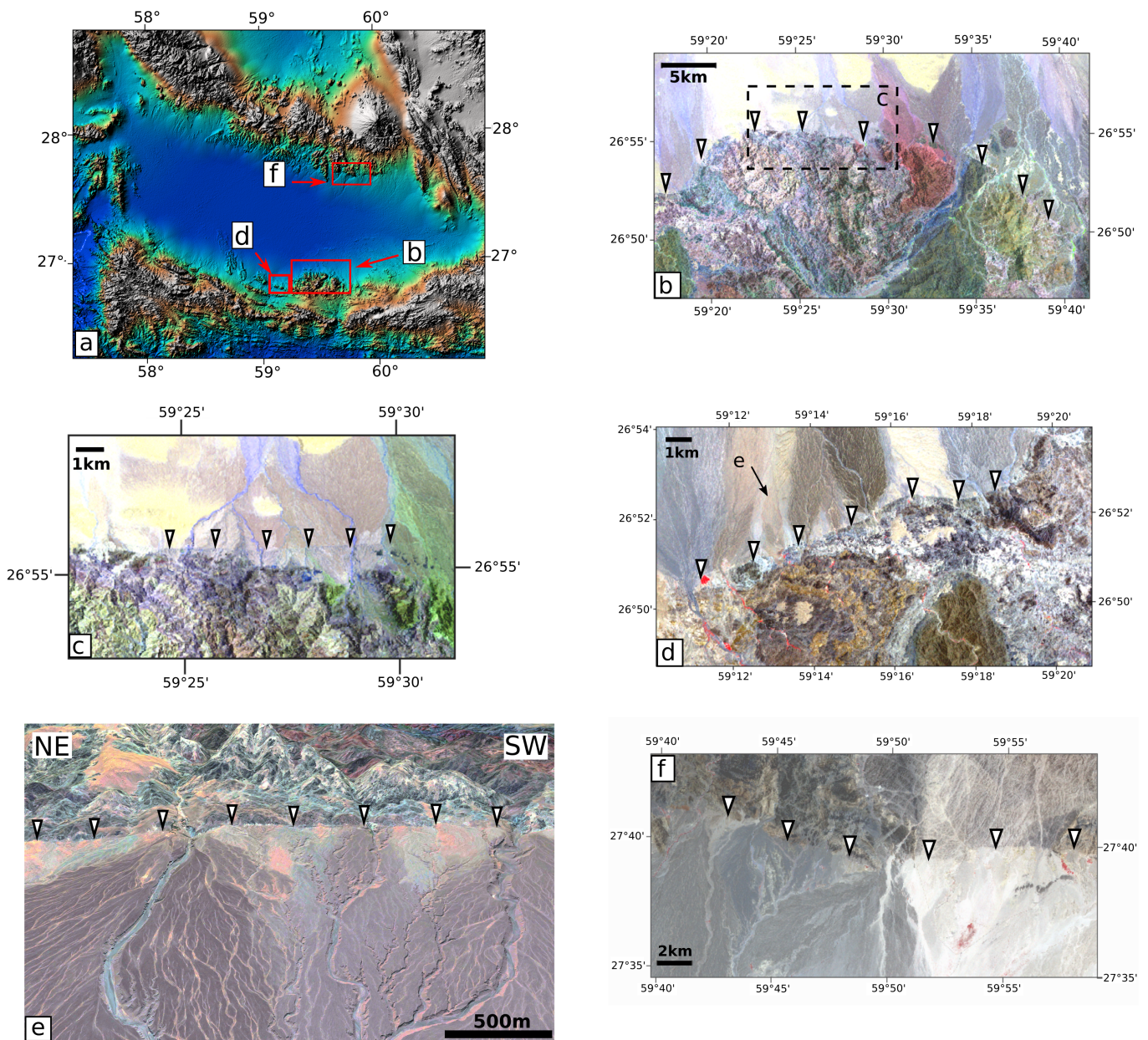


Figure 4.4: Geomorphology of the Jaz Murian depression. a) SRTM topography of the Jaz Murian depression, shaded by elevation, showing locations of b, d and f. b) Landsat TM image (bands 5, 4, 1 shown as R, G, B) of part of the southern edge of the Jaz Murian depression, location shown in a. White arrows highlight the topographic discontinuity associated with the edges of the basin. c) Landsat image (bands 7, 5, 1 as R, G, B), location shown in b. A discontinuity in fan surfaces is picked out by the white arrows. d) ASTER image (bands 3, 2, 1 as R, G, B), showing straight topographic discontinuity. e) shows the same discontinuity in Digital Globe imagery (©Google, ©DigitalGlobe, <http://www.google.com/earth/>) looking SE, along arrow marked in d). f) ASTER image (spectral bands 3, 2, 1) of straight topographic discontinuity along the northern edge of the Jaz Murian. Note that the edge cuts the lithological contrast seen in the change from white to grey rocks.

I now consider the sense of motion on these bounding faults. Thrust faults are very common in Iran and often have a clear geomorphological expression, even where they do not reach the surface or their scarps are not preserved (e.g. Berberian, 1981). In particular, anticlines in alluvium are often diagnostic of thrust-faulting, and were seen to move in the Tabas and Sefidabeh earthquakes (e.g. Berberian et al., 2000; Walker et al., 2003). I do not see any evidence of such folding around the edges of the Jaz Murian depression. I see nothing in the geomorphology that is diagnostic of a particular sense of slip, although the lack of folding may be suggestive of normal faulting. Dolati (2010) and Haghypour et al. (2012) suggested that a series of normal faults run along the south-eastern edge of the depression, based on structural mapping of serpentinites. The locations of these faults are consistent with my geomorphological observations of dip-slip faulting on the southern boundary of the Jaz Murian depression, and the faults are 10–20 km long so, if active, would break the entire seismogenic layer and be important for the regional tectonics. However, Dolati (2010) was not able to establish the timing of activity on these faults and it is therefore not clear whether the active deformation is also normal faulting.

4.4.3 Temporal Strain Variations

No shallow earthquakes with $m_b > 4.0$ have been reported on the northern or southern margins of the Jaz Murian depression between 1945 and 2013 (Figure 3.2b), suggesting that if shallow extensional earthquakes occur they are likely to have a repeat time longer than my records. GPS velocities over the last 15 years show compression across the Jaz Murian depression (Peyret et al., 2009; Walpersdorf et al., 2014). However, this compression may be due to elastic strain accumulation above a locked megathrust. Whether this is the case depends on the degree of coupling on the subduction interface in the western Makran, which was discussed in Section 3.3. Recent studies in other subduction zones have reported time-varying strain in the overriding plate, linked to the megathrust earthquake cycle (e.g. Loveless et al., 2010; Arriagada et al., 2011; Baker et al., 2013; Aron et al., 2013; Scott et al., 2016). In the megathrust's interseismic period the overriding plate is in a compressional stress regime so normal-faulting earthquakes are suppressed and GPS signals indicate shortening. Immediately after a megathrust earthquake (perhaps even during the coseismic period; Hicks and Rietbrock, 2015) compressive stresses in the overriding plate are reduced and normal-faulting earthquakes can occur. This temporal variation in the style of earthquakes has been observed extensively in Chile (e.g. Farías et al., 2011) and in Japan (e.g. Asano et al., 2011; McKenzie and Jackson, 2012). Although the permanent extension associated with individual episodes of normal-faulting is small (Baker et al., 2013), over many earthquake cycles significant deformation could be accumulated. Such time-dependent deformation of the overriding plate requires the megathrust to be locked, accumulating elastic strain, and to move in earthquakes, rather than sliding continuously.

In Chapter 3 I showed that GPS data in the western Makran are consistent with the megathrust being locked. The absence of normal-faulting earthquakes on the bounding faults of the Jaz Murian depression, and the present-day compression seen in the GPS velocities, may, therefore, be due to compressive stresses and elastic strain accumulation in the overriding plate above a locked megathrust interface. This conclusion would be confirmed by the observation of normal-faulting earthquakes after an earthquake on the western Makran megathrust.

4.5 Conclusion

GPS, geomorphology and structural analysis demonstrate that the N–S right-lateral shear across the Sistan Suture Zone is not accommodated either by thrusts or by rotating left-lateral faults at the zone's southern end. Geomorphological analysis suggests that the Jaz Murian depression is bounded by \sim E–W striking dip-slip faults, which are probably extensional. This normal-fault bounded basin may allow the right-lateral motion of the SSZ to be transferred onto the faults of the Minab-Zendan-Palami fault zone and adjacent strike-slip faults. Unlike vertical-axis rotations or thrusting at the back of the accretionary prism, such a transfer of motion provides a geologically plausible mechanism to transmit the right-lateral motion on the faults within the Sistan Suture Zone to the subduction zone, which is consistent with the present-day motions. This mechanism is viable because compression in the GPS velocities across the boundaries of the Jaz Murian depression may be due to locking on the subduction interface. This suggests that normal-faulting earthquakes might be expected to occur on the faults bounding the Jaz Murian depression after an earthquake on the western Makran megathrust.

Chapter 5

Kinematics and dynamics of accretionary prism deformation[†]

Overview

In Chapters 3 and 4 I showed that strain in the Makran accretionary prism is likely to be time-dependent, on the time-scale of the megathrust earthquake cycle. In this chapter I consider how the relative importance of compressional and gravitational forces changes during accretionary prism growth. By considering the kinematics of the 2013 Balochistan and Minab earthquakes, I infer that the local gravitational and far-field compressive forces in the Makran accretionary prism are in balance. This force balance allows me to calculate the mean shear stress and effective coefficient of friction on the Makran megathrust, which I find to be 5–35 MPa and 0.01–0.03 respectively. These values are similar to those found in other subduction zones, showing that the abnormally high sediment thickness in the offshore Makran does not significantly reduce the shear stress on the megathrust.

5.1 Introduction

The Makran hosts the world's largest sub-aerial accretionary prism (Fruehn et al., 1997, Figure 3.1). The sediments in this prism are thought to derive from the Proto-Indus fan (Harms et al., 1982) and have been thickened as the Arabian plate has subducted northwards. The extensive ($\sim 200 \times 1000$ km) onshore part of the prism provides an ideal setting in

[†]This chapter is adapted from part of Penney, C., Tavakoli, F., Saadat, A., Nankali, H. R., Sedighi, M., Khorrani, F., Sobouti, F., Rafi, Z., Copley, A., Jackson, J., and Priestley, K. (2017). Megathrust and accretionary wedge properties and behaviour in the Makran subduction zone. *Geophys. J. Int.*, 209:1800–1830. doi:10.1093/gji/ggx126

which to study prism deformation. The offshore part of the accretionary prism, near the Musandam peninsula and the Omani coast, was imaged using seismic reflection and refraction experiments in the 1970s and early 1980s (e.g. White and Klitgord, 1976; White and Loudon, 1982) and the eastern offshore section has been the subject of recent research (e.g. Kukowski et al., 2000; Smith et al., 2012). Offshore seismic data, and onshore geological studies give a time-integrated picture of the deformation but do not constrain the evolution of the prism through time. Prism evolution is controlled by both the forces acting on the prism, which may be time-dependent, and the prism's response to these forces, which is controlled by the behaviour of faults and folds within the prism and the rheology of the underlying megathrust.

The forces controlling the dynamics of accretionary prisms are basal shear stress, compressive stress on the back of the prism, and gravity (Dahlen et al., 1984). In the initial phase of prism growth, basal and compressive stresses dominate and the prism thickens, supported by shear stress on the megathrust at its base. Thrusts form perpendicular to the maximum compression direction (e.g. Davis et al., 1983), which in the Makran is approximately N–S, forming E–W trending folds and thrust faults (e.g. Harms et al., 1982). Once the gravitational potential energy due to the growth of topography reaches the maximum shear stress that can be supported on the megathrust, the topographic elevation can no longer increase and the range instead grows laterally by outwards migration of the thrust front (e.g. Molnar and Lyon-Caen, 1988). The gravitational forces then balance the compressive stresses and the topography develops a wide, flat top, such as is seen in the Tibetan Plateau (e.g. Houseman and England, 1986). Thrust structures which have been active during shortening and topographic growth may then become inactive, or be reactivated as strike-slip or normal faults.

In map view the shallow earthquakes in the Makran show clear spatial variations in the style of strain (Figure 5.1a). Shallow thrust earthquakes (blue in Figure 5.1a) occur offshore or near the coast, and most onshore earthquakes are strike-slip (red in Figure 5.1a). Three strike-slip earthquakes, and an isolated thrust event, are the only examples of shallow (<15 km) seismic deformation in the central part of the onshore accretionary prism. The majority of the strike-slip earthquakes are concentrated at the lateral edges of the prism. This distribution of strain, and specifically the recent strike-slip earthquakes in the onshore Makran (e.g. Avouac et al., 2014, Chapter 2), imply that the top of the Makran accretionary prism is no longer thickening. Additionally, the topography of the prism shows a flat top (see Figure 3.4), indicating that a balance may have been reached between gravitational potential energy contrasts and the shear stresses on the megathrust. In this case, I can estimate the mean shear stress on the megathrust using the method of Lamb (2006). I first discuss the deformation of the onshore part of the wedge and then the material properties of the megathrust.

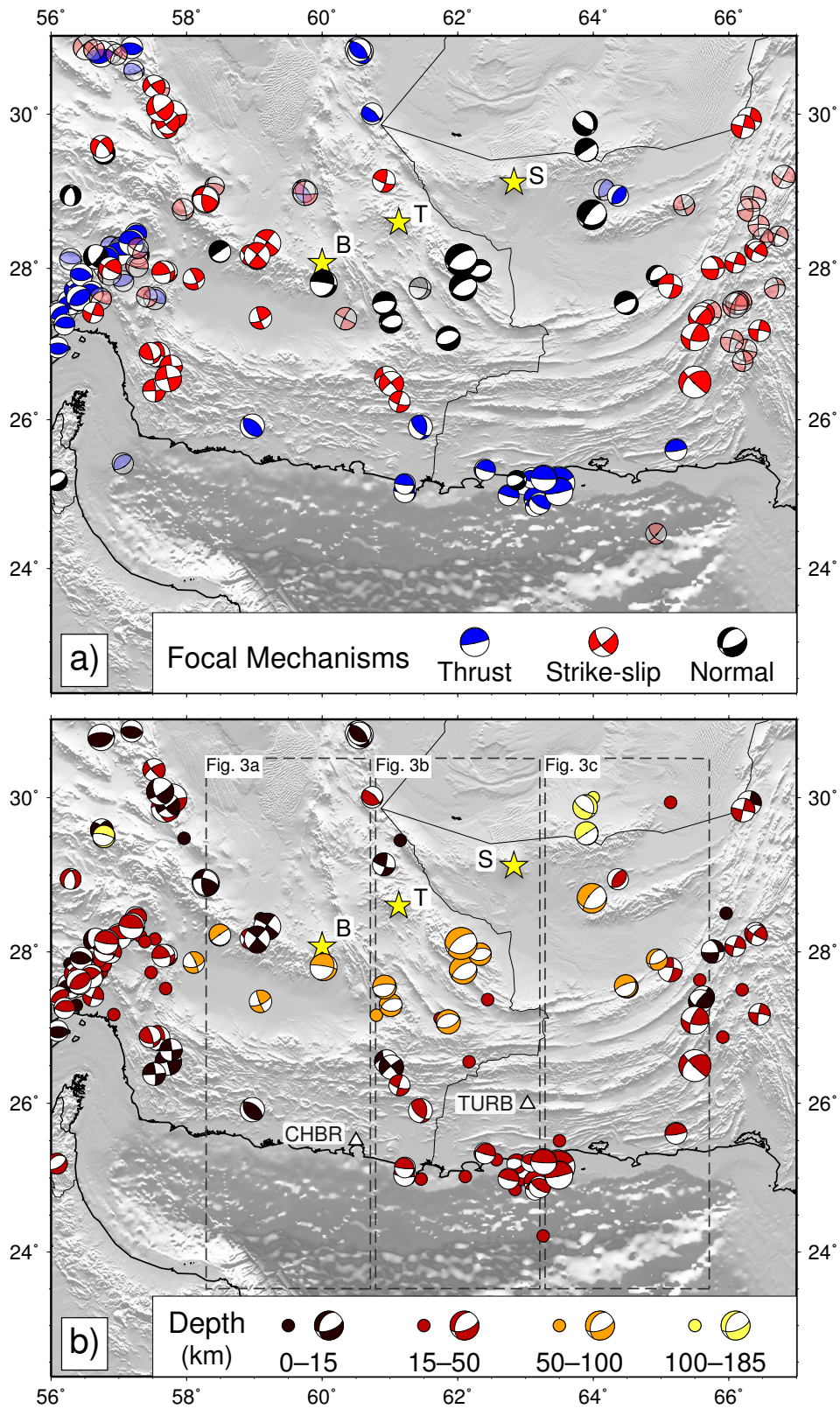


Figure 5.1: Earthquakes in the Makran. This figure is identical to Figure 3.2 but is reproduced here for the reader's convenience.

5.2 Strike-Slip Faulting on the Wedge Top

The September 2013 M_w 7.7 Balochistan earthquake occurred on the Hoshab fault (Figure 3.1; Figure 5.2) at the eastern end of the Makran accretionary prism. The Hoshab fault is curved, possibly as a result of the interaction between compression in the Makran and shear along the Chaman fault (Harms et al., 1982), and the sense of motion was left-lateral strike-slip along the entire 200 km rupture length (e.g. Avouac et al., 2014). This earthquake has been extensively studied (e.g. Avouac et al., 2014; Jolivet et al., 2014; Barnhart et al., 2014a), both because of its clear surface ruptures (e.g. Vallage et al., 2015) and its unusual geometry (e.g. Zhou et al., 2015). I do not address the complexities of the rupture dynamics here, but consider the earthquake’s role in the regional deformation and its implications for the dynamics of the accretionary prism. Avouac et al. (2014) proposed that the southern part of the Makran accretionary prism is being extruded to the east, such that strike-slip motion on the Hoshab fault is kinematically favourable. However, GPS velocities south of the Hoshab fault do not show eastwards extrusion of the prism (Figure 5.2b). The velocity field shows N–S compression of ~ 10 mm/yr across the region of the fault (Figure 5.2; Frohling and Szeliga, 2016). Barnhart et al. (2014b) proposed “ball-and-socket” rotations, whereby the regions north and south of the Hoshab fault rotate relative to each other about a pole in central Afghanistan. However, Barnhart et al. (2015) pointed out that such rotations cannot accommodate the shortening observed in the GPS, and appeal to alternating earthquake styles on the Hoshab fault, with a mixture of thrust and strike-slip events. From detailed comparison of the offsets resulting from the 2013 earthquake with other Quaternary offsets visible along the Hoshab fault, Zhou et al. (2015) found the Balochistan earthquake to be typical of Quaternary events on the Hoshab fault, making alternating earthquake styles unlikely.

NE–SW left-lateral faulting, such as that observed in the Balochistan earthquake, can accommodate N–S compression if the fault-bounded blocks rotate about vertical axes (Figure 5.2a; McKenzie and Jackson, 1983; Campbell et al., 2013). Unlike the vertical-axis rotations described in Section 4.3, which accommodate simple shear of horizontal planes, the configuration shown in Figure 5.2a accommodates pure shear. I use the geometry shown in Figure 5.3 to calculate the required rotation rate on the Hoshab fault (the detailed calculations are given in Appendix C.2). Since the 2013 Balochistan earthquake on this fault had a thrust component (Zhou et al., 2015), I use a reduced value of S , the shortening, such that the total shortening accommodated by thrust faulting and the mechanism shown in this diagram is equal to the GPS shortening rate across the fault (~ 10 mm/yr). I find that a rotation rate of $2.4^\circ/\text{Myr}$ would allow the Hoshab fault, and other nearby structures, to accommodate the regional shortening by strike-slip faulting, without requiring that the sense of slip changes between earthquakes. The E–W extension resulting from these rotations is very small, which is in

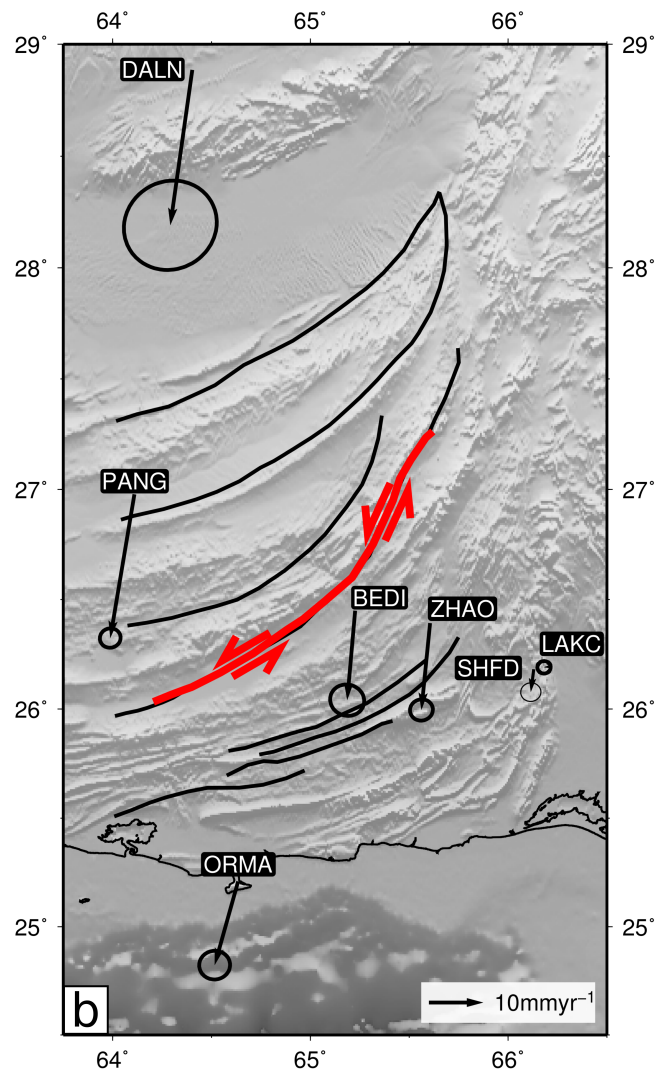
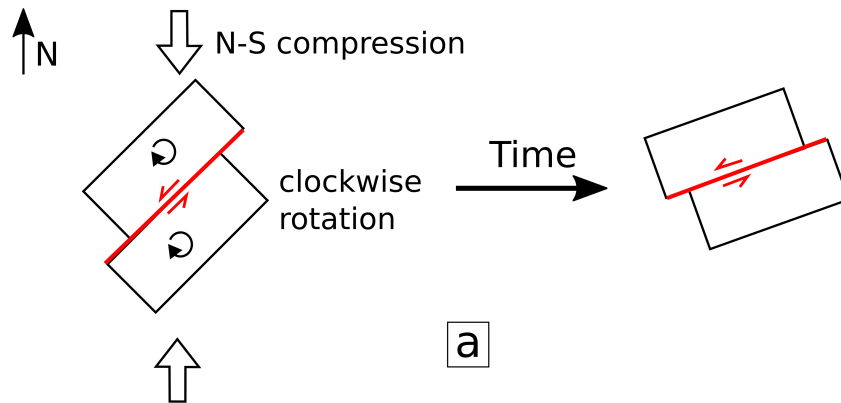


Figure 5.2: Kinematics of the Hoshab fault. a) The Hoshab fault accommodates N-S compression (white arrows) by clockwise rotation and left-lateral faulting. b) Fault map of the eastern Makran, after Lawrence et al. (1981). The trace of surface ruptures on the Hoshab fault from Avouac et al. (2014) is shown in red. Black arrows show GPS velocities relative to stable Arabia with 95% confidence ellipses (Frohling and Szeliga, 2016). The velocity difference between PANG, to the north, and BED1 and ZHAO, to the south, shows only shortening, with no eastwards extrusion of the southern part of the prism.

better agreement with the almost purely N–S velocity field (Figure 5.2b) than the extrusion model of Avouac et al. (2014). My kinematic model is, therefore, consistent with both the GPS and the geometry of the Balochistan earthquake, in contrast to models proposed by earlier authors (Avouac et al., 2014; Barnhart et al., 2014b, 2015). There is, however, an outstanding question as to why shortening is not accommodated by thrusting, since the southern end of the Hoshab fault is optimally oriented to accommodate N–S compression by thrusting and topographic growth, as it strikes E–W and dips 50–70° N (Avouac et al., 2014). The alternative kinematic style I observe, in which N–S compression is accommodated by strike-slip faulting and rotation, suggests that the Hoshab fault, and similar sub-parallel structures, acted as thrusts in the early period of prism growth, when compressive stresses dominated, and have been reactivated as strike-slip faults, now that the gravitational potential energy of the wedge has reached the maximum that can be supported by shear stresses on the megathrust.

As discussed in Chapter 2 the M_w 6.1 2013 Minab earthquake, occurred on a fault aligned approximately perpendicular to the regional compression direction. This fault, and the adjacent faults, which accommodate N–S right-lateral simple shear in the velocity field by rotating clockwise about vertical axes, are thought to be reactivated thrust faults which have been steepened during prism growth. The adjacent faults of the MZP accommodate part of the shear by simple right-lateral motion on N–S planes. It is likely that this contrast in kinematic styles is due to reactivation of pre-existing E–W trending structures in the region of the Minab earthquake. This suggests that there has been a change in strain regime through time in the western Makran, as well as in the eastern Makran. Such a change in strain regime in the Makran was proposed by Platt et al. (1988). Those authors observed steeply dipping faults at low angle to bedding planes in the eastern Makran, which they infer to mean that these faults formed at low angle and have been progressively steepened within the accretionary prism. Some of these faults show a bimodal distribution of slip vectors, consistent with a change from predominantly thrust faulting to a strike-slip dominated regime.

Fault reactivation in a new strain regime, seen in both the Minab and Balochistan earthquakes, supports my conclusion that the gravitational potential energy of the wedge and the shear stresses on the megathrust are now in balance in the Makran prism, such that the wedge has reached a limiting upper elevation, and now grows by outwards migration of the thrust front.

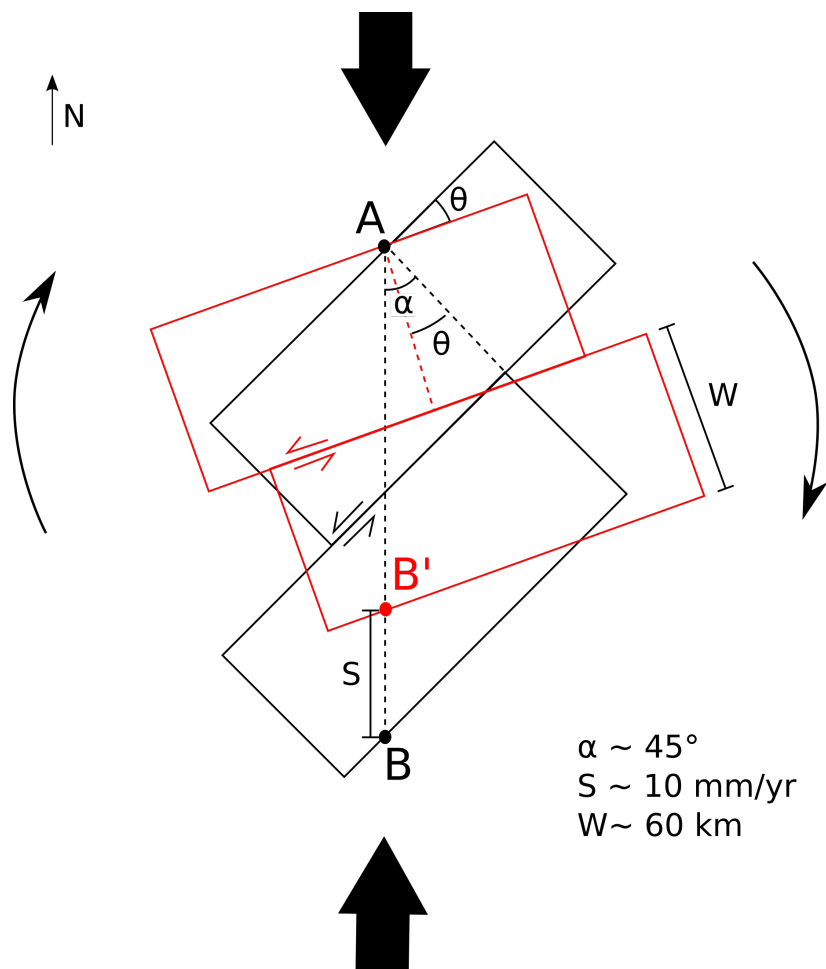


Figure 5.3: Accommodation of N–S shortening (pure shear) by vertical-axis rotations. Black blocks shows initial configuration, red blocks shows configuration after rotation through an angle θ and slip such that B moves directly towards A. S is the shortening rate across the blocks. For the Hoshab fault, where the 2013 Balochistan earthquake occurred: $W \approx 60 \text{ km}$, $\alpha \approx 45^\circ$, $S \approx 7 \text{ mm/yr}$. This gives a rotation rate of $2.4^\circ/\text{Myr}$ and a slip rate on the Hoshab fault of $\sim 10 \text{ mm/yr}$, if the motion is all on the Hoshab fault. If the motion is distributed across multiple faults each will have a lower slip rate. Further details of this calculation are given in Appendix C.2.

5.3 Megathrust Shear Stress

The balance between gravitational potential energy contrasts and megathrust shear stresses in the Makran allows me to use the method of Lamb (2006) to calculate the mean shear stress required on the Makran megathrust to support the elevation contrast I observe between the bathymetric trench and the top of the prism. These calculations assume that the mean horizontal and vertical normal stresses within the prism are equal; equivalent to the balance between gravitational and far-field compressive forces discussed above. The geometry for my calculations is shown in Figure 5.4a. I will refer to the overriding plate material in this model as the subduction wedge, after Lamb (2006). The total force on the wedge, per unit length along strike, depends on the density structure of this subduction wedge and its thickness. The balance between gravitational and far-field compressive forces means that the compressive force on the prism, P , is equal to the lithostatic pressure at the back of the wedge:

$$\begin{aligned} P &= g \int_0^L \int_0^z \rho(z') dz' dz \\ &= \frac{g}{2} \left((\rho_c - \rho_m)(h + d)^2 + \rho_m L^2 \right) \text{ using the notation defined in Figure 5.4a.} \end{aligned}$$

The mass of the subduction wedge, M , including water, is:

$$M = \frac{1}{2 \tan \theta} \left(\rho_w h \alpha + \rho_c (h \alpha - d^2 + 2d\alpha) + \rho_m (\alpha - d)^2 \right), \quad \text{where } \alpha = L - h.$$

The shear and normal stress, τ and σ respectively, on the megathrust are:

$$\tau = \frac{\sin \theta}{\alpha} (P \cos \theta - Mg \sin \theta), \quad (5.1)$$

$$\sigma = \frac{\sin \theta}{\alpha} (P \sin \theta + Mg \cos \theta). \quad (5.2)$$

(5.1) and (5.2) give a coefficient of friction, μ

$$\mu = \frac{\tau}{\sigma} = \frac{P - Mg \tan \theta}{P \tan \theta + Mg}. \quad (5.3)$$

I assume a constant crustal density, ρ_c , of 2860 kg/m³ to a depth of 40 km (d in Figure 5.4a), which Maggi et al. (2000b) and Manaman et al. (2011) suggest as the Moho depth in the Makran. For greater depths I use a constant mantle density, ρ_m , of 3300 kg/m³. Lamb (2006) suggests that the volcanic arc should be considered as the back of the subduction wedge, so I consider total wedge thicknesses, L , between 40 and 80 km, consistent with the range of subduction interface depths inferred in Section 3.2.3. The mean elevation contrast between the bathymetric slope break, which I use as a proxy for the surface projection of the

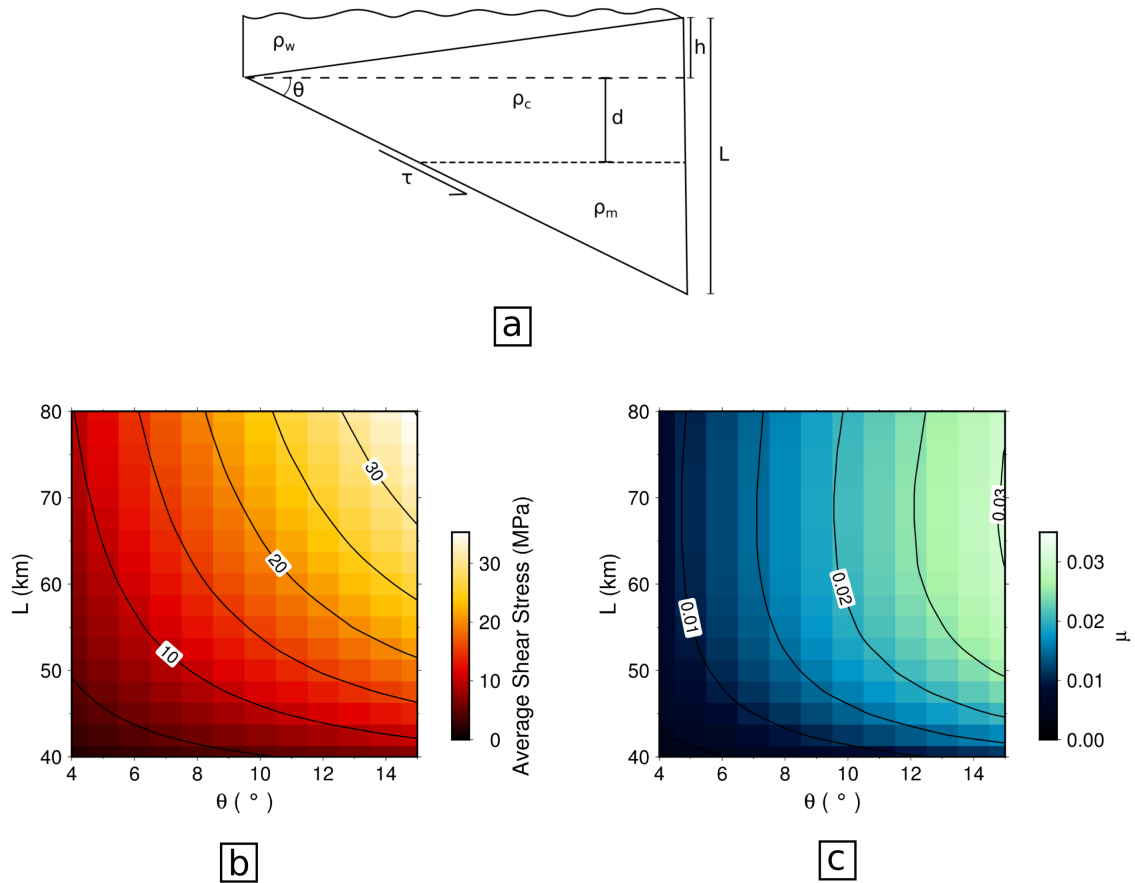


Figure 5.4: Megathrust rheology. a) Geometry for calculating mean shear stress and coefficient of friction on the megathrust (after Lamb, 2006). θ is the mean dip angle of the subduction interface. ρ_w , ρ_c and ρ_m are the water, crust and mantle densities respectively. d is the Moho depth. L is the depth of the back of the subduction wedge and h is the elevation contrast between the trench and the volcanic arc ($h \ll L$). τ is the mean shear stress on the megathrust. b) Plot of the average shear stress required to support the topographic contrast above the subduction interface for different average dips, θ , and thicknesses of the subduction wedge, L . Contours are spaced at 5MPa. c) Plot of the effective coefficient of friction (mean shear stress divided by effective normal stress) required for different average dips, θ , and thicknesses of the subduction wedge, L . Contours are spaced at 0.005.

megathrust, and the back of the subduction wedge is ~ 5 km, which I take as h in Figure 5.4a. I assume that the topographic contrast is covered by water with a density of 1000 kg/m^3 (Figure 5.4a).

As discussed in Chapter 3, Sections 3.2.3 and 3.3, the mean dip of the Arabian slab is poorly constrained. Since the volcanic arc lies slightly north of the increase in dip of the subduction interface that I infer from my earthquake profiles (Figures 5.1b and 3.4) I allow for steeper average dips than in my locking calculations (Chapter 3), and use a range of dips from 4 to 15° .

Figure 5.4b and 5.4c show the results of calculating the shear stress and coefficient of friction, using equations (5.1) and (5.3), as a function of subduction wedge thickness, L , and mean dip angle, θ , calculated using the expressions of Lamb (2006). I estimate the mean shear stress on the interface to be between ~ 5 and 35 MPa, and the effective coefficient of friction to be ~ 0.01 – 0.03 . These values of shear stress are consistent with those reported in other subduction zones (e.g. Lamb, 2006; Von Herzen et al., 2001; Duarte et al., 2015). This suggests that neither the large sediment thickness of the Makran, which has been proposed to lubricate the plate interface through sediment underplating (e.g. Bayer et al., 2006), nor the low dip of the subduction interface, affect the mean shear stress on the megathrust.

Conclusions

There is strong evidence, from the Balochistan and Minab earthquakes, for a change from thrust to strike-slip faulting in the Makran accretionary prism at some point in the prism's history, suggesting that the gravitational potential energy of the prism has reached the maximum that can be supported by the shear stress on the megathrust. The mean shear stress (5 – 35 MPa) and effective coefficient of friction (0.01 – 0.03) are of similar magnitudes to those in other subduction zones, despite the large sediment thicknesses on the subducting plate and the low dip angle of the subduction interface.

Part II

South East Tibet

Chapter 6

The role of lateral rheology contrasts in the evolution of mountain ranges

Overview

Controversy surrounds the rheology of the continental lithosphere and how this controls the evolution and behaviour of mountain ranges. In this chapter I address this question using numerical modelling and recently published results from stable-isotope palaeoaltimetry. Stable-isotope palaeoaltimetry provides the constraints on vertical motions required to distinguish between competing models for lithosphere rheology in South East Tibet. Such results suggest that parts of South East Tibet have been at or near their present-day elevations since the late Eocene, meaning that uplift rates are likely to be much lower (<0.2 mm/yr) than has previously been suggested based on river incision. I use numerical modelling of the temporal evolution of a gravity-driven fluid to investigate the effect of lateral rheology contrasts on the shape and evolution of mountain ranges. I find that lateral rheology contrasts, analogous to the contrast between the relatively undeforming Sichuan Basin and Central Lowlands of Myanmar and the rapidly deforming south-eastern margin of Tibet, result in deformation that mirrors the main features of the present-day topography, GPS velocity field and earthquake-derived strain rate in South East Tibet, without the need for the low-viscosity, lower-crustal channel which has previously been proposed. The first-order similarity between this simple model and key features of the deformation and topography of South East Tibet suggests that lateral rheology contrasts play a first-order role in determining the shape and temporal evolution of topography. Such contrasts are likely to be important in the development of other mountain ranges, such as the Andes and the Zagros, and this modelling provides an explanation for the correlation between cratonic regions and the steep range fronts of mountain ranges. In addition, my modelling suggests that sediments deposited at or near the surface

may be transported hundreds of kilometres, an effect which is important in interpreting palaeoaltimetric results.

6.1 Introduction

What controls the shape and evolution of mountain ranges? This question is fundamental to many branches of geoscience and has exercised authors for centuries (e.g. Dufrénoy and de Beaumont, 1833; Lyell, 1853). The forces driving the development of topography, and the rheology determining how these forces relate to deformation, are still the subject of significant debate (e.g. Tapponnier et al., 2001; Clark et al., 2005a; Hubbard et al., 2010; Copley et al., 2011b; Flesch et al., 2018). Contrasts in rheology between relatively undeforming regions and weaker adjacent material have long been recognised to play an important role in controlling the distribution of strain in the continents (e.g. Molnar and Tapponnier, 1975; Tapponnier and Molnar, 1976; Molnar and Tapponnier, 1981; Vilotte et al., 1984; England and Houseman, 1985; Jackson et al., 2008). In this chapter I combine numerical modelling with recently published palaeoaltimetric information to investigate the role of lateral rheology contrasts in determining the form and temporal evolution of topography in growing mountain ranges.

South East Tibet is an ideal area in which to address the question of how lateral rheology contrasts affect the growth of mountain ranges. The low elevations and strain rates (both seismic and geodetic) in the Sichuan Basin and Central Lowlands of Myanmar suggest that these regions are relatively undeforming, so likely to be strong in comparison to the high region between them, which has numerous earthquakes, and the deformation belts which surround them (Figure 6.1b; England and Houseman, 1985; Copley and McKenzie, 2007, Section 6.2). Rheological contrasts across the Longmen Shan (Figure 6.1a) have also been inferred from observations of differential postseismic motion following the 2008 Wenchuan earthquake (Huang et al., 2014). The development of topography in South East Tibet, particularly across the Longmen Shan, and the associated lithosphere rheology, is controversial (e.g. Clark and Royden, 2000; Clark et al., 2005b; Copley, 2008; Burchfiel et al., 2008; Hubbard and Shaw, 2009; Hubbard et al., 2010; Wang et al., 2012; Fielding and McKenzie, 2012; Shi et al., 2018, discussed in section 6.2). Recent attempts to address this question have been based on instantaneous models which reproduce the present-day horizontal GPS velocity field (Copley and McKenzie, 2007; Copley, 2008). However, vertical variations in rheology cannot be resolved using only horizontal motions; knowledge of vertical motions is also required (Copley, 2008; Flesch et al., 2018). Previous studies of vertical motions in South East Tibet have been based on thermochronology and river incision (e.g. Kirby et al., 2002; Clark et al., 2004; Wang et al., 2012, 2016b). Thermochronometric ages give information about exhumation,

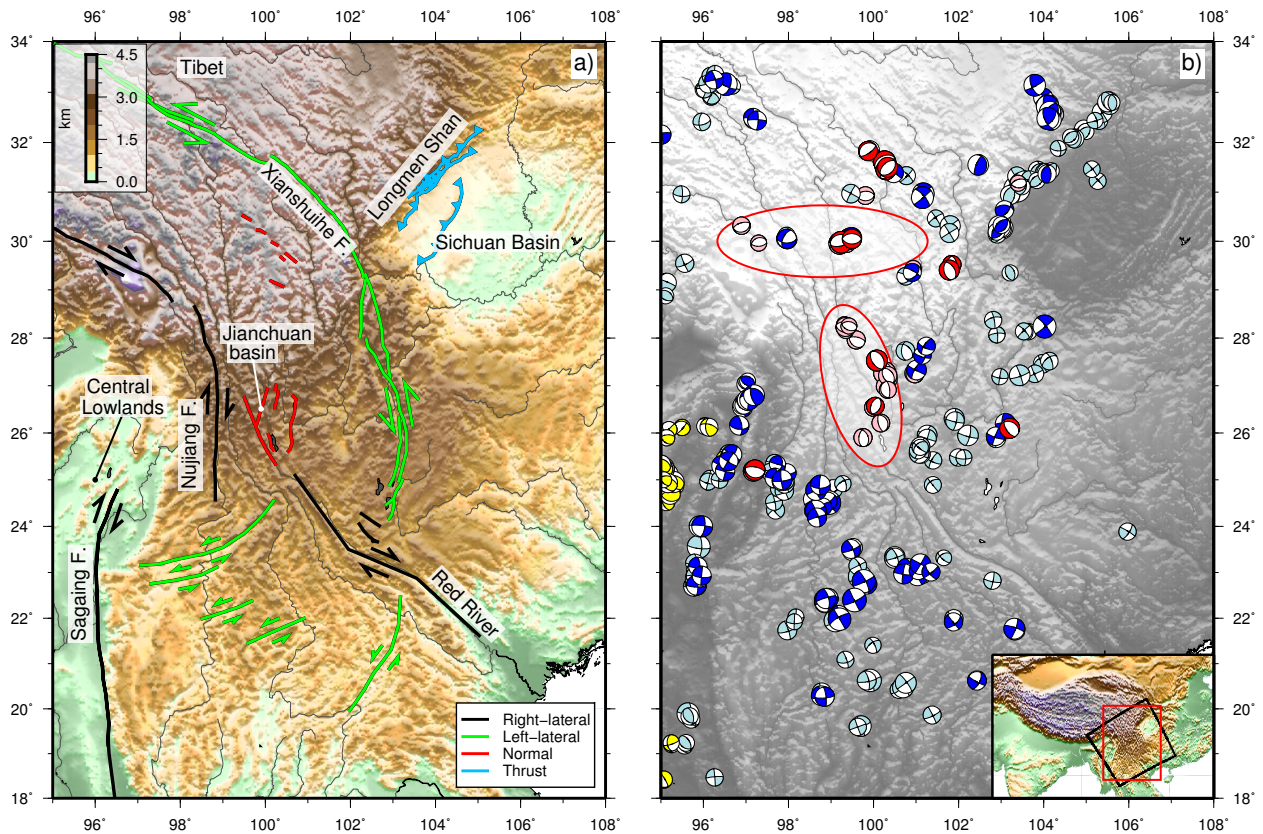


Figure 6.1: a) Major active faults in South East Tibet, from Copley (2008); Hubbard and Shaw (2009); Wang et al. (2016b). Black and green lines are right- and left-lateral strike-slip faults respectively. Note the opposite sense of shear adjacent to the Central Lowlands of Myanmar and Sichuan Basin. Red lines show normal faults. Blue lines show thrust faults with triangles in the direction of dip. b) Focal mechanisms of earthquakes in South East Tibet. Focal mechanisms determined from body-waveform modelling by Zhou et al. (1983), Jones et al. (1984), Molnar and Lyon-Caen (1989), Holt et al. (1995) (and references therein), Li et al. (2011), Sloan et al. (2011), Han et al. (2014), Bai et al. (2017), Han et al. (2018) are shown in red if they have a rake of $-90 \pm 35^\circ$ (normal faulting), and dark blue otherwise. Yellow focal mechanisms are >50 km deep and are associated with subduction beneath the Indo-Burman ranges, all other earthquakes have depths ≤ 20 km. Focal mechanisms in pink (normal faulting, with rakes of $-90 \pm 35^\circ$) and pale blue are those from the CMT catalogue with $>70\%$ double couple and >50 depth phases in the EHB catalogue if the earthquake occurred before 2009. Two regions of normal faulting discussed in the text are circled in red. Red box in inset shows location of these figures, black box shows location of Figure 6.2.

which may result from increased erosion due to changes in base level or climate, rather than uplift directly. Such ages have been interpreted to imply that rapid uplift occurred $\sim 13\text{--}5$ Ma, based on the identification of geomorphic surfaces presumed to have formed at low elevation (Clark et al., 2005a, 2006). However, it has been suggested that such low-relief, erosional surfaces can form at high elevations (e.g. Liu-Zeng et al., 2008; Yang et al., 2015) and that increased exhumation may have been related to changes in base level (e.g. Tang et al., 2017). The interpretation of the existing thermochronometric data in terms of elevation history is therefore unclear.

New estimates of palaeoelevation from stable-isotope geochemistry provide an exciting opportunity to constrain this elevation history, and, therefore, to distinguish between competing models for the evolution and rheology of mountain ranges. South East Tibet is a good region in which to use stable isotopes for palaeoaltimetry, since the region is likely to have had much simpler moisture transport paths than the central Tibetan plateau (e.g. Hren et al., 2009; Molnar et al., 2010; Hoke et al., 2014), making the interpretation of stable isotope data clearer.

Although the results presented here are in the context of South East Tibet, the presence of lateral rheology contrasts is a common feature of mountain ranges globally (e.g. Lamb, 2000; Nissen et al., 2011; Reynolds et al., 2015). In particular, many mountain ranges, both active and older, have edges adjacent to cratons, regions of continental lithosphere, usually composed of Proterozoic or Archean crust, which have remained relatively undeformed through multiple deformation cycles (McKenzie and Priestley, 2008). These results are therefore applicable to the temporal evolution of mountain ranges generally.

I first discuss the tectonics of South East Tibet and outline some of the key debates in the region (Section 6.2). I then present a compilation of recent palaeoaltimetric results (Section 6.3). Using a dynamical model I then investigate the effects of lateral rheology contrasts on topographic evolution (Section 6.4), and discuss the implications of this modelling for the rheology of continental lithosphere and the interpretation of palaeoaltimetric results (Section 6.5).

6.2 Regional Kinematics

Figure 6.1 shows the major active faults and focal mechanisms of earthquakes in South East Tibet. Copley (2008) provided a comprehensive review of the kinematics of this region, with the main difference between Figure 6.1b and his Figure 3 being the occurrence of the Wenchuan and Lushan earthquakes, at the NW edge of the Sichuan Basin, and their associated

aftershocks. These earthquakes confirm that the Longmen Shan is a region of active thrust faulting. Therefore, I do not repeat his analysis, but summarise the key points below.

Much of the morphology of South East Tibet is dominated by deeply-incised river valleys which often follow the traces of strike-slip faults. The Xianshuihe and Sagaing faults (Figure 6.1a) have left- and right-lateral geodetic slip rates of $\sim 7\text{--}9$ mm/yr and ~ 18 mm/yr respectively (Maurin et al., 2010; Zheng et al., 2017). There is also a region of distributed left-lateral faulting east of the Sagaing fault, which accommodates right-lateral shear through rotations about vertical axes (Copley, 2008, in a similar manner to the Minab earthquake in discussed in Chapter 2). Collectively the strike-slip faults in South East Tibet accommodate south-eastwards motion of the high region relative to both the low-elevation Sichuan Basin and the Central Lowlands of Myanmar (Copley and McKenzie, 2007). The faults on opposite sides of the high region accommodate opposite senses of shear (Figure 6.1a).

The low topography in both the Sichuan Basin and the Central Lowlands of Myanmar (Figure 6.1) suggests that they have experienced relatively little deformation as a result of the current orogeny, in comparison to the high regions between them and on their other margins. GPS measurements in the Sichuan Basin also demonstrate that it has low internal deformation (< 2 mm/yr – Shen et al., 2005, Figure 6.2). The Sichuan Basin is composed of 36–40 km thick Paleoproterozoic crust (Burchfiel et al., 1995; Zhang et al., 2010). Ambient-noise Rayleigh-wave tomography shows a low shear-wave velocity layer down to 10 km, probably corresponding to sedimentary cover, with an underlying high shear-wave velocity layer which truncates at the basin edge (Li et al., 2009) and may correspond to relatively low-temperature material. The Sichuan Basin has also been inferred to have a high viscosity in comparison to its surroundings based on differential post-seismic motion across the Longmen Shan following the Wenchuan earthquake (Huang et al., 2014). The small amplitude of the flexural basin (discussed below) implies that the basin has a high effective elastic thickness in comparison to the surrounding regions (Fielding and McKenzie, 2012). In contrast to the Sichuan Basin, there is relatively little information on deformation in the Central Lowlands of Myanmar. Initial GPS measurements by Maurin et al. (2010) suggest that central Myanmar, west of the Sagaing fault, deforms in a coherent manner, however, they have few stations and these are concentrated in the region adjacent to the Sagaing fault so do not provide a tight bound on the rate at which deformation could be occurring. The earthquakes in the SW of Figure 6.1b are associated either with strike-slip motion on the Sagaing fault or with active subduction beneath the Indo-Burman ranges (e.g. Stork et al., 2008; Steckler et al., 2016, yellow focal mechanisms in Figure 6.1b). The seismic strain rate within the Central Lowlands of Myanmar is therefore low based on seismicity in the instrumental period. The presence of undeformed Miocene sediments in the Central Lowlands of Myanmar also suggests low rates of recent deformation (Wang et al., 2014).

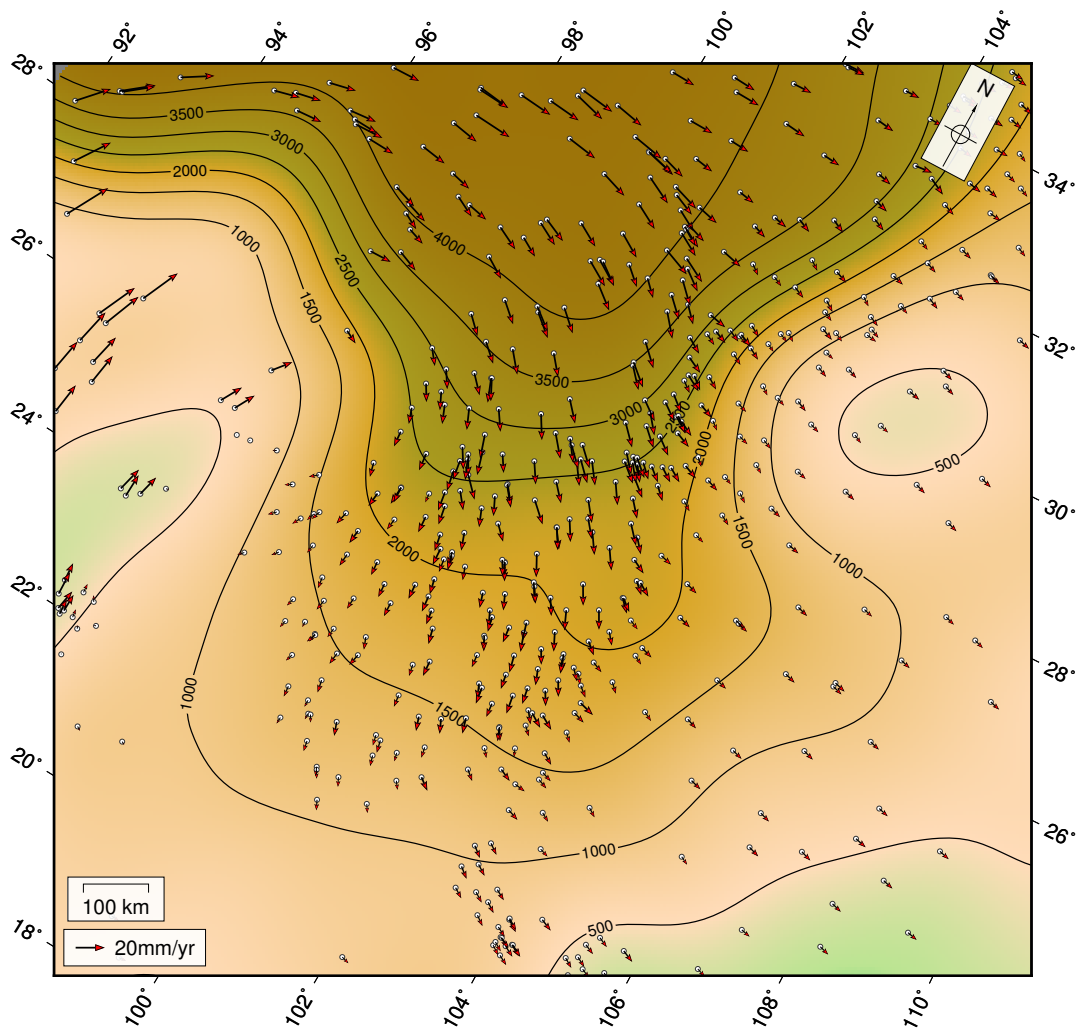


Figure 6.2: Topography of South East Tibet after applying a low-pass 500 km-diameter Gaussian filter in an oblique Mercator projection (centred on 101.5° E, 26.5° N, location shown in Figure 6.1b) for comparison to my model set-up (Figure 6.4) and results (Figures 6.5 and 6.8, Section 6.4.3). GPS velocities from Zheng et al. (2017) are shown in a Eurasia-fixed reference frame.

The development of the very high topographic gradients in the Longmen Shan, adjacent to the Sichuan Basin, ($\sim 4\text{km}$ increase in average elevation over $\sim 50\text{km}$, Figure 6.1) has been the subject of significant debate and has implications for the rheology of the continental lithosphere (e.g. Clark and Royden, 2000; Clark et al., 2005a; Burchfiel et al., 2008; Hubbard and Shaw, 2009; Hubbard et al., 2010). Low GPS shortening rates across the margin of the Sichuan Basin ($< 3\text{ mm/yr}$ – Shen et al., 2005; $1\text{--}2\text{ mm/yr}$ – Zheng et al., 2017; Figure 6.2), combined with an increase in river incision rates at $\sim 13\text{--}5\text{ Ma}$ (Kirby et al., 2002; Clark et al., 2005b, discussed in Section 6.3) have been used to argue that flow in a low-viscosity, lower-crustal channel is required (Clark and Royden, 2000; Clark et al., 2005b, see Section 6.4.1). However, the 2008 Wenchuan earthquake, and subsequent analysis of shortening on structures imaged in seismic profiles have demonstrated that active shortening of the brittle upper crust is occurring across the Longmen Shan (Hubbard and Shaw, 2009; Hubbard et al., 2010). Fielding and McKenzie (2012) used free-air gravity anomalies to analyse the flexure of the Sichuan Basin in response to the applied topographic load, the presumed absence of which had previously been used as an argument for channel flow (Burchfiel et al., 2008). As Hubbard et al. (2010) point out, the absence of syn-flexural sedimentary deposits may be related to sediment being transported away from the basin by the Yangtze River; that is, a lack of sediment deposition rather than a lack of flexure.

A significant feature of the earthquake distribution in South East Tibet is the two groups of normal-faulting earthquakes highlighted by red circles and red/pink focal mechanisms in Figure 6.1b. The northernmost group of earthquakes strike approximately perpendicular to the topographic gradient (so accommodate extension parallel to this gradient). Copley (2008) suggested that these faults are related to an increase in topographic gradient leading to increased velocities, a feature which is also seen in instantaneous dynamical models (Copley, 2008, Section 6.4.1). The second group of normal-faulting earthquakes are further south and have strikes sub-parallel to the direction of motion of South East Tibet relative to Eurasia and South East China. Copley (2008) suggested that these earthquakes are related to extension south of the region between the Sichuan Basin and the Central Lowlands of Myanmar where the high topography is no longer constrained to a narrow region and can expand perpendicular to topographic gradients. Possible dynamical explanations for these normal-faulting earthquakes are discussed in Section 6.5.

6.3 Palaeoaltimetry

Previous studies of topographic evolution in SE Tibet have concentrated on thermochronology (e.g. Kirby et al., 2002; Clark et al., 2004; Wang et al., 2012, 2016a). In this chapter I use recently published constraints on palaeoaltimetry from stable isotopes. These techniques have been developed in order to place quantitative constraints on the elevation history of orogenies, such as Tibet, and to address questions about the elevation of the plateau prior to the collision of India. Elevation histories have previously been based on qualitative indicators, such as leaf and fossil morphology and diet (e.g. Wang and Deng, 2005; Wang et al., 2007), which are potentially indicative of environment rather than elevation. Although stable-isotope palaeoaltimetry studies have significant associated uncertainties, discussed below, they provide a direct estimate of palaeoelevation. In contrast, thermochronology gives information about exhumation, which may be related to topographic elevation, gradient or other controls on erosion, such as increasing precipitation, changes in local base level or the reorganisation of drainage networks.

Stable isotope palaeoaltimetry uses systematic variations in the isotopic composition of precipitation – usually measured as $\delta^{18}O = \left(\frac{\left(\frac{^{18}O}{^{16}O} \right)_{sample}}{\left(\frac{^{18}O}{^{16}O} \right)_{ref}} - 1 \right) \times 1000 \text{ ‰}$ – with elevation to derive the palaeoelevation of sample sites (e.g. Rowley et al., 2001; Rowley, 2007; Mulch, 2016). The relationship between isotopic composition and elevation is derived from thermodynamic arguments (Rowley et al., 2001). As a packet of air rises adjacent to topography, it cools and expands adiabatically. Once the air is saturated it will condense out water as precipitation, which preferentially incorporates ^{18}O over ^{16}O and thus reduces $\delta^{18}O$ in the remaining vapour. The composition of this residual vapour can be related to altitude, and is preserved at altitude when precipitated in carbonates. The Rayleigh fractionation model, used to describe the progressive depletion of water vapour with altitude, assumes that condensed water is removed from the rising air packet, which does not mix with the surrounding air (Dansgaard, 1964). These theoretical assumptions can be tested at the present day using water collected from rivers at a range of altitudes, and have been shown to produce a good agreement for South East Tibet (e.g. Hren et al., 2009; Hoke et al., 2014). In other areas (e.g. the central Tibetan Plateau) spatial and temporal variations in moisture transport paths mean that precipitation may have incorporated water from different sources (which have different initial $\delta^{18}O$) or have been re-evaporated from the plateau surface, making the relationship between $\delta^{18}O$ and elevation more complex (e.g. Molnar et al., 2010; Bershaw et al., 2012).

Stable isotope palaeoaltimetry therefore requires an estimate of the isotopic composition of palaeo-precipitation; in the studies discussed below $\delta^{18}O$ in carbonates is taken to represent

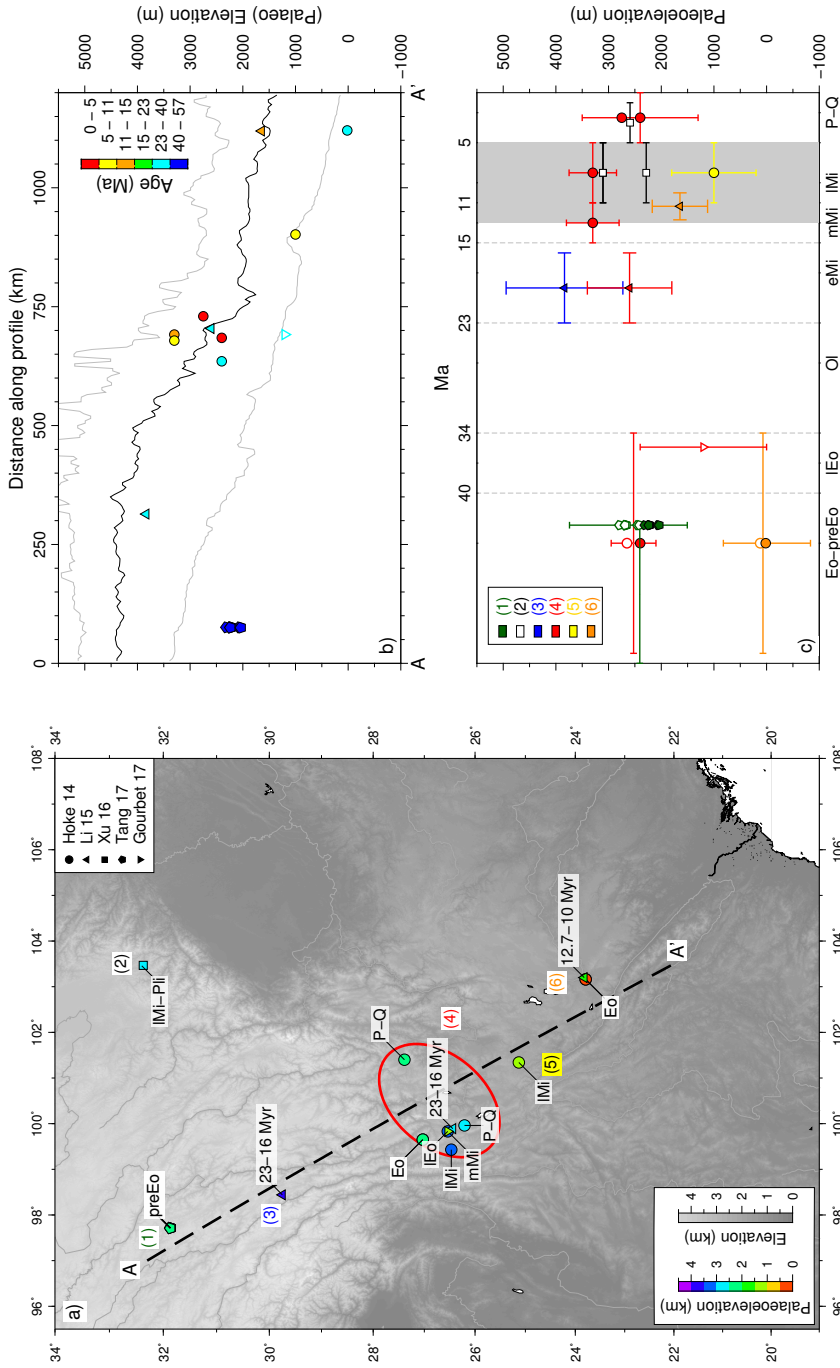


Figure 6.3: Results of stable-isotope palaeoaltimetry studies in South East Tibet. a) Sample localities from Hoke et al. (2014); Li et al. (2015); Xu et al. (2016); Tang et al. (2017); Gourbet et al. (2017) are coloured by palaeoelevation and labelled with their reported age (Eo-preEo: Eocene-pre Eocene >40 Ma, IEO: late Eocene: 40–34 Ma, OI: Oligocene 34–23 Ma, eMi: early Miocene 23–15 Ma, mMi: middle Miocene 15–11 Ma, IMi: late Miocene 7–5 Ma, P-Q: Pliocene–Quaternary 5–0 Ma). Black dashed line shows location of profile in b. 6 regions are labelled, which are referred to in the text, the red ellipse indicates the extent of the region included in (4). The colour of the region numbers corresponds to the colour of points in c. b) profile through present-day topography and estimates of palaeoelevation. Black (gray) line(s) show the mean (maximum and minimum) elevation in 10 km bins over a 200 km-wide swath centred on the profile. Palaeoelevation estimates are coloured by age and have shapes as in a. Elevation estimates are those using modern temperatures for the $\delta^{18}\text{O}$ -palaeoelevation relationship, with the exception of the result from Gourbet et al. (2017) which is shown unfilled, as these provide a lower bound on palaeoelevation (see Section 6.3). c) Uncertainties in sample age and elevation. Epoch labels are as in a. Where multiple samples from the same author are reported in the same region only a single error bar (representing the highest and lowest palaeoelevation estimates) is plotted. Palaeoelevation estimates using a modern temperature-elevation relationship are shown as filled symbols, those using a higher Eocene temperature estimate are unfilled. The colour of symbols corresponds to their region in a. Symbol shapes are as in a. White squares are soil-deposited samples from Xu et al. (2016) which are not included in b. Grey bar shows the timing of increased exhumation and erosion rates suggested by Clark et al. (2005b) to indicate rapid uplift.

$\delta^{18}\text{O}$ of precipitation when they were deposited, after applying corrections. The results shown in Figure 6.3 are taken from five recent palaeoaltimetry studies (Hoke et al., 2014; Li et al., 2015; Xu et al., 2016; Gourbet et al., 2017; Tang et al., 2017), which use soil-deposited (Hoke et al., 2014; Xu et al., 2016; Tang et al., 2017) or lacustrine (Li et al., 2015; Xu et al., 2016) carbonates. Lacustrine carbonates are less clearly interpreted than those deposited in soil (Rowley, 2007) since they represent a weighted average of the precipitation in the associated catchment, and can also experience significant evaporation, reversing the effect of Rayleigh fractionation, leading to less negative $\delta^{18}\text{O}$ and therefore lower elevation estimates (as seen in the results of Xu et al., 2016). The lacustrine carbonates discussed by Xu et al. (2016) have a very high scatter in $\delta^{18}\text{O}$, and, therefore, palaeoelevation estimates, so only their results from soil-deposited carbonates are shown in Figure 6.3. The conversion of carbonate isotopic compositions to palaeoelevation requires: 1) an estimate of the temperature at which carbonates formed, 2) knowledge of the isotopic composition of water at low elevations at the time of sample deposition (the starting point for changing $\delta^{18}\text{O}$ with elevation) and 3) a relationship between isotopic composition and elevation. All of these factors introduce uncertainties into estimates of palaeoelevation dependent on the age of sampled formations, which themselves often have large uncertainties (Gourbet et al., 2017, Figure 6.3c).

There are two main differences in the approach to converting isotopic composition to palaeoelevation taken by the studies in South East Tibet. First, different estimates are used for the temperature of carbonate formation. The temperature at which carbonates form is not necessarily equivalent to mean air temperature, since carbonates tend to form preferentially in particular seasons (e.g. Rowley, 2007). Past mean air temperature is already subject to significant uncertainty, and depends on elevation, meaning that its effect on palaeoelevation results is complex. Using hotter temperatures for Eocene samples leads to higher elevation estimates than using modern day temperatures (e.g. Hoke et al., 2014). Hoke et al. (2014), Tang et al. (2017) and Gourbet et al. (2017) all give results using a $\delta^{18}\text{O}$ –elevation based on Rayleigh fractionation at Eocene temperatures, assumed to be hotter than present day (unfilled symbols in Figure 6.3c). Li et al. (2015) and Xu et al. (2016) only use late Miocene-Pliocene samples so do not apply a temperature correction. However, the dating of the samples used by Li et al. (2015) in region (4) (Figure 6.3a) has been questioned (Gourbet et al., 2017), and an Eocene $\delta^{18}\text{O}$ –elevation relationship may be more appropriate. Results using a modern relationship between $\delta^{18}\text{O}$ and elevation are shown as filled symbols in Figure 6.3c. The variations in palaeoelevation estimates due to these different modelling approaches increase with elevation but are less than the reported errors of ~ 1 km at the elevations discussed here (as shown by the elevations of filled and unfilled symbols in Figure 6.3c).

The second difference in approach comes in correcting for “continentality”, whereby the $\delta^{18}O$ of precipitation decreases further from the coast at $\sim 2\%$ per 1000 km (Dansgaard, 1964), such that incorporating greater continentality leads to lower elevation estimates (Gourbet et al., 2017). Whilst some authors have argued that continentality plays an important role in SE Tibet (e.g. Li et al., 2015; Gourbet et al., 2017), Tang et al. (2017) neglect this effect because of its decreased importance in high humidity regions. Such corrections can have a significant effect on elevation estimates (e.g. Gourbet et al., 2017, found elevations of 1200 ± 1200 m and 2800 ± 1000 m with and without correcting for continentality). Continentality may be important if material undergoes significant lateral transport, such that samples record elevation in locations different to where they are found at the present day (see Section 6.5). Additional variations in the degree of testing for diagenetic effects and the choice of low-level reference $\delta^{18}O$ also affect palaeoelevation estimates. However, these variations are likely to be less than the ~ 1 km reported errors.

This study is concerned with first-order topographic features on lateral length scales which incorporate multiple sample localities, and vertical length scales greater than the ~ 1 km errors in palaeoelevation estimates. The locations of the regions discussed below are shown in Figure 6.3a. Tang et al. (2017) suggest that region 1 was at >2100 – 2500 m before the Eocene, within error of its present-day elevation (~ 3800 m). The results of Xu et al. (2016) from lacustrine carbonates in region 2 show significant scatter so I show only their results from soil-deposited carbonates (white squares in Figure 6.3c), although there is still significant uncertainty in these, associated with the moisture source and evaporation. However, in using the most negative values of $\delta^{18}O$, Xu et al.’s palaeoelevation estimate is likely to be a lower bound, suggesting that region 2, adjacent to the Longmen Shan, may have been at or near present-day elevations (~ 3000 m, with present-day elevations of 2800 – 3700 m) by the late Miocene. Since no earlier rocks have been sampled this represents the latest date at which such elevations were reached, an observation also applicable to regions 1, 3 and 5. In region 3, Li et al. (2015) suggest that elevations of 3800_{-1600}^{+1100} m (similar to present day) may have been attained by the early Miocene. Region 4, which includes the Jianchuan basin (Figure 6.1a) and the adjacent area was at 1200 ± 1200 m – 2650 ± 300 m in the late Eocene but had reached present-day elevations (3300 ± 500 m) by the mid-Miocene (with a maximum uplift rate of ~ 0.2 mm/yr). Region 5 was at 1000 ± 800 m, slightly below its present elevation (1900 m), by the late Miocene. Material in region 6 was likely lower than its present-day elevation (1400 m) in the Eocene (16 ± 850 m) but had reached elevations similar to today (1600_{-800}^{+500} m) by the late Miocene (Hoke et al., 2014; Li et al., 2015, orange points in c), giving an uplift rate of ~ 0.06 mm/yr for a 1.5 km increase in elevation over ~ 25 Myr.

Despite significant uncertainties, stable-isotope palaeoaltimetry suggests that at least some areas of present-day South East Tibet have been high since the late Eocene, and are likely to have reached present-day elevations prior to the onset of rapid exhumation described by Clark et al. (2005b), based on the date of incision of river gorges (gray region in Figure 6.3c). This suggests that uplift rates are likely to be much lower than would be predicted if all the uplift in the region had occurred since the late Miocene, as previous authors have suggested (Kirby et al., 2002; Clark et al., 2005b, 2006).

6.4 Dynamical modelling

6.4.1 Previous models

Numerous authors have considered the continental lithosphere in regions of distributed deformation as a viscous fluid whose motion is driven by horizontal pressure gradients, resulting from elevation contrasts, and by imposed boundary conditions (e.g. England and McKenzie, 1982; Houseman and England, 1986; England and Jackson, 1989; Royden, 1996; Lamb, 2000; Flesch et al., 2001; D'Agostino et al., 2014; Reynolds et al., 2015; Walters et al., 2017; Flesch et al., 2018). Many of these studies use a thin-viscous-sheet formulation, which assumes that there are no vertical variations in horizontal velocity (England and McKenzie, 1982). This assumption means that the top and base of the flow must have no shear tractions, corresponding to flow over a much less viscous fluid (here referred to as a stress-free boundary condition after McKenzie et al., 2000). Neglecting vertical variations in horizontal velocities implicitly takes a vertical average of the rheological properties of the lithosphere, meaning that the flow velocity is controlled by the highest viscosity layer (England and McKenzie, 1982). This assumption breaks down in regions with large gradients of crustal thickness or where the base of the flow is not stress-free, due, for example, to the underthrusting of relatively strong material (e.g. England and McKenzie, 1982; Houseman and England, 1986).

The importance of lateral rheology contrasts in determining the distribution of strain in the continents has been suggested in many mountain ranges (e.g. Molnar and Tapponnier, 1981; England and Houseman, 1985; Lamb, 2000; McKenzie and Priestley, 2008; Nissen et al., 2011; Reynolds et al., 2015). Initial investigations of the effects of lateral rheology contrasts in determining how continents deform were conducted by Vilotte et al. (1984), neglecting the effects of gravity. England and Houseman (1985) considered the effects of a high viscosity region with a thin-viscous-sheet model. Flesch et al. (2001) extended the thin-viscous-sheet formulation to include lateral viscosity variations. However, lateral rheology contrasts are often associated with large gradients in crustal thickness and, if less viscous material flows over

a higher viscosity region, this is equivalent to flow over a rigid base (defined as zero-horizontal velocity, after McKenzie et al., 2000), meaning that the thin-viscous sheet approximation breaks down, as the assumption that vertical variations in horizontal velocities are negligible no longer applies.

To address the problems of the thin-viscous-sheet approximation, Copley (2008) incorporated vertical variations in horizontal velocity in an instantaneous model, using methods proposed by Pattyn (2003) for ice-sheet modelling. The model of Copley (2008) is discussed in more detail below. Copley et al. (2011b) used this model to demonstrate that variations in basal boundary condition can explain the main features of present-day strain-rate field in Tibet. The models of Copley (2008) and Copley et al. (2011b) do not include time-dependence. Reynolds et al. (2015) extended the approach of Copley (2008) to include temporal evolution, and demonstrated that the topography of the Sulaiman Ranges in Pakistan may be controlled by lateral variations in basal boundary condition, due to the range propagating over a weak, pre-existing basin on the Indian plate. Here I follow Reynolds et al.'s approach but improve the numerical stability of the solution (see Section 6.4.2), and investigate the growth of mountain ranges in the presence of lithosphere-scale strength contrasts.

A suite of continuum models of South East Tibet have focussed on the possibility of a low-viscosity lower crustal channel. Royden et al. (1997) used a depth-dependent Newtonian viscosity chosen to reproduce the shape of the Tibetan plateau and the eastern syntaxis to suggest that lower crustal flow is required to explain steep topographic gradients adjacent to the Sichuan Basin. Clark and Royden (2000) proposed that flow in a low-viscosity channel of constant thickness, in which material accreted to the base and roof causes vertical uplift but does not change the width of the channel, could explain the variations in topographic gradients across Tibet. Clark et al. (2005a) considered the effect of material in such a channel encountering a rigid region, such as the Sichuan Basin. Their model predicts topography which is not isostatically compensated, and no active shortening across the Longmen Shan (see Section 6.2).

Copley and McKenzie (2007) considered the instantaneous flow of a power-law fluid bounded by lateral no-slip walls corresponding to the Sichuan Basin and the Central Lowlands of Myanmar. This modelling showed little difference in fits to the GPS velocity field using a power-law as opposed to a Newtonian rheology. Copley and McKenzie found that an effective viscosity of 10^{22} Pas gave the best fit to the GPS, but noted that their model has no vertical sensitivity (similar to the thin-viscous sheet formulation; England and McKenzie, 1982) so this is likely to correspond to the highest viscosity layer.

Copley (2008) also performed instantaneous calculations but incorporated the temperature and strain-rate dependence of viscosity, based on experimentally-derived flow laws. He demonstrated that GPS measurements imply that gravity is important in driving the deformation of South East Tibet but that horizontal motions alone cannot resolve the depth variation of viscosity. However, any rapid flow at depth associated with a weak mid-to-lower crust leads to rapid (~ 5 mm/yr) crustal thinning near the high Tibetan plateau and thickening at similar rates in lower elevation regions. In contrast, for the case of uniform viscosities at depth the crustal thickening and thinning rates are low (< 1.5 mm/yr). Copley also found that low viscosity regions at depth, which are consistent with experimental constraints on rock rheology and geologically plausible materials, do not lead to channel flow in the sense proposed by Royden et al. (1997) and Clark and Royden (2000). Either low viscosities are concentrated in a mid-crustal channel which is too thin to introduce a vertical gradient in horizontal velocities, or a weak mid-to-lower crust requires a weak upper mantle in which case the basal boundary condition is not rigid, as assumed by Clark and Royden (2000), a result also predicted by McKenzie et al. (2000).

Here I extend this work to consider the three dimensional temporal evolution of an isoviscous gravity current, and examine the effects of lateral rheology contrasts on the evolution of topography. I first describe my modelling set-up, then present the results and discuss the implications for lithosphere rheology and the temporal evolution of topography.

6.4.2 Model set-up

Figure 6.2 shows the topography of South East Tibet after applying a 500 km-diameter, low-pass Gaussian filter, which forms the basis for the model set-up described below (with the top boundary of Figure 6.2 being analogous to $y = 0$ in Figure 6.4). I emphasise, however, that my model is not intended to simulate the details of the topography, but rather to investigate the first-order effects of lateral rheology contrasts on the evolution of mountain ranges in general.

I model the lithosphere as a viscous fluid driven by gravity acting on isostatically-compensated crustal-thickness contrasts. As discussed above, the thin-viscous-sheet approximation is not applicable if large lateral rheology contrasts are present, and in particular if a less viscous material flows over a higher viscosity base, as is likely to be occurring in the Sichuan Basin (Fielding and McKenzie, 2012, see Section 6.2). I therefore include vertical variations in horizontal velocities and solve the low Reynolds' number Stokes' equations using the formulation proposed by Pattyn (2003). Copley (2008) used the same formulation to calculate the instantaneous velocity field for South East Tibet (see Section 6.4.1). This approach still

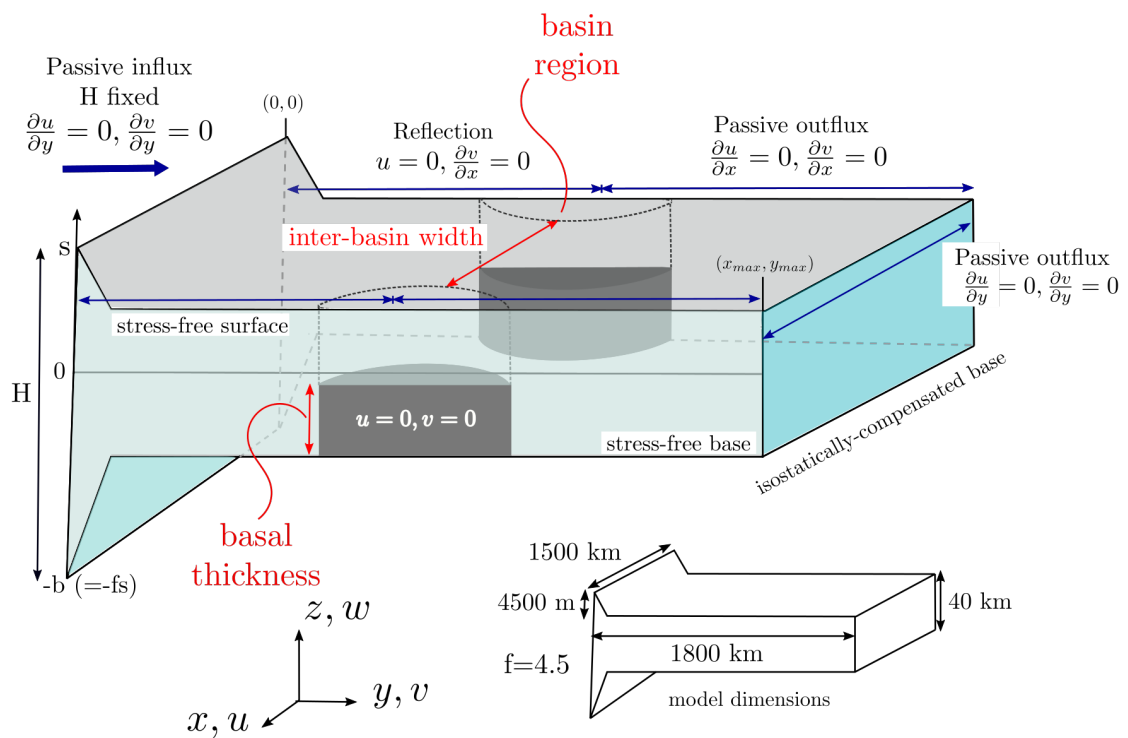


Figure 6.4: Model geometry, showing the initial topography and symmetric rigid regions. Boundary conditions on $x = x_{max}$ are the same as those on $x = 0$. Inset shows dimensions of model domain. The isostatic root is not shown to scale.

neglects horizontal derivatives of vertical velocities. These terms may become important immediately adjacent to the transition from a stress-free to a rigid base. However, for the analogous problem of ice-sheet flow across a grounding line Pattyn (2000) showed that these terms, equivalent to vertical tractions on vertical planes, remain at least an order of magnitude smaller than vertical derivatives of horizontal velocities, and I assume this to be applicable here. The temporal evolution of the current is calculated by re-writing the incompressibility condition as a diffusion equation for topography (Pattyn, 2003; Reynolds et al., 2015). I take the same approach as Reynolds et al. (2015), but use an improved method for the solution of these equations. I write the diffusion equation (Appendix D, eqn. D.9) as a sparse matrix equation using a Crank-Nicolson scheme for the finite differences, with diffusivities calculated on a staggered grid. Solving both x and y terms in the same linear system, rather than separating the components means that the matrix does not have a simple form (the separated case is tridiagonal, which was the form used by Reynolds et al., 2015). I therefore solve the sparse system using the generalised minimum residual method (Saad and Schultz, 1986, in sparskit2). Further details of this approach are given in Appendix D.

The fluid has an isoviscous Newtonian rheology and is isostatically compensated at the base of the crust (cf. Copley, 2008), relative to a column of mantle of density 3300 kg/m^3 (Flesch et al., 2001). McKenzie et al. (2000) showed that the crustal thickness evolves on much longer timescales than those taken to reach isostatic equilibrium, suggesting that this is a reasonable approximation. As discussed above Copley and McKenzie (2007) demonstrated that the difference between using a power-law rheology and a Newtonian rheology, in terms of the fit to GPS velocities in the region, was small. I acknowledge that an isoviscous fluid is an oversimplification, however using a simple rheology allows me to test which topographic features are the result of lateral rheology contrasts, and which may require additional rheological complexity. The velocity of the current is linearly dependent on the choice of viscosity, so although I use a viscosity of 10^{22} Pas here (Copley and McKenzie, 2007), the models can be considered to apply to different viscosities by scaling the time and velocities.

In order to investigate the lateral and vertical motion of particles at the surface of the flow, analogous to the lateral transport of the soil-deposited or lacustrine carbonates used in palaeoaltimetric studies, I track a series of points which move with the horizontal velocity at their surface location at each timestep.

High viscosity regions, analogous to the Sichuan Basin and the Central Lowlands of Myanmar, are included by setting flow velocities to zero in part of the model domain with a specified thickness (grey areas in Figure 6.4). Flow can occur over and around these rigid regions. The

parts of the domain where the current is flowing over such a region are referred to below as basin regions. This approach is suggested by the inferences of the strength of the Sichuan Basin discussed in Section 6.2 (Copley and McKenzie, 2007; Copley, 2008; Fielding and McKenzie, 2012). In the absence of further information about the Central Lowlands of Myanmar I take the same approach to modelling that region. I initially consider a symmetric set-up to determine the effect of changing the inter-basin width and basal thickness (defined in Figure 6.4), where the basal thickness is analogous to the thickness of strong, undeforming lower crust. In the remainder of the model domain I use a stress-free basal boundary (England and McKenzie, 1982; Copley and McKenzie, 2007), and the top surface of the flow is stress-free throughout the model domain, representing the lack of significant tractions imposed by the atmosphere.

The boundary conditions I use are shown in Figure 6.4. Fluid enters the model domain along a fixed-height boundary with zero gradients of horizontal velocity perpendicular to the boundary. This is equivalent to assuming that there is a reservoir of high material outside the model domain which can supply material to the flow at the same rate at which it moves away from the boundary (Copley, 2012; Reynolds et al., 2015). I set this height to be 4.5 km above the 40 km thick lowlands in the remainder of the initial model set-up, similar to the mean elevation of Tibet above the Sichuan Basin (e.g. Figure 6.1) and to the “thick-layer” case of McKenzie et al. (2000). Using a fixed-height boundary condition is analogous to assuming that the central Tibetan plateau has been high throughout the development of high topography in South East Tibet. The elevation history of the plateau is controversial; Rowley and Currie (2006) and Polissar et al. (2009) suggest that the plateau has been high since at least the Eocene, however palaeoaltimetric data in the plateau region are complicated by spatial and temporal variations in moisture sources and transport paths (e.g. Bershaw et al., 2012; Molnar et al., 2010, discussed in Section 6.3). Given that any additional variation in plateau height over this time is uncertain, I choose to use the simple approximation of a fixed-height boundary. The velocity condition I impose ($\frac{\partial u}{\partial y} = 0$, $\frac{\partial v}{\partial x} = 0$, where u and v are the components of velocity in the x and y directions respectively) was suggested by Copley (2012) for the case of a reservoir of thickened material overlying a stress-free base supplying the current. The lack of topographic step associated with the eastern margin of the plateau (Figure 6.1) implies that the rate of supply of material from the central plateau balances the flow in the current, and so this velocity condition is a reasonable approximation.

On the lateral ($x = 0, x_{max}$) edges of the model domain near the inflowing current I use reflection boundaries (i.e. $u = 0$, $\frac{\partial v}{\partial x} = 0$), analogous to high topography continuing to the north of the Sichuan Basin and the Central Lowlands of Myanmar. Beyond the basin regions I use passive outflow boundaries ($\frac{\partial u}{\partial x} = 0$, $\frac{\partial v}{\partial x} = 0$ on $x = 0, x_{max}$, $\frac{\partial u}{\partial y} = 0$, $\frac{\partial v}{\partial y} = 0$ on $y = y_{max}$). This is analogous to crustal material being free to move out of the region shown

in Figure 6.2 south of the Sichuan basin and Central Lowlands of Myanmar, and neglects the resistive force which would be imposed by the south China craton and the Indochinese peninsula. GPS velocities relative to Eurasia continue to be oriented south-eastwards into South East Asia even at low topographic gradients, suggesting that this is a reasonable boundary condition. The change in boundary conditions occurs in the rigid region where velocities are low, in order to minimise the impact of a discrete change in boundary conditions on the model behaviour. The application of these boundary conditions is discussed in Appendix D.

Finally, in some models I incorporate an erosive term of the form $\frac{\partial s}{\partial t} = -\kappa|\partial s|_{max}$, where κ is the erosion rate and $|\partial s|_{max}$ is the maximum topographic gradient, in order to investigate the interaction between erosion and propagation of the current in determining the evolution of topography. Richardson et al. (2008) suggested that more erosion has occurred on the Longmen Shan than in the interior of the Sichuan Basin and Tibetan Plateau, suggesting that gradient-dependent erosion is appropriate. Hubbard et al. (2010) suggested an erosion rate of 1–2 mm/yr in order to balance the uplift associated with 3 mm/yr shortening across the Longmen Shan. I test three values of κ equivalent to 3, 4 and 6 mm/yr of erosion to determine their effect.

6.4.3 Results

This section presents the results of my numerical modelling. I initially describe the results of a symmetric set-up, with two semi-circular basin regions (Figure 6.5). I use these models to investigate the effects of changing basal thickness and inter-basin width (defined in Figure 6.4). I then describe an asymmetric set-up, where the shape of the basin regions is more similar to the Sichuan Basin and the Central Lowlands of Myanmar.

Figure 6.5 shows results for two rigid, semi-circular rigid regions of 450 km radius with an inter-basin width of 600 km, and 15 km basal thickness (i.e. a 15 km-thick rigid region at the base of the current). Topographic profiles from this model are shown in Figures 6.6c, d and 6.7c (gray, white and black lines – Figure 6.5). Figure 6.5a shows the topography after 50 Myr of model evolution with elevations given relative to the surface of 40 km-thick, isostatically-compensated crust. Regions with a stress-free base develop gentle topographic gradients, consistent with the results of McKenzie et al. (2000). These gentle topographic gradients result from the low vertical gradients in horizontal velocity, meaning that deformation is effectively by pure shear. Gentle topographic gradients are also a feature of thin-viscous-sheet models using a Newtonian rheology (England and McKenzie, 1982), which have the same stress-free basal boundary condition. In contrast, the dependence of velocity on the thickness

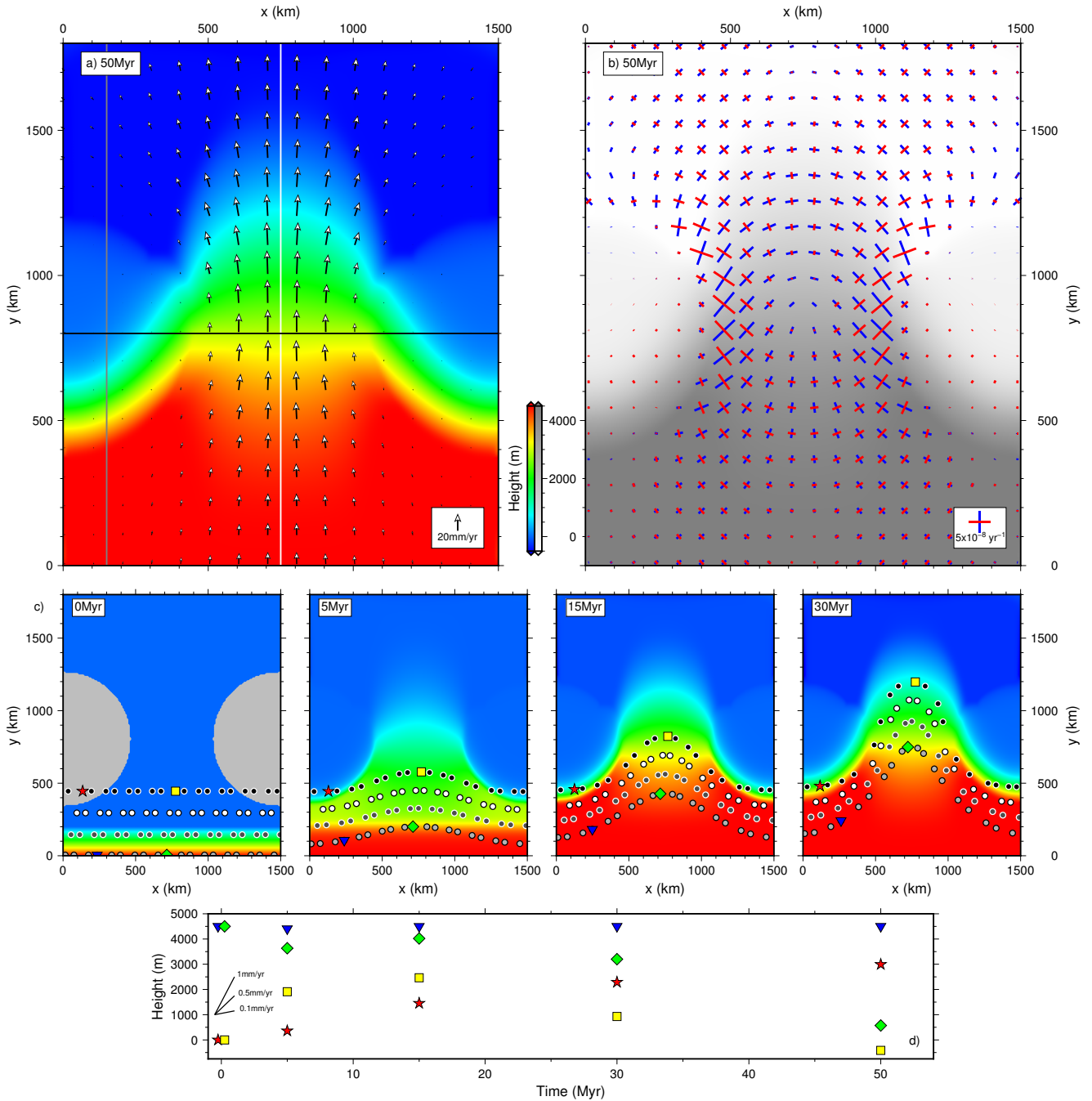


Figure 6.5: Modelling results for symmetric model with 450 km-radius basin regions (grey semicircles at 0 Myr in c) with a 15 km thick rigid base a) topography and velocities after 50 Myr for a fluid with a viscosity of 10^{22} Pas (or equivalently 5 Myr with 10^{21} Pas, as discussed in Section 6.4). Topography is plotted relative to the surface of 40 km-thick, isostatically-compensated crust. Gray, white and black lines show the locations of profiles in Figures 6.6c, d and 6.7c respectively b) principle axes of the horizontal strain-rate tensor after 50 Myr. Blue bars are maximum extensional strain rate, red maximum compressional strain rate. c) Evolution of topography through time. Dots show large-scale lateral transport of particles moving along the surface of the flow and can be viewed as analogous to the motion of near-surface carbonates used for palaeoaltimetry (see Section 6.4.2). d) shows the elevation of the shaped particles in c) with time. Since the particles are advected with the flow their elevation can increase as well as decrease. Points at 0 Myr are offset for clarity.

of the current leads to the development of steep topographic gradients in the basin regions, analogous to regions with rigid lower crust. The current also propagates more slowly in these regions (compare Figure 6.6 c and d), for the same reason. This is similar to the results of Huppert (1982) for the propagation of a viscous gravity current over a rigid base. However, the form of the current is not directly comparable to such a current as the sharp nose seen in Huppert's solution only develops where there is a large thickness contrast between the current and the layer into which it flows (McKenzie et al., 2000). In Figure 6.5 the height of the current is less than the thickness of the layer into which it flows so the topography which develops does not have the steep front seen in Huppert's model, but does develop a steeper slope than in regions where the base is stress-free (see profile in Figure 6.6).

As discussed in Section 6.4.2, the flow velocities, and therefore the rate of topographic evolution, scale linearly with the choice of viscosity, so 50 Myr of flow with a viscosity of 10^{22} Pas would correspond to 5 Myr for a viscosity of 10^{21} Pas. A viscosity of 10^{22} Pas matches the magnitude of the present day GPS with a similar form of topography, suggesting that this is a reasonable choice. The velocities in the model presented here are fastest in the centre of the inter-basin region, as are GPS velocities relative to Eurasia in South East Tibet (Figures 6.2 and 6.7b, d, f). This results in shear at the edges of the basin regions in opposite senses on different sides of the domain (Figure 6.5b, Section 6.5).

High-elevation material tends to spread laterally once it has passed the basin regions which constrain the flow. Material leaves the model domain in the regions with passive outflux boundary conditions ($y > 800\text{km}$) but this is not important in determining the shape of the topography. Applying a force boundary condition, analogous to the resistance to motion of the South China Craton and the Indochinese peninsula, would reduce this outflux. This lateral spreading can be seen from the principal axes of the horizontal strain-rate tensor (Figure 6.5b) which show extension parallel to the nose of the current. There is also extension in the y direction (parallel to the maximum topographic gradient) in the higher topography where the basin regions are initially encountered. The locations and sense of these extensional regions are discussed in Section 6.5.

Figure 6.5c shows the evolution of topography through time, and the motion of particles at the surface, which are passively advected with the flow. Particles which start within the basin regions move only very short distances in comparison to those in the part of the flow which has a stress-free base. How this lateral transport relates to brittle deformation in the upper crust, and its implications for stable-isotope palaeoaltimetry are discussed below.

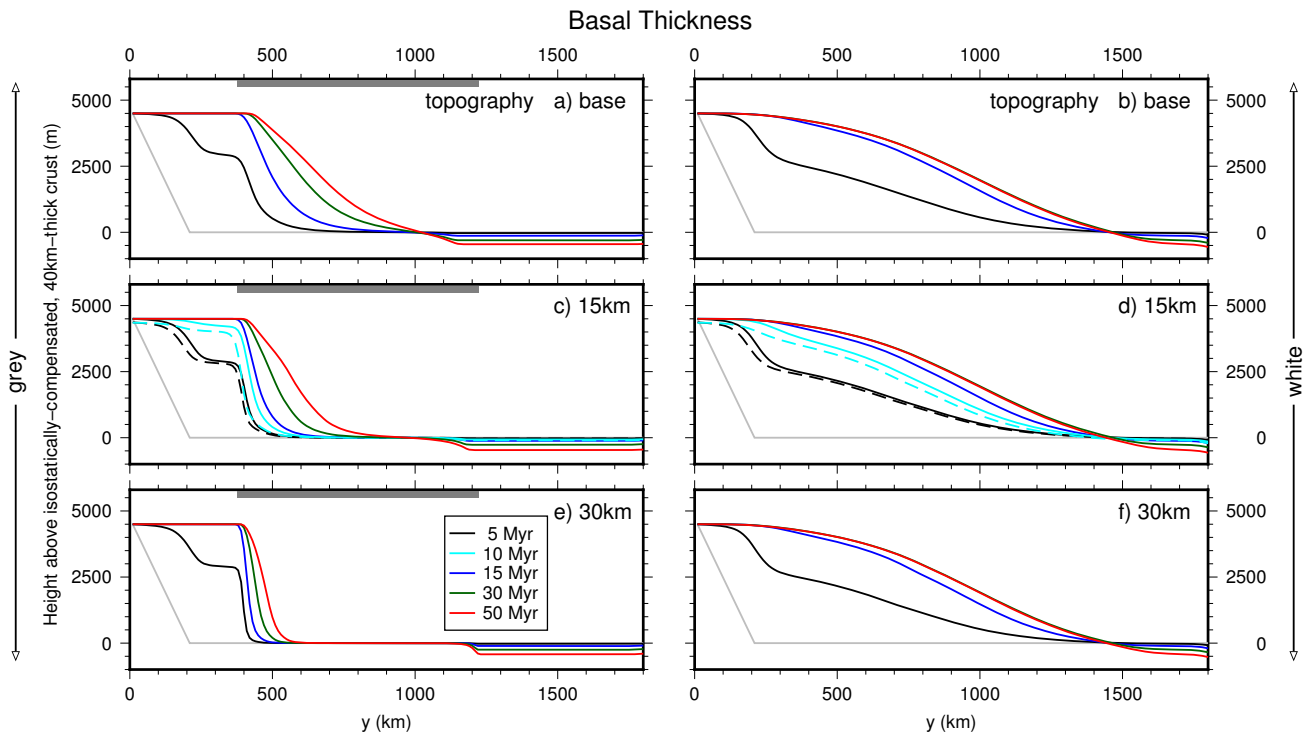


Figure 6.6: Effect of changing the basal thickness of the rigid region (analogous to the thickness of undeforming lower crust) on the propagation of topography. The lateral extent of the basin region which has a rigid basal thickness is indicated by the grey bars in a, c and e. Elevations are relative to the surface of 40 km-thick, isostatically-compensated crust. a), c) and e) show profiles through the basin region for basal thicknesses of 0 km (rigid base), 15 km and 30 km respectively (location shown by gray line in Figure 6.5a). b), d) and f) show profiles through the inter-basin (stress-free base) region for basal thicknesses of 0 km (rigid base), 15 km and 30 km respectively (location shown by white line in Figure 6.5a). Dashed lines in c and d show topography with an erosion rate of ~ 6 mm/yr. There is a change in lateral boundary condition in all profiles at $y=900$ km (Figure 6.4).

Figure 6.6 shows profiles through models with varying basal thickness with the same basal regions as in Figure 6.5 (the location of the profiles in the model domain is shown in Figure 6.5). The extent of the basin region, which has a rigid base, is shown by grey bars on the profiles. Figures 6.6 a & b, c & d and e & f have basal thicknesses of 0 km (only the base is rigid), 15 km and 30 km respectively. As discussed above, flow over a rigid region results in steeper topography than flow over stress-free base (compare Figures 6.6a, c and e to Figures 6.6b, d and f), consistent with previous fluid dynamics' results (e.g. Huppert, 1982; McKenzie et al., 2000). Increasing the basal thickness, analogous to having a thicker rigid lower crust, reduces the distance which the current propagates into the basin region, and also results in steeper topographic profiles in this region. This is consistent with the results of McKenzie et al. (2000), as a thicker rigid region (Figure 6.6a) means that the current is flowing into a thinner fluid layer so tends to develop a sharper nose.

The topography in the Longmen Shan rises ~ 4.5 km over 50 km, which is most similar to the case of a 30 km-thick rigid region (similar to the thickness of the low shear-wave velocity anomaly thought to be associated the Paleoproterozoic crust in the basin Li et al., 2009). However, erosion may also play an important role in determining how far topography propagates into the basin region. The dashed lines in Figure 6.6c and d show the results of eroding the topography at a rate of $\kappa \sim 6$ mm/yr (Section 6.4.2). Erosion leads to steeper topographic gradients and results in the current propagating less far into the basin region. The form of the erosive term means that it tends to affect steeper gradients more – compare the dashed lines in Figure 6.6c to those in Figures 6.6d and 6.7c. The extent in the y direction of topography adjacent to the basin region is stationary between 5 and 10 Myr (black and cyan dashed lines in Figure 6.6c), demonstrating that erosion can stop the propagation of topography. This is consistent with the results of Yong et al. (2003) and Richardson et al. (2008) who suggest that the Longmen Shan has not propagated significantly further into the Sichuan Basin than the Mesozoic deformation front. This is consistent with the suggestion of Koons (1989), based on the South Island of New Zealand, that erosion can stop the propagation of a range front.

The second important variable in controlling the temporal evolution of the topography is the inter-basin width. Figure 6.7 shows the topographic and velocity profiles resulting from different inter-basin widths but keeping the basal thickness constant (15 km). Greater inter-basin widths result in faster velocities perpendicular to the profile (v), meaning that the topography propagates more rapidly. The high velocities in the 900 km wide case require a prohibitively large number of time steps to advance the model in a stable manner (as well as taking longer per timestep due to the larger number of degrees of freedom associated with having smaller rigid regions) so I do not show velocities or topographic profiles later than 15 Myr for this case. However, since the topography is already high, and in my model the

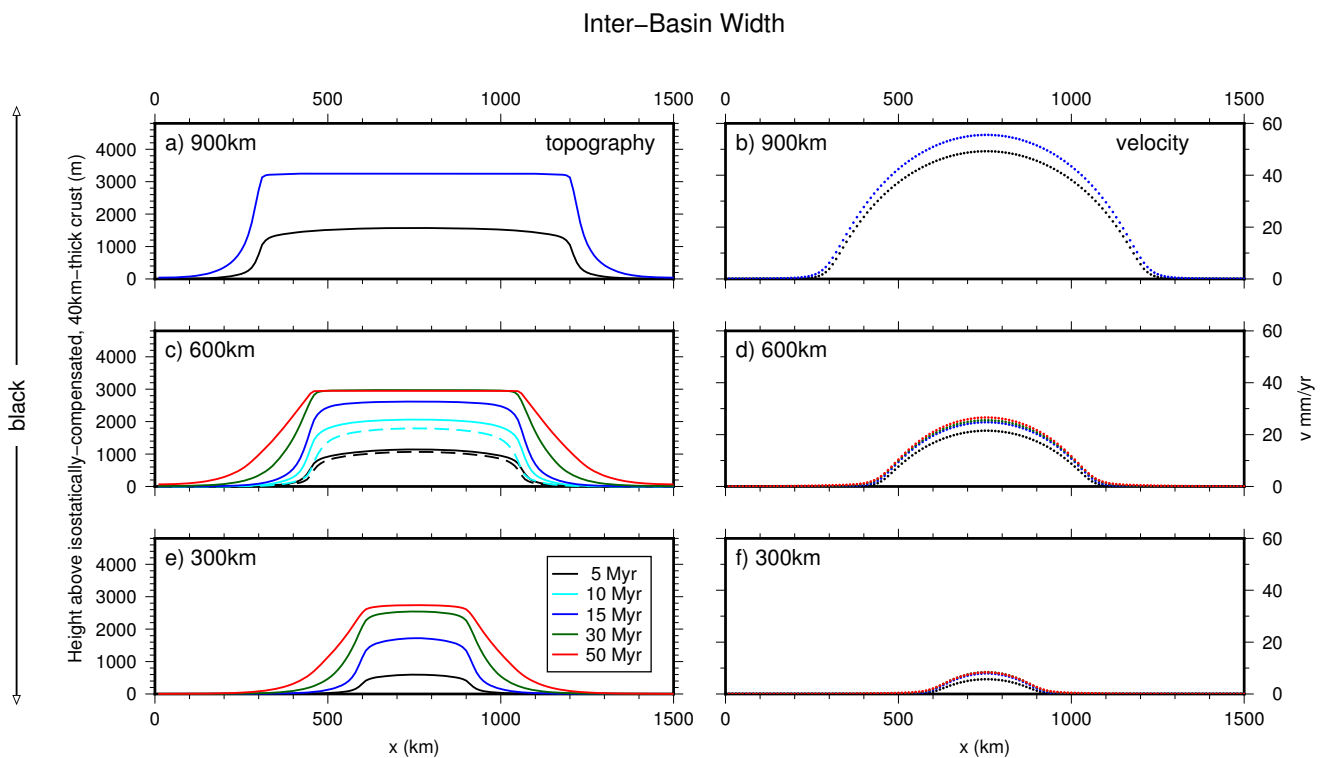


Figure 6.7: Effect of changing the distance between basin regions (inter-basin width, Figure 6.4). In each case profiles are taken at the centre of the semi-circular regions, which have a basal thickness of 15 km (black line in Figure 6.5a shows location of c and d). Elevations are relative to the surface of 40 km-thick, isostatically-compensated crust. a) and b) 900 km inter-basin width. a) shows the evolution of topography through time, b) the velocity perpendicular to the profile after 50 Myr. c) and d) as for a and b but for an inter-basin width of 600 km. Dashed lines in c show the topography with an erosion rate of ~ 6 mm/yr. e) and f) as for a and b but for an inter-basin width of 300 km.

elevation is limited by the height of the reservoir driving the flow (equivalent to the Tibetan Plateau), the velocities will not change significantly at later times.

Profiles of surface velocity in the stress-free region (Figures 6.7b, d, f) are similar to the profiles resulting from flow between two no-slip walls (Copley and McKenzie, 2007). The observed GPS velocities in the centre of this region are ~ 20 mm/yr, most similar to the 600 km inter-basin width. This is in good agreement with the results of Copley and McKenzie (2007), who found that the instantaneous velocities from a 500 km wide flow, with the same viscosity used here, gave the best fit to present-day GPS.

Figure 6.8 shows the results of an asymmetric model in which one basin region extends to the edge of the model domain in the y direction (grey patches in Figure 6.8c, 0 Myr). This geometry is similar to South East Tibet, where the Central Lowlands of Myanmar extend south to $\sim 19^\circ$ N (Figure 6.1). The results of this model are similar to the symmetric model described above, although the flow is now diverted towards $x = 0$ for values of $y > 1250$ km (beyond the semi-circular basin region) because of the wider basin region. I also see a wider region where the principle axes of the horizontal strain-rate tensor correspond to strike-slip motion adjacent to the rectangular basin region than in the semi-circular case. This is likely to be because the flow is approximately parallel to the change in basal boundary condition, so experiences greater tractions on vertical planes.

6.5 Discussion

I now compare my modelling results to South East Tibet and discuss their implications for the temporal evolution of mountain ranges in general.

I find that steep topography develops where the current flows over rigid regions; equivalent to steep topographic gradients forming at the edge of regions of rigid lower crust. This is consistent with previous fluid dynamics' results which show that flow over a rigid base results in steeper gradients than flow over a stress-free base (McKenzie et al., 2000). The shortening rates adjacent to this steep topography are small in comparison to the rates of shear where flow is parallel to the basin regions (Figure 6.8b). In the context of South East Tibet this suggests that the steep topography across the Longmen Shan could have resulted from the Paleoproterozoic crust of the Sichuan Basin acting as a rigid block, which weaker material can flow over (Copley, 2008; Fielding and McKenzie, 2012), without the need for a low-viscosity, lower-crustal channel to explain the topography. Erosion can stop the forward propagation of topography (dashed lines in Figure 6.7c). The similar position of the present-day Longmen

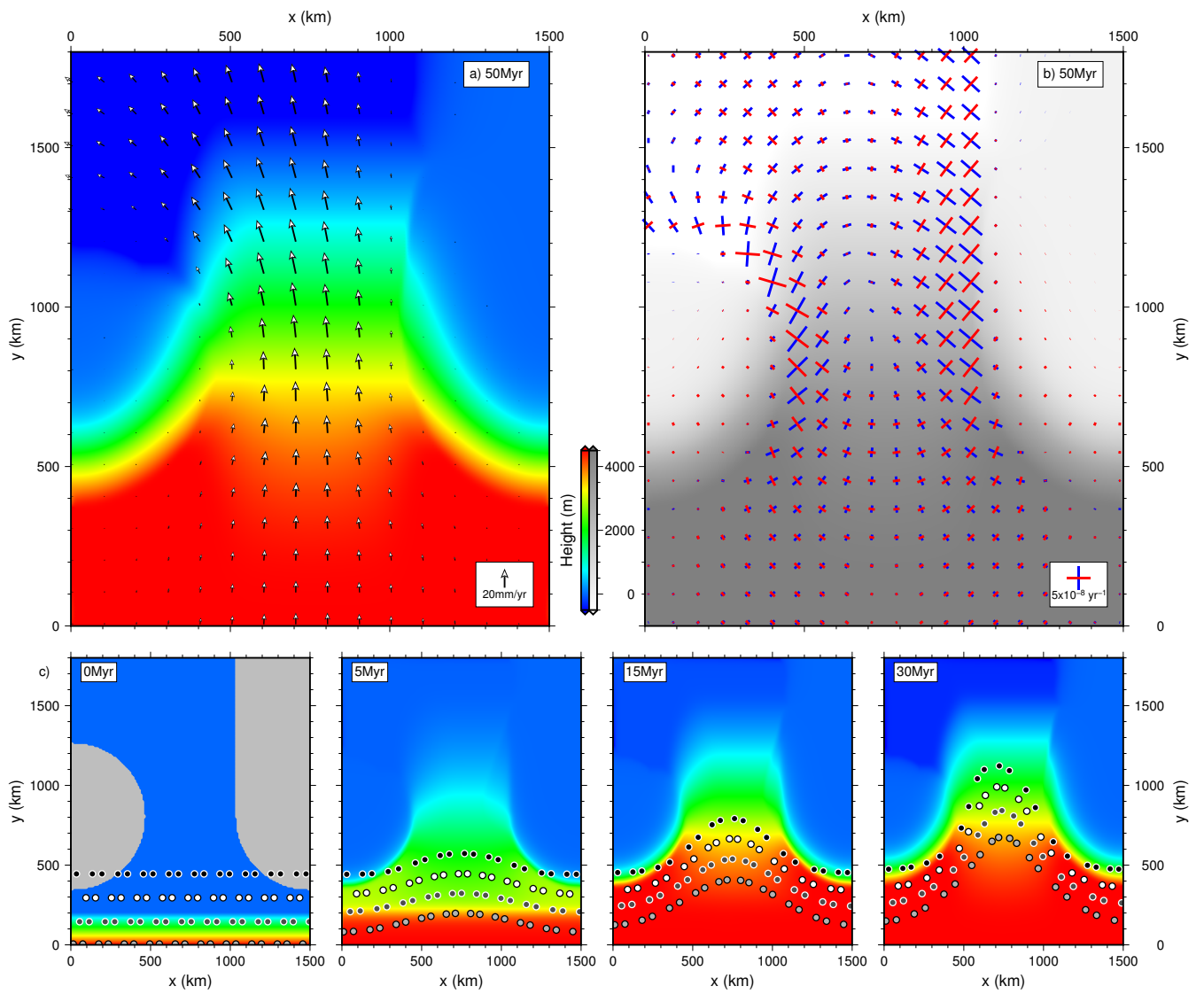


Figure 6.8: Modelling results for an asymmetric model set-up with 15 km basal thickness in the regions shown in grey in the 0 Myr panel of c. Panels are as for Figure 6.5.

Shan and the Mesozoic deformation front adjacent to the Sichuan Basin (Yong et al., 2003; Richardson et al., 2008) could, therefore, result from erosion acting on topography which would otherwise be propagating over the basin. The Longmen Shan lies at the intersection of two major moisture sources, the Westerlies and the East Asian Monsoon (Xu et al., 2014), so high precipitation likely contributes to the high-erosion rates, as do earthquake-induced landslides (Li et al., 2017).

The gentle topographic slopes in the inter-basin region (Figure 6.2) are consistent with the topography developed by flow over a stress-free base (e.g. England and McKenzie, 1982; Flesch et al., 2001, Figures 6.6 b, d, f). The results of particle tracking show that material at the surface where the crust flows over a stress-free base may be transported long distances (hundreds of kilometres over millions of years for the viscosity used here). An important question is how finite deformation in a viscous layer can be achieved at the surface by brittle deformation, which is neglected in the continuum modelling approach used here. The deeply eroded river valleys of South East Tibet can obscure indicators of active faulting and offset features, making it difficult to estimate the total offset across the many strike-slip faults in the region. However, where total offsets have been reported they are 10s km over ~ 10 Myr (e.g. Wang et al., 1998), suggesting that 100s km of lateral motion are possible on the much longer timescales of topographic evolution in my model. The elevations of the particles with time, shown in Figure 6.5d, shows that uplift rates from my model are ~ 0.1 – 0.5 mm/yr in the centre of the inter-basin region (yellow square in Figure 6.5d), similar to the 0.2 mm/yr uplift rate for the Jianchuan basin region (region 4 in Figure 6.3). However, the advection of the particles with the flow means that elevation histories may be complex, with particle elevations decreasing in the region south (towards $y = y_{max}$) of the inter-basin region as the current spreads laterally (the same effect leads to extensional strain rates perpendicular to the topographic gradient, discussed below). Altitude histories may be further complicated by the effects of erosion on the rate of advection, discussed above. Lateral transport complicates both the conversion of carbonate isotopic data to palaeoaltitude (possibly requiring greater continentality corrections – see Section 6.3) and the interpretation of such elevations. Calculated palaeoaltitudes give information about the height of the sample at the time of deposition, rather than the height of its present-day location. For example, pedogenic carbonates which are found to have been high in the late Eocene-early Miocene (Hoke et al., 2014; Li et al., 2015; Gourbet et al., 2017) could have been at similar latitudes to samples from the Longmen Shan, which had attained their present elevation by the late Miocene (Xu et al., 2016). Such lateral transport could explain the pre-Eocene high elevations found by Tang et al. (2017) for material near to the Central Tibetan plateau. This material may have been in the Central Plateau at the time of deposition. The ~ 1 km differences in elevation estimates associated with continentality corrections (Section 6.3) suggests that lateral transport of material could

have a significant effect on palaeoaltitude estimates.

In the following discussion I assume the style of strain-rate in my modelled fluid, represented by the principal axes of the horizontal strain-rate tensor, corresponds to brittle deformation at the surface (McKenzie and Jackson, 1983; England and Houseman, 1985). The opposite senses of lateral-shear adjacent to basin regions on opposite sides of the model domain are analogous to the opposite sense of shear adjacent to the Sichuan Basin and the Central Lowlands of Myanmar, accommodated by left-lateral slip on the Xianshuihe Fault and right-lateral slip on the Sagaing and Nujiang faults respectively. The broader region of shear adjacent to the extended basin region in my asymmetric model (Figure 6.8) is similar to the area of distributed left-lateral faulting east of the Sagaing fault (Figure 6.1a), which accommodates right-lateral shear through vertical axis rotations (Copley, 2008, Section 6.2). Whilst the likely reason for right-lateral \sim N–S shear being accommodated by conjugate left-lateral faults is still reactivation of pre-existing weaknesses (Copley, 2008), the lateral extent of this shear may be controlled by the geometry of the rigid lower crust in the Central Lowlands of Myanmar. A relatively low strain-rate region, equivalent to N–S right-lateral shear, also forms towards $y = y_{max}$ in the asymmetric model, where material is diverted towards $x = 0$ around the semi-circular basin. This feature is qualitatively similar to the Red River fault (Figure 6.1a), which is not on the boundary of a lateral rheology contrast but accommodates right-lateral shear at lower rates than the Sagaing Fault. The strain rates associated with shear where the flow is parallel to lateral rheology contrasts are higher than the extensional strain rates discussed below, which is consistent with the dominant observed faulting in South East Tibet being strike-slip. The rotation of velocities towards $x = 0$ which leads to this shear is similar to the trend in GPS velocities relative to Eurasia and South China south of the Sichuan Basin (Figure 6.2).

There are two extension-dominated regions within the models (Figures 6.5b and 6.8b), with similar locations and orientations to the two regions of normal faulting in South East Tibet (red circles and focal mechanisms in Figure 6.1b). The region in which extension is in the y direction is comparable to the north-western region of normal-faults, which strike perpendicular to the topographic gradient (accommodating extension parallel to the topographic gradient). In South East Tibet this region of normal faulting is associated with an increase in topographic gradient at the edge of the inter-basin region. My modelling suggests that the increase in topographic gradient may result from faster velocities in the inter-basin region, as the region through which material can flow is narrower. This is consistent with the suggestion of Copley (2008) that the increase in topographic gradient adjacent to the inter-basin region leads to an increase in velocities, resulting in extension parallel to the maximum topographic gradient. The second region of extension in my model is perpendicular to topographic gradients and

occurs south (towards $y = y_{max}$) of the basin regions. This region is similar to the southern group of normal faults shown in Figure 6.1, which strike \sim NW-SE, sub-parallel to the south-eastwards topographic gradients (accommodating extension perpendicular to the topographic gradient). In my model this extension results from the flow, which was constrained laterally in the inter-basin region, diverging in the region south (towards $y = y_{max}$) of the basin regions, such that the surface area of the current increases. Copley (2008) suggested the same mechanism for producing this normal faulting, based on modelling of the instantaneous strain-rate field.

My model allows me to reproduce the main features of the present day topography, strain-rate and velocity field in South East Tibet. This demonstrates that lateral rheology contrasts provide a first-order control on the temporal evolution of mountain ranges. This result is a generalisation of the finding of Reynolds et al. (2015) that varying basal boundary conditions can control the rate of propagation and shape of mountain ranges. Reynolds et al. suggested that the presence of stress-free basal regions could explain the form of the topography in the Sulaiman Ranges of Pakistan, which overlie a region of low viscosity sediment, and the embayments of the Zagros mountains, which are thought to be associated with the presence or absence of evaporites (Nissen et al., 2011). By improving the method for solving the temporal evolution equations I have generalised this result to show that rigid regions in a Newtonian fluid lead to first-order variations in the temporal evolution of topography. In thin-viscous-sheet models, where the base of the flow is stress-free, steep topographic gradients can only be produced by using a power-law rheology with a high stress exponent (usually 10 England and Houseman, 1986). Stress exponents of 3 or greater suggest that viscous deformation in the lower crust occurs by dislocation creep (e.g. Bürgmann and Dresen, 2008). My modelling demonstrates that viscous deformation by diffusion creep, which has a Newtonian rheology, can also produce steep topographic gradients where flow occurs over a rigid base, such as relatively strong lower crust. Steep-fronted mountain ranges do not, therefore, constrain whether flow in the ductile part of the lithosphere occurs by diffusion or dislocation creep.

The result that lateral rheology contrasts can explain variations in the shape and temporal-evolution of mountain ranges has general application outside South East Tibet. The relatively small amount of deformation in India as a result of the India-Eurasia collision is a major feature of the region (e.g. Tapponnier and Molnar, 1976). My modelling demonstrates that, as well as explaining the present-day velocity field (Copley et al., 2011b), the flow of weaker Tibetan material over rigid Indian material (Craig et al., 2012) can lead to the steep-fronted topography which characterises the southern margin of Tibet, even if the basal boundary in Northern Tibet is stress-free. Further north, the Tarim Basin has experienced little internal deformation as a result of the India-Eurasia collision (e.g. Molnar and Tapponnier, 1975;

Matte et al., 1996; Zheng et al., 2017), although deformation associated with the collision continues to the north in the Tien Shan. The steep topographic gradients adjacent to this basin (~ 3 km over 50 km) and the low rate of shortening (0–3 mm/yr, e.g. Zheng et al., 2017) across the basin margin are similar to those in the Longmen Shan. The western edge of the Tarim Basin is thought to underthrust the western Kunlun ranges (e.g. as demonstrated by flexure of the basin, Matte et al., 1996), which would provide a rigid base to the flow of crustal material from northern Tibet, in a similar manner to the Sichuan Basin in South East Tibet. The results of my modelling therefore suggest that the temporal evolution of topography adjacent to the Tarim Basin may also result from the lateral rheology contrast, proposed by Ainscoe et al. (2017), between rigid crust in the Tarim basin and lower viscosity crust in Tibet.

The dependence of how far a current propagates into a region with a rigid base on the thickness of the layer it flows into, is also applicable to the Bolivian Andes. The occurrence of thin-skinned deformation of sediments above the edges of the South American craton in the foothills of the Eastern Cordillera suggests that the deformation in this region is comparable to flow over a rigid base (Lamb, 2000). The lateral extent of the foothills in the southern Bolivian Andes is much greater than that in the north, with lower topographic gradients. This broader foothill region correlates with higher sediment thicknesses in the bounding basin (McGroder et al., 2014), analogous to the result from my modelling that a current flowing into a thicker deformable layer over a rigid base propagates further (Figure 6.6c and e).

More generally, the control on topographic evolution provided by lateral rheology contrasts suggests an explanation for the correlation of cratonic regions with the edges of mountain belts (including the Atlas mountains, the Caucasus and older orogenies such as the Appalachians and Rockies in North America) noted by McKenzie and Priestley (2008). Cratonic regions are likely to have relatively strong lower crust (e.g. Jackson et al., 2008), so propagation of topography into these regions will be slow in comparison to adjacent regions where the lower crust has lower viscosity. Although such regions are commonly associated with thick lithosphere (McKenzie and Priestley, 2008), it is the rigid lower crust, rather than the lithospheric thickness, which provides the lateral rheology contrast likely to control the extent of mountain ranges, explaining why the correlation is with the edge of cratons rather than thick lithosphere.

6.6 Conclusions

By implementing a stable method for calculating the temporal evolution of topography in a large-scale, gravity-driven viscous fluid, I have investigated the role of lateral rheology contrasts in controlling the shape and evolution of mountain ranges. The model described above allows me to reproduce the main features of the present day topography, strain-rate and velocity field in South East Tibet. This suggests that lateral rheology contrasts provide a first-order control on the temporal evolution and shape of mountain ranges, and provides an explanation for the correlation between cratonic regions and the shape of mountain ranges. In South East Tibet stable-isotope palaeoaltimetry suggests that parts of the topography may have been at or near their present-day elevations since the late Eocene and that uplift is likely to have occurred more slowly than had previously been inferred. My models demonstrate that flow in a low-viscosity, lower-crustal channel is not required to produce these uplift rates, and that lateral rheology contrasts are sufficient to explain first-order features of the deformation and topography in South East Tibet.

Chapter 7

Concluding remarks

This dissertation has investigated the kinematics and dynamics of continental deformation. Although the studies presented here are geographically specific, they illustrate principles which are globally applicable in the context of continental deformation, which I discuss below.

In Chapter 2 I studied the source parameters and slip distribution of the 2013 Minab earthquake. This earthquake was a left-lateral strike-slip event and occurred on an ENE–WSW striking fault approximately perpendicular to previously mapped faults in the region. I suggested that this fault, and other nearby left-lateral faults with geomorphic expression, accommodate a regional velocity field equivalent to right-lateral shear on N–S striking planes by rotating clockwise about vertical axes. The accommodation of this velocity field by vertical axis rotations demonstrates that knowledge of the velocity field alone is not sufficient to understand the kinematics of continental deformation. This principle was also demonstrated in Chapter 4, where the accommodation of right-lateral motion at the south end of the Sistan Suture Zone is discussed, and I put forward a new proposal for how it is achieved, consistent with all the available observations.

The strike-slip earthquakes I have discussed within the Makran accretionary prism likely reactivated pre-existing structures; as discussed in Chapters 2 and 5. Such reactivation suggests that the pre-existing weaknesses are important in determining how the velocity field is accommodated by faulting. Since accretionary prisms are formed by the consolidation of sediment within subduction zones, faults within them are formed during prism growth. This makes it possible to resolve temporal variations in the style of strain in a way which might be less clear in a continent–continent collision, in which pre-existing weaknesses could be inherited from any previous phase of deformation. Strike-slip faulting within the Makran accretionary prism, therefore allows me to infer a change in the style of strain within the

accretionary prism with time (discussed in Chapter 5). This demonstrates that the style of strain in accretionary prisms can change without the need to change the basal boundary condition (Davis et al., 1983) or the strength of the material entering the prism (Craig and Copley, 2018), although for gravity to become dominant over compressional forces, rather than in balance as at present, would require such a change (England and Houseman, 1988).

The balance between gravitational and compressive forces in the Makran accretionary prism allowed me to calculate the range of possible shear stresses and effective coefficients of friction on the subduction interface. The values I obtain are similar to those from other subduction zones globally (e.g. Lamb, 2006; Duarte et al., 2015), suggesting that the large sediment thicknesses in the Makran do not substantially alter the mechanical properties of the megathrust. This finding is consistent with similar, low (<0.3) coefficients of friction which have been determined for intraplate faults (Copley et al., 2011b; Copley, 2018), where overpressured sediment is not available to reduce the coefficient of friction. Importantly, however, I also demonstrated in Chapter 3 that the megathrust in the western Makran is likely to be accumulating elastic strain, so may move in large earthquakes. The observation that low coefficients of friction do not necessarily correspond to aseismic sliding is an important one in terms of understanding the mechanics of faults, and has implications for the wide spectrum of slip behaviours now being observed on subduction megathrusts (e.g. Wang and Dixon, 2004; Peng and Gomberg, 2010).

In Chapter 4 I demonstrated that the strain within accretionary prisms may be time-dependent on the timescale of the megathrust seismic cycle, as well as that of prism growth. This time dependence is consistent with recent observations of normal-faulting aftershocks in the overriding plate after megathrust earthquakes (e.g. Asano et al., 2011), and is important for seismic hazard, as well as for understanding the mechanics of faulting. Of particular relevance for continental deformation is the observation that, in addition to generating the highest magnitude earthquakes globally, subduction megathrusts may also control the style and timing of earthquakes in the adjacent continents, closest to populations and on distributed faults, so their relevance to continental deformation should not be dismissed (c.f. Jackson et al., 2002).

In Chapter 6 I showed that lateral rheology contrasts, analogous to those between the Sichuan Basin, the Central Lowlands of Myanmar and the rapidly deforming regions around them, can reproduce first-order features of the topography, GPS velocity field and earthquake-derived strain rates in South East Tibet. Uplift rates of <0.2 mm/yr from stable-isotope palaeoaltimetry demonstrate that there is no low-viscosity, lower-crustal channel in South East Tibet. My modelling suggests that where particles are advected with a flow they may have

complex altitude histories, rather than simply becoming and staying high, as has previously been assumed. Palaeoaltimetric measurements should, therefore, be interpreted as estimates of the altitude at which samples were deposited. The potential for long distance lateral transport of rocks within gravity-dominated mountain ranges is also important in the interpretation of such data. My results suggest that lateral rheology contrasts provide a first-order control on the temporal evolution of mountain belts. These results emphasise my findings from a subduction setting that lateral rheology contrasts and pre-existing weaknesses play an important role in continental deformation.

References

- Acton, C. E., Priestley, K., Gaur, V. K., and Rai, S. S. (2010). Group velocity tomography of the Indo-Eurasian collision zone. *J. Geophys. Res. Solid Earth*, 115:B12335. doi:10.1029/2009JB007021.
- Ainscoe, E. A., Elliott, J. R., Copley, A., Craig, T. J., Li, T., Parsons, B. E., and Walker, R. T. (2017). Blind Thrusting, Surface Folding and the Development of Geological Structure in the Mw 6.3 2015 Pishan (China) Earthquake. *J. Geophys. Res. Solid Earth*, 122:9359–9382. doi:10.1002/2017JB014268.
- Allen, M., Jackson, J., and Walker, R. (2004). Late Cenozoic reorganization of the Arabia-Eurasia collision and the comparison of short-term and long-term deformation rates. *Tectonics*, 23:TC2008. doi:10.1029/2003TC001530.
- Ambraseys, N. N. and Melville, C. P. (1982). *A history of Persian earthquakes*. Cambridge University Press.
- Argand, É. (1924). La tectonique de l'Asie. *Proc. 13th Int. Geol. Cong.*, pages 171–372.
- Aron, F., Allmendinger, R. W., Cembrano, J., González, G., and Yáñez, G. (2013). Permanent fore-arc extension and seismic segmentation: Insights from the 2010 Maule earthquake, Chile. *J. Geophys. Res. Solid Earth*, 118:724–739. doi:10.1029/2012JB009339.
- Arriagada, C., Arancibia, G., Cembrano, J., Martínez, F., Carrizo, D., Van Sint Jan, M., Sáez, E., González, G., Rebolledo, S., Sepúlveda, S. A., Contreras-Reyes, E., Jensen, E., and Yáñez, G. (2011). Nature and tectonic significance of co-seismic structures associated with the Mw 8.8 Maule earthquake, central-southern Chile forearc. *J. Struct. Geol.*, 33:891–897. doi:10.1016/j.jsg.2011.03.004.
- Arrian (100). 6.24.1-6.26.5. In *Anabasis*, pages 6.24.1–6.26.5.
- Asano, Y., Saito, T., Ito, Y., Shiomi, K., Hirose, H., Matsumoto, T., Aoi, S., Hori, S., and Sekiguchi, S. (2011). Spatial distribution and focal mechanisms of aftershocks of the 2011 off the Pacific coast of Tohoku Earthquake. *Earth, Planets Sp.*, 63:669–673. doi:10.5047/eps.2011.06.016.
- Atwater, B. F. (1987). Evidence for great Holocene earthquakes along the outer coast of Washington state. *Science*, 236(4804):942–944. doi:10.1126/science.236.4804.942.
- Aubourg, C., Smith, B., Bakhtari, H. R., Guya, N., and Eshraghi, A. (2008). Tertiary block rotations in the Fars Arc (Zagros, Iran). *Geophys. J. Int.*, 173:659–673. doi:10.1111/j.1365-246X.2008.03732.x.

- Avouac, J.-P., Ayoub, F., Wei, S., Ampuero, J.-P., Meng, L., Leprince, S., Jolivet, R., Duputel, Z., and Helmberger, D. (2014). The 2013, Mw 7.7 Balochistan earthquake, energetic strike-slip reactivation of a thrust fault. *EPSL*, 391:128–134. doi:10.1016/j.epsl.2014.01.036.
- Avouac, J. P., Tapponnier, P., Bai, M., You, H., and Wang, G. (1993). Active Thrusting and Folding Along the Northern Tien Shan and Late Cenozoic Rotation of the Tarim Relative to Dzungaria and Kazakhstan. *JGR*, 98(B4):6755–6804. doi:10.1029/92JB01963.
- Bai, L., Li, G., Khan, N. G., Zhao, J., and Ding, L. (2017). Focal depths and mechanisms of shallow earthquakes in the Himalayan–Tibetan region. *Gondwana Res.*, 41:390–399. doi:10.1016/j.gr.2015.07.009.
- Baker, A., Allmendinger, R. W., Owen, L. A., and Rech, J. A. (2013). Permanent deformation caused by subduction earthquakes in northern Chile. *Nat. Geosci.*, 6:492–496. doi:10.1038/ngeo1789.
- Baker, C. (1993). *The Active Seismicity and Tectonics of Iran*. PhD thesis, University of Cambridge.
- Barnhart, W., Briggs, R., Reitman, N., Gold, R., and Hayes, G. (2015). Evidence for slip partitioning and bimodal slip behavior on a single fault: Surface slip characteristics of the 2013 Mw7.7 Balochistan, Pakistan earthquake. *EPSL*, 420:1–11. doi:10.1016/j.epsl.2015.03.027.
- Barnhart, W., Hayes, G., Briggs, R., Gold, R., and Bilham, R. (2014a). Ball-and-socket tectonic rotation during the 2013 Mw 7.7 Balochistan earthquake. *EPSL*, 403:210–216. doi:10.1016/j.epsl.2014.07.001.
- Barnhart, W. D., Hayes, G. P., Samsonov, S. V., Fielding, E. J., and Seidman, L. E. (2014b). Breaking the oceanic lithosphere of a subducting slab: The 2013 Khash, Iran earthquake. *Geophys. Res. Lett.*, 41:32–36. doi:10.1002/2013GL058096.
- Bayasgalan, A., Jackson, J., Ritz, J., and Carretier, S. (1999a). Field examples of strike-slip fault terminations in Mongolia and their tectonic significance. *Tectonics*, 18(3):394–411. doi:10.1029/1999TC900007.
- Bayasgalan, A., Jackson, J., Ritz, J. F., and Carretier, S. (1999b). ‘Forebergs’, flower structures, and the development of large intracontinental strike-slip faults: The Gurvan Bogd fault system in Mongolia. *J. Struct. Geol.*, 21:1285–1302. doi:10.1016/S0191-8141(99)00064-4.
- Bayer, R., Chery, J., Tatar, M., Vernant, P., Abbassi, M., Masson, F., Nilforoushan, F., Doerflinger, E., Regard, V., and Bellier, O. (2006). Active deformation in Zagros-Makran transition zone inferred from GPS measurements. *Geophys. J. Int.*, 165:373–381. doi:10.1111/j.1365-246X.2006.02879.x.
- Berberian, M. (1981). Active faulting and Tectonics of Iran. *Zagros, Hindu Kush Himalaya Geodynamic Evolution Series*, 3:33–72. doi:10.1017/CBO9781107415324.004.
- Berberian, M., Jackson, J., Qorashi, M., Khatib, M. M., Priestley, K., Talebian, M., and Ghafuri-Ashtiani, M. (1999). The 1997 May 10 Zirkuh (Qa’enat) earthquake (Mw 7.2): faulting along the Sistan suture zone of eastern Iran. *Geophys. J. Int.*, 136:671–694. doi:10.1046/j.1365-246x.1999.00762.x.
- Berberian, M., Jackson, J., Qorashi, M., Talebian, M., Khatib, M., and Priestley, K. (2000). The 1994 Sefidabeh earthquakes in eastern Iran: blind thrusting and bedding-plane slip on a growing anticline, and active tectonics of the Sistan suture zone. *Geophys. J. Int.*, 142:283–299. doi:10.1046/j.1365-246x.2000.00158.x.

- Berberian, M., Jackson, J. A., Fielding, E., Parsons, B. E., Priestley, K., Qorashi, M., Talebian, M., Walker, R., Wright, T. J., and Baker, C. (2001). The 1998 March 14 Fandoqa earthquake (Mw 6.6) in Kerman province, Southeast Iran: Re-rupture of the 1981 Sirch earthquake fault, triggering of slip on adjacent thrusts and the active tectonics of the Gowk fault zone. *Geophys. J. Int.*, 146:371–398. doi:10.1046/j.1365-246X.2001.01459.x.
- Bershaw, J., Penny, S. M., and Garzione, C. N. (2012). Stable isotopes of modern water across the Himalaya and eastern Tibetan Plateau: Implications for estimates of paleoelevation and paleoclimate. *J. Geophys. Res. Atmos.*, 117:D02110. doi:10.1029/2011JD016132.
- Biabangard, H. and Moradian, A. (2008). Geology and geochemical evaluation of Taftan Volcano, Sistan and Baluchestan Province, southeast of Iran. *Chinese J. Geochemistry*, 27:356–369. doi:10.1007/s11631-008-0356-z.
- Bilham, R., Lodi, S., and Hough, S. (2007). Seismic hazard in Karachi, Pakistan: uncertain past, uncertain future. *Seismol. Res. Lett.*, 78(6):601–613. doi:10.1785/gssrl.78.6.601.
- Bouchon, M., Marsan, D., Durand, V., Campillo, M., Perfettini, H., Madariaga, R., and Gardonio, B. (2016). Potential slab deformation and plunge prior to the Tohoku, Iquique and Maule earthquakes. *Nat. Geosci.*, 9:380–384. doi:10.1038/ngeo2701.
- Bröcker, M., Fotoohi Rad, G., Burgess, R., Theunissen, S., Paderin, I., Rodionov, N., and Salimi, Z. (2013). New age constraints for the geodynamic evolution of the Sistan Suture Zone, eastern Iran. *Lithos*, 170-171:17–34. doi:10.1016/j.lithos.2013.02.012.
- Burchfiel, B., Royden, L., van der Hilst, R., Hager, B., Chen, Z., King, R., Li, C., Lü, J., Yao, H., and Kirby, E. (2008). A geological and geophysical context for the Wenchuan earthquake of 12 May 2008, Sichuan, People’s Republic of China. *GSA Today*, 18(7):4. doi:10.1130/GSATG18A.1.
- Burchfiel, B. C., Zhiliang, C., Yupinc, L., and Royden, L. H. (1995). Tectonics of the Longmen Shan and Adjacent Regions, Central China. *Int. Geol. Rev.*, 37(8):661–735. doi:10.1080/00206819509465424.
- Bürgmann, R. and Dresen, G. (2008). Rheology of the Lower Crust and Upper Mantle: Evidence from Rock Mechanics, Geodesy, and Field Observations. *Annu. Rev. Earth Planet. Sci.*, 36:531–567. doi:10.1146/annurev.earth.36.031207.124326.
- Byrne, D. E., Sykes, L. R., and Davis, D. M. (1992). Great thrust earthquakes and aseismic slip along the plate boundary of the Makran subduction zone. *JGR*, 97(B1):449–478. doi:10.1029/91JB02165.
- Campbell, G. E., Walker, R. T., Abdrakhmatov, K., Schwenninger, J., Jackson, J., Elliott, J. R., and Copley, A. (2013). The Dzhungarian fault: Late Quaternary tectonics and slip rate of a major right-lateral strike-slip fault in the northern Tien Shan region. *J. Geophys. Res. Solid Earth*, 118:5681–5698. doi:10.1002/jgrb.50367.
- Chandra, U. (1981). Focal mechanism solutions and their tectonic implications for the Eastern Alpine-Himalayan region. *Zagros, Hindu Kush, Himalaya Geodynamic Evolution Series*, 3:243–271.
- Chandra, U. (1984). Focal mechanism solutions for earthquakes in Iran. *Phys. Earth Planet Inter.*, 34:9–16.

- Chlieh, M., Avouac, J. P., Sieh, K., Natawidjaja, D. H., and Galetzka, J. (2008). Heterogeneous coupling of the Sumatran megathrust constrained by geodetic and paleogeodetic measurements. *JGR*, 113:B05305. doi:10.1029/2007JB004981.
- Clark, M. K., Bush, J. W., and Royden, L. H. (2005a). Dynamic topography produced by lower crustal flow against rheological strength heterogeneities bordering the Tibetan Plateau. *Geophys. J. Int.*, 162:575–590. doi:10.1111/j.1365-246X.2005.02580.x.
- Clark, M. K., House, M. A., Royden, L. H., Whipple, K. X., Burchfiel, B. C., Zhang, X., and Tang, W. (2005b). Late Cenozoic uplift of southeastern Tibet. *Geology*, 33(6):525–528. doi:10.1130/G21265.1.
- Clark, M. K. and Royden, L. H. (2000). Topographic ooze: Building the eastern margin of Tibet by lower crustal flow. *Geology*, 28(8):703–706. doi:10.1130/0091-7613(2000)28<703:Tobtem>2.0.Co;2.
- Clark, M. K., Royden, L. H., Whipple, K. X., Burchfiel, B. C., Zhang, X., and Tang, W. (2006). Use of a regional, relict landscape to measure vertical deformation of the eastern Tibetan Plateau. *J. Geophys. Res. Earth Surf.*, 111:F03002. doi:10.1029/2005JF000294.
- Clark, M. K., Schoenbohm, L. M., Royden, L. H., Whipple, K. X., Burchfiel, B. C., Zhang, X., Tang, W., Wang, E., and Chen, L. (2004). Surface uplift, tectonics, and erosion of eastern Tibet from large-scale drainage patterns. *Tectonics*, 23:TC1006. doi:10.1029/2002TC001402.
- Conrad, G., Montigny, R., Thuizat, R., and Westphal, M. (1981). Tertiary and Quaternary geodynamics of southern Lut (Iran) as deduced from palaeomagnetic, isotopic and structural data. *Tectonophysics*, 75:T11–T17. doi:10.1016/0040-1951(81)90272-9.
- Copley, A. (2008). Kinematics and dynamics of the southeastern margin of the Tibetan Plateau. *Geophys. J. Int.*, 174:1081–1100. doi:10.1111/j.1365-246X.2008.03853.x.
- Copley, A. (2012). The formation of mountain range curvature by gravitational spreading. *EPSL*, 351-352:208–214. doi:10.1016/j.epsl.2012.07.036.
- Copley, A. (2018). The strength of earthquake-generating faults. *J. Geol. Soc. London.*, 175:1–12. doi:10.1144/jgs2017-037.
- Copley, A., Avouac, J. P., Hollingsworth, J., and Leprince, S. (2011a). The 2001 Mw 7.6 Bhuj earthquake, low fault friction, and the crustal support of plate driving forces in India. *J. Geophys. Res. Solid Earth*, 116:B08405. doi:10.1029/2010JB008137.
- Copley, A., Avouac, J.-P., and Wernicke, B. P. (2011b). Evidence for mechanical coupling and strong Indian lower crust beneath southern Tibet. *Nature*, 472:79–81. doi:10.1038/nature09926.
- Copley, A., Boait, F., Hollingsworth, J., Jackson, J., and McKenzie, D. (2009). Subparallel thrust and normal faulting in Albania and the roles of gravitational potential energy and rheology contrasts in mountain belts. *J. Geophys. Res. Solid Earth*, 114:B05407. doi:10.1029/2008JB005931.
- Copley, A. and Jackson, J. (2006). Active tectonics of the Turkish-Iranian Plateau. *Tectonics*, 25:TC6006. doi:10.1029/2005TC001906.
- Copley, A. and McKenzie, D. (2007). Models of crustal flow in the India-Asia collision zone. *Geophys. J. Int.*, 169:683–698. doi:10.1111/j.1365-246X.2007.03343.x.

- Copley, A., Mitra, S., Sloan, R. A., Gaonkar, S., and Reynolds, K. (2014). Active faulting in apparently stable peninsular India: Rift inversion and a Holocene-age great earthquake on the Tapti Fault. *J. Geophys. Res. B Solid Earth*, 119(8):6650–6666. doi:10.1002/2014JB011294.
- Craig, T. and Copley, A. (2018). Forearc collapse, plate flexure, and seismicity within the downgoing plate along the Sunda Arc west of Sumatra. *EPSL*, 484:81–91. doi:10.1016/j.epsl.2017.12.004.
- Craig, T. J., Copley, A., and Jackson, J. (2012). Thermal and tectonic consequences of India underthrusting Tibet. *EPSL*, 353-354:231–239. doi:10.1016/j.epsl.2012.07.010.
- Craig, T. J., Copley, A., and Jackson, J. (2014a). A reassessment of outer-rise seismicity and its implications for the mechanics of oceanic lithosphere. *Geophys. J. Int.*, 197:63–89. doi:10.1093/gji/ggu013.
- Craig, T. J., Copley, A., and Middleton, T. A. (2014b). Constraining fault friction in oceanic lithosphere using the dip angles of newly-formed faults at outer rises. *EPSL*, 392:94–99. doi:10.1016/j.epsl.2014.02.024.
- D’Agostino, N., England, P., Hunstad, I., and Selvaggi, G. (2014). Gravitational potential energy and active deformation in the Apennines. *EPSL*, 397:121–132. doi:10.1016/j.epsl.2014.04.013.
- Dahlen, F. A., Suppe, J., and Davis, D. (1984). Mechanics of fold-and-thrust belts and accretionary wedges: Cohesive Coulomb theory. *JGR*, 89(B12):10087–10101. doi:10.1029/JB089iB12p10087.
- Dansgaard, W. (1964). Stable isotopes in precipitation. *Tellus*, 16(4):436–468. doi:10.3402/tellusa.v16i4.8993.
- Davis, D., Suppe, J., and Dahlen, F. A. (1983). Mechanics of fold-and-thrust belts and accretionary wedges. *JGR*, 88(B2):1153–1172. doi:10.1029/JB088iB02p01153.
- Dolati, A. (2010). *Stratigraphy, structural geology and low-temperature thermochronology across the Makran accretionary wedge in Iran*. PhD thesis, ETH Zurich.
- Duarte, J. C., Schellart, W. P., and Cruden, A. R. (2015). How weak is the subduction zone interface? *Geophys. Res. Lett.*, 42:2664–2673. doi:10.1002/2014GL062876.
- Dufrénoy, A. and de Beaumont, L. É. (1833). Mémoire sur les groupes du Cantal, du Mont-Dore, et sur les soulèvements auxquels ces montagnes doivent leur relief actuel. In *Ann. des mines*. Carilian-Goeury, Paris, iii edition.
- Dugda, M. T., Nyblade, A. A., and Julia, J. (2007). Thin lithosphere beneath the Ethiopian Plateau revealed by a joint inversion of Rayleigh wave group velocities and receiver functions. *J. Geophys. Res. Solid Earth*, 112:B08305. doi:10.1029/2006JB004918.
- Dykstra, J. D. and Birnie, R. W. (1979). Segmentation of the Quaternary Subduction Zone under the Baluchistan Region of Pakistan and Iran. In Farah, A. and DeJong, K. A., editors, *Geodynamics of Pakistan*, pages 319–323. Geological Survey of Pakistan.
- Dziewonski, A. M., Chou, T., and Woodhouse, J. H. (1981). Determination of earthquake source parameters from waveform data for studies of global and regional seismicity. *JGR*, 86(B4):2825–2852. doi:10.1029/JB086iB04p02825.

- Ebel, J. E., Bonjer, K.-P., and Oncescu, M. (2000). Paleoseismicity: Seismicity evidence for past large earthquakes. *Seismol. Res. Lett.*, 71(2):283–294. doi:10.1785/gssrl.71.2.283.
- Ekström, G., Nettles, M., and Dziewoński, A. M. (2012). The global CMT project 2004-2010: Centroid-moment tensors for 13,017 earthquakes. *Phys. Earth Planet Inter.*, 200-201:1–9. doi:10.1016/j.pepi.2012.04.002.
- Ellouz-Zimmermann, N., Deville, E., Müller, C., Lallemand, S., Subhani, A., and Tabreez, A. (2007). Impact of sedimentation on convergent margin tectonics: Example of the Makran accretionary prism (Pakistan). In *Thrust Belts and Foreland Basins*, chapter 17, pages 327–350. Springer Berlin Heidelberg.
- Engdahl, E. R., Jackson, J., Myers, S., Bergman, E., and Priestley, K. (2006). Relocation and assessment of seismicity in the Iran region. *Geophys. J. Int.*, 167:761–778. doi:10.1111/j.1365-246X.2006.03127.x.
- Engdahl, E. R., van der Hilst, R., and Buland, R. (1998). Global teleseismic earthquake relocation with improved travel times and procedures for depth determination. *Bull. Seismol. Soc. Am.*, 88(3):722–743.
- England, P., Engdahl, R., and Thatcher, W. (2004). Systematic variation in the depths of slabs beneath arc volcanoes. *Geophys. J. Int.*, 156:377–408. doi:10.1111/j.1365-246X.2003.02132.x.
- England, P. and Houseman, G. (1985). Role of lithospheric strength heterogeneities in the tectonics of Tibet and neighbouring regions. *Nature*, 315:297–301. doi:10.1038/314141a0.
- England, P. and Houseman, G. (1986). Finite strain calculations of continental deformation: 2. Comparison with the India-Asia Collision Zone. *J. Geophys. Res. Solid Earth*, 91(B3):3664–3676. doi:10.1029/JB091iB03p03664.
- England, P. and Jackson, J. (1989). Active Deformation Of The Continents. *Annu. Rev. Earth Planet. Sci.*, 17:197–226. doi:10.1146/annurev.earth.17.1.197.
- England, P. and Jackson, J. (2011). Uncharted seismic risk. *Nat. Geosci.*, 4(6):348–349. doi:10.1038/ngeo1168.
- England, P. and McKenzie, D. (1982). A thin viscous sheet model for continental deformation. *Geophys. J. Int.*, 70:295–321. doi:10.1111/j.1365-246X.1982.tb04969.x.
- England, P. and Wilkins, C. (2004). A simple analytical approximation to the temperature structure in subduction zones. *Geophys. J. Int.*, 159:1138–1154. doi:10.1111/j.1365-246X.2004.02419.x.
- England, P. C. and Houseman, G. A. (1988). The mechanics of the Tibetan Plateau. *Philos. Trans. R. Soc. London*, 326:301–320. doi:10.1098/rsta.1988.0089.
- Falcon, N. (1974). An outline of the geology of the Iranian Makran. *Geographical Journal*, 140(2):284–291. <http://www.jstor.org/stable/1797086>.
- Fariás, M., Comte, D., Roecker, S., Carrizo, D., and Pardo, M. (2011). Crustal extensional faulting triggered by the 2010 Chilean earthquake: The Pichilemu Seismic Sequence. *Tectonics*, 30:TC6010. doi:10.1029/2011TC002888.
- Fielding, E. J. and McKenzie, D. (2012). Lithospheric flexure in the Sichuan Basin and Longmen Shan at the eastern edge of Tibet. *Geophys. Res. Lett.*, 39:L09311. doi:10.1029/2012GL051680.

- Flesch, L., Bendick, R., and Bischoff, S. (2018). Limitations on inferring 3D architecture and dynamics from surface velocities in the India-Eurasia collision zone. *Geophys. Res. Lett.*, 45:1379–1386. doi:10.1002/2017GL076503.
- Flesch, L. M., Haines, J. A., and Holt, W. E. (2001). Dynamics of the India-Eurasia Shortening. *JGR*, 106(B8):16,435–16,460. doi:10.1029/2001JB000208.
- Freund, R. (1970). Rotation of strike slip faults in Sistan, southeast Iran. *The Journal of Geology*, 78(2):188–200. <http://www.jstor.org/stable/30063787>.
- Frey Mueller, J., King, N., and Segall, P. (1994). The co-seismic slip distribution of the Landers earthquake. *Bull. Seismol. Soc. Am.*, 84(3):646–659.
- Frohling, E. and Szeliga, W. (2016). GPS constraints on interplate locking within the Makran subduction zone. *Geophys. J. Int.*, 205:67–76. doi:10.1093/gji/ggw001.
- Fruehn, J., White, R. S., and Minshull, T. A. (1997). Internal deformation and compaction of the Makran accretionary wedge. *Terra Nov.*, 9:101–104. doi:10.1046/j.1365-3121.1997.d01-13.x.
- Goldsworthy, M. and Jackson, J. (2001). Migration of activity within normal fault systems: Examples from the Quaternary of mainland Greece. *J. Struct. Geol.*, 23:489–506. doi:10.1016/S0191-8141(00)00121-8.
- Gourbet, L., Hervé, P., Paquette, J.-L., Sorrel, P., Maheo, G., Wang, G., Yadong, X., Cao, K., Antoine, P.-O., Eymard, I., Liu, W., Lu, H., Replumaz, A., Chevalier, M.-L., Kexin, Z., Jing, W., and Shen, T. (2017). Reappraisal of the Jianchuan Cenozoic basin stratigraphy and its implications on the SE Tibetan plateau evolution. *Tectonophysics*, 700-701:162–179. doi:10.1016/j.tecto.2017.02.007.
- Grützner, C., Walker, R. T., Abdrakhmatov, K. E., Mukambaev, A., Elliott, A. J., and Elliott, J. R. (2017). Active Tectonics Around Almaty and along the Zailisky Alatau Ranges. *Tectonics*, 36:2192–2226. doi:10.1002/2017TC004657.
- Haghipour, N. and Burg, J.-P. (2014). Geomorphological analysis of the drainage system on the growing Makran accretionary wedge. *Geomorphology*, 209:111–132. doi:10.1016/j.geomorph.2013.11.030.
- Haghipour, N., Burg, J.-P., Kober, F., Zeilinger, G., Ivy-Ochs, S., Kubik, P. W., and Faridi, M. (2012). Rate of crustal shortening and non-Coulomb behaviour of an active accretionary wedge: The folded fluvial terraces in Makran (SE, Iran). *EPSL*, 355-356:187–198. doi:10.1016/j.epsl.2012.09.001.
- Han, L., Cheng, J., An, Y., Fang, L., Jiang, C., Chen, B., Wu, Z., Liu, J., Xu, X., Liu, R., Yao, Z., Wang, C., and Wang, Y. (2018). Preliminary Report on the 8 August 2017 Ms 7.0 Jiuzhaigou, Sichuan, China, Earthquake. *Seismol. Res. Lett.*, 89(2A):557–569. doi:10.1785/0220170158.
- Han, L., Zeng, X., Jiang, C., Ni, S., Zhang, H., and Long, F. (2014). Focal Mechanisms of the 2013 Mw 6.6 Lushan, China Earthquake and High-Resolution Aftershock Relocations. *Seismol. Res. Lett.*, 85(1):8–14. doi:10.1785/0220130083.
- Harms, J. C., Cappel, H. N., and Francis, D. C. (1982). Geology and Petroleum Potential of the Makran Coast, Pakistan. *Offshore South East Asia 82 Conf.* doi:10.2118/10423-MS.

- Harrison, J. V. (1943). The Jaz Murian Depression, Persian Baluchistan. *Geographical Journal*, 101(5/6):206–225. <http://www.jstor.org/stable/1789627>.
- Heidarzadeh, M. and Kijko, A. (2011). A probabilistic tsunami hazard assessment for the Makran subduction zone at the northwestern Indian Ocean. *Nat. Hazards*, 56:577–593. doi:10.1007/s11069-010-9574-x.
- Herring, T., King, R., and McClusky, S. (2010). Documentation for the GAMIT/GLOBK GPS processing software release 10.4. Technical report, Mass. Inst. of Technol., Cambridge.
- Hicks, S. P. and Rietbrock, A. (2015). Seismic slip on an upper-plate normal fault during a large subduction megathrust rupture. *Nat. Geosci.*, 8:955–961. doi:10.1038/ngeo2585.
- Hoffmann, G., Grützner, C., Reicherter, K., and Preusser, F. (2015). Geo-archaeological evidence for a Holocene extreme flooding event within the Arabian Sea (Ras al Hadd, Oman). *Quat. Sci. Rev.*, 113:123–133. doi:10.1016/j.quascirev.2014.09.033.
- Hoffmann, G., Rupprechter, M., Balushi, N. A., Grützner, C., and Reicherter, K. (2013). The impact of the 1945 Makran tsunami along the coastlines of the Arabian Sea (Northern Indian Ocean) – a review. *Zeitschrift für Geomorphol. Suppl. Issues*, 57(4):257–277. doi:10.1127/0372-8854/2013/S-00134.
- Hoke, G. D., Liu-Zeng, J., Hren, M. T., Wissink, G. K., and Garzzone, C. N. (2014). Stable isotopes reveal high southeast Tibetan Plateau margin since the Paleogene. *EPSL*, 394:270–278. doi:10.1016/j.epsl.2014.03.007.
- Holt, W. E., Li, M., and Haines, A. J. (1995). Earthquake strain rates and instantaneous relative motions within central and eastern Asia. *Geophys. J. Int.*, 122:569–593. doi:10.1111/j.1365-246X.1995.tb07014.x.
- Houseman, G. and England, P. (1986). Finite strain calculations of continental deformation. 1. Method and general results for convergence zones. *J. Geophys. Res.*, 91(B3):3651–3663. doi:10.1029/JB091iB03p03651.
- Hren, M. T., Bookhagen, B., Blisniuk, P. M., Booth, A. L., and Chamberlain, C. P. (2009). $\delta^{18}\text{O}$ and δD of streamwaters across the Himalaya and Tibetan Plateau: Implications for moisture sources and paleoelevation reconstructions. *EPSL*, 288:20–32. doi:10.1016/j.epsl.2009.08.041.
- Huang, M. H., Bürgmann, R., and Freed, A. M. (2014). Probing the lithospheric rheology across the eastern margin of the Tibetan Plateau. *EPSL*, 396:88–96. doi:10.1016/j.epsl.2014.04.003.
- Hubbard, J. and Shaw, J. H. (2009). Uplift of the Longmen Shan and Tibetan plateau, and the 2008 Wenchuan ($M = 7.9$) earthquake. *Nature*, 458:194–197. doi:10.1038/nature07837.
- Hubbard, J., Shaw, J. H., and Klinger, Y. (2010). Structural setting of the 2008 Mw7.9 Wenchuan, China, earthquake. *Bull. Seismol. Soc. Am.*, 100(5B):2713–2735. doi:10.1785/0120090341.
- Huppert, H. E. (1982). The propagation of two-dimensional and axisymmetric viscous gravity currents over a rigid horizontal surface. *J. Fluid Mech.*, 121:43–58. doi:10.1017/S0022112082001797.
- Hyndman, R., Yamano, M., and Oleskevich, D. (1997). The Seismogenic Zone of Subduction Thrust Faults. *The Island Arc*, 6:244–260. doi:10.1785/gssrl.79.4.572.

- International Seismological Centre (2015). Online Bulletin. <http://www.isc.ac.uk>.
- Isacks, B. L. and Barazangi, M. (1977). Geometry of Benioff Zones: Lateral segmentation and downwards bending of the subducted lithosphere. In Talwani, M. and Pitman, W. C., editors, *Island Arcs, Deep Sea Trenches and Back-Arc Basins*, pages 99–114. doi:10.1029/ME001p0099.
- Jackson, J. (1980). Errors in focal depth determination and the depth of seismicity in Iran and Turkey. *Geophys. J. R. Astr. Soc.*, 61:285–301. doi:10.1111/j.1365-246X.1980.tb04318.x.
- Jackson, J., Bouchon, M., Fielding, E., Funning, G., Ghorashi, M., Hatzfeld, D., Nazari, H., Parsons, B., Priestley, K., Talebian, M., Tatar, M., Walker, R., and Wright, T. (2006). Seismotectonic, rupture process, and earthquake-hazard aspects of the 2003 December 26 Bam, Iran, earthquake. *Geophys. J. Int.*, 166:1270–1292. doi:10.1111/j.1365-246X.2006.03056.x.
- Jackson, J. and McKenzie, D. (1984). Active tectonics of the Alpine-Himalayan Belt between western Turkey and Pakistan. *Geophys. J. Int.*, 77:185–264. doi:10.1111/j.1365-246X.1984.tb01931.x.
- Jackson, J. and McKenzie, D. (1988). The relationship between plate motions and seismic moment tensors, and the rates of active deformation in the Mediterranean and Middle East. *Geophys. J. Int.*, 93:45–73. doi:10.1111/j.1365-246X.1988.tb01387.x.
- Jackson, J., McKenzie, D., Priestley, K., and Emmerson, B. (2008). New views on the structure and rheology of the lithosphere. *J. Geol. Soc. London.*, 165:453–465. doi:10.1144/0016-76492007-109.
- Jackson, J., Priestley, K., Allen, M., and Berberian, M. (2002). Active tectonics of the South Caspian Basin. *Geophys. J. Int.*, 148:214–245. doi:10.1046/j.1365-246X.2002.01588.x.
- Jackson, J. A., Austrheim, H., McKenzie, D., and Priestley, K. (2004). Metastability, mechanical strength, and the support of mountain belts. *Geology*, 32(7):625–628. doi:10.1130/G20397.1.
- Jacob, K. H. and Quittmeyer, R. (1979). The Makran region of Pakistan and Iran: trench-arc system with active plate subduction. In Farah, A. and DeJong, K. A., editors, *Geodynamics of Pakistan*, pages 305–318. Geological Survey of Pakistan.
- Ji, C., Wald, D., and Helmberger, D. (2002). Source description of the 1999 Hector Mine, California, earthquake, part I: Wavelet domain inversion theory and resolution analysis. *Bull. Seismol. Soc. Am.*, 92(4):1192–1207. doi:10.1785/0120000916.
- Jolivet, R., Duputel, Z., Riel, B., Simons, M., Rivera, L., Minson, S. E., Zhang, H., Aivazis, M. A. G., Ayoub, F., Leprince, S., Samsonov, S., Motagh, M., and Fielding, E. J. (2014). The 2013 Mw 7.7 Balochistan Earthquake: Seismic Potential of an Accretionary Wedge. *Bull. Seismol. Soc. Am.*, 104(2):1020–1030. doi:10.1785/0120130313.
- Jones, L. M., Han, W. B., Hauksson, E., Jin, A. S., Zhang, Y. G., and Luo, Z. L. (1984). Focal Mechanisms and Aftershock Locations of the Songpan Earthquakes of August 1976 in Sichuan, China. *JGR*, 89(B9):7697–7707. doi:10.1029/JB089iB09p07697.
- Jónsson, S. and Zebker, H. (2002). Fault slip distribution of the 1999 Mw 7.1 Hector Mine, California, earthquake, estimated from satellite radar and GPS measurements. *Bull. Seismol. Soc. Am.*, 92(4):1377–1389. doi:10.1785/0120000922.

- Julià, J., Ammon, C. J., and Herrmann, R. B. (2003). Lithospheric structure of the Arabian Shield from the joint inversion of receiver functions and surface-wave group velocities. *Tectonophysics*, 371:1–21. doi:10.1016/S0040-1951(03)00196-3.
- Julià, J., Ammon, C. J., Herrmann, R. B., and Correig, A. M. (2000). Joint inversion of receiver function and surface wave dispersion observations. *Geophys. J. Int.*, 143:99–112. doi:10.1046/j.1365-246x.2000.00217.x.
- Kadinsky-Cade, K. and Barazangi, M. (1982). Seismotectonics of southern Iran: the Oman line. *Tectonics*, 1(5):389–412. doi:10.1029/TC001i005p00389.
- Kennett, B. L. N., Engdahl, E. R., and Buland, R. (1995). Constraints on seismic velocities in the Earth from traveltimes. *Geophys. J. Int.*, 122:108–124. doi:10.1111/j.1365-246X.1995.tb03540.x.
- Kintner, J. A., Ammon, C. J., Cleveland, K. M., and Herman, M. (2018). Rupture Processes of the 2013-14 Minab Earthquake Sequence , Iran. *Geophys. J. Int.*, 213:1898–1911. doi:10.1093/gji/ggy085/4923052.
- Kirby, E., Reiners, P. W., Krol, M. A., Whipple, K. X., Hodges, K. V., Farley, K. A., Tang, W., and Chen, Z. (2002). Late Cenozoic evolution of the eastern margin of the Tibetan Plateau: Inferences from 40 Ar/ 39 Ar and (U-Th)/He thermochronology. *Tectonics*, 21(1):1001–1019. doi:10.1029/2000TC001246.
- Konca, O., Avouac, J.-P., Sladen, A., Meltzner, A. J., Sieh, K., Fang, P., Li, Z., Galetzka, J., Genrich, J., Chlieh, M., Natawidjaja, D. H., Bock, Y., Fielding, E. J., Ji, C., and Helmberger, D. V. (2008). Partial rupture of a locked patch of the Sumatra megathrust during the 2007 earthquake sequence. *Nature*, 456:631–635. doi:10.1038/nature07572.
- Konca, O., Leprince, S., Avouac, J.-P., and Helmberger, D. V. (2010). Rupture Process of the 1999 Mw 7.1 Duzce Earthquake from Joint Analysis of SPOT, GPS, InSAR, Strong-Motion, and Teleseismic Data: A Supershear Rupture with Variable Rupture Velocity. *Bull. Seismol. Soc. Am.*, 100(1):267–288. doi:10.1785/0120090072.
- Koons, P. O. (1989). The topographic evolution of collisional mountain belts: a numerical look at the Southern Alps, New Zealand. *Am. J. Sci.*, 289(9):1041–1069. doi:10.2475/ajs.289.9.1041.
- Kopp, C., Fruehn, J., Flueh, E., Reichert, C., Kukowski, N., Bialas, J., and Klaeschen, D. (2000). Structure of the Makran subduction zone from wide-angle and reflection seismic data. *Tectonophysics*, 329:171–191. doi:10.1016/S0040-1951(00)00195-5.
- Kreemer, C., Haines, J., Holt, W. E., Blewitt, G., and Lavallee, D. (2000). On the determination of a global strain rate model. *Earth, Planets Sp.*, 52:765–770. doi:10.1186/BF03352279.
- Kreemer, C., Klein, E., Shen, Z.-K., Wang, M., Estey, L., Wier, S., and Boler, F. (2014). A geodetic platemotion and Global Strain Rate Model. *Geochemistry, Geophys. Geosystems*, 15:3849–3889. doi:10.1002/2014GC005407.Received.
- Kukowski, N., Schillhorn, T., Flueh, E., and Huhn, K. (2000). Newly identified strike-slip plate boundary in the northeastern Arabian Sea. *Geology*, 28(4):355–358. doi:10.1130/0091-7613(2000)28<355:NISPBI>2.0.CO;2.
- Laane, J. L. and Chen, W.-P. (1989). The Makran earthquake of 1983 April 18: A possible analogue to the Puget Sound earthquake of 1965? *Geophys. J. Int.*, 98:1–9. doi:10.1111/j.1365-246X.1989.tb05509.x.

- Lamb, S. (2000). Active deformation in the Bolivian Andes, South America. *J. Geophys. Res. Solid Earth*, 105(B11):25627–25653. doi:10.1029/2000JB900187.
- Lamb, S. (2006). Shear stresses on megathrusts: Implications for mountain building behind subduction zones. *JGR*, 111:B07401. doi:10.1029/2005JB003916.
- Langston, C. A. (1979). Structure under Mount Rainier, Washington, inferred from teleseismic body waves. *JGR*, 84(B9):4749–4762. doi:10.1029/JB084iB09p04749.
- Lawrence, R. D., Yeats, R. S., Khan, S. H., Farah, A., and DeJong, K. A. (1981). Thrust and strike slip fault interaction along the Chaman transform zone, Pakistan. *Geol. Soc. London, Spec. Publ.*, 9:363–370. doi:10.1144/GSL.SP.1981.009.01.33.
- Lay, T., Kanamori, H., Ammon, C. J., Nettles, M., Ward, S. N., Aster, R. C., Beck, S. L., Bilek, S. L., Brudzinski, M. R., Butler, R., DeShon, H. R., Ekstrom, G., Satake, K., and Sipkin, S. (2005). The Great Sumatra-Andaman Earthquake of 26 December 2004. *Science*, 308(5725):1127–1133. doi:10.1126/science.1112250.
- Li, G., West, A. J., Densmore, A. L., Jin, Z., Zhang, F., Wang, J., Clark, M., and Hilton, R. G. (2017). Earthquakes drive focused denudation along a tectonically active mountain front. *EPSL*, 472:253–265. doi:10.1016/j.epsl.2017.04.040.
- Li, H., Su, W., Wang, C.-Y., and Huang, Z. (2009). Ambient noise Rayleigh wave tomography in western Sichuan and eastern Tibet. *EPSL*, 282:201–211. doi:10.1016/j.epsl.2009.03.021.
- Li, S., Currie, B. S., Rowley, D. B., and Ingalls, M. (2015). Cenozoic paleoaltimetry of the SE margin of the Tibetan Plateau: Constraints on the tectonic evolution of the region. *EPSL*, 432:415–424. doi:10.1016/j.epsl.2015.09.044.
- Li, Z., Elliott, J. R., Feng, W., Jackson, J. A., Parsons, B. E., and Walters, R. J. (2011). The 2010 Mw 6.8 Yushu (Qinghai, China) earthquake: Constraints provided by InSAR and body wave seismology. *J. Geophys. Res. Solid Earth*, 116:B10302. doi:10.1029/2011JB008358.
- Ligorria, J. P. and Ammon, C. J. (1999). Iterative deconvolution and receiver-function estimation. *Bull. Seismol. Soc. Am.*, 89(5):1395–1400.
- Lin, N. Y., Jolivet, R., Simons, M., Agram, P. S., Martens, H. R., Li, Z., and Lodi, S. H. (2015). High interseismic coupling in the Eastern Makran (Pakistan) subduction zone. *EPSL*, 420:116–126. doi:10.1016/j.epsl.2015.03.037.
- Liu-Zeng, J., Tapponnier, P., Gaudemer, Y., and Ding, L. (2008). Quantifying landscape differences across the Tibetan plateau: Implications for topographic relief evolution. *J. Geophys. Res. Earth Surf.*, 113:F04018. doi:10.1029/2007JF000897.
- Lohman, R. B. and Simons, M. (2005). Locations of selected small earthquakes in the Zagros mountains. *Geochemistry, Geophys. Geosystems*, 6:Q03001. doi:10.1029/2004GC000849.
- Loveless, J. P., Allmendinger, R. W., Pritchard, M. E., and González, G. (2010). Normal and reverse faulting driven by the subduction zone earthquake cycle in the northern Chilean fore arc. *Tectonics*, 29:TC2001. doi:10.1029/2009TC002465.
- Lyell, C. (1853). On the former intensity of the igneous forces. In *Principles of Geology*, chapter XI. D. Appleton & Co., 9th edition.
- Maggi, A., Jackson, J. A., McKenzie, D., and Priestley, K. (2000a). Earthquake focal depths, effective elastic thickness, and the strength of the continental lithosphere. *Geology*, 28(6):495–498. doi:10.1130/0091-7613(2000)28<495:EFDEET>2.0.CO;2.

- Maggi, A., Jackson, J. A., Priestley, K., and Baker, C. (2000b). A re-assessment of focal depth distributions in southern Iran, the Tien Shan and northern India: do earthquakes really occur in the continental mantle? *Geophys. J. Int.*, 143:629–661. doi:10.1046/j.1365-246X.2000.00254.x.
- Manaman, N. S., Shomali, H., and Koyi, H. (2011). New constraints on upper-mantle S-velocity structure and crustal thickness of the Iranian plateau using partitioned waveform inversion. *Geophys. J. Int.*, 184:247–267. doi:10.1111/j.1365-246X.2010.04822.x.
- Masson, F., Anvari, M., Djamour, Y., Walpersdorf, A., Tavakoli, F., Daignières, M., Nankali, H., and Van Gorp, S. (2007). Large-scale velocity field and strain tensor in Iran inferred from GPS measurements: new insight for the present-day deformation pattern within NE Iran. *Geophys. J. Int.*, 170:436–440. doi:10.1111/j.1365-246X.2007.03477.x.
- Masson, F., Chéry, J., Hatzfeld, D., Martinod, J., Vernant, P., Tavakoli, F., and Ghafory-Ashtiani, M. (2004). Seismic versus aseismic deformation in Iran inferred from earthquakes and geodetic data. *Geophys. J. Int.*, 160:217–226. doi:10.1111/j.1365-246X.2004.02465.x.
- Matte, P., Tapponnier, P., Arnaud, N., Bourjot, L., Avouac, J. P., Vidal, P., Quing, L., Pan, Y., and Yi, W. (1996). Tectonics of Western Tibet, between the Tarim and the Indus. *EPSL*, 142:311–330. doi:10.1016/0012-821X(96)00086-6.
- Maurin, T., Masson, F., Rangin, C., Min, U. T., and Collard, P. (2010). First global positioning system results in northern Myanmar: Constant and localized slip rate along the Sagaing fault. *Geology*, 38(7):591–594. doi:10.1130/G30872.1.
- McCaffrey, R. and Abers, G. (1988). SYN3: A program for inversion of teleseismic body waveforms on microcomputers. Technical report, Air Force Geophysics Laboratory Technical Report.
- McCaffrey, R., Abers, G., and Zwick, P. (1991). Inversion of teleseismic body waves. In Lee, W., editor, *Digital Seismogram Analysis and Waveform Inversion*, pages 81–166. Int. Assoc. Seismol. Phys. Earth Inter. Software Library.
- McGroder, M. F., Lease, R. O., and Pearson, D. M. (2014). Along-strike variation in structural styles and hydrocarbon occurrences, Subandean fold-and-thrust belt and inner foreland, Colombia to Argentina. In *Geol. Soc. Am. Mem.*, volume 212, pages 79–113. doi:10.1130/2015.1212(05).
- McKenzie, D. (1972). Active Tectonics of the Mediterranean Region. *Geophys. J. R. Astron. Soc.*, 30:109–185. doi:10.1111/j.1365-246X.1972.tb02351.x.
- McKenzie, D. and Jackson, J. (1983). The relationship between strain rates, crustal thickening, paleomagnetism, finite strain, and fault movement within a deforming zone. *EPSL*, 65:182–202. doi:10.1016/0012-821X(83)90198-X.
- McKenzie, D. and Jackson, J. (1986). A block model of distributed deformation by faulting. *J. Geol. Soc. London.*, 143:349–353. doi:10.1144/gsjgs.143.2.0349.
- McKenzie, D. and Jackson, J. (2012). Tsunami earthquake generation by the release of gravitational potential energy. *EPSL*, 345-348:1–8. doi:10.1016/j.epsl.2012.06.036.
- McKenzie, D., Jackson, J., and Priestley, K. (2005). Thermal structure of oceanic and continental lithosphere. *EPSL*, 233:337–349. doi:10.1016/j.epsl.2005.02.005.

- McKenzie, D., Nimmo, F., Jackson, J. A., Gans, P. B., and Miller, E. L. (2000). Characteristics and consequences of flow in the lower crust. *J. Geophys. Res. Solid Earth*, 105(B5):11029–11046. doi:10.1029/1999JB900446.
- McKenzie, D. and Priestley, K. (2008). The influence of lithospheric thickness variations on continental evolution. *Lithos*, 102:1–11. doi:10.1016/j.lithos.2007.05.005.
- McKenzie, D. P. and Parker, R. L. (1967). The North Pacific: an Example of Tectonics on a Sphere. *Nature*, 216:1276–1280. doi:10.1038/2161276a0.
- Meyer, B. and Le Dortz, K. (2007). Strike-slip kinematics in Central and Eastern Iran: Estimating fault slip-rates averaged over the Holocene. *Tectonics*, 26:TC5009. doi:10.1029/2006TC002073.
- Molnar, P. (1988). Continental tectonics in the aftermath of plate tectonics. *Nature*, 335:131–137. doi:10.1038/332141a0.
- Molnar, P., Boos, W. R., and Battisti, D. S. (2010). Orographic Controls on Climate and Paleoclimate of Asia: Thermal and Mechanical Roles for the Tibetan Plateau. *Annu. Rev. Earth Planet. Sci.*, 38:77–102. doi:10.1146/annurev-earth-040809-152456.
- Molnar, P. and Lyon-Caen, H. (1988). Some simple physical aspects of the support, structure, and evolution of mountain belts. In *GSA Spec. Pap.*, volume 218, pages 179–208. doi:10.1130/SPE218-p179.
- Molnar, P. and Lyon-Caen, H. (1989). Fault plane solutions of earthquakes and active tectonics of the Tibetan Plateau and its margins. *Geophys. J. Int.*, 99:123–154. doi:10.1111/j.1365-246X.1989.tb02020.x.
- Molnar, P. and Tapponnier, P. (1975). Cenozoic Tectonics of Asia: Effects of a Continental Collision. *Science*, 189(4201):419–426. doi:10.1126/science.189.4201.419.
- Molnar, P. and Tapponnier, P. (1981). A possible dependence of tectonic strength on the age of the crust in Asia. *EPSL*, 52:107–114. doi:10.1016/0012-821X(81)90213-2.
- Morgan, K. H., McCall, G. J. H., and Huber, H. (1979). Minab Quadrangle. Technical report, Geological and Mineral Survey of Iran.
- Mulch, A. (2016). Stable isotope paleoaltimetry and the evolution of landscapes and life. *EPSL*, 433:180–191. doi:10.1016/j.epsl.2015.10.034.
- Musson, R. (2009). Subduction in the Western Makran: the historian’s contribution. *J. Geol. Soc. London.*, 166(3):387–391. doi:10.1144/0016-76492008-119.
- Natawidjaja, D. H., Sieh, K., Ward, S. N., Cheng, H., Edwards, R. L., Galetzka, J., and Suwargadi, B. W. (2004). Paleogeodetic records of seismic and aseismic subduction from central Sumatran microatolls, Indonesia. *J. Geophys. Res. Solid Earth*, 109:B04306. doi:10.1029/2003JB002398.
- Niazi, M., Shimamura, H., and Matsu’ura, M. (1980). Microearthquakes and crustal structure off the Makran coast of Iran. *Geophys. Res. Lett.*, 7(5):297–300. doi:10.1029/GL007i005p00297.
- Nicholson, K. N., Khan, M., and Mahmood, K. (2010). Geochemistry of the Chagai-Raskoh arc, Pakistan: Complex arc dynamics spanning the Cretaceous to the Quaternary. *Lithos*, 118:338–348. doi:DOI 10.1016/j.lithos.2010.05.008.

- Nissen, E., Tatar, M., Jackson, J., and Allen, M. (2011). New views on earthquake faulting in the Zagros fold-and-thrust belt of Iran. *Geophys. J. Int.*, 186:928–944. doi:10.1111/j.1365-246X.2011.5119.x.
- Nissen, E., Yamini-Fard, F., Tatar, M., Gholamzadeh, A., Bergman, E., Elliott, J., Jackson, J., and Parsons, B. (2010). The vertical separation of mainshock rupture and microseismicity at Qeshm island in the Zagros fold-and-thrust belt, Iran. *EPSL*, 296(3-4):181–194. doi:10.1016/j.epsl.2010.04.049.
- Nur, A., Ron, H., and Scotti, O. (1986). Fault mechanics and the kinematics of block rotations. *Geology*, 14(9):746–749. doi:10.1130/0091-7613(1986)14<746:FMATKO>2.0.CO;2.
- Okada, Y. (1985). Surface deformation due to shear and tensile faults in a half-space. *Bull. Seismol. Soc. Am.*, 75(4):1135–1154.
- Page, W. D., Alt, J. N., Cluff, L. S., and Plafker, G. (1979). Evidence for the recurrence of large-magnitude earthquakes along the Makran coast of Iran and Pakistan. *Tectonophysics*, 52:533–547. doi:10.1016/0040-1951(79)90269-5.
- Pattyn, F. (2000). Ice-sheet modelling at different spatial resolutions: focus on the grounding zone. *Ann. Glaciol.*, 31:211–216. doi:10.3189/172756400781820435.
- Pattyn, F. (2003). A new three-dimensional higher-order thermomechanical ice sheet model: Basic sensitivity, ice stream development, and ice flow across subglacial lakes. *JGR*, 108(B8):1–15. doi:10.1029/2002JB002329.
- Peng, Z. and Gombert, J. (2010). An integrated perspective of the continuum between earthquakes and slow-slip phenomena. *Nat. Geosci.*, 3:599–607. doi:10.1038/ngeo940.
- Penney, C., Copley, A., and Oveisi, B. (2015). Subduction tractions and vertical axis rotations in the Zagros-Makran transition zone, SE Iran: the 2013 May 11 Mw 6.1 Minab earthquake. *Geophys. J. Int.*, 202:1122–1136. doi:10.1093/gji/ggv202.
- Penney, C., Tavakoli, F., Saadat, A., Nankali, H. R., Sedighi, M., Khorrami, F., Sobouti, F., Rafi, Z., Copley, A., Jackson, J., and Priestley, K. (2017). Megathrust and accretionary wedge properties and behaviour in the Makran subduction zone. *Geophys. J. Int.*, 209:1800–1830. doi:10.1093/gji/ggx126.
- Peyret, M., Djamour, Y., Hessami, K., Regard, V., Bellier, O., Vernant, P., Daignières, M., Nankali, H., Van Gorp, S., Goudarzi, M., Chéry, J., Bayer, R., and Rigoulay, M. (2009). Present-day strain distribution across the Minab-Zendan-Palami fault system from dense GPS transects. *Geophys. J. Int.*, 179:751–762. doi:10.1111/j.1365-246X.2009.04321.x.
- Platt, J. P., Leggett, J. K., and Alam, S. (1988). Slip vectors and fault mechanics in the Makran Accretionary Wedge, southwest Pakistan. *JGR*, 93(B7):7955–7973. doi:10.1029/JB093iB07p07955.
- Platt, J. P., Leggett, J. K., Young, J., Raza, H., and Alam, S. (1985). Large-scale sediment underplating in the Makran accretionary prism, southwest Pakistan. *Geology*, 13(7):507–511. doi:10.1130/0091-7613(1985)13<507:LSUITM>2.0.CO;2.
- Polissar, P. J., Freeman, K. H., Rowley, D. B., McInerney, F. A., and Currie, B. S. (2009). Paleoaltimetry of the Tibetan Plateau from D/H ratios of lipid biomarkers. *EPSL*, 287:64–76. doi:10.1016/j.epsl.2009.07.037.

- Press, W. H., Teukolsky, S. A., Vetterling, W. T., and Flannery, B. P. (2006). *Numerical Recipes in Fortran 77*. Cambridge University Press, 2nd edition.
- Priestley, K., Jackson, J., and McKenzie, D. (2008). Lithospheric structure and deep earthquakes beneath India, the Himalaya and southern Tibet. *Geophys. J. Int.*, 172:345–362. doi:10.1111/j.1365-246X.2007.03636.x.
- Regard, V., Bellier, O., Thomas, J.-C., Abbassi, M. R., Mercier, J., Shabanian, E., Feghhi, K., and Soleymani, S. (2004). Accommodation of Arabia-Eurasia convergence in the Zagros-Makran transfer zone, SE Iran: A transition between collision and subduction through a young deforming system. *Tectonics*, 23:TC4007. doi:10.1029/2003TC001599.
- Regard, V., Bellier, O., Thomas, J.-C., Bourlès, D., Bonnet, S., Abbassi, M. R., Braucher, R., Mercier, J., Shabanian, E., Soleymani, S., and Feghhi, K. (2005). Cumulative right-lateral fault slip rate across the Zagros-Makran transfer zone: role of the Minab-Zendan fault system in accommodating Arabia-Eurasia convergence in southeast Iran. *Geophys. J. Int.*, 162:177–203. doi:10.1111/j.1365-246X.2005.02558.x.
- Reilinger, R., McClusky, S., Vernant, P., Lawrence, S., Ergintav, S., Cakmak, R., Ozener, H., Kadirov, F., Guliev, I., Stepanyan, R., Nadariya, M., Hahubia, G., Mahmoud, S., Sakr, K., ArRajehi, A., Paradissis, D., Al-Aydrus, A., Prilepin, M., Guseva, T., Evren, E., Dmitrova, A., Filikov, S. V., Gomez, F., Al-Ghazzi, R., and Karam, G. (2006). GPS constraints on continental deformation in the Africa-Arabia-Eurasia continental collision zone and implications for the dynamics of plate interactions. *JGR*, 111(B5):B05411. doi:10.1029/2005JB004051.
- Reynolds, K., Copley, A., and Hussain, E. (2015). Evolution and dynamics of a fold-thrust belt: The Sulaiman Range of Pakistan. *Geophys. J. Int.*, 201:683–710. doi:10.1093/gji/ggv005.
- Richardson, N. J., Densmore, A. L., Seward, D., Fowler, A., Wipf, M., Ellis, M. A., Yong, L., and Zhang, Y. (2008). Extraordinary denudation in the Sichuan Basin: Insights from low-temperature thermochronology adjacent to the eastern margin of the Tibetan Plateau. *J. Geophys. Res. Solid Earth*, 113:B04409. doi:10.1029/2006JB004739.
- Roustaei, M., Nissen, E., Abbassi, M., Gholamzadeh, A., Ghorashi, M., Tatar, M., Yamini-Fard, F., Bergman, E., Jackson, J., and Parsons, B. (2010). The 2006 March 25 Fin earthquakes (Iran)-insights into the vertical extents of faulting in the Zagros Simply Folded Belt. *Geophys. J. Int.*, 181:1275–1291. doi:10.1111/j.1365-246X.2010.04601.x.
- Rowley, D. B. (2007). Stable Isotope-Based Paleoaltimetry: Theory and Validation. *Rev. Mineral. Geochemistry*, 66:23–52. doi:10.2138/rmg.2007.66.2.
- Rowley, D. B. and Currie, B. S. (2006). Palaeo-altimetry of the late Eocene to Miocene Lunpola basin, central Tibet. *Nature*, 439:677–681. doi:10.1038/nature04506.
- Rowley, D. B., Pierrehumbert, R. T., and Currie, B. S. (2001). A new approach to stable isotope-based paleoaltimetry: Implications for paleoaltimetry and paleohypsometry of the High Himalaya since the late Miocene. *EPSL*, 188:253–268. doi:10.1016/S0012-821X(01)00324-7.
- Royden, L. (1996). Coupling and decoupling of crust and mantle in convergent orogens: Implications for strain partitioning in the crust. *JGR*, 101(B8):17,679–17,705. doi:10.1029/96JB00951.

- Royden, L. H., Burchfiel, B. C., King, R. W., Wang, E., Chen, Z., Shen, F., and Liu, Y. (1997). Surface Deformation and Lower Crustal Flow in Eastern Tibet. *Science*, 276(5313):788–790. doi:10.1126/science.276.5313.788.
- Saad, Y. and Schultz, M. H. (1986). GMRES: A Generalized Minimal Residual Algorithm for Solving Nonsymmetric Linear Systems. *SIAM J. Sci. Stat. Comput.*, 7(3):856–869. doi:https://doi.org/10.1137/0907058.
- Saadat, S. and Stern, C. R. (2011). Petrochemistry and genesis of olivine basalts from small monogenetic parasitic cones of Bazman stratovolcano, Makran arc, southeastern Iran. *Lithos*, 125:607–619. doi:10.1016/j.lithos.2011.03.014.
- Samsonov, S. V. and Czarnogorska, M. (2013). Ground deformation produced by 2013 M6.1 Minab earthquake in Iran mapped with RADARSAT-2 DInSAR, Open File 7528. Technical report, Geological Survey of Canada. doi:10.4095/293320.
- Savage, J. C. (1983). A dislocation model of strain accumulation and release at a subduction zone. *JGR*, 88(B6):4984–4996. doi:10.1029/JB088iB06p04984.
- Scott, C. P., Allmendinger, R. W., González, G., and Loveless, J. P. (2016). Coseismic extension from surface cracks reopened by the 2014 Pisagua, northern Chile, earthquake sequence. *Geology*, 44(5):387–390. doi:10.1130/G37662.1.
- Shen, Z. K., Lü, J., Wang, M., and Bürgmann, R. (2005). Contemporary crustal deformation around the southeast borderland of the Tibetan Plateau. *J. Geophys. Res. Solid Earth*, 110:B11409. doi:10.1029/2004JB003421.
- Shi, X., Wang, Y., Sieh, K., Weldon, R., Feng, L., Chan, C.-H., and Liu-Zeng, J. (2018). Fault Slip and GPS Velocities Across the Shan Plateau Define a Curved Southwestward Crustal Motion Around the Eastern Himalayan Syntaxis. *J. Geophys. Res. Solid Earth*, 123:2502–2518. doi:10.1002/2017JB015206.
- Sloan, R. A., Jackson, J. A., McKenzie, D., and Priestley, K. (2011). Earthquake depth distributions in central Asia, and their relations with lithosphere thickness, shortening and extension. *Geophys. J. Int.*, 185:1–29. doi:10.1111/j.1365-246X.2010.04882.x.
- Smith, G., McNeill, L., Henstock, T. J., and Bull, J. (2012). The structure and fault activity of the Makran accretionary prism. *JGR*, 117:B07407. doi:10.1029/2012JB009312.
- Smith, G. L., McNeill, L. C., Wang, K., He, J., and Henstock, T. J. (2013). Thermal structure and megathrust seismogenic potential of the Makran subduction zone. *Geophys. Res. Lett.*, 40:1528–1533. doi:10.1002/grl.50374.
- Steckler, M. S., Mondal, D. R., Akhter, S. H., Seeber, L., Feng, L., Gale, J., Hill, E. M., and Howe, M. (2016). Locked and loading megathrust linked to active subduction beneath the Indo-Burman Ranges. *Nat. Geosci.*, 9:615–618. doi:10.1038/ngeo2760.
- Stork, A. L., Selby, N. D., Heyburn, R., and Searle, M. P. (2008). Accurate relative earthquake hypocenters reveal structure of the Burma subduction zone. *Bull. Seismol. Soc. Am.*, 98(6):2815–2827. doi:10.1785/0120080088.
- Syracuse, E. M. and Abers, G. A. (2006). Global compilation of variations in slab depth beneath arc volcanoes and implications. *Geochemistry, Geophys. Geosystems*, 7:Q05017. doi:10.1029/2005GC001045.

- Talebian, M., Biggs, J., Bolourchi, M., Copley, A., Ghassemi, A., Ghorashi, M., Hollingsworth, J., Jackson, J., Nissen, E., Oveisi, B., Parsons, B., Priestley, K., and Saiidi, A. (2006). The Dahuiyeh (Zarand) earthquake of 2005 February 22 in central Iran: reactivation of an intramountain reverse fault. *Geophys. J. Int.*, 164:137–148. doi:10.1111/j.1365-246X.2005.02839.x.
- Talebian, M., Copley, A. C., Fattahi, M., Ghorashi, M., Jackson, J. A., Nazari, H., Sloan, R. A., and Walker, R. T. (2016). Active faulting within a megacity: The geometry and slip rate of the Pardisan thrust in central Tehran, Iran. *Geophys. J. Int.*, 207:1688–1699. doi:10.1093/gji/ggw347.
- Tang, M., Liu-zeng, J., Hoke, G. D., Xu, Q., Wang, W., Li, Z., Zhang, J., and Wang, W. (2017). Paleoelevation reconstruction of the Paleocene-Eocene Gonjo basin, SE-central Tibet. *Tectonophysics*, 712-713:170–181. doi:10.1016/j.tecto.2017.05.018.
- Tapponnier, P. and Molnar, P. (1976). Slip-line field theory and large-scale continental tectonics. *Nature*, 264:319–324. doi:10.1038/264319a0.
- Tapponnier, P., Peltzer, G., Le Dain, a. Y., Armijo, R., and Cobbold, P. R. (1982). Propagation extrusion tectonics in Asia: New insights from experiments with plasticine. *Geology*, 10(12):611–616. doi:10.1130/0091-7613(1982)10<611:PETIAN>2.0.CO;2.
- Tapponnier, P., Zhiqin, X., Roger, F., Meyer, B., Arnaud, N., Wittlinger, G., and Jingsui, Y. (2001). Oblique Stepwise Rise and Growth of the Tibet Plateau. *Science*, 294(5547):1671–1677. doi:10.1126/science.105978.
- Taymaz, T. (1990). Earthquake mechanisms in the Hellenic Trench near Crete. *Geophys. J. Int.*, 102:695–731. doi:10.1111/j.1365-246X.1990.tb04590.x.
- Tichelaar, B. W. and Ruff, L. J. (1993). Depth of seismic coupling along subduction zones. *JGR*, 98(B2):2017–2037. doi:10.1029/92JB02045.
- Tirrul, R., Bell, I. R., Griffis, R. J., and Camp, V. E. (1983). The Sistan suture zone of eastern Iran. *Geol. Soc. Am. Bull.*, 94:134–150. doi:10.1130/0016-7606(1983)94<134:TSSZOE>2.0.CO;2.
- Tirrul, R., Griffis, R. J., and Camp, V. E. (1980). Geology of the Zabol Quadrangle, 1:250,000: Report submitted to the Geological and Mineral Survey of Iran.
- Vallage, A., Klinger, Y., Grandin, R., Bhat, H. S., and Pierrot-Deseilligny, M. (2015). Inelastic surface deformation during the 2013 Mw 7.7 Balochistan, Pakistan, earthquake. *Geology*, 43(12):1079–1082. doi:10.1130/G37290.1.
- Vergne, J., Cattin, R., and Avouac, J. P. (2001). On the use of dislocations to model interseismic strain and stress build-up at intracontinental thrust faults. *Geophys. J. Int.*, 147:155–162. doi:10.1046/j.1365-246X.2001.00524.x.
- Vernant, P., Nilforoushan, F., Hatzfeld, D., Abbassi, M. R., Vigny, C., Masson, F., Nankali, H., Martinod, J., Ashtiani, A., Bayer, R., Tavakoli, F., and Chéry, J. (2004). Present-day crustal deformation and plate kinematics in the Middle East constrained by GPS measurements in Iran and northern Oman. *Geophys. J. Int.*, 157:381–398. doi:10.1111/j.1365-246X.2004.02222.x.
- Vilotte, J. P., Daignieres, M., Madariaga, R., and Zienkiewicz, O. C. (1984). The role of a heterogeneous inclusion during continental collision. *Phys. Earth Planet Inter.*, 36:236–259. doi:10.1016/0031-9201(84)90049-9.

- Von Herzen, R., Ruppel, C., Molnar, P., Nettles, M., Nagihara, S., and Ekström, G. (2001). A constraint on the shear stress at the Pacific-Australian plate boundary from heat flow and seismicity at the Kermadec forearc. *JGR*, 106(B4):6817–6833. doi:10.1029/2000JB900469.
- Walker, R. and Jackson, J. (2004). Active tectonics and late Cenozoic strain distribution in central and eastern Iran. *Tectonics*, 23:TC5010. doi:10.1029/2003TC001529.
- Walker, R., Jackson, J., and Baker, C. (2003). Surface expression of thrust faulting in eastern Iran: source parameters and surface deformation of the 1978 Tabas and 1968 Ferdows earthquake sequences. *Geophys. J. Int.*, 152:749–765. doi:10.1046/j.1365-246X.2003.01886.x.
- Walker, R., Jackson, J., and Baker, C. (2004). Active faulting and seismicity of the Dasht-e-Bayaz region, eastern Iran. *Geophys. J. Int.*, 157:265–282. doi:10.1111/j.1365-2966.2004.02179.x.
- Walker, R. T. (2003). *Active Faulting and Tectonics of Eastern Iran*. PhD thesis, University of Cambridge.
- Walker, R. T., Bergman, E., Elliott, J. R., Fielding, E. J., Ghods, R., Ghoraiishi, M., Jackson, J., Nazari, H., Nemati, M., Oveisi, B., Talebian, M., and Walters, R. J. (2013). The 2010–2011 South Rigan (Baluchestan) earthquake sequence and its implications for distributed deformation and earthquake hazard in southeast Iran. *Geophys. J. Int.*, 193:349–374. doi:10.1093/gji/ggs109.
- Walker, R. T., Talebian, M., Sloan, R. A., Rasheedi, A., Fattahi, M., and Bryant, C. (2010). Holocene slip-rate on the Gowk strike-slip fault and implications for the distribution of tectonic strain in eastern Iran. *Geophys. J. Int.*, 181:221–228. doi:10.1111/j.1365-246X.2010.04538.x.
- Walpersdorf, A., Hatzfeld, D., Nankali, H., Tavakoli, F., Nilforoushan, F., Tatar, M., Vernant, P., Chéry, J., and Masson, F. (2006). Difference in the GPS deformation pattern of North and Central Zagros (Iran). *Geophys. J. Int.*, 167:1077–1088. doi:10.1111/j.1365-246X.2006.03147.x.
- Walpersdorf, A., Manighetti, I., Mousavi, Z., Tavakoli, F., Vergnolle, M., Jadidi, A., Hatzfeld, D., Aghamohammadi, A., Bigot, A., Djamour, Y., Nankali, H., and Sedighi, M. (2014). Present-day kinematics and fault slip rates in eastern Iran, derived from 11 years of GPS data. *J. Geophys. Res. Solid Earth*, 119:1359–1383. doi:10.1002/2013JB010620.
- Walters, R. J., England, P. C., and Houseman, G. A. (2017). Constraints from GPS measurements on the dynamics of the zone of convergence between Arabia and Eurasia. *J. Geophys. Res. Solid Earth*, 122:1470–1495. doi:10.1002/2016JB013370.
- Wang, E., Burchfiel, B., Royden, L., Liangzhong, C., Jishen, C., Wenxin, L., and Zhiliang, C. (1998). *Late Cenozoic Xianshuihe-Xiaojiang, Red River, and Dali Fault Systems of Southwestern Sichuan and Central Yunnan, China*. doi:10.1130/SPE327.
- Wang, E., Kirby, E., Furlong, K. P., Van Soest, M., Xu, G., Shi, X., Kamp, P. J. J., and Hodges, K. V. (2012). Two-phase growth of high topography in eastern Tibet during the Cenozoic. *Nat. Geosci.*, 5:640–645. doi:10.1038/geo1538.
- Wang, K. and Dixon, T. (2004). "Coupling" Semantics and Science in Earthquake Research. *EOS Trans.*, 85(18):180–181. doi:10.1029/2003.

- Wang, W., Zhang, P., Liu, C., Zheng, D., Yu, J., Zheng, W., Wang, Y., Zhang, H., and Chen, X. (2016a). Pulsed growth of the West Qinling at ~ 30 Ma in northeastern Tibet: Evidence from Lanzhou Basin magnetostratigraphy and provenance. *J. Geophys. Res. Solid Earth*, 121:7754–7774. doi:10.1002/2016JB013279.
- Wang, X., Qiu, Z., Li, Q., Wang, B., Qiu, Z., Downs, W. R., Xie, G., Xie, J., Deng, T., Takeuchi, G. T., Tseng, Z. J., Chang, M., Liu, J., Wang, Y., Biasatti, D., Sun, Z., Fang, X., and Meng, Q. (2007). Vertebrate paleontology, biostratigraphy, geochronology, and paleoenvironment of Qaidam Basin in northern Tibetan Plateau. *Palaeogeogr. Palaeoclimatol. Palaeoecol.*, 254:363–385. doi:10.1016/j.palaeo.2007.06.007.
- Wang, Y. and Deng, T. (2005). A 25 m.y. isotopic record of paleodiet and environmental change from fossil mammals and paleosols from the NE margin of the Tibetan Plateau. *EPSL*, 236:322–338. doi:10.1016/j.epsl.2005.05.006.
- Wang, Y., Sieh, K., Tun, S. T., Lai, K.-Y., and Myint, T. (2014). Active tectonics and earthquake potential of the Myanmar region. *J. Geophys. Res. Solid Earth*, 119:3767–3822. doi:10.1002/2013JB010762.
- Wang, Y., Zhang, B., Schoenbohm, L. M., Zhang, J., Zhou, R., Hou, J., and Ai, S. (2016b). Late Cenozoic tectonic evolution of the Ailao Shan-Red River fault (SE Tibet): Implications for kinematic change during plateau growth. *Tectonics*, 35:1969–1988. doi:10.1002/2016TC004229.
- White, R. and Klitgord, K. (1976). Sediment deformation and plate tectonics in the Gulf of Oman. *EPSL*, 32:199–209.
- White, R. S. and Loudon, K. E. (1982). The Makran continental margin: structure of a thickly sedimented convergent plate boundary. In Watkins, J. and Drake, C., editors, *Stud. Cont. Margin Geol.*, volume 34, pages 499–518.
- White, R. S. and Ross, D. A. (1979). Tectonics of the western Gulf of Oman. *JGR*, 84(B7):3479–3489. doi:10.1029/JB084iB07p03479.
- Xu, Q., Hoke, G. D., Liu-Zeng, J., Ding, L., Wang, W., and Yang, Y. (2014). Stable isotopes of surface water across the Longmenshan margin of the eastern Tibetan Plateau Qiang. *Geochemistry, Geophys. Geosystems*, 15:3416–3429. doi:10.1002/2014GC005252.
- Xu, Q., Liu, X., and Ding, L. (2016). Miocene high-elevation landscape of the eastern Tibetan Plateau. *Geochemistry, Geophys. Geosystems*, 17(10):4254–4267. doi:10.1002/2016GC006437.
- Yamini-Fard, F. and Hatzfeld, D. (2008). Seismic Structure Beneath Zagros-Makran Transition Zone (Iran) from Teleseismic Study: Seismological Evidence for Underthrusting and Buckling of the Arabian Plate beneath Central Iran. *JSEE*, 10(1):11–24.
- Yamini-Fard, F., Hatzfeld, D., Farahbod, A. M., Paul, A., and Mokhtari, M. (2007). The diffuse transition between the Zagros continental collision and the Makran oceanic subduction (Iran): microearthquake seismicity and crustal structure. *Geophys. J. Int.*, 170:182–194. doi:10.1111/j.1365-246X.2006.03232.x.
- Yang, R., Willett, S. D., and Goren, L. (2015). In situ low-relief landscape formation as a result of river network disruption. *Nature*, 520:526–529. doi:10.1038/nature14354.

- Ye, L., Lay, T., Kanamori, H., and Rivera, L. (2016). Rupture Characteristics of Major and Great ($M_w \geq 7.0$) Megathrust Earthquakes from 1990-2015 : II . Depth-Dependence. *J. Geophys. Res. Solid Earth*, 121:845–863. doi:10.1002/2015JB012427.
- Yong, L., Allen, P. A., Densmore, A. L., and Qiang, X. (2003). Evolution of the Longmen Shan Foreland Basin (Western Sichuan, China) during the Late Triassic Indosinian orogeny. *Basin Res.*, 15:117–138. doi:10.1046/j.1365-2117.2003.00197.x.
- Zhang, Z., Yuan, X., Chen, Y., Tian, X., Kind, R., Li, X., and Teng, J. (2010). Seismic signature of the collision between the east Tibetan escape flow and the Sichuan Basin. *EPSL*, 292(3-4):254–264. doi:10.1016/j.epsl.2010.01.046.
- Zheng, G., Wang, H., Wright, T. J., Lou, Y., Zhang, R., Zhang, W., Shi, C., Huang, J., and Wei, N. (2017). Crustal deformation in the India-Eurasia collision zone from 25 years of GPS measurements. *J. Geophys. Res. Solid Earth*, 122:9290–9312. doi:10.1002/2017JB014465.
- Zhou, H., Liu, H. L., and Kanamori, H. (1983). Source processes of large earthquakes along the Xianshuihe fault in southwestern China. *Bull. Seismol. Soc. Am.*, 73(2):537–551.
- Zhou, Y., Elliott, J. R., Parsons, B., and Walker, R. T. (2015). The 2013 Balochistan earthquake: An extraordinary or completely ordinary event? *Geophys. Res. Lett.*, 42:6236–6243. doi:10.1002/2015GL065096.
- Zinke, R., Hollingsworth, J., and Dolan, J. (2014). Slip and off-fault deformation patterns in the 2013 MW 7.7 Balochistan, Pakistan earthquake: Implications for controls on the distribution of near-surface coseismic slip. *Geochemistry, Geophys. Geosystems*, 15:5034–5050. doi:10.1002/2014GC005538.
- Zwick, P., McCaffrey, R., and Abers, G. (1994). MT5 program. Technical report, IASPEI Software Library 4.

Appendix A

Body-Waveform Modelling

This appendix shows my minimum misfit earthquake solutions from body-waveform modelling, for events in the Makran and the aftershocks of the Minab earthquake. I use Zwick et al. (1994)'s MT5 implementation of the method proposed by McCaffrey and Abers (1988) and McCaffrey et al. (1991). I use teleseismic (30° – 90° epicentral distance) P and SH arrivals at GDSN stations downloaded from the IRIS DMC. These are deconvolved from their original instrument response and reconvolved with a WWSSN Long Period (15–100) response. Earthquakes are modelled as double-couple point sources and I invert direct waves and their associated depth phases for centroid depth, source geometry (strike, dip and rake), seismic moment and source-time function. The arrivals are manually picked from the broadband seismogram where possible. The details of this technique have been described extensively elsewhere (e.g. Taymaz, 1990; Maggi et al., 2000b) and a summary of the main points is given in Section 2.2 so will not be repeated here. A realistic velocity model for this region is likely to be highly complex but, since the velocity structure is not well-constrained, I adopt a simplified velocity model. For the aftershocks of the Minab earthquake I use the velocity model described in Chapter 2. For the 7th February 2017 event I use a single layer velocity model with V_p 6.5 km/s, V_s 3.7 km/s and density 2800 kg/m³. Four of the earthquakes for which I present solutions had catalogue depths significantly deeper than 40 km, which is the Moho depth reported in this region (Maggi et al., 2000b; Manaman et al., 2011). For these events I use a two-layer velocity model; a 40 km upper layer with V_p 6.5 km/s, V_s 3.75 km/s and density 2860 kg/m³ and a half-space with V_p 7.8 km/s, V_s 4.5 km/s and density 3300 kg/m³. The other two events have EHB depths of \sim 40 km, making the choice of velocity model problematic. I try the two-layer velocity model described above in both cases but find that a simpler single layer model with V_p 6.5 km/s, V_s 3.7 km/s and density 2800 kg/m³ is sufficient to provide a good fit to the data.

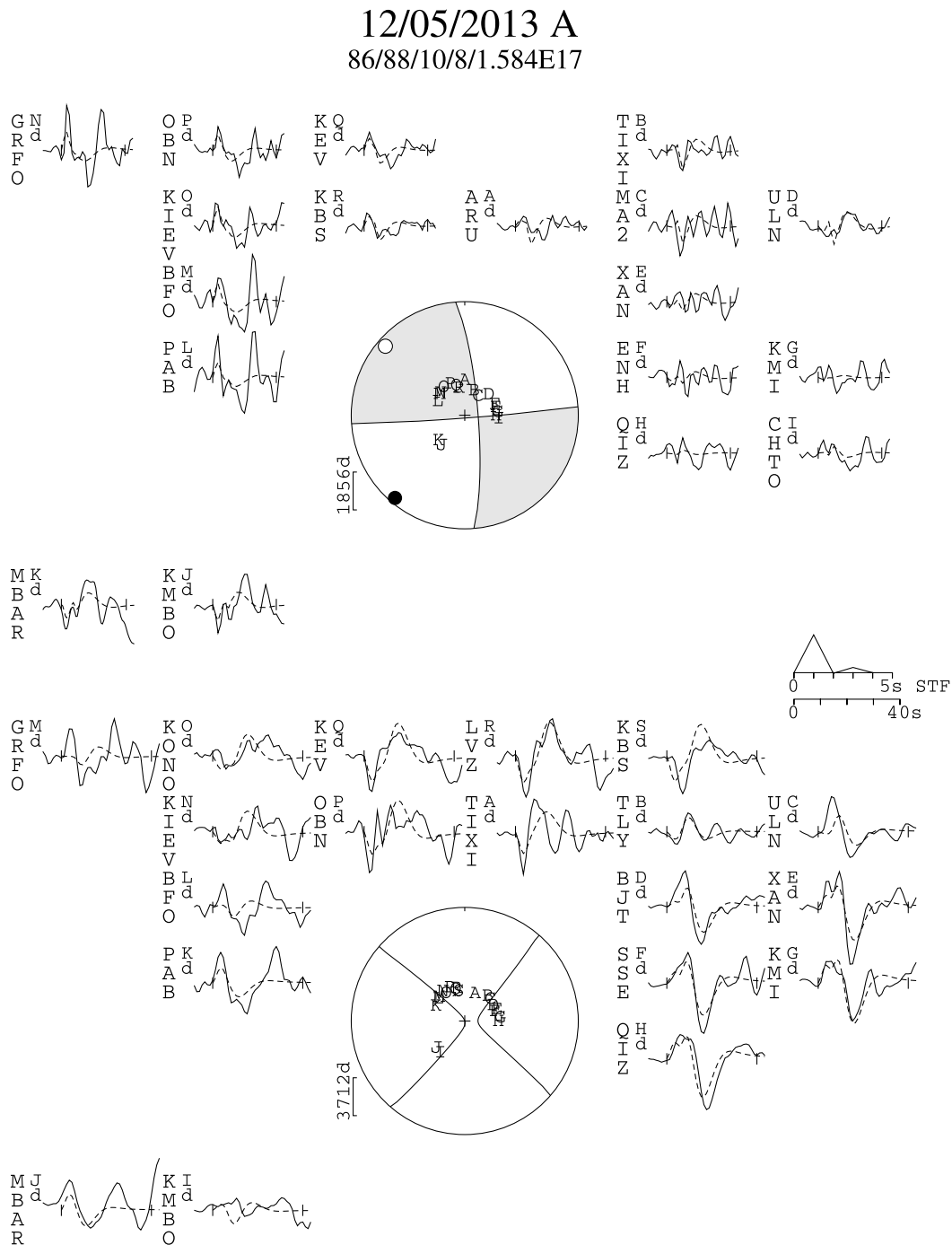


Figure A.1: 12th May 2013, largest aftershock of Minab earthquake. The top panel shows the P-wave focal mechanism and P-wave arrivals (plotted with twice the magnification of SH-wave arrivals), the bottom panel shows the SH-wave focal mechanism and SH-wave arrivals. Solid lines are recorded seismograms, dashed lines are the synthetics corresponding to the minimum misfit model. The timescale for the seismograms is shown in the bottom right of the top panel, beneath the source-time function. Each station is labelled with a letter which is then plotted on the focal sphere to show the station's location. Stations marked with an asterisk were not included in the inversion. The tension axis is plotted on the focal sphere as an open circle, the pressure axis as a filled circle. Numbers under title give source parameters for the minimum misfit solution: strike 86° , dip 88° , rake 10° , depth 8 km, seismic moment 1.58×10^{17} Nm. The other nodal plane has strike 356° , dip 80° , rake 178° .

12/05/2013 B
85/85/5/9/1.437E17

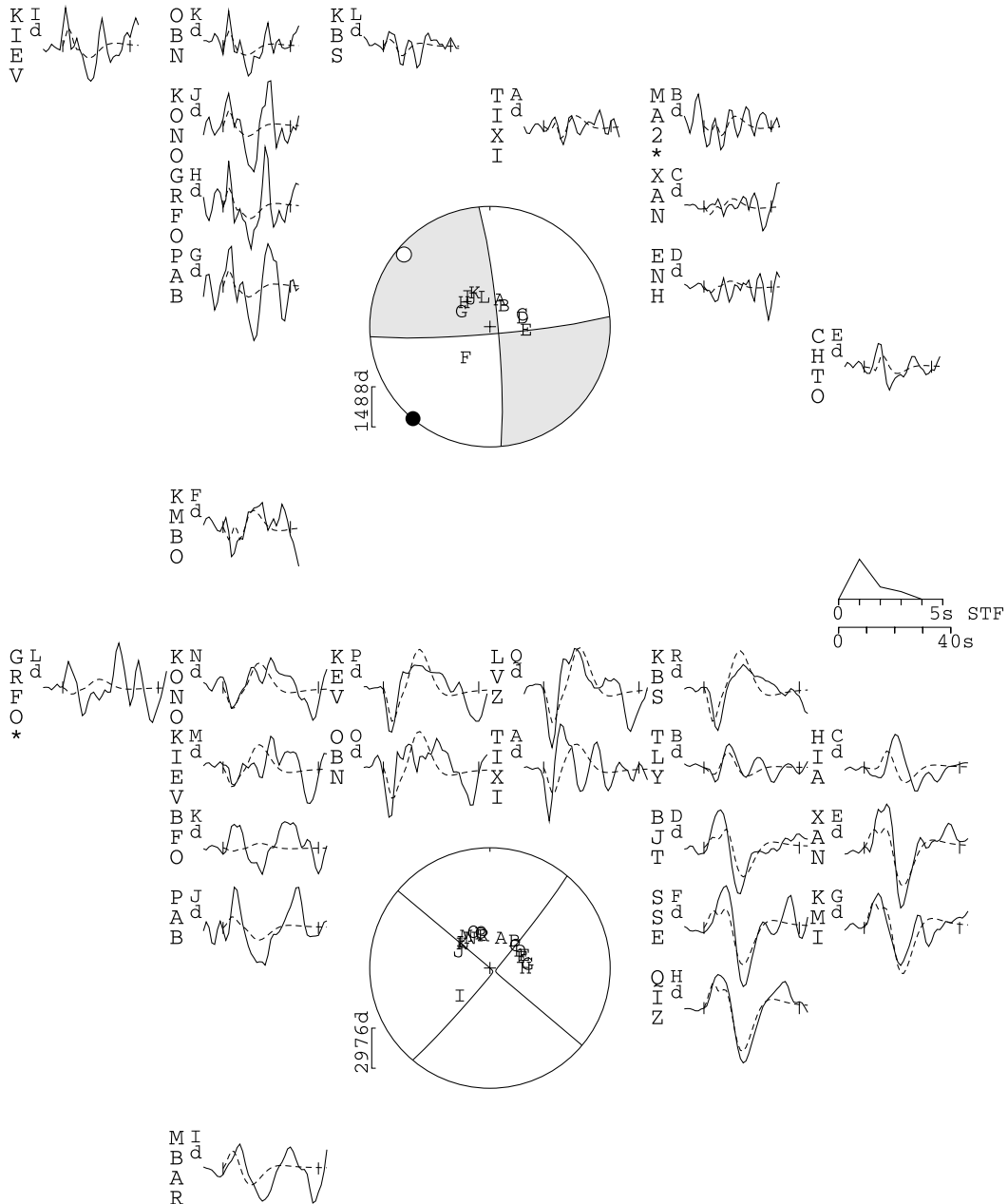


Figure A.2: 12th May 2013, aftershock of Minab earthquake. Minimum misfit solution: strike 85° , dip 85° , rake 5° , depth 9 km. The other nodal plane has strike 355° , dip 85° , rake 175° . Layout as for Figure A.1.

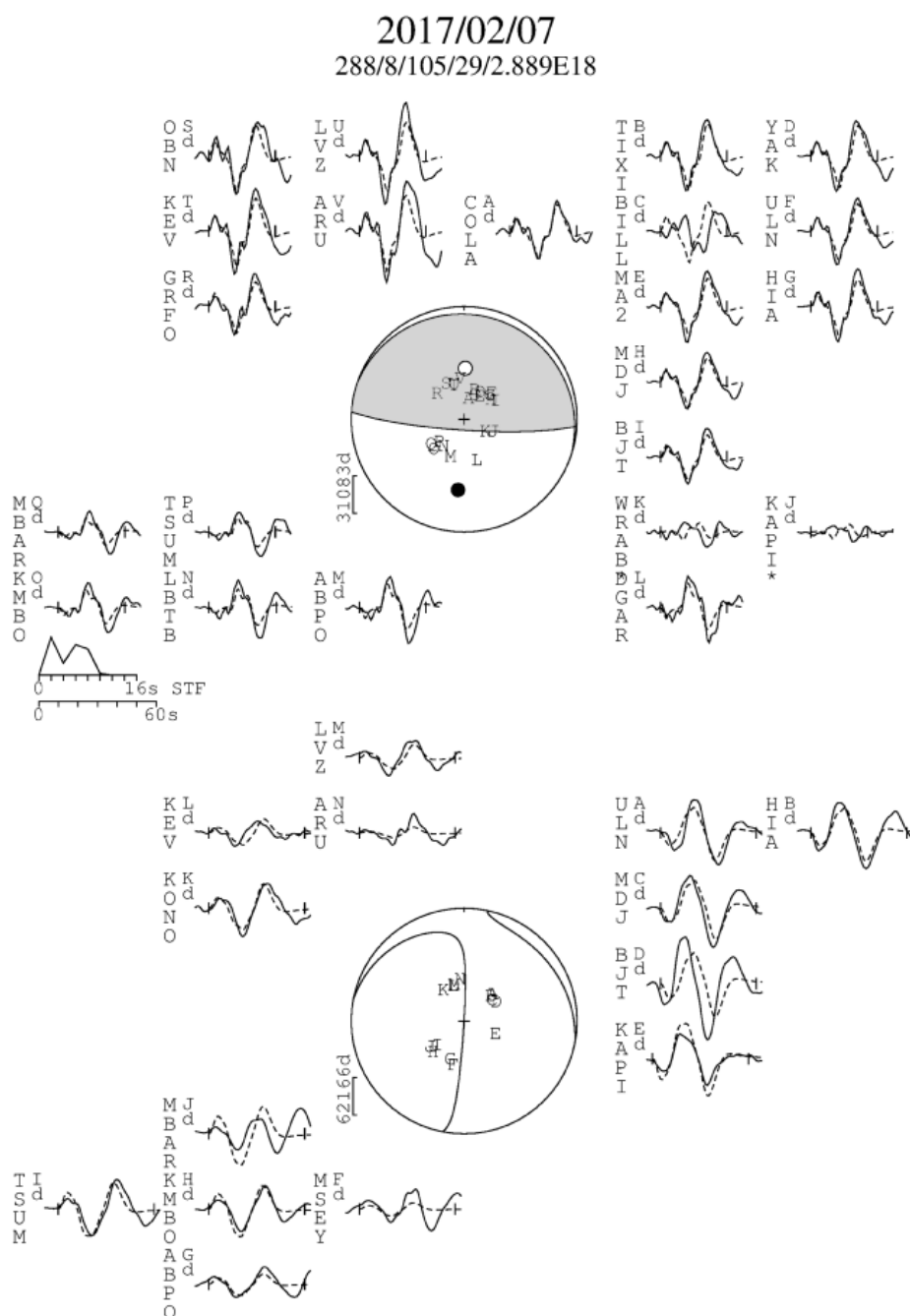


Figure A.3: 7th February 2017, offshore central Makran, near Pasni. Layout as for Figure A.1. Minimum misfit solution: strike 288° , dip 8° , rake 105° , depth 29 km and seismic moment 2.89×10^{18} Nm. The source-time function is unusually long for an earthquake of this size, suggesting that this may have been a double event. However, the misfit between the synthetic and observed seismograms is low so any second event is likely to have had a similar focal mechanism.

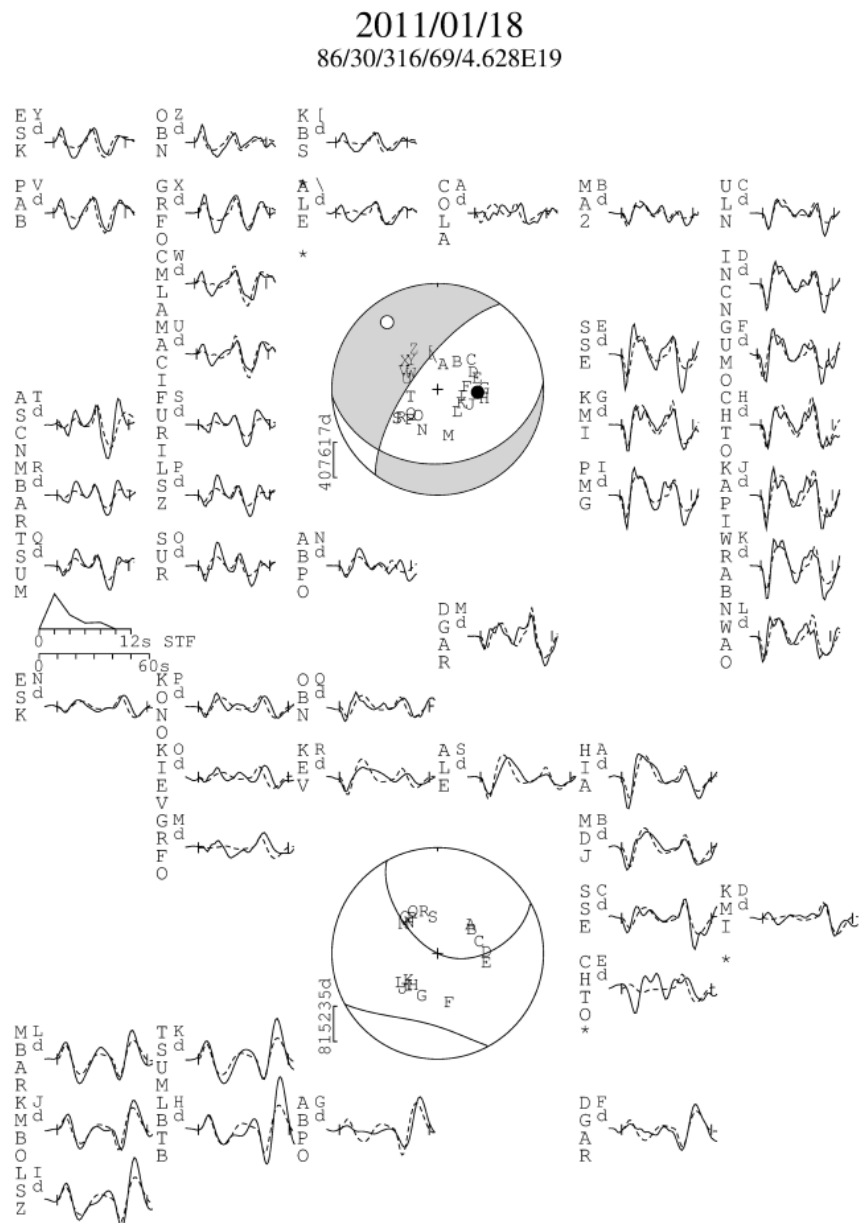


Figure A.4: 18th January 2011, north-eastern Makran, ~50km west of Dalbandin. Layout as for Figure A.1. Minimum misfit solution: strike 86° , dip 29° , rake 316° , depth 69 km.

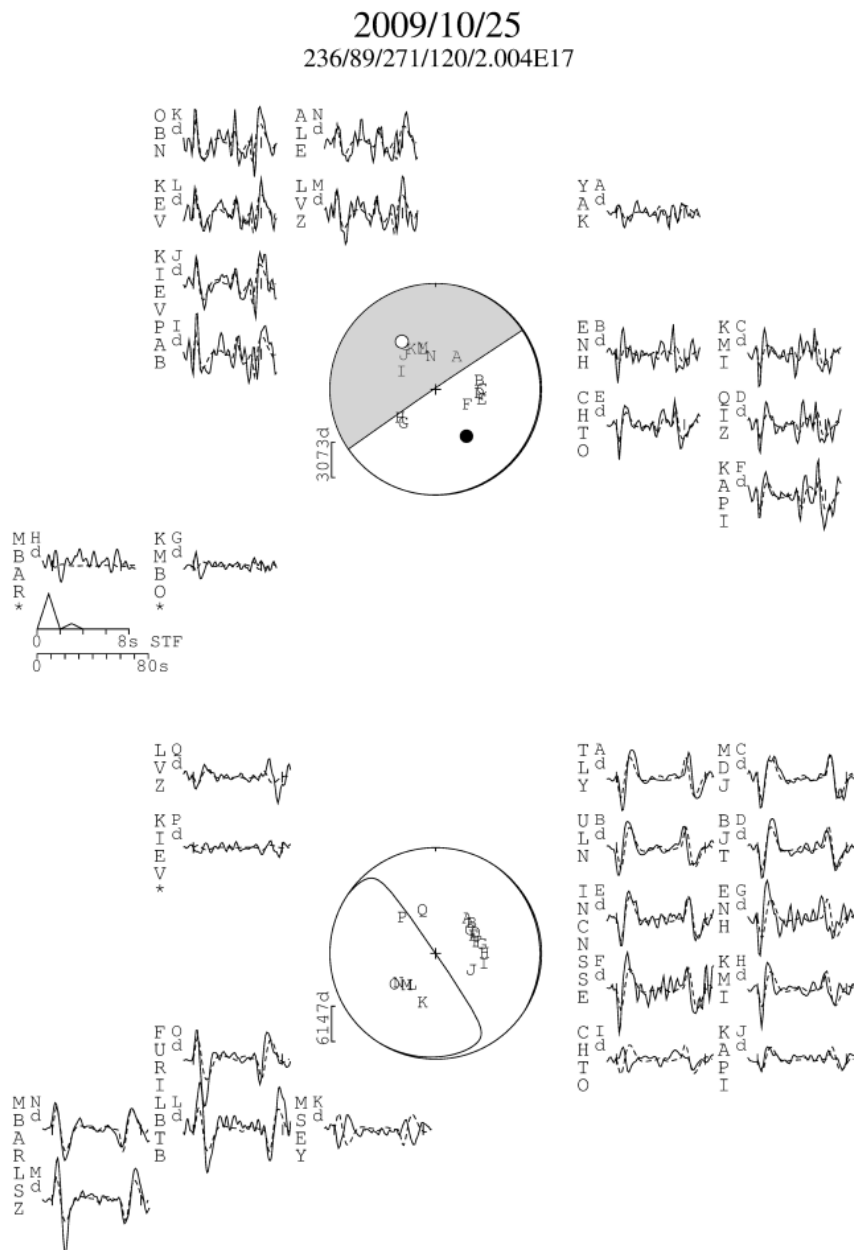


Figure A.5: 25th October 2009, southern Afghanistan. Layout as for Figure A.1. Minimum misfit solution: strike 236° , dip 89° , rake 271° , depth 120 km.

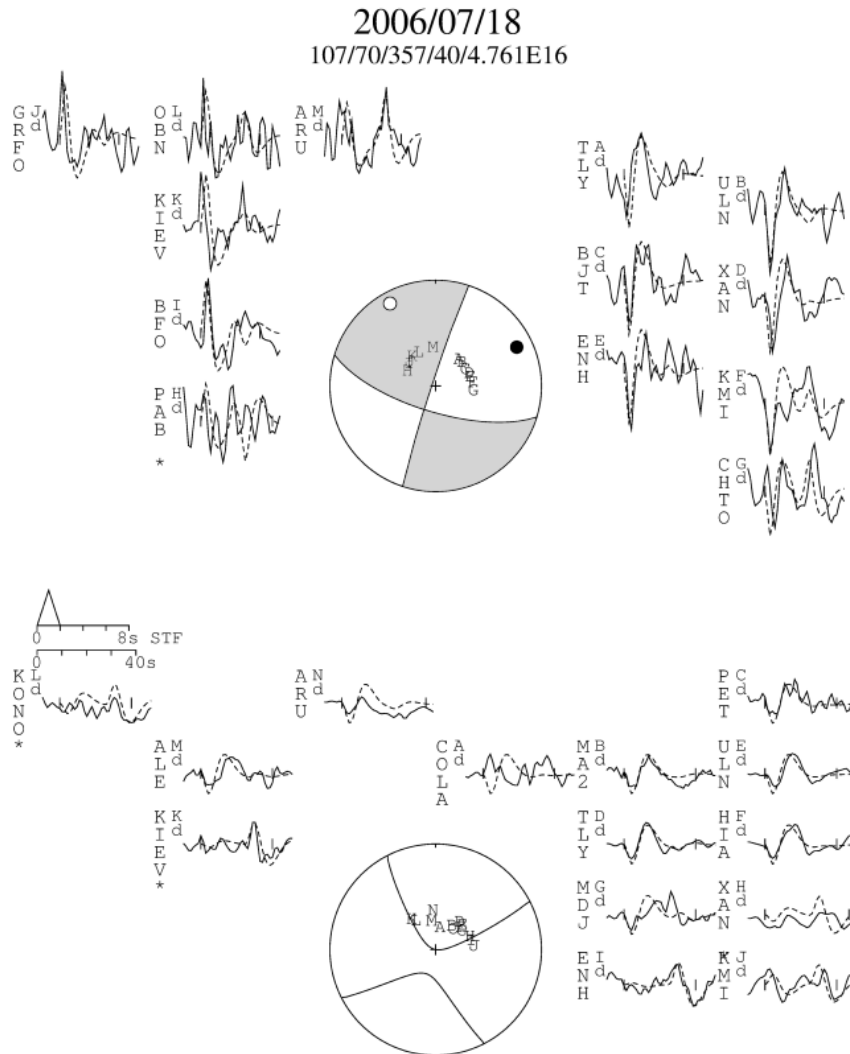


Figure A.6: 18th July 2006, central Makran. Layout as for Figure A.1. Minimum misfit solution: strike 107° , dip 70° , rake 357° , depth 40 km. Although many of the waveforms are noisy ARU (P), KIEV (SH) and ENH (SH) provide tight constraints on the depth.

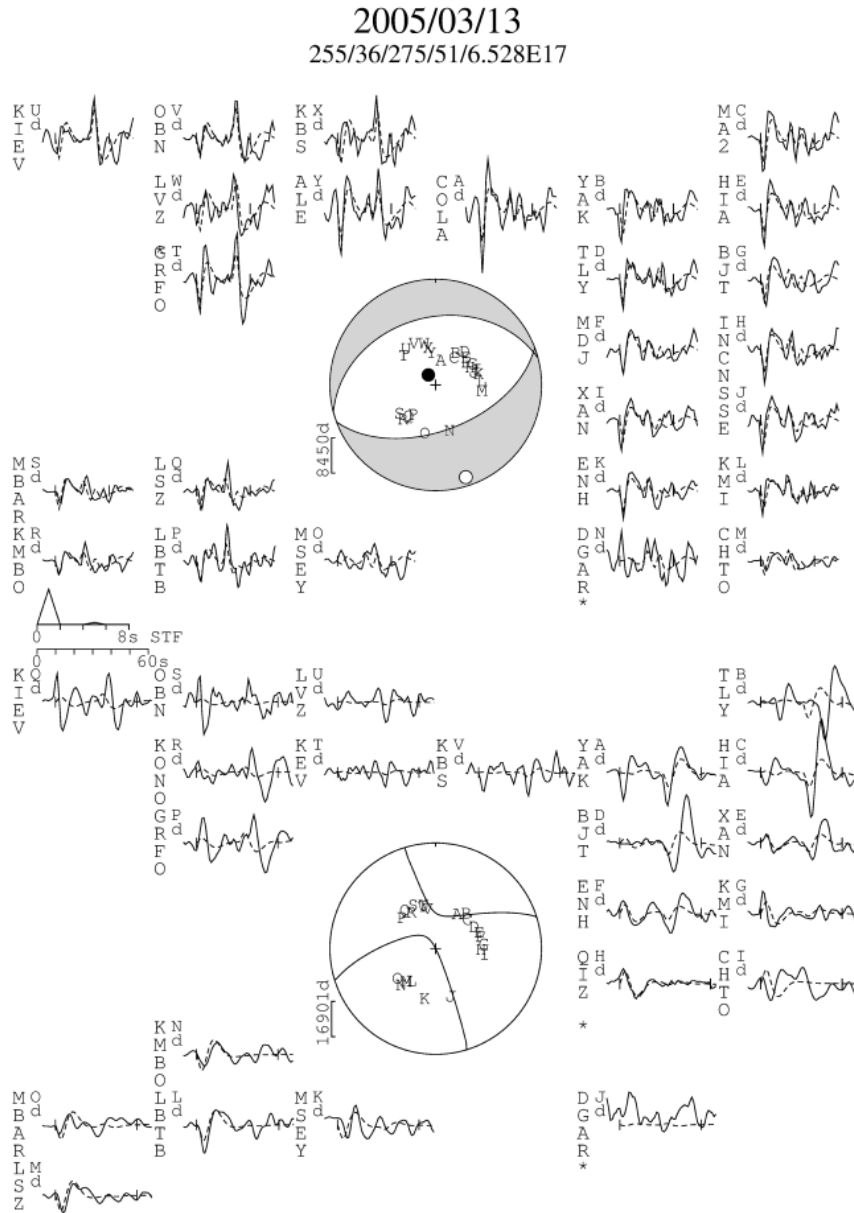


Figure A.7: 13th March 2005, north-central Makran, ~50 km W of Saravand. Layout as for Figure A.1. Minimum misfit solution: strike 255° , dip 36° , rake 275° , depth 51 km.

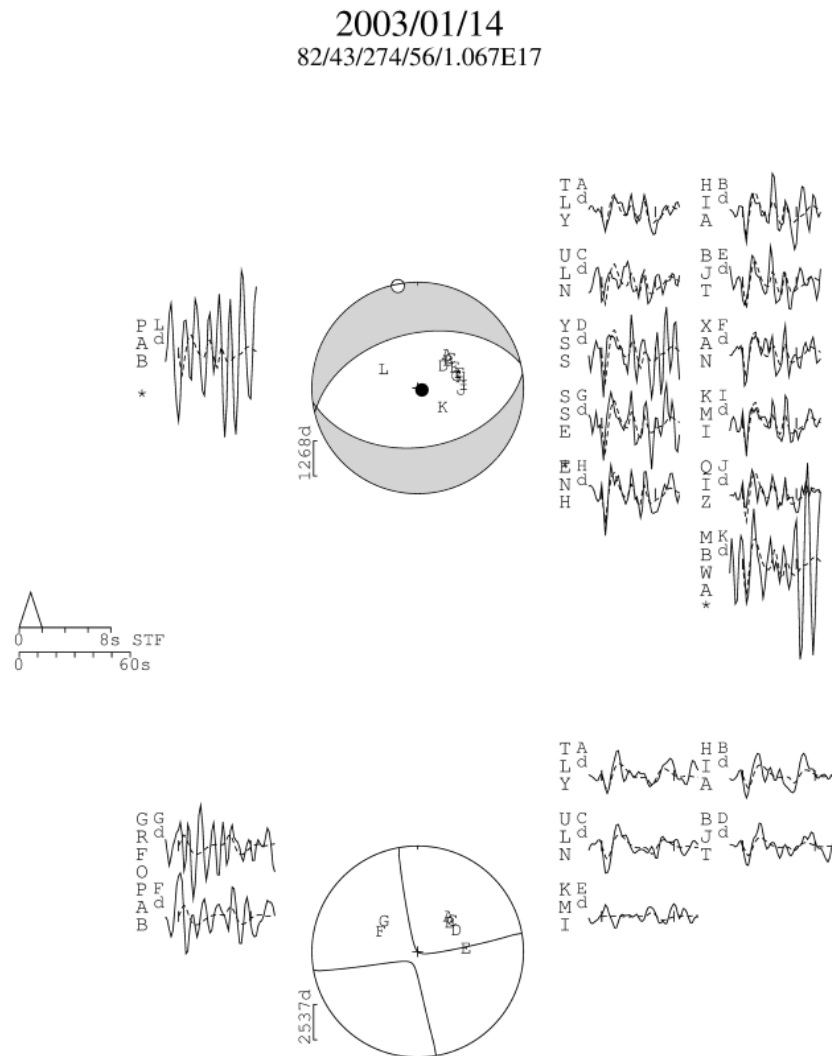


Figure A.8: 14th January 2003, north-central Makran, ~ 100 km E of Khash (the site of a large normal-faulting earthquake in 2013). Layout as for Figure A.1. Minimum misfit solution: strike 82° , dip 43° , rake 274° , depth 56 km.

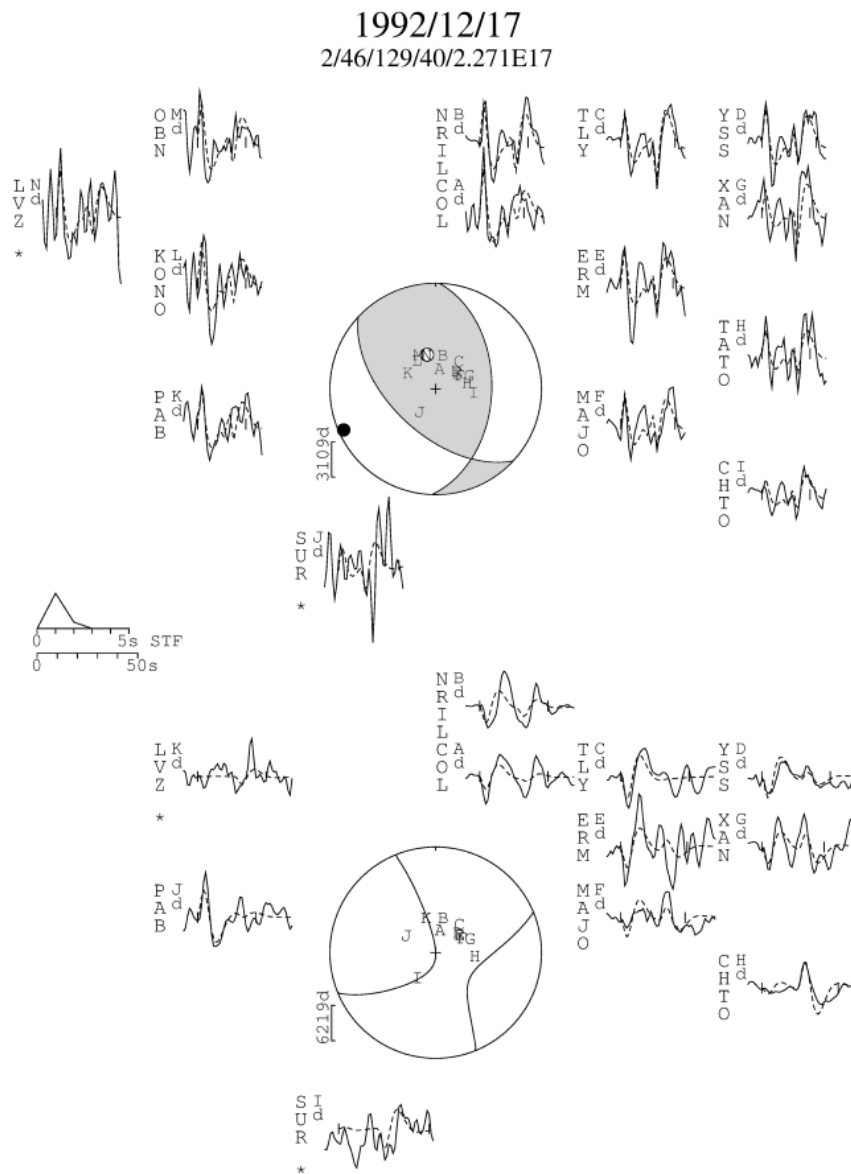


Figure A.9: 17th December 1992, central Makran. Layout as for Figure A.1. Minimum misfit solution; strike 2° , dip 46° , rake 40° , depth 40 km.

Appendix B

Earthquake Compilation

Table B.1 gives the source parameters of the well-constrained earthquakes plotted in Figures 3.2b and 3.4, and references where relevant. 1: Byrne et al. (1992), 2: Jackson and McKenzie (1984), 3: Jacob and Quittmeyer (1979), 4: Baker (1993), 5: Maggi et al. (2000b) († indicates that only the earthquake depth has been waveform modelled, with the mechanism from the CMT), 6: Berberian et al. (2001), 7: Laane and Chen (1989), 8: Berberian et al. (2000), 9: Walker (2003), 10: Nissen et al. (2011), 11: Jackson et al. (2006), 12: Talebian et al. (2006), 13: Nissen et al. (2010), 14: Barnhart et al. (2014b), 15: Jolivet et al. (2014), *: this dissertation.

Date	Time	Lat	Lon	Depth (km)	Mw	Strike	Dip	Rake	Method	Ref
1945/11/27	21:57	25.15	63.48	27	8.1	246	7	89	BWM	1
1947/08/05	14:24	25.04	63.49	20	6.8	236	7	68	BWM	1
1962/09/01	15:51	25.60	65.22	18	5.3	251	10	80	FM	1
1964/12/22	04:37	28.2	57.00	18	6.1	92	76	90	FM	2
1966/10/29	08:59	27.631	65.572	47	-	-	-	-	d	-
1968/08/02	13:30	27.54	60.92	67	5.7	265	70	-80	FM	3
1968/08/03	14:02	25.19	62.87	26	4.7	290	49	-50	FM	1
1968/04/23	12:39	27.736	56.744	21	-	-	-	-	d	-
1969/02/13	11:11	24.99	62.75	28	5.1	279	9	84	FM	1
1969/11/07	18:34	27.80	60.02	74	6.5	279	82	-65	FM	3
1970/11/09	17:41	29.50	56.78	100	5.4	68	19	-124	BWM	4
1970/02/28	19:58	27.811	56.309	12	-	-	-	-	d	-
1970/04/01	23:54	27.918	56.687	28	-	-	-	-	d	-
1971/12/09	01:42	27.297	56.373	9	-	-	-	-	d	-
1972/08/08	19:10	25.14	61.22	18	5.0	95	82	77	BWM	1
1972/08/06	01:13	25.04	61.22	20	5.4	321	17	134	FM	1
1972/08/18	10:03	24.83	63.14	20	4.6	277	9	84	FM	1
1972/11/17	09:09	27.35	59.09	65	5.4	66	70	171	FM	2
1972/06/30	17:49	27.176	56.925	27	-	-	-	-	d	-
1972/08/02	21:33	27.953	56.814	21	-	-	-	-	d	-
1973/09/02	07:23	24.88	63.21	27	5.2	281	23	70	FM	1
1973/04/26	14:30	27.168	60.800	57	-	-	-	-	d	-
1973/08/25	14:58	28.111	56.762	17	-	-	-	-	d	-
1975/07/29	13:25	25.22	63.09	24	5.0	278	27	88	FM	1
1975/03/07	14:26	27.486	56.237	15	-	-	-	-	d	-
1977/03/22	11:57	27.60	56.42	12	6.0	77	34	112	BWM	5
1977/12/10	05:46	27.68	56.60	18	5.6	59	72	68	BWM	5
1977/12/19	23:34	30.851	56.508	7	5.9	231	69	4	ENG	-
1977/03/24	00:13	27.590	56.480	14	-	-	-	-	d	-
1977/04/30	14:35	27.562	56.499	13	-	-	-	-	d	-
1977/06/26	02:25	27.469	56.135	7	-	-	-	-	d	-
1977/06/28	03:44	27.514	56.158	6	-	-	-	-	d	-
1977/09/13	00:16	27.634	56.440	14	-	-	-	-	d	-
1978/02/10	20:51	25.33	62.40	24	5.1	106	85	105	FM	1
1978/03/16	02:01	29.93	66.30	10	5.9	193	89.9	-0.01	FM	2
1978/05/06	11:16	29.84	66.21	15	5.7	193	89.9	-0.01	FM	2
1978/02/22	20:17	28.116	56.885	20	-	-	-	-	d	-
1978/02/23	23:24	28.152	56.846	20	-	-	-	-	d	-
1979/01/10	01:26	26.55	60.95	3	5.8	256	61	13	BWM	1
1979/01/10	15:05	26.48	61.02	2	5.9	230	82	-4	BWM	1
1980/04/28	07:04	27.55	64.48	54	5.5	249	75	-82	BWM	5†
1980/04/28	07:05	27.54	64.50	60	5.3	259	87	-70	FM	1

Table B.1: Source parameters of well-constrained earthquakes.

Date	Time	Lat	Lon	Depth (km)	Mw	Strike	Dip	Rake	Method	Ref
1980/11/28	21:15	27.616	56.534	8	5.4	311	37	134	ENG	-
1980/09/06	21:29	28.505	65.962	9	-	-	-	-	d	-
1981/06/11	7:24	29.86	57.68	20	6.58	169	52	156	BWM	6
1981/07/28	17:22	29.99	57.79	18	6.98	177	69	-176	BWM	6
1981/04/16	10:27	27.715	56.353	29	5.1	125	85	132	ENG	-
1981/06/21	13:08	29.810	57.792	17	-	-	-	-	d	-
1981/07/28	19:05	30.107	57.598	10	-	-	-	-	d	-
1981/07/28	21:54	29.959	57.691	13	-	-	-	-	d	-
1981/10/14	09:12	29.805	57.689	11	-	-	-	-	d	-
1982/02/25	20:13	29.841	57.811	23	-	-	-	-	d	-
1982/07/11	13:19	27.843	56.278	13	-	-	-	-	d	-
1983/04/18	10:58	27.76	62.08	65	6.65	83	32	-67	BWM	7
1983/07/12	11:34	27.61	56.41	17	5.93	227	50	75	BWM	5
1983/02/07	15:06	26.866	57.570	21	6.0	5	42	172	ENG	-
1984/08/06	11:14	30.85	57.19	11	5.29	94	35	86	BWM	4
1984/01/18	14:08	28.005	65.765	8	5.6	349	50	-13	ENG	-
1984/10/02	03:19	26.922	66.253	3	5.3	191	76	0	ENG	-
1984/04/22	13:39	27.628	56.645	23	-	-	-	-	d	-
1984/10/11	05:09	29.476	57.962	14	-	-	-	-	d	-
1985/03/03	13:54	31.805	56.159	7	-	-	-	-	d	-
1985/06/22	12:41	29.450	61.152	13	-	-	-	-	d	-
1986/12/31	16:56	25.259	63.251	24	-	-	-	-	d	-
1987/04/19	05:53	28.00	56.87	19	5.5	219	47	13	BWM	5
1987/08/10	10:52	29.88	63.88	155	5.9	346	31	-50	BWM	5
1987/04/11	23:50	31.609	56.079	7	-	-	-	-	d	-
1987/05/26	19:23	31.595	60.176	16	-	-	-	-	d	-
1988/03/14	02:26	24.977	62.923	23	-	-	-	-	d	-
1989/11/20	04:19	29.90	57.72	10	5.83	145	69	-172	BWM	6
1989/12/07	12:59	25.915	58.970	11	5.9	142	37	103	ENG	-
1990/07/26	06:53	27.35	65.58	8	5.7	216	76	44	BWM	5
1990/09/26	15:32	29.14	60.91	8	5.5	15	76	166	BWM	4
1990/03/04	19:46	28.905	66.361	4	6.1	278	78	-176	ENG	-
1990/03/15	00:12	31.674	60.165	15	5.2	100	82	-1	ENG	-
1990/06/17	17:17	27.402	65.621	14	5.5	115	56	173	ENG	-
1990/08/14	00:50	27.043	66.046	15	5.5	287	71	-170	ENG	-
1990/06/26	04:59	28.433	59.094	12	-	-	-	-	d	-
1991/12/07	14:22	25.153	62.971	29	5.6	309	8	133	ENG	-
1991/08/08	11:12	26.878	65.911	46	-	-	-	-	d	-
1992/12/17	10:39	25.90	61.45	40	5.8	2	46	129	BWM	*
1992/01/20	08:58	27.549	66.118	18	5.5	99	72	170	ENG	-
1992/01/30	05:22	24.947	63.160	27	5.9	298	10	126	ENG	-
1992/02/05	23:10	31.391	66.840	15	5.5	299	87	-177	ENG	-

Table B.1: cont.

Date	Time	Lat	Lon	Depth (km)	Mw	Strike	Dip	Rake	Method	Ref
1992/08/28	00:50	29.193	66.808	7	5.6	118	67	179	ENG	-
1992/09/11	18:24	30.006	60.738	19	5.2	91	25	51	ENG	-
1992/03/09	16:59	27.503	66.197	17	-	-	-	-	d	-
1992/09/11	17:04	29.995	60.705	14	-	-	-	-	d	-
1993/04/12	14:00	28.269	57.130	29	5.0	292	44	97	ENG	-
1993/02/04	19:41	24.845	62.846	26	-	-	-	-	d	-
1993/12/19	11:45	25.245	62.573	25	-	-	-	-	d	-
1994/02/23	08:02	30.80	60.57	7	6.05	143	29	96	BWM	8
1994/02/24	00:11	30.82	60.53	10	6.20	155	45	110	BWM	8
1994/02/26	02:31	30.78	60.55	5	5.95	146	36	107	BWM	8
1994/02/28	11:13	30.82	60.55	6	5.49	122	33	78	BWM	8
1994/12/10	12:16	27.90	64.94	72	5.1	204	37	-130	BWM	5†
1994/02/23	11:54	30.830	60.514	9	5.5	108	31	62	ENG	-
1996/03/04	01:35	27.523	56.236	14	-	-	-	-	d	-
1996/04/10	21:50	28.080	56.773	21	-	-	-	-	d	-
1997/10/20	06:09	28.45	57.25	28	5.2	244	19	47	BWM	5
1997/07/27	23:33	27.419	56.621	22	5.1	108	76	175	ENG	-
1997/01/24	17:12	28.168	57.533	39	-	-	-	-	d	-
1997/02/17	04:31	27.376	56.141	17	-	-	-	-	d	-
1997/04/19	22:31	27.860	56.800	21	-	-	-	-	d	-
1997/09/08	06:31	24.218	63.260	27	-	-	-	-	d	-
1997/10/06	16:09	28.428	57.209	29	-	-	-	-	d	-
1998/03/14	19:40	30.08	57.61	5	6.57	156	54	-165	BWM	6
1998/06/10	8:30	28.22	58.49	85	5.25	235	87	-96	BWM	5
1998/01/05	16:58	28.947	64.364	15	5.1	48	37	104	ENG	-
1998/04/19	19:57	25.007	63.275	25	-	-	-	-	d	-
1998/05/28	20:32	26.551	62.167	36	-	-	-	-	d	-
1999/03/04	05:38	28.34	57.19	28	6.2	314	18	128	BWM	9
1999/01/14	22:12	28.951	56.288	25	5.0	210	44	-57	ENG	-
2001/05/26	23:14	31.670	63.742	17	-	-	-	-	d	-
2001/08/04	14:07	24.985	61.460	28	-	-	-	-	d	-
2001/08/12	11:03	27.519	57.691	19	-	-	-	-	d	-
2001/08/14	21:19	29.939	65.141	27	-	-	-	-	d	-
2001/11/22	17:00	27.731	57.476	25	-	-	-	-	d	-
2002/03/11	20:06	25.191	56.087	27	5.0	224	32	-103	ENG	-
2002/06/03	20:17	25.499	63.501	30	-	-	-	-	d	-
2003/01/14	14:14	27.97	62.33	56	5.4	82	43	-86	BWM	*
2003/02/14	10:29	27.96	56.78	23	5.2	312	25	115	BWM	10

Table B.1: cont.

Date	Time	Lat	Lon	Depth (km)	Mw	Strike	Dip	Rake	Method	Ref
2003/12/26	01:57	28.90	58.28	6	6.6	354	86	-178	BWM	11
2003/12/26	01:57	28.90	58.28	7	6.1	180	64	150	BWM	11
2003/06/24	06:52	27.301	61.010	60	5.5	97	45	-65	ENG	-
2003/07/06	16:04	27.953	57.710	24	5.0	102	48	7	ENG	-
2003/11/05	07:58	27.416	56.114	17	4.9	70	39	105	ENG	-
2003/03/25	01:33	27.704	65.165	50	-	-	-	-	d	-
2004/01/28	09:06	26.881	57.460	26	5.2	92	40	24	ENG	-
2005/02/22	02:25	30.77	56.74	7	6.4	270	60	104	BWM	12
2005/03/13	03:31	27.08	61.86	51	5.8	255	36	-85	BWM	*
2006/07/18	23:27	26.24	61.14	40	5.1	107	70	-3	BWM	*
2006/02/28	07:31	28.13	56.82	15	5.9	302	12	113	BWM	10
2006/08/31	02:28	30.267	57.545	19	-	-	-	-	d	-
2006/09/09	12:22	25.019	62.112	28	-	-	-	-	d	-
2008/09/17	17:43	26.96	56.10	6	5.1	269	56	88	BWM	13
2009/10/25	17:48	29.54	63.90	120	5.6	236	89	-89	BWM	*
2009/02/02	08:36	27.180	66.453	15	5.2	189	81	-6	ISC	-
2009/11/03	23:26	27.261	56.195	23	5.1	246	30	63	ISC	-
2010/12/20	18:42	28.33	59.19	5	6.5	213	85	173	BWM	9
2010/06/05	16:59	28.076	66.095	16	5.1	196	83	6	ISC	-
2010/07/31	06:52	29.582	56.748	15	5.5	211	60	-25	ISC	-
2010/08/14	20:18	28.244	66.394	27	5.2	208	83	-5	ISC	-
2011/01/18	20:23	28.70	63.98	69	7.1	216	70	-112	BWM	*
2011/01/27	08:39	28.17	59.04	9	6.2	221	87	176	BWM	9
2011/01/27	07:02	28.174	58.940	22	5.0	122	64	-29	ISC	-
2011/01/28	04:20	28.129	59.040	26	5.3	133	74	-14	ISC	-
2011/03/05	20:42	28.281	57.130	28	5.2	93	87	86	ISC	-
2011/06/15	01:05	27.950	57.657	33	5.5	333	45	157	ISC	-
2011/06/26	19:46	30.035	57.653	25	5.2	114	36	71	ISC	-
2011/07/24	10:38	28.218	66.417	32	5.0	213	64	8	ISC	-
2011/08/10	00:53	27.767	65.136	44	5.9	11	72	-163	ISC	-
2012/02/27	18:48	31.401	56.778	24	5.3	89	40	59	ISC	-
2012/04/18	17:40	27.861	58.106	71	5.2	76	54	-164	ISC	-
2013/04/16	10:44	28.11	62.05	60	7.7	233	59	-109	BWM	14
2013/05/11	02:08	26.55	57.73	6	6.4	259	89	5	BWM	*
2013/05/12	00:07	26.39	57.52	8	5.5	86	88	10	BWM	*
2013/05/12	10:54	26.71	57.77	9	5.4	85	85	5	BWM	*
2013/09/24	11:30	26.50	65.50	15	7.7	230	47	8	BWM	15
2013/09/28	07:34	27.10	65.50	15	6.7	200	70	26	BWM	15
2013/01/21	19:48	30.356	57.518	15	5.4	235	70	13	ISC	-
2017/02/07	22:03	25.22	63.27	29	6.3	288	8	105	BWM	*

Table B.1: cont.

Appendix C

Vertical-Axis Rotations

C.1 Vertical-Axis Rotations accommodating Simple Shear

This appendix discusses vertical-axis rotations accommodating simple shear; the kinematic regime which I proposed in section 2.6.1 for the Minab earthquake. Here I apply the same principle to look at how a series of rotating blocks could accommodate right-lateral shear at the southern end of the Sistan Suture Zone, as discussed in section 4.3.

For a series of blocks of length L and width W to accommodate an amount of right-lateral shear, y , they must rotate through an angle θ (Figure C.1), given by:

$$\theta = \arcsin\left(\frac{y}{L}\right). \quad (\text{C.1})$$

The amount of left-lateral slip on each block-bounding fault, q , is then:

$$q = W \tan(\theta). \quad (\text{C.2})$$

Although there is no time-dependence in these equations, if y is taken as the per year right-lateral slip then the seismic moment accumulated per year will be:

$$M_0 = \mu L D q, \quad (\text{C.3})$$

where μ is the shear modulus of the rock, taken here as $3 \times 10^{10} \text{N/m}^2$ and D is the downdip width of the fault plane.

Substituting (C.1) and (C.2) into (C.3) we find

$$\begin{aligned}
 M_0 &= \mu L D W \tan \left(\arcsin \left(\frac{y}{L} \right) \right), \\
 &= \mu L D W \tan \left(\arctan \left(\frac{\frac{y}{L}}{\left(\sqrt{1 - \left(\frac{y}{L} \right)^2} \right)} \right) \right), \\
 &= \frac{\mu D W y}{\sqrt{1 - \left(\frac{y}{L} \right)^2}}, \\
 &= \mu D W y + O \left(\left(\frac{y}{L} \right)^2 \right),
 \end{aligned}$$

i.e. to first order the seismic moment is independent of $\frac{y}{L}$, which is small since $L \gg y$. By considering the number of blocks of given W which can fit between 27° N and the coast, and multiplying the moment accumulated on each fault by the number of blocks, I can estimate the moment accumulated per year across the whole system for a given y . With a distance to the coast λ , the total moment is:

$$M_{0_{tot}} = \frac{\mu D y \lambda}{\sqrt{1 - \left(\frac{y}{L} \right)^2}},$$

which, to first order, is independent of both length and width as discussed in Section 4.3.

C.2 Vertical-Axis Rotations accommodating Pure Shear

In section 5.2 I discussed how block rotations could allow shortening across the Hoshab fault without significant lateral extension. This appendix shows the calculations for the rotation rate.

The geometry shown in Figure C.2 allows the derivation of an expression for the angle of rotation, θ . First finding expressions for the lengths AB and BB' :

$$AB = \frac{2W}{\cos(\alpha)} = AB', \quad (C.4)$$

$$BB' = \frac{4W \sin\left(\frac{\theta}{2}\right)}{\cos(\alpha)}, \quad (C.5)$$

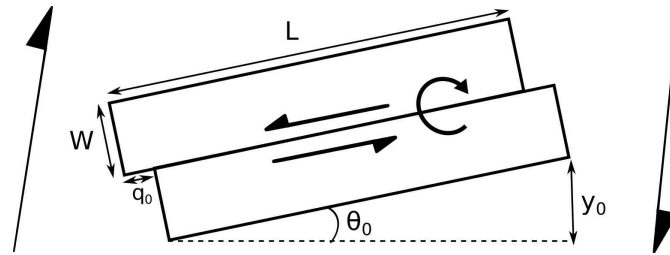


Figure C.1: Geometry of vertical-axis rotations accommodating simple shear on horizontal planes, discussed in Sections 2.6.1, 4.3 and C.1. L and W are the block dimensions, q is the amount of slip on the fault between the blocks (if the blocks start aligned), y is the amount of right-lateral shear accommodated and θ is the angle of the blocks anticlockwise from East.

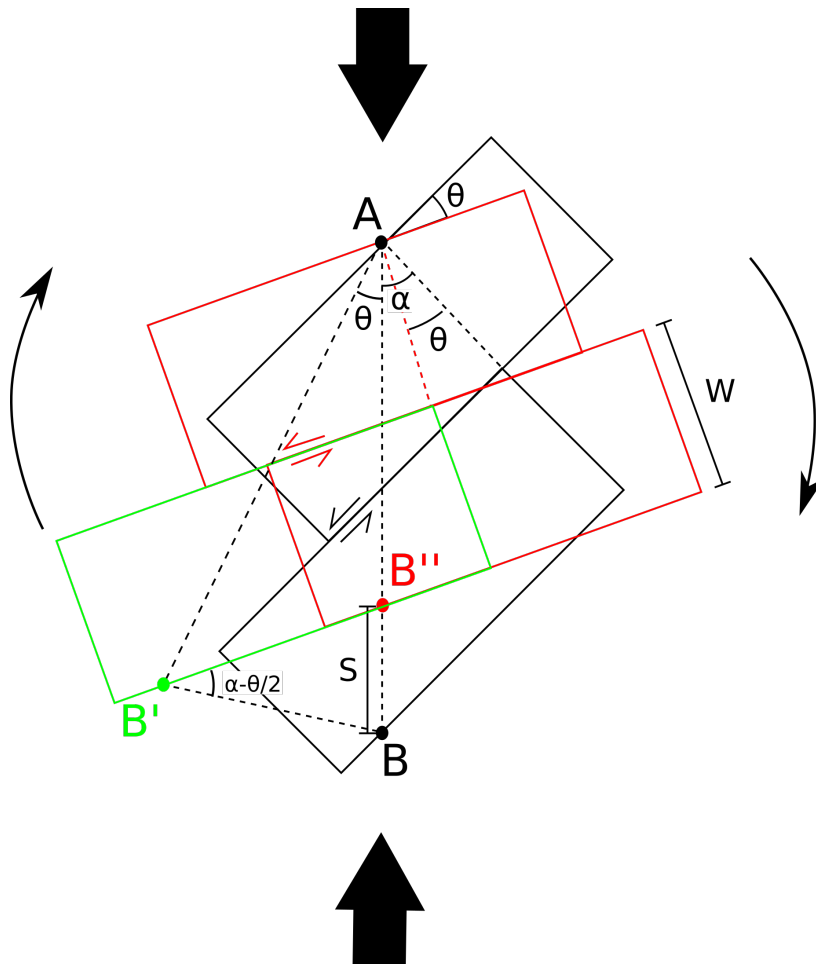


Figure C.2: Geometry of vertical-axis rotations accommodating pure shear, as described in Sections 5.2 and C.2. Red blocks show initial configuration, green block is after rotation by θ about A, and red is after strike-slip motion such that B'' is directly north of B. The green block is only to make the geometry of the calculation clearer. The relative timing of rotation and strike-slip motion are not important.

$$\begin{aligned}\frac{S}{\sin\left(\alpha - \frac{\theta}{2}\right)} &= \frac{4W \sin\left(\frac{\theta}{2}\right)}{\cos(\alpha)} \frac{1}{\sin\left(\frac{\pi}{2} - \alpha + \theta\right)}, \\ S \cos(\theta - \alpha) &= \frac{4W \sin\left(\frac{\theta}{2}\right)}{\cos(\alpha)} \sin\left(\alpha - \frac{\theta}{2}\right), \\ S(\cos(\theta) \cos(\alpha) + \sin(\theta) \sin(\alpha)) &= \frac{4W \sin\left(\frac{\theta}{2}\right)}{\cos(\alpha)} \sin\left(\alpha - \frac{\theta}{2}\right).\end{aligned}$$

Then assuming that θ is small:

$$\begin{aligned}S(\cos(\alpha) + \theta \sin(\alpha)) &= \frac{2W\theta \sin(\alpha)}{\cos(\alpha)} + O(\theta^2), \\ \theta &\approx \frac{S \cos^2(\alpha)}{\sin(\alpha)(2W - S \cos(\alpha))}.\end{aligned}\tag{C.6}$$

The amount of strike-slip motion ($B'B''$) on the fault is:

$$\begin{aligned}\frac{B'B''}{\sin\left(\frac{\pi}{2} - \frac{\theta}{2}\right)} &= \frac{4W \sin\left(\frac{\theta}{2}\right)}{\cos(\alpha) \sin\left(\frac{\pi}{2} - \alpha + \theta\right)}, \\ \frac{B'B''}{\cos\left(\frac{\theta}{2}\right)} &= \frac{4W \sin\left(\frac{\theta}{2}\right)}{\cos(\alpha) \cos(\theta - \alpha)}, \\ B'B'' &= \frac{2W \sin(\theta)}{\cos(\alpha) \cos(\theta - \alpha)}, \\ &= \frac{2W \sin(\theta)}{\cos(\alpha)(\cos(\theta) \cos(\alpha) + \sin(\theta) \sin(\alpha))}, \\ &= \frac{2W \tan(\theta)}{\cos^2(\alpha)} (1 + \tan(\alpha) \tan(\theta))^{-1} \\ B'B'' &= \frac{2W\theta}{\cos^2(\alpha)} + O(\theta^2).\end{aligned}\tag{C.7}$$

There was a shortening component of the motion in the 2013 Balochistan, which Zhou et al. (2015) estimated to be 1.6 m. The shortening accommodated by block rotations is then

$$S = V - \frac{y}{t},\tag{C.8}$$

where V is the total shortening rate, y is the co-seismic shortening and t is the earthquake recurrence interval. Substituting for S in equation (C.6) and using the resulting expression for θ in equation (C.7) gives an expression for the amount of strike-slip motion per unit time, a:

$$a = \frac{2W(Vt - y)t}{\sin(\alpha)(2Wt - (Vt - y) \cos(\alpha))},\tag{C.9}$$

which gives an expression for t :

$$t = \frac{-(a \sin \alpha (V \cos \alpha - 2W) - 2Wy)}{4WV} \pm \frac{\sqrt{4W^2y^2 - 4Wya \sin \alpha (V \cos \alpha - 2W) + a^2 \sin^2 \alpha (V \cos \alpha - 2W)^2 + 8WVya \sin \alpha \cos \alpha}}{4WV}. \quad (\text{C.10})$$

For the Hoshab fault: $\alpha \sim 45^\circ$, $W \sim 60$ km and $V \approx 10$ mm/yr, the difference in southwards velocities between PANG and BEDI (Figure 3.1). This gives $t = 583$ yr. S can then be found from equation (C.8) and substituted into equation (C.6) to find $\theta \approx 2.4^\circ/\text{Myr}$.

Appendix D

Calculating the temporal evolution of topography

This appendix discusses the implementation of the temporal evolution of topography by re-writing the incompressibility condition as a diffusion equation, as discussed in Chapter 6. I first derive the diffusion equation and then discuss its solution.

From conservation of mass

$$\nabla \cdot \mathbf{u} = 0.$$

In cartesian formulation:

$$\begin{aligned} \mathbf{u} &= (u, v, w), \\ \partial_x u + \partial_y v + \partial_z w &= 0. \end{aligned} \tag{D.1}$$

Integrating equation (D.1) over the layer thickness, where s is the z coordinate of the top of the layer, $-b$ is the z coordinate of the base of the layer and H is the layer thickness (Figure 6.4):

$$\begin{aligned} \int_{-b}^s \frac{\partial w}{\partial z} dz &= - \int_{-b}^s \frac{\partial u}{\partial x} + \frac{\partial v}{\partial y} dz, \\ w(s) - w(-b) &= - \int_{-b}^s \nabla_x \cdot \mathbf{u} dz, \quad \text{where } \nabla_x = (\partial_x, \partial_y), \\ &= - \nabla_x \cdot \int_{-b}^s \mathbf{u} dz + u(s) \frac{\partial s}{\partial x} + v(s) \frac{\partial s}{\partial y} - u(-b) \frac{\partial(-b)}{\partial x} - v(-b) \frac{\partial(-b)}{\partial y}. \end{aligned} \tag{D.2}$$

The variation in layer thickness at a point in the domain is given by:

$$\frac{\partial H}{\partial t} = w(s) - w(-b) - u(s) \frac{\partial s}{\partial x} - v(s) \frac{\partial s}{\partial y} + u(-b) \frac{\partial(-b)}{\partial x} + v(-b) \frac{\partial(-b)}{\partial y}. \tag{D.3}$$

Substituting equation (D.2) into equation (D.3) gives:

$$\frac{\partial H}{\partial t} = - \nabla_x \cdot \int_{-b}^s \mathbf{u} dz,$$

and

$$\begin{aligned}\bar{\mathbf{u}} &= \frac{1}{H} \int_{-b}^s \mathbf{u} \, dz \\ \Rightarrow \frac{\partial H}{\partial t} &= -\nabla \cdot (H\bar{\mathbf{u}}),\end{aligned}\tag{D.4}$$

which is equivalent to equation (22) in Pattyn (2003), neglecting removal or addition of material at the top and base of the flow. I define diffusivities:

$$D_x = \left| \bar{u}H \left(\frac{\partial s}{\partial x} \right)^{-1} \right|,\tag{D.5}$$

$$D_y = \left| \bar{v}H \left(\frac{\partial s}{\partial y} \right)^{-1} \right|.\tag{D.6}$$

Since positive u , v are associated with negative $\frac{\partial s}{\partial x}$, $\frac{\partial s}{\partial y}$, i.e. material flows towards regions with lower topography:

$$\begin{aligned}D_x \left| \frac{\partial s}{\partial x} \right| &= |\bar{u}H|, \\ D_x \frac{\partial s}{\partial x} &= \text{sgn} \left(\frac{\partial s}{\partial x} \right) |\bar{u}H|, \\ &= -\text{sgn}(\bar{u}H) |\bar{u}H|\end{aligned}\tag{D.7}$$

The same expression, substituting u for v and y for x , holds for D_y , meaning that,

$$\frac{\partial H}{\partial t} = (\partial_x (D_x \partial_x s) + \partial_y (D_y \partial_y s)).\tag{D.8}$$

I use a formulation with adaptive vertical grid spacing such that the base and top of the flow are mapped to 0 and 1 respectively (see e.g. Pattyn, 2003; Copley, 2008). The vertical velocity at the base of the flow, $w(-b)$, is therefore set to 0 but b and s will change over time. Here $s = H + b$, since I define z to be positive upwards and $z = 0$ at the height of a column of mantle of density $\rho_m = 3300 \text{ kg/m}^3$ in isostatic balance. Hence,

$$\frac{\partial H}{\partial t} = \nabla_x \cdot (D_x \partial_x H, D_y \partial_y H) + \nabla_x \cdot (D_x \partial_x b, D_y \partial_y b),\tag{D.9}$$

which is written as

$$\frac{\partial H}{\partial t} = \nabla(\mathbf{D}\nabla H) + \nabla(\mathbf{D}\nabla b),$$

in equation (55) of Pattyn (2003). For the isostatic case $H = (f + 1)s$ and $-b = -fs$ where $f = \frac{\rho_c}{\rho_m - \rho_c}$ (McKenzie et al., 2000). Here I take $\rho_c = 2700 \text{ kg/m}^3$, so $f = 4.5$. Substituting for b in (D.9):

$$\frac{\partial H}{\partial t} = \left(1 - \frac{f}{f + 1} \right) (\partial_x (D_x \partial_x H) + \partial_y (D_y \partial_y H)),\tag{D.10}$$

which I write as a sparse matrix equation using a Crank-Nicolson scheme with spatially centred differences. I use a staggered grid for the diffusivities. Away from the boundaries,

this gives:

$$\begin{aligned}
& H_{i-1j}^{n+1} \left(-\alpha_x D_{xi-\frac{1}{2}j} \right) + H_{ij-1}^{n+1} \left(-\alpha_y D_{yij-\frac{1}{2}} \right) + \\
& H_{ij}^{n+1} \left(1 + \alpha_x \left(D_{xi-\frac{1}{2}j} + D_{xi+\frac{1}{2}j} \right) + \alpha_y \left(D_{yij-\frac{1}{2}} + D_{yij+\frac{1}{2}} \right) \right) + \\
& H_{i+1j}^{n+1} \left(-\alpha_x D_{xi+\frac{1}{2}j} \right) + \\
& H_{ij+1}^{n+1} \left(-\alpha_y D_{yij+\frac{1}{2}} \right) = H_{i-1j}^n \left(\alpha_x D_{xi-\frac{1}{2}j} \right) + \\
& H_{ij-1}^n \left(\alpha_y D_{yij-\frac{1}{2}} \right) + \\
& H_{ij}^n \left(1 - \alpha_x \left(D_{xi-\frac{1}{2}j} + D_{xi+\frac{1}{2}j} \right) - \alpha_y \left(D_{yij-\frac{1}{2}} + D_{yij+\frac{1}{2}} \right) \right) + \\
& H_{i+1j}^n \left(\alpha_x D_{xi+\frac{1}{2}j} \right) + H_{ij+1}^n \left(\alpha_y D_{yij+\frac{1}{2}} \right). \quad (\text{D.11})
\end{aligned}$$

where i and j label grid position in the x and y directions respectively, n labels the timestep and

$$\alpha_x = \frac{1}{2dx^2} \left(1 - \frac{f}{f+1} \right) dt,$$

with a similar expression for α_y . As discussed in Section 6.4.2, solving both the x and y terms in the same linear system rather than separating the components, means that the matrix has to be solved using general sparse matrix methods, rather than the simpler methods for tridiagonal systems applicable in the separated case (Reynolds et al., 2015). However, I find that solving a single linear system gives better stability. I initially solved this system of equations for H^{n+1} at each timestep using the linear biconjugate gradient method given by Press et al. (2006, pp.78-82), but find that the generalised minimum residual method (Saad and Schultz, 1986, in sparskit2) is more stable so use this method to obtain the results presented here.

An issue with the diffusivity formulation is that diffusivities as defined in (D.6) become infinite in regions of zero topographic gradient. Such regions necessarily occur in the symmetric current described here. Physically the situation in which the topographic gradient corresponds to there being no lateral pressure gradient to drive to flow, meaning that $\partial_t H$ should be zero. I find that stability of the model, and the form of the results, are not significantly affected by the whether infinite diffusivities are replaced by a small value or zero.

Boundary Conditions

The choice of boundary conditions is critical in any modelling study. In the formulation used here, the velocity equations are solved first and then used as inputs to advance the topography. I therefore apply the boundary conditions in the velocity equations and solve equation (D.4) on the boundaries, with the exception of the fixed height condition on $j = 1$. I use equation (D.4), which explicitly references the velocities, at the lateral boundaries of the model domain since the diffusion formulation is not strictly mass conserving (Pattyn, 2003). Equation (D.4) is solved using forward differences on $x = 0$ and backwards differences on

$x = x_{max}$ and $y = y_{max}$, taking explicit derivatives of $\bar{\mathbf{u}}H$ e.g. for $x = 0$ ($i = 1$):

$$(\partial_t H)_{ij} = -\frac{1}{dx} \left(\bar{u}_{i+1j} \frac{H_{i+1j}^n + H_{i+1j}^{n+1}}{2} - \bar{u}_{ij} \frac{H_{ij}^n + H_{ij}^{n+1}}{2} \right) - \frac{1}{2dy} \left(\bar{v}_{ij+1} \frac{H_{ij+1}^n + H_{ij+1}^{n+1}}{2} - \bar{v}_{ij-1} \frac{H_{ij-1}^n + H_{ij-1}^{n+1}}{2} \right).$$

As discussed in the main text, the assumption that material is supplied at a rate which allows $\frac{\partial u}{\partial y} = 0$, $\frac{\partial v}{\partial y} = 0$ on $y = 0$ may be lead to an inward flux which is unrealistically high. An alternative approach is to use a height-dependent velocity boundary condition:

$$\nabla \cdot (H\bar{\mathbf{u}}) = 0,$$

such that (from equation D.4)

$$\frac{\partial H}{\partial t} = 0.$$

This would increase the time taken for the flow to develop as it leads to a slower influx of material, so could change the appropriate choice of viscosity. However, this would not significantly change the form of the topography.

“The great revelation had never come. The great revelation perhaps never did come. Instead there were little daily miracles, illuminations, matches struck unexpectedly in the dark; here was one.”

Virginia Woolf, *To The Lighthouse*